

Microsystems Manufacturing Technologies for Pharmaceutical Toxicity Testing

Niall Patrick Macdonald

A thesis submitted to

The School of Engineering

College of Science and Engineering

The University of Glasgow

In fulfilment of the requirements for

The Degree of Doctor of Philosophy

29th November 2013

Abstract

To meet the demands of political, ethical and scientific pressures on animal testing, research into possible alternatives is required. Data obtained with animal models often cannot be related to humans. Testing with current cell-based assays, microdosing and pharmacokinetic models contribute to reducing animal testing and improving the drug development process. Micro-fabrication and rapid prototyping techniques offer potential solutions to reduce the need for animal toxicity testing.

The aim of this research was to develop biological platforms for *in vitro* toxicity testing to provide physiologically relevant, high-throughput solutions to reduce animal testing. This was achieved by investigating and integrating microfabrication methods of microfluidics, dielectrophoresis and additive manufacturing.

Three approaches were taken: (i) micro-pattern protein arrays for primary hepatocyte cell culture enclosed within microfluidics devices for high-throughput toxicity testing. It was observed that hepatocytes attached to the micro-pattern within microfluidics and maintained viability, however liver specific functions observed by fluorescence assays, the P450 enzymes, were observed to be reduced compared to Petri dish conditions. (ii) A biomimetic dielectrophoretic cell patterning technique to form liver lobule-like tissue structures within agar on a paper substrate was developed for toxicity testing. Observation of these biomimetic micro liver structures showed high viability (80-90%) and an increase in liver specific function marker albumin protein (20%) compared to control samples after 48 hours. (iii) Rapid prototyping methods were explored with regard to fabrication of microfluidic chips for the automated trapping, imaging and analysis of zebrafish embryos. Monolithic microfluidic chips for zebrafish were developed to be suitable for optical based toxicity assays. The biocompatibility of 3D printed materials was investigated. A method to render the photopolymer Dreve Fototec 7150 compatible with zebrafish culture was observed to provide 100% viability.

Future development of this research will aim to (i) develop the liver lobule-like system to use layers of multiple cell types to form complex micro-liver models using additive manufactured microfluidic systems for toxicity testing. (ii) Automation of zebrafish handling using additive manufactured microfluidic devices for *in-situ* analysis of dechorionated zebrafish for high-throughput toxicity studies.

List of Conferences and Awards

Conferences

Poster presentation entitled: “Additive manufacturing of Lab-on-a-Chip devices: Promises and Challenges”. *SPIE Micro+Nano Materials*, Melbourne, Australia, Dec 2013

Oral presentation entitled: “Development of a biomimetic micro liver through dielectrophoretic patterning in agarose”. *IEEE EMBS PGBiomed*, Guilford, UK, July 2013

Poster presentation entitled: “3D printed miniaturised trapping arrays for the development of automated analysis of zebrafish embryos”. *Engineering Industry Day*, University of Glasgow, UK, 2013

Poster presentation entitled: “Development of a microfluidic biochip for absorption, distribution, metabolism and excretion toxicology studies (ADME-TOX)”. *IEEE EMBS PGBiomed*, Glasgow, UK, 2011

Awards

IEEE UKRI EMBS Medical Engineering presentation prize, IEEE UKRI EMBS, July 2013

Mobility Scholarship, University of Glasgow, School of Engineering, 2012

John Moyes Lessells Scholarship, Royal Society of Edinburgh, June 2010

Table of contents

ABSTRACT.....	II
LIST OF CONFERENCES AND AWARDS	III
LIST OF TABLES	IX
LIST OF FIGURES	X
ACKNOWLEDGEMENTS	XXIII
AUTHORS DECLARATION	XXIV
LIST OF ABBREVIATIONS.....	XXV
1 INTRODUCTION AND REVIEW OF LITERATURE	27
1.1 ANIMAL TESTING AND THE NEED FOR ALTERNATIVES.....	27
1.2 THE 3R'S OF ANIMAL TESTING	29
1.3 ALTERNATIVE METHODS TO ANIMAL TESTING	30
1.3.1 HUMAN VOLUNTEERING.....	30
1.3.2 CELL LINE DRUG TESTING	30
1.3.3 MATHEMATICAL MODELLING OF PHARMACOKINETICS.....	31
1.4 LIVER TISSUE AND CELLS FOR TOXICITY TESTING.....	33
1.4.1 OTHER LIVER CELL MODELS.....	34
1.4.2 HEPATOCYTE CELL LINES	35
1.5 MODEL <i>IN VITRO</i> SYSTEMS	35
1.5.1 INTRODUCTION	35
1.5.2 LAB-ON-A-CHIP DEVICES (LOC).....	36
1.5.3 MICROFLUIDICS	38
1.5.4 MICROFLUIDICS THEORY	39
1.5.5 LIVER ON-A-CHIP DEVICES	39
1.6 DIELECTROPHORESIS.....	40
1.6.1 INTRODUCTION	40
1.6.2 THEORY	41
1.6.3 JOULE HEATING	44
1.7 SMALL MODEL ORGANISMS	45
1.7.1 INTRODUCTION	45
1.7.2 ZEBRAFISH AS A MODEL ORGANISM.....	46
1.7.3 LOC DEVICES FOR SMALL ORGANISM MANIPULATION	47
1.8 RAPID PROTOTYPING TECHNOLOGIES.....	48
1.8.1 INTRODUCTION	48
1.8.2 STEREO LITHOGRAPHY (SLA)	49
1.8.3 FUSED DEPOSITION MODELLING (FDM).....	50
1.8.4 MULTI-JET-MODELLING (MJM).....	51
1.8.5 CURRENT APPLICATIONS IN BIOMEDICAL ENGINEERING.....	52
1.9 THEORETICAL SUMMARY AND PREAMBLE OF EXPERIMENTAL WORK DESCRIBED HEREIN	53
2 MATERIALS AND METHODS - MICROFABRICATION	55
2.1 ABSTRACT	55
2.2 INTRODUCTION.....	55
2.3 MATERIALS	56
2.3.1 CELL CULTURE	56
2.3.2 CELL ASSAYS.....	56
2.3.3 CELL PATTERNING IN HYDROGEL WITH PAPER SUBSTRATE	56
2.3.4 MICROFABRICATION.....	57

2.3.5	MICROFLUIDICS.....	57
2.4	GENERAL METHODS.....	57
2.4.1	CELL CULTURE.....	57
2.4.2	CELL COUNTING.....	58
2.4.3	CELL VIABILITY.....	58
2.4.4	LONG-TERM CELL STORAGE.....	58
2.4.5	STATISTICAL ANALYSIS.....	58
2.4.6	MICROFABRICATION.....	58
2.4.6.1	<i>General processes.....</i>	<i>58</i>
2.4.6.2	<i>Soft lithography (PDMS).....</i>	<i>59</i>
2.4.6.3	<i>Dielectrophoresis electrodes (metallisation).....</i>	<i>59</i>
2.5	CHARACTERISATION.....	59
2.5.1	SCANNING ELECTRON MICROSCOPY (SEM).....	59
2.5.2	ABSORPTION SPECTROSCOPY.....	59
2.5.3	FLUORESCENCE MICROSCOPY - CELLS.....	60
2.5.3.1	<i>Inverted microscopy.....</i>	<i>60</i>
2.5.3.2	<i>Confocal microscopy.....</i>	<i>60</i>
2.5.4	OSMOLARITY, CONDUCTIVITY AND PH MEASUREMENTS.....	60
2.5.5	THERMAL MEASUREMENTS.....	60
2.6	MULTI-CHAMBER MICROFLUIDIC DEVICES.....	61
2.6.1	DESIGN.....	61
2.6.2	CLEANING.....	61
2.6.3	RESIST SPINNING.....	61
2.6.4	PHOTOLITHOGRAPHY.....	61
2.6.5	DEVELOPMENT.....	62
2.6.6	ETCHING.....	62
2.6.7	SOFT LITHOGRAPHY.....	63
2.6.8	MICROFLUIDIC CONNECTIONS.....	63
2.6.9	PIEZOELECTRIC PRINTING.....	64
2.6.9.1	<i>Sample preparation.....</i>	<i>64</i>
2.6.9.2	<i>Collagen printing.....</i>	<i>64</i>
2.7	DIELECTROPHORETIC PATTERNING MICRO LIVER SYSTEM.....	65
2.7.1	ELECTRODE DESIGN PRINCIPLE.....	65
2.7.2	FABRICATION OF ELECTRODES FOR DIELECTROPHORESIS.....	69
2.7.2.1	<i>Design.....</i>	<i>69</i>
2.7.2.2	<i>Cleaning.....</i>	<i>70</i>
2.7.2.3	<i>Resist Spinning.....</i>	<i>70</i>
2.7.2.4	<i>Photolithography.....</i>	<i>70</i>
2.7.2.5	<i>Development.....</i>	<i>70</i>
2.7.2.6	<i>Titanium and gold metallisation and lift-off.....</i>	<i>70</i>
2.7.2.7	<i>Connections.....</i>	<i>70</i>
2.7.2.8	<i>Results and discussion.....</i>	<i>71</i>
2.7.2.8.1	<i>Optimisation of soft-baking temperature.....</i>	<i>71</i>
2.7.2.8.2	<i>Effect of over-exposure.....</i>	<i>71</i>
2.7.2.8.3	<i>Fabrication and electrode selection.....</i>	<i>72</i>
2.7.3	HYDROGEL AND PAPER SUBSTRATE PREPARATION FOR CELL PATTERNING.....	73
2.7.3.1	<i>Cell culture and media.....</i>	<i>73</i>
2.7.3.2	<i>Cell preparation for DEP manipulation.....</i>	<i>73</i>
2.7.3.3	<i>Agar gel preparation.....</i>	<i>74</i>
2.7.3.4	<i>Results and Discussion.....</i>	<i>74</i>
2.7.3.4.1	<i>Agar and paper substrate handling.....</i>	<i>74</i>
2.7.3.4.2	<i>Medium conductivity.....</i>	<i>75</i>
2.7.3.4.3	<i>Cell concentration and preparation.....</i>	<i>76</i>
2.7.3.4.4	<i>Agar definition temperature and conductivity.....</i>	<i>76</i>
2.7.4	SYSTEM DESIGN.....	77
2.7.4.1	<i>Patterning variable optimisation.....</i>	<i>79</i>
2.7.4.2	<i>Micro liver patterning efficiency.....</i>	<i>79</i>
2.7.4.3	<i>Mask template generation.....</i>	<i>80</i>
2.7.4.4	<i>Mask ROI generation.....</i>	<i>81</i>

2.7.4.5	<i>Image analysis</i>	81
2.7.4.6	<i>Results and discussion</i>	82
2.7.4.6.1	<i>Voltage optimisation</i>	82
2.7.4.6.2	<i>Temperature optimisation</i>	84
2.7.4.6.3	<i>Frequency optimisation</i>	85
2.8	CONCLUSIONS	88
3	MATERIALS AND METHODS - RAPID PROTOTYPING AND ZEBRAFISH	89
3.1	ABSTRACT	89
3.2	INTRODUCTION	89
3.3	MATERIALS	89
3.3.1	ZEBRAFISH.....	89
3.3.2	RAPID PROTOTYPING MATERIALS	90
3.4	GENERAL METHODS	90
3.4.1	ADDITIVE MANUFACTURING	90
3.4.1.1	<i>3D design</i>	91
3.4.1.2	<i>Post processing – HP DesignJet</i>	91
3.4.1.3	<i>Post processing – Viper Pro</i>	91
3.4.1.4	<i>Post processing – HD3500+</i>	91
3.4.2	LASER CUTTING	93
3.4.2.1	<i>PMMA</i>	93
3.4.2.2	<i>Filter Paper</i>	93
3.4.3	IMAGING AND DATA ANALYSIS OF ZEBRAFISH.....	93
3.5	ADDITIVE MANUFACTURING FOR MICROFLUIDIC DEVICES	93
3.5.1	CHIP DESIGN.....	93
3.5.2	POST PROCESSING OF MICROFLUIDIC CHIPS.....	96
3.5.3	MICRO ANALYSIS PLATFORM (μ AP) DESIGN AND CONSTRUCTION	97
3.5.4	RESULTS AND DISCUSSION	98
3.5.4.1	<i>Surface quality of 3D printed materials from VisiJet Crystal and Watershed 11122XC polymers</i>	98
3.5.4.2	<i>Fabrication and optical quality of microfluidic chips</i>	101
3.5.4.3	<i>Effect of chemical exposure on optical quality</i>	102
3.5.4.4	<i>Nozzle design optimisation</i>	103
3.5.4.5	<i>3D model resolution parameter adjustment</i>	104
3.5.4.6	<i>Non-processed vs. polished</i>	105
3.5.4.7	<i>Difference in optical quality with fluorescent zebrafish</i>	106
3.6	CONCLUSIONS	107
4	MICROFLUIDIC DEVICES FOR THE CULTURE OF HEPATOCYTES ON MICRO-ARRAYS	108
4.1	ABSTRACT	108
4.2	INTRODUCTION	108
4.2.1	INTEGRATION OF MICRO-ARRAY TECHNOLOGY WITH MICROFLUIDICS	110
4.2.2	AIMS OF THIS CHAPTER	110
4.3	MATERIALS	111
4.4	METHODS	111
4.4.1	DOLOMITE MICROFLUIDIC DEVICE FOR ON-CHIP ANALYSIS OF HEPATOCYTE ARRAYS	111
4.4.1.1	<i>Assembly</i>	111
4.4.1.2	<i>Connections and Operation</i>	112
4.4.1.3	<i>7-ethoxyresorufin-O-deethylase (EROD) assay in Dolomite device</i>	113
4.4.2	MICROFLUIDIC DEVICES FOR CELL CULTURE AND ANALYSIS ON MICRO PATTERN ARRAYS.....	113
4.4.2.1	<i>Clamp Device Design</i>	114
4.4.2.2	<i>Fabrication of microfluidic channels</i>	115

4.4.2.3	Single chamber culture device design	115
4.4.2.4	Single chamber setup and operation	116
4.4.2.5	Four chamber culture device design	117
4.4.2.6	Four chamber setup and operation	118
4.4.3	7-ETHOXYRESORUFIN-O-DEETHYLASE (EROD) ASSAY IN MICROFLUIDIC DEVICES	121
4.4.3.1	Calibration	122
4.4.3.2	Microfluidic assay procedure	123
4.5	RESULTS AND DISCUSSION	123
4.5.1	FIBROBLAST ARRAYS	123
4.5.2	HEPATOCTE ARRAYS	124
4.5.3	MICRO-PATTERN OF CELLS INSIDE MICROFLUIDIC CHANNELS	126
4.5.3.1	Dolomite Device	126
4.5.3.2	Single Chamber Device	127
4.6	7-ETHOXYRESORUFIN-O-DEETHYLASE (EROD) ASSAY IN MICROFLUIDICS	129
4.6.1	DOLOMITE DEVICE	129
4.6.2	MULTIPLE CHAMBER DEVICE	129
4.7	CONCLUSIONS	132
5	MICRO LIVER FABRICATION PLATFORM	133
5.1	ABSTRACT	133
5.2	INTRODUCTION	133
5.2.1	DIELECTROPHORESIS METHODS FOR PATTERNING LIVER LIKE CELL STRUCTURES	134
5.2.2	AIMS OF THIS CHAPTER	134
5.3	NUMERICAL SIMULATION OF DIELECTROPHORESIS	135
5.3.1	MESHING AND MODELLING	136
5.3.2	ELECTRIC FIELD ANALYSIS	137
5.3.3	POSITIVE DIELECTROPHORESIS FORCE DIRECTION ANALYSIS	139
5.4	METHODS	142
5.4.1	MICROFABRICATION	142
5.4.2	OPERATION OF THE MICRO LIVER PATTERNING SYSTEM FOR HETEROGENEOUS HEPATIC CELLS	142
5.4.3	CELL PATTERNING PROCESS	144
5.4.3.1	STEP 1 – Sterilisation	144
5.4.3.2	STEP 2 – Assembly	144
5.4.3.3	STEP 3 – Patterning of C3A cells in agar (HEATING)	144
5.4.3.4	STEP 4 - Patterning of C3A cells in agar (COOLING)	146
5.4.3.5	STEP 5 - Micro liver cell pattern removal to culture	146
5.4.4	CELL VIABILITY ASSAY	146
5.4.5	ALBUMIN PROTEIN SYNTHESIS ELISA ASSAY	147
5.5	RESULTS AND DISCUSSION	147
5.5.1	PATTERNING USING AGAR AND PAPER HANDING	147
5.5.2	CELL VIABILITY ASSESSMENT FOR DEP CELL PATTERNING IN AGAR	149
5.5.3	MICRO LIVER FUNCTION ASSESSMENT VIA ALBUMIN SECRETION	153
5.6	CONCLUSIONS	155
6	ADDITIVE MANUFACTURED MICROFLUIDICS	156
6.1	ABSTRACT	156
6.2	INTRODUCTION	156
6.2.1	3D PRINTING AS A NOVEL FABRICATION TECHNIQUE	157
6.2.2	AIMS OF THIS CHAPTER	158
6.3	MATERIALS AND METHODS	159

6.3.1	ON CHIP DEVELOPMENT SYSTEM SETUP, LOADING AND OPERATION	159
6.3.2	BIOCOMPATIBILITY OF 3D PRINTED MATERIALS	161
6.3.3	ZEBRAFISH HUSBANDRY	162
6.3.4	EMBRYO CULTURE, TREATMENT AND PHENOTYPE ANALYSIS	162
6.3.5	IMAGING	163
6.3.6	DATA ANALYSIS AND CONTROLS.....	163
6.4	RESULTS AND DISCUSSION	164
6.4.1	ON CHIP EMBRYO TRAPPING AND CULTURE USING THE MICRO ANALYSIS PLATFORM	164
6.4.2	BIOCOMPATIBILITY TESTING OF 3D PRINTED MATERIALS.....	166
6.4.3	LONG TERM CULTURE ZEBRAFISH EMBRYOS IN VISIJET CRYSTAL AND S300 WAX SUPPORT MATERIAL	166
6.4.4	REDUCTION OF TOXICITY OF 3D PRINTED MATERIALS AND IMPROVEMENTS TO BIOCOMPATIBILITY.....	168
6.4.5	STUDY OF HATCHING SUCCESS AND SURVIVAL RATE WITH RELATION TO INCUBATION WITH 3D PRINTED MATERIALS.....	170
6.4.6	LONG TERM ZEBRAFISH EMBRYOS CULTURE IN 3D PRINTED SINGLE WELLS	174
6.5	CONCLUSIONS.....	178
7	CONCLUSIONS AND FUTURE WORK.....	179
7.1	SUMMARY.....	179
7.2	ACHIEVEMENTS AND IMPACT	179
7.3	LIMITATIONS OF THE THESIS.....	181
7.4	FUTURE RESEARCH DIRECTIONS	182
7.4.1	METHODS.....	182
7.4.2	DESIGN AND 3D PRINTING	182
7.4.3	RESULT AND DISCUSSION.....	182
7.5	CONCLUSION	184
APPENDIX A	185
APPENDIX B	187
APPENDIX C	188
BIBLIOGRAPHY	189

List of Tables

Table 1.7-1 - Attributes of some key animals used to model human disease. Note in particular the high cost of mice and rat models and the large range of molecular biology tools available for zebrafish research. Source: ¹⁴⁴	45
Table 2.7-1 – Typical values of dimensional quantities from physiological conditions of the human liver	67
Table 3.4-1 – List of additive manufacturing machines used in this project with main specifications.	92
Table 4.4-1 – Resorufin concentrations for calibration	123

List of Figures

- Figure 1.1-1 – International Cooperation on Alternative Test Methods (ICATM): On April 27, 2009 the U.S., Canada, Japan and EU signed a memorandum of cooperation that could reduce the number of animals required for consumer product safety testing worldwide. The agreement will yield globally coordinated scientific recommendations on alternative toxicity testing methods that should speed their adoption in each of these countries, thus reducing the number of animals needed for product safety testing.¹² ICH: The International Conference on Harmonisation of Technical Requirements for Registration of Pharmaceuticals for Human Use. OECD: The Organisation for Economic Co-operation and Development has a Test Guideline program that deals with chemicals. ICCR: The International Cooperation on Cosmetics Regulation (ICCR) is an international group of cosmetic regulatory authorities from the U.S. (FDA), Japan (Ministry of Health, Labour, and Welfare), the EU (EC, DG Enterprise), and Canada (Health Canada). 28
- Figure 1.3-1 - An example of a physiologically based pharmacokinetic model. The compartments represent tissues and organs; connecting arrows represent blood supplies; ST is stomach; SPL are splanchnic organs; and CL_{int} is intrinsic hepatic clearance. Reproduced from reference ³¹ 31
- Figure 1.4-1 – The liver is the largest internal organ in the human body weighing approximately 1500g. It performs over 500 metabolic functions, resulting in the synthesis of products that are released into the blood stream or that are excreted to the intestinal tract (bile). The portal tract supplies the vast majority of blood which is low O₂ content from the gastrointestinal tract as well as from the spleen, pancreas and gallbladder. The second blood supply is the hepatic artery; a high pressure O₂ saturated supply. The building blocks of the liver are hexagonal structures, hepatic lobules that are composed almost primarily of hepatocytes with in most cases 3 portal triads in the corners. Sinusoidal canals formed by the spaces between the hepatocytes are approximately 8-10 μm in diameter, orientated in a radial direction from the central vein. Sinusoids are lined with endothelial cells and Kupffer cells which have a phagocytic function. On the opposite sides of the hepatocytes are bile canaliculi (1 μm diameter). Bile produced by the hepatocytes is transported away in the opposite direction from blood flow to the main bile duct and finally the gallbladder ⁴⁴. Image reproduced from reference. ⁴⁵ 33
- Figure 1.4-2 – Classic lobule sketches by Francis Kiernan. Fig 5 of this illustration in particular shows the structure of the liver lobule with a hexagonal like geometry (c) identifying the hepatocyte plates and (d) the central vein. Reproduced from ⁴⁶ 34
- Figure 1.5-1 – 2D vs 3D cell culture, (a) represents the progression from a single atom through to a full organism. (b) 2D static cell culture is the current industry standard for toxicity testing. The environment is constantly changing as nutrients in the media are depleted and metabolites accumulate. (c) 3D cell culture offers a practical alternative to natural tissue models ^{67, 68}. These systems provide an environment in which one or more cell types can be encouraged to form tissues-like constructs, often using natural or synthetic scaffolds, such as collagen, alginate, polyethylene glycol hydrogels and nanofibres to provide structural support to the growing tissue construct. Scaffolds can also provide - through modification or by virtue of their natural composition - growth factors and other proteins to replicate the biochemical cues offered by the extracellular matrix (ECM) in native tissues. Figure formed through reproduction of images from. ^{69, 70} 36
- Figure 1.5-2 - Enabling technologies for on-chip tissue models. (a) Patterned microenvironment regulates differentiation of embryoid bodies. Scale bars 300 μm. Source: Qiet al. ⁷³, (b) Dynamic substrate enables co-culture harvesting. Scale bar 1 μm. Source: Tsuda et al. ⁶¹, (c) Directed assembly of cell-laden hydrogels for generating hierarchical tissue constructs. Scale bars 500 μm (left), 100 μm (right). Source: Zamanian et al. ⁷⁴, (d) Micromechanical substrates enable micrometer-resolution cell positioning and co-culture. Scalebars 10 mm (left), 250 μm (right). Source: Hui and Bhatia et al ⁷⁵, (e) Microfluidic cell culture chambers with integrated electrodes to assemble liver sinusoids by dielectrophoresis. Scalebars 500 μm (left), 200 μm (right). Source: Schütte et al. ⁷⁶, (f) A microfluidic channel with an array of valves for single cell co-culture. Scale bars 100 μm (left), 20 μm (right). Source: Frimat et al. ⁷⁷ 37
- Figure 1.5-3 – Microfluidics and microdevices (g) Flow of growth factor directs the migration of one cell type into the other within a co-culture. Scale bars 5 mm (left), 100 μm (right). Source: Kaji et al. ¹⁰² (h) Multiwell plate with an array of perfusion bioreactors for 3D

liver tissue culture. Source: Domansky et al.¹⁰³, (i) Pneumatic microfluidic chip for the differentiation of stem cells under mechanical stimulation. Scale bars 10 mm (left), 1 mm (right). Source: Sim et al.¹⁰⁴, (j) Capillary-flow-driven gradient generation within a fluid stripe for synthesizing gradient biomaterials to regulate cellular behaviour such as spreading. Scale bars 100 mm (left), 100 μm (right). Sources: Hancock et al.¹⁰⁵ (k) A microfluidic device for separating motile and non-motile sperm. Scale bar 200 μm. Sources: Cho et al.¹⁰⁶ (left), and Wu et al.¹⁰⁷ (right), (l) CMOS chip from webcam used to detect cardiomyocyte beating within a cell-based biosensor. Source: Kim et al.¹⁰⁸38

- Figure 1.5-4- Liver on-chip models (a) Photograph of a 24-well device with repeating hepatic microstructures (37 colonies of 500-μm diameter in each well), stained purple by MTT. Scale bars, 2 cm and 1 cm for enlargement. Phase-contrast micrographs of micropatterned cocultures, primary human hepatocytes are spatially arranged in B500-μm collagen coated islands with B1,200 μm centre-to-centre spacing, surrounded by 3T3-J2 fibroblasts. Scale bars, 500 μm. Source Khentani and Bhatia¹¹⁹. (b) Sinusoid like structures to promote cell-cell interaction. An array of 30 x 50 μm pillars separated the channel into 3 compartments: a central cell culture compartment and 2 side media perfusion compartments. Source: Toh et al.¹²⁰. (c) Sinusoid structure through dielectrophoresis. Concept of the HepaChip. Hepatocytes (orange) and endothelial cells (green) are arranged in a sinusoid-like fashion. The cell chamber features two electrodes on the outer channel walls for dielectrophoretic cell assembly, extra cellular matrix support in the cell seeding area and allows for an organ-like perfusion of the culture. Source Schütte et al.⁷⁶. (d) Intact liver tissue integrated on-chip for *in vitro* metabolism and toxicity testing. Source: Midwoud et al.¹²¹. (e) Lobule pattern on-chip constructed with DEP. Source: Ho et al.¹²². (f) Rat hepatocytes patterned in various biomimetic microstructures within a PEG hydrogel. Source: Albrecht et al.¹²³40
- Figure 1.6-1 – Response of a polarisable particle to (A) uniform and (B) non-uniform electric fields. The electric field lines are bent towards the cell provided that the conductive buffer is less polarisable than the cells. A net force is exerted on the particle within a non-uniform electric field and is pushed towards the maxima of the electric field gradient. Reproduced from reference.¹²⁶41
- Figure 1.6-2 – Graph illustrating relative DEP response in relation to frequency (Hz). The solid line is the DEP response modelled for a viable cell normalised against the DEP response for a sphere composed of the same electrolyte as the cell cytoplasm. As the frequency is increased the cell's DEP behaviour approaches that of the conducting sphere, making the transition from negative to positive DEP at the “cross-over” frequency f_{xo} . The dashed line shows the DEP response for a larger cell (radius $R_2 > R_1$). The cross-over frequency f_{xo} is affected by cell size, however the cross-over at higher frequency f_{hxo} is not effected by cell size. All other dielectric factors remain constant. The highlighted band indicates the frequency band of 1-10 MHz, here the relative DEP response is the most positive. In this work this frequency band was selected as it was only of interest to achieve positive DEP forces. This was because the electrode design required cells to be attracted to the electrode edges and not be repelled which would be the case for negative DEP. Additionally, the DEP response for positive DEP is stronger than that of negative DEP. Thus as the frequency range selected was 1-10 MHz, which is greater than the cross-over frequency f_{xo} of any cell line used in this work, the cross-over frequency was not of concern. Adapted from reference.¹²⁸43
- Figure 1.6-3 – A non-uniform electric field created by a metallic microelectrode patterned on a substrate. When the $Re[fCM]$ is >0 cells are attracted to the electric-field maxima, when $Re[fCM]$ is <0 cells are repelled to the electric-field gradient minima. Reproduced from reference.¹²⁶44
- Figure 1.7-1 – (a) Zebrafish life cycle – After fertilisation the cells of the embryo rapidly divide during the cleave stage. This then leads to the sphere stage after a further 2 hrs, then the shield stage at 6 hrs total. By 16 hrs the pronephros forms during the somite stages. Organogenesis occurs over the next 8 hrs; the body plan becomes visible and major organs develop. After about 48 hrs hatching start to occur of larvae swimmers during which time fins, mouth, pigment and teeth develop. The first signs of bone development occur mark the end of embryogenesis. By 90 hrs the larvae are now full developed adult zebrafish. Scale bars are 0.5 mm and 1 mm respectively. (b) Zebrafish, like humans, have a backbone and many genes in common with humans. In one laboratory test, the addition of the chemical ketamine—a pediatric

anesthetic—lowers the fish’s heart rate and reduces the number of neurons (nerve cells), shown in the slide as short, vertical lines coming down from the horizontal spinal cord ¹⁴⁶ (c) Photographs showing zebrafish culture facilities. Zebrafish culture and husbandry is most commonly done by hand. (d) 4 day old zebrafish embryo labelled with SV2 and acetylated tubulin antibodies showing axon tracts(green) and neuropil(red)viewed from lateral(top) and dorsal(bottom) orientations. Source: UCL ¹⁴⁷

- 46
- Figure 1.7-2 – Examples of LOC devices for manipulation of small model organisms. (a) Images of *C. elegans* inside the LOC device. The microfluidic system immobilised the worms and allowed study over the 9 day life-cycle. Source: Hulme *et al.* ¹⁵² (b) This device relies on laminar flow of two streams of liquid with different temperature using rapid-prototyping technique polydimethylsiloxane (PDMS) to control the micro environment of a living *D. melanogaster* fruitfly embryo. Source: Lucchetta *et al.* ¹⁵³.(c) Assembled DEP manifold with an array of microelectrodes and a microculture PDMS chamber: The eggs trapped along the surface of microelectrodes under the DEP force at 20 MHz. Source: *Khoshmanesh et al* ¹⁵⁴ 47
- Figure 1.7-3 – (a) Layout of the biochip, an example of a 32-well chip. Embryos cultured in the biochip. Consecutive photos of the same embryo developing in the same well (1.8 mm internal diameter) of a 32 well biochip. Each picture is framed by a circular hole in the metal clamp that holds the lid in place. Source: *Wielhouwer et al* ¹⁵⁵. (b) A three-layer PDMS microfluidic chip to create gradients of test drugs to the embryos. Source: *Yang et al* ¹⁵⁶. (c) 24-well plate system for FET tests using zebrafish embryos. Source: ¹⁵⁷. (d) Schematic of zebrafish manipulation and imaging platform. Source: ¹⁵⁸. (e) Zebrafish embryos trapped on a microfluidic chip by use of steady fluid flow for LOC based studies. Scale bar 0.5 mm. Source: *Akagi et al.* ¹⁵⁹ 48
- Figure 1.8-1 - Schematic description of the rapid prototyping (RP) process using the HD 3500+ MJM system from 3D Systems, Inc. Abbreviations: CAD, computer-aided design; stl, standard tessellation language; MJM, Multi-jet-modelling. Scale bar 10 mm. 49
- Figure 1.8-2 - 3D rendering illustrating the basic operational components of stereolithography. Stereolithography is an additive manufacturing method employing UV laser light and UV sensitive photopolymers. A beam of UV laser light is reflected to the surface of the liquid photopolymer resin forming layers of hard cured resin. Each slice of the model is fabricated by scanning the laser across the surface, before the build platform is lowered (typically 50-150 µm) for the next layer. This process bonds the new layer to the previous layer below. As the process is repeated the model gradually is lowered into the resin until the model is complete, where the platform is then raised revealing the finished model. Reproduced from reference. ¹⁷⁶ 50
- Figure 1.8-3 – 3D rendering illustrating the main components required for fused deposition moulding (FDM). Material extruded by a heated nozzle deposits lines into the build platform tracing out each layer. On completion of each layer the build platform is lowered (typically in the range of 250-300 µm), for the next layer to be deposited. This process bonds to the new layer as the polymer is in a molten state. A second nozzle is often used to deposit a support material for overhanging features. Illustration reproduced from reference. ¹⁷⁶ 51
- Figure 1.8-4 – 3D rendered schematic illustrating the major components of MJM modelling. Multi-jet modelling (MJM) also known as polyjet technology is a form of fused deposition modelling (FDM). The materials used are either thermopolymers or liquid photopolymers which require an additional UV source during printing. An array of linearly arranged nozzles similar to an inkjet printer spray tiny droplets of melted liquid material which cool and harden on impact to form the solid object. Slices of the model are fabricated as the nozzles scan in the x-y axis; both material for the model itself is deposited and support materials as required. Completed models require no further post-printing treatment to cure the polymer. Illustration reproduced from reference. ¹⁷⁶ 52
- Figure 1.9-1 – Lab-on-a-chip (LOC) device for high-throughput screening of human hepatocytes. (a) Photograph of experimental setup and LOC device installed with fluidic connections and valves. (b) Schematic of microfluidic chamber design with micro-patterns. 53
- Figure 1.9-2 – Dielectrophoresis system for the patterning of liver cells (HepG2/C3A) to form liver lobule like arrays within a hydro-gel. (a) Scale 3D render of the patterning system. Scale bar is 10 mm. (b) Schematic showing the design of the patterning volume. ... 54
- Figure 1.9-3 – Micro analysis platform for on-chip zebrafish development studies. (a) Photograph of the analysis platform with fluidic connections, USB microscope, light source and

	installed 3D printed chip. (b) Microscope image of a healthy zebrafish after 72 hrs of development with a 3D printed material. Scale bar is 1 mm.	54
Figure 2.6-1	- Schematic of fabrication procedure: (a) - Cleaned Silicon wafer; (b) - AZ-4562 spun onto the surface of the silicon wafer to make a 6.2 μm layer; (c) – Exposure of UV radiation to transfer the mask pattern to the polymer; spun onto the glass substrate; (d) – Development of AZ-4562 to remove areas exposed leaving a positive structure of the pattern; (e) – Etching using an STS multiplex inductively coupled plasma (ICP) machine to a depth of 100 μm ; (f) Cleaning of remaining AZ-4562 using organic solvents and ultrasonics; (g) Soft lithography moulding of PDMS using the silicon etched pattern; (h) Completed PDMS microfluidic chip removed from the silicon master and prepared for use by cutting connections using an appropriate punch.	62
Figure 2.6-2	– Piezoelectric printing – Microscopy images showing a 150 μm diameter collagen dot array printed on PEG treated glass substrate shown at (a) x5 (b) x10 and (c) x20 magnifications.	64
Figure 2.7-1	– Human liver basic physiology. (a) The liver is the largest glad in the body and receives blood from two main sources the hepatic portal vein and the hepatic artery. The liver is composed of small units, which can be described in a number of ways. One of the common descriptions is the “classic lobule” ⁴⁴ . Approximately the lobules are hexagonal in cross-section, with the central vein (80 μm diameter) in the centre surrounded radially by sinusoids constructed of hepatocytes. Liver cross-section illustration reproduced from reference ²⁰⁵	65
Figure 2.7-2	– Microelectrode design for inducing DEP forces to pattern cells into a micro liver lobule array. (a) Using a biomimetic electrode design hepatocytes are patterned into an array 19 lobules in size using DEP forces. The largest gap is 60 μm between the electrodes. The thickness of the electrodes is 10 μm . (b) Microscope image showing C3A liver cells being held in place by DEP forces to form liver lobule like structures. Scale bar is 200 μm	66
Figure 2.7-3	– Schematic of a single electrode lobule unit. (a) Shows the centre lobule of the array indicating major feature dimensions. (b) Detail showing a quarter of the lobule unit fine dimensions of the design are indicated. Electrodes are 10 μm in width.	68
Figure 2.7-4	– Schematics illustrating the 3 electrode lobules used. Each was designed to fit within the anatomial restrictions of considered constants. The variable changed was the minimum distance between the inner and outer electrodes. Distances used were (a) 30 μm (b) 50 μm and (c) 60 μm . All lobules were 1 mm in width.	68
Figure 2.7-5	– Process for fabricating electrodes for dielectrophoretic patterning (a) Cleaned glass slide by Opticlear and organic solvents using ultrasonics; (b) Spinning of S1818 resist (negative photopolymer) followed by soft-baking at 95 $^{\circ}\text{C}$ for 5 minutes; (c) Exposure using lithography and chrome mask to polymerise areas to be removed; (d) Developed S1818 showing exposed glass in the pattern of the mask; (e) Metallisation through use of metal evaporator to deposit Ti and Au (10 nm, 100 nm), the Ti layer improves adhesion of Au to the glass; (f) Lift-off, removal of excess Ti and Au by removing remaining S1818; (g) Completed electrodes with wires soldered to make connections to the signal generator.	69
Figure 2.7-6	– Incorrect soft-baking - Microscope image showing identically processed samples with the exception of soft-bake temperature (a) 110 $^{\circ}\text{C}$ (actual 94 $^{\circ}\text{C}$) and the (b) 95 $^{\circ}\text{C}$ (actual 75 $^{\circ}\text{C}$). The features were barely visible when the development process was completed.	71
Figure 2.7-7	- Influence of exposure time on structures – Microscope image showing a sample exposed for 7.5 seconds (a) and 15 seconds (b). The structure has bulged out losing the definition of the pattern.	72
Figure 2.7-8	– SEM images of fabricated electrodes designed for dielectrophoresis patterning of cells. Each image shows the result of different spacing between the electrodes. (a) Angled view showing the complete array with 30 μm spacing. Scale bar 1 mm (b) Top down view of electrodes with 50 μm spacing. Scale bar 500 μm . (c) Top down view showing electrodes with 60 μm spacing. Scale bar 500 μm	72
Figure 2.7-9	– Microscope images of electrodes show C3A cells patterned by DEP forces under the same conditions. (a) Spacing of 30 μm resulted in patterning however visualisation of the pattern proved difficult. (b) Spacing of 50 μm also resulted in patterning with improved visualisation of the pattern. (c) Spacing of 60 μm resulted in patterning and further improved visualisation. Scale bar 200 μm	73
Figure 2.7-10	– Agar moulding results using a 0.5 mm thick silicon gasket with 6, 5 and 3 mm punched holes. (a) Agar 0.5% (wt/vol) removed from the punched gasket. Agar was	

	observed to be structurally unstable. (b) Agar 1% (wt/vol) removed from the punched gasket. Straight edged discs of agar were observed.	74
Figure 2.7-11	– Paper handling results. (a) Computer aided design (CAD) drawing of 6.2 mm OD, 5 mm ID circles. (b) Laser cut paper rings cut from paper using the CAD design. (c) Paper ring used as a substrate to manipulate thin discs of agar with patterned cells using dielectrophoresis (DEP). All scale bars are 5 mm.	75
Figure 2.7-12	– Cell viability due to wash steps in DEP buffer. Cell concentration was 1.0×10^6 cells/ml. Cell viability was assessed through Trypan blue staining and cell counting. There is a significant drop off after 4 wash steps therefore 3 steps was selected as the optimal number of wash steps.	76
Figure 2.7-13	– Graph showing the relationship of temperature ($^{\circ}\text{C}$) and conductivity (mSm^{-1}) of 13 mSm^{-1} DEP buffer mixed 1:1 with 2% agar solution (resulting in 1% agar solution) allowed to cool at room temperature (25°C).....	77
Figure 2.7-14	– Physical setup of the patterning system: Illustration at the top shows the patterning system placed inside a laminar hood along with a multimeter for air temperature readings via thermocouple. An infrared camera (not pictured) was also used for surface temperature measurements. The function generator and current supply were located outside of the laminar hood. Below are two 3D model renderings of the micro liver patterning system at 1:1 scale and realistic material properties. (a) Exploded view shows the patterning system design. The base is a copper heat sink on which the Peltier was reversibly attached using thermal paste. Glass with microfabricated electrodes for DEP patterned are placed on top on the Peltier loosely interfaced with DI water. To define the volume of the agar cell solution a $100 \mu\text{m}$ gasket was pressed onto the electrode with a 5 mm hole cut in the centre. A 6 mm laser cut paper ring was placed around the perimeter of this hole. Agar cell solution to be patterned was pipetted into this volume. A 3D printed cover was placed over the top enclosing the system during the patterning process. (b) Cut-away view illustrating the system. The insertions for electrical connections through the cover can be seen to the left of the Peltier. Scale bars are 15 mm.	78
Figure 2.7-15	– Illustration showing the design of the patterning volume. A Nesofilm gasket ($100 \mu\text{m}$) was pressed onto the surface of glass substrate with DEP electrodes. Around the circumference of this gasket a 5 mm ID, 6.2 mm OD paper ring previously soaked in 2% (wt/vol) agar was placed. This defined a 7.7 pl volume for electrode patterning. The paper ring was soaked to stop the wicking of 1% agar DEP buffer cell solution into the paper.....	78
Figure 2.7-16	– Process of mask generation. (a) Microscope image (Z.D1 at $\times 10$) taken of electrodes. (b) Microscope image adjusted with threshold to reduce the image to black and white only isolating the electrodes from the image, coloured here in red. (c) Electrodes imported as a layer into Photoshop on top of the electrode design. The electrode array was adjusted until it scaled correcting with the reference electrode image from (b). Electrode thickness is $10 \mu\text{m}$	80
Figure 2.7-17	- Mask processing. (a) Scaled electrode array previously shown in Figure 2.7-16(c) was aligned manually with a microscope image of patterned cells in agar by dielectrophoresis (DEP). (b) The aligned electrodes then have a 23 pixel stroke applied, increasing over all thickness of the electrodes by adding extra pixels to perimeter of the electrodes. This compensates for the designed effect of cells attaching to the edges of the electrodes. (c) Finally the mask is completed by merging the electrodes and stroke effect.	80
Figure 2.7-18	– Image analysis using ImageJ. (a) Processed image of live cells after 72 hrs culture. Threshold and binary processing has been done on this image. Cells aggregates are black. (b) The processed cell pattern image superimposed with a positive mask (green), covering the area in which cells are designed to be patterned. (b) This image shows the same processed image but with the negative mask (red) superimposed. This is represented by the inversion of the electrode mask from (b) covering the area where cells should not be. Scale bar is $100 \mu\text{m}$	81
Figure 2.7-19	– Pattern ratio and viability of patterned cells as a function of voltage. Both live and dead pattern ratios were observed to increase with voltage. The electric-field was induced for two minutes (10 MHz) at 37°C . Viability of the patterned cells was observed to be constant as the voltage was increased. Error bar represents standard deviation of the mean ($n = 3$).....	83
Figure 2.7-20	– Pattern ratio and viability of patterned cells after 24 hrs of culture as a function of temperature at the surface of the patterning volume. Temperature values were measured by infrared camera immediately after removing the cover. Both live and	

- dead pattern ratio were observed to increase with temperature. The electric-field was induced for two minutes (10 MHz, 10 Vpp). Viability of the patterned cells was shown to be stable at 80% across this temperature range. Error bar represents standard deviation of the mean (n = 4).85
- Figure 2.7-21 – Temperature near the surface of the as a function of electric field frequency. Measurements were made using an infra-red camera (± 0.09 °C). The black solid line represents the temperature when no AC signal is applied, only the Peltier is heating the system (+0.28 A) to 36 °C. The average temperature over this frequency range was 37.13 °C ± 0.47 . The measured solution was 1% agar, voltage during this sweep was 10 Vpp, buffer conductivity 13 mSm⁻¹. As a result, over this frequency sweep only a 1.24 °C ± 0.33 increase in temperature was detected.....86
- Figure 2.7-22 – Pattern ratio and viability of patterned cells as a function of frequency. Both live and dead pattern ratios were observed to increase with frequency. The electric-field was induced for two minutes (10 Vpp) at 37 °C . Viability of the patterned cells was shown to increase marginally as the frequency was increased. Error bar represents standard deviation of the mean (n = 3).87
- Figure 3.4-1 – Photographs of 3D printers used in this thesis. (a) The HD3500 Plus professional 3D printer (HD3500+) used multi-jet modelling (MJM) method to fabricate microfluidic devices and culture dishes with VisiJet Crystal material. (b) Viper Pro SLA System (Viper Pro) used the stereolithography (SLA) method to fabricate microfluidic devices and culture dishes using Watershed 11122XC and Dreve Fototec 7150 Clear. (c) HP DesignJet 3D printer fused deposition moulding (FDM) method to fabricate culture dishes and prototype elements for experimental setups. All scale bars are 0.5 m. ..92
- Figure 3.5-1 – 2D CAD sketches of four connector types designed for the 3D printed chip. a) Large connector with a 1.9 mm ID and 2.0 mm OD b) same shape as 1a but with a 1.6 ID and OD of 1.8 mm. c) Different shape and design with a more flanged top ID 1.6 mm OD 1.8 mm d) Final design with a ID 1.6 mm and OD 2.2 mm. 300 μ m thick sidewalls stopped the connectors from breaking off from repeated connections to the tubing.94
- Figure 3.5-2 – Image showing design of microfluidic embryo array chip for automatic trapping and immobilisation of zebrafish embryos. (a) SolidWorks CAD package used to design the chip. (b) 2D rendered image showing the x-y profile of the chip. Detail A shows the trapping area and Detail B shows the connector. This is a monolithic design as the lid and connectors are included in the fabrication process and hence are not added to the device in a later stage of manufacture.....95
- Figure 3.5-3 – HD3500+ printed monolithic microfluidic device post processing steps – This figure shows the development process required to fabricate 3D printed devices using an HD3500+ pictured in the centre (a) The device was removed from the metal printing tray. This requires cooling to allow the support wax to detach from the tray. (b) Printed devices were then placed upright in an oven at 70 °C allowing the bulk of the support wax to melt and drain out of the material. To remove remaining material the devices were placed in an ultrasonic bath at 55 °C, filled with cannoli oil. Fluidic channels were cleared of support material by connecting 1/16" polyurethane tubing flexible tubing to the connections and using a peristaltic pump melted wax was flushed out for 5 minutes. This was performed in both directions to aid removal; (4) Optical quality of the device was improved by high-grit sandpaper P1500, followed by P2000 and finally buffed using 9 μ m polishing paste and soft, cylindrical modelling head using a head. The device was finally washing in warm soapy water to remove residual polish and pumped through with DI water to complete the process.96
- Figure 3.5-4 – 3D rendered image of the micro analysis platform. The system consisted of a PMMA laser cut frame connected with nuts and bolts. A polished steel metal light reflector was attached by two 3M bolts allowing for rotation around the axis. This allowed for adjustment of the bottom lighting solution. The 3D printed chip was held in place by a laser engraved PMMA piece with small clips to keep the chip fixed when tubing was attached. A 3D printed stand was attached to the PMMA base to which the microscope stand could be fitted securely with a screw bolt (not rendered). Scale bar is 20 mm.....98
- Figure 3.5-5 – SEM images of HD3500 printed discs with VisiJet Crystal material. (a) Image of printed engraved "D" from a side on perspective. Scale bar 500 μ m. (b) Top view of printed engraved text reading "350", stitch marks are observed across the surface. Scale bar 1 mm. C) Close up of "D" showing texture of layers used to form the model. Scale bar 20 μ m.99

Figure 3.5-6 – SEM images of Viper Pro printed discs with Watershed material: A) Low magnification image showing engraved lettering. B) High magnification of interior of engraved letter. C) High magnification of engraved letter.	100
Figure 3.5-7 – Comparison of SEM images of Watershed and VisiJet Crystal surface profiles. A) Watershed (left) next to VisiJet Crystal right) printed disc. Watershed had a smooth surface profile with rough edges. VisiJet Crystal had a rougher surface with stitch lines every 500 µm, edges were sharper than the Watershed but lines appeared in the sidewalls of the disc. Scale bar 1mm. B and C) higher magnification showing detail. Scale bars 2 mm and 500 µm respectively.	100
Figure 3.5-8 – Stereomicroscopy of 3D printed zebrafish traps. A-C) Uncovered HD3500+ fabricated zebrafish trap model showing definition of trapping features and channels. Scale bars are 2, 1 and 1 mm respectively. D-F) Enclosed Viper Pro fabricated zebrafish trap model, showing definition of trapping features and channels. Scale bars are 2, 1 and 1 mm respectively.	101
Figure 3.5-9 – Effect of EtOH on optical quality of VisiJet Crystal material – This figure shows 3 chips with identical fluidic channels but with different connectors. Each had EtOH:DI water of varying concentration pumped through them with a peristaltic pump, (a) 40%, (b) 50% and (c) 60%. The optical quality of the channels has remained unaffected in (a) and (b) but in (c) the EtOH has reacted with the VisiJet Crystal polymer, darkening the channels. With increased concentrations of EtOH the material distorts further to the point of being opaque white. Scale bar 10 mm.	103
Figure 3.5-10 – Stereomicroscopy photographs of three nozzle designs fabricated using the HD3500+ with VisiJet Crystal. Inner diameter was kept constant throughout the designs (a) Nozzle 1a (b) Nozzle 2a (c) Nozzle 2b	103
Figure 3.5-11 – Design of the final nozzle – (a) Computer render of the device with the nozzle showing triangle edges. (b) Photograph of the device with final nozzle design fabricated using the HD3500+ with VisiJet Crystal. Scale bar 500 µm.	104
Figure 3.5-12 - Changes to tessellation by altering the angle and deviation tolerances. The figure shows wireframe rendered 3D cylinders (OD, ID = 3, 1.5 mm) after processing to .stl format for printing. (a) Resolution parameters - deviation tolerance 0.002, angle tolerance 5. Tessellation resolution was high formed by 576 triangles and resulting file size of 28884 Bytes. (b) Resolution parameters - , deviation tolerance 0.0129, angle tolerance 10. Tessellation resolution was low having only formed the model with 288 triangles and resulting in a file size of 14484 Bytes. This resulted in flat spots for representing curves in the model.	104
Figure 3.5-14 – Effect of changes in resolution by altering angle and deviation of MJM printed parts – (a) Micrograph showing top surface of a 3D printed cylinder (OD, ID = 3, 1.5 mm). Deviation constant is 0.02, the angle has been changed to 5. This has resulted in a finer surface finish but has over smoothed the opening of the cylinder to make the ID 1.63 mm, rather than the designed 1.5 mm. (b) using the same design, here the angle has remained at 10, the deviation is 0.0129. The surface quality is lower than when lower angle values are used but the ID was measured to be 1.5 mm as designed.	105
Figure 3.5-15 – Stereomicroscopy of 3D printed chips before and after polishing. A and C) HD3500+ printed chip showing the feature used to create the zebrafish trap. A stitch line is visible on the edge of the trap which was then removed in C) by polishing. Water was injected into the channels to demonstrate the optical quality expected during zebrafish analysis. Faint horizontal lines are visible through the trap pillar which are internal to the printing process and hence not removable. The clarity of the chip was improved significantly by polishing. B and D) Viper Pro printed chips showing 3 trapping areas before polishing B) Scanlines are visible at this stage. D) Polishing removed the stepped visualisation of the features however the scanlines remain. Polishing of the Viper Pro produced traps did not improve optical quality significantly.	106
Figure 3.5-16 – On-chip visualisation of transgenic zebrafish line with different 3D printed materials. a) Fluorescent image of a zebrafish within a Viper Pro printed chip. The scanlines created during printing impede the visualisation of the zebrafish. The ISV were indistinguishable from the tail, only the eye of the zebrafish was recognisable. b) Fluorescent image showing a transgenic zebrafish larva within a HD3500+ printed chip. Re arrows indicate ISV in the tail of the zebrafish. Developing patterns of ISV were clearly visible at low magnification. c) Image of a zebrafish control sample in a petri dish clearly showing the ISV. Scale bars are 1 mm.	107

- Figure 4.4-1 – Photographs and diagram illustrating the Dolomite resealable device used for analysis of on-chip micropattern arrays of hepatocytes. (a) Photograph showing the Dolomite resealable device, twisted clockwise to release the lid and anti-clockwise to seal. A PDMS gasket (100 μm) placed around the channels seals the chip to the selected base substrate. This is illustrated by the outer line of the chamber design shown in (c). (b) Photograph of the 4-way linear fluidic connector by Dolomite. Only two connections were used in these experiments as the chamber only has two inlets. (c) Schematic of the Dolomite two-inlet, two-outlet microreaction chamber. A PDMS gasket 1 mm wide and 100 μm thick follows the edge of the design to provide a seal to the chosen substrate (glass with micropatterned collagen dots). 112
- Figure 4.4-2 – Illustration of microfluidic connections for the Dolomite microfluidic device. Two disposable syringes were connected to the inputs of the microfluidic chamber used for injecting cells, medium and assay reagents. Waste fluids was be collected by Eppendorf tubes. 113
- Figure 4.4-3 – Microfluidic biochip device for toxicity testing – This figure shows both a 3D rendered image of the device as well as schematic of the channel design and a microscope image of the protein micro-arrays. The device consists of a milled Perspex top, PDMS with four soft-lithography mould microfluidic chambers, PEG treated glass slide with 4 printed protein micro-arrays and an aluminium bottom. The device was clamped together with the use of eight M3 screws. (a) shows a microscope image of the printed collagen pattern; (b) shows the microfluidic chamber design. 114
- Figure 4.4-4 - Single chamber microfluidic device for culture of cells on collagen micropattern arrays. (a) Schematic of microfluidic channels. The main chamber was 6.5 x 5 mm, the depth of the channels was 100 μm . Channels for inlets and the outlet were 500 μm in width. Inlet and outlet connections were 1 mm in diameter. The two inlet design allowed for the injection of two different fluids without disconnecting the system. Superimposed in the chamber is a 20 x 10, 150 μm dot array. This array was fabricated on a glass substrate and aligned by hand to fit into the chamber during assembly of the device. (b) Microscopy image showing a 4 x 4 portion of an array of collagen dots printed onto a PEG treated glass slide. Scale bar is 300 μm 115
- Figure 4.4-5 – Illustration of microfluidic connections for the single chamber microfluidic device. Two disposable syringes were connected to the inputs of the microfluidic chamber used for injecting cells, medium and assay reagents. A single channel is used to dispose of waste fluids collected by Eppendorf tubes. 116
- Figure 4.4-6 – Design of 4-chamber microfluidic device to enclose micro pattern protein arrays. (a) Photograph showing the microfluidic device assembled and setup with fluidic connections on a microscope stage. (b) Schematic illustrating the microfluidic chambers and dimensions. Micro-arrays can be seen in the chambers (10 x 5, 150 μm dots). A full technical drawing of the design can be found in Appendix A. 117
- Figure 4.4-7 – Illustration showing the general operation of the 4 chamber microfluidic device, this process is applicable to each chamber. (a) Cells were first injected gently into the 3-way valve using a 5 ml disposable syringe, flowing from 1 to 2. The system was previously primed with the same protocol with phosphate-buffered saline solution (PBS) illustrated as blue filled areas. Once no bubbles were visible at the waste outlet the valve was switched to flow from 1 to 3. (b) Cell solution was then injected into the chamber with waste flowing to the output. On filling the chamber, the flow was stopped and a stopper was inserted into the tubing on connection 2. (c) The valve was then switched to close the input (syringe) from the chamber. The system was then sealed, as a stopper was then placed in the output tubing (connection 2). 119
- Figure 4.4-8 – Illustration showing the fluidic setup used for culturing cells using the multiple chamber culture device. The system consisted of 4 syringe pumps each connected to a separate 3-way valve by PTFE tubing. The valves were in turn connected to the chambers of the microfluidic device, terminating in a waste collection Eppendorf tube. The illustration shows the system in cell culture operation using a flow rate of 0.1 $\mu\text{L}/\text{min}$ (direction of flow indicted by red arrows), therefore the valve is opened to allow flow from port 1 to 3 of the 3-way valve. A stopper is inserted into the tubing of port 2 to seal the tubing to aid in the reduction of air into the system. 120
- Figure 4.4-9 – Microfluidic device experimental setup using a confocal microscope with incubation enclosure. (a) Photograph showing the confocal microscope Zeiss LSM 510 Meta with incubator enclosure and heater. (b) The highlighted area shows enclosed within the incubator housing syringe pumps to provide flow for the biochip connected to 3-

	way valves; (c) Photograph shows the biochip assembled and connected to 3-way valves and waste collection Eppendorfs. Scale bar is 40 mm.	121
Figure 4.4-10	- A standard curve with resorufin concentrations of 0, 0.01, 0.05, 0.1, 0.5, and 10 μm needed to compare and interpret results from the EROD assay. Excitation 530 nm and emission 584 nm.....	122
Figure 4.5-2	– Fluorescent microscopy images of primary rat hepatocyte arrays showing live/dead analysis. (a) Micro-array live/dead analysis after 24 hours incubation at 37°C, 5% CO ₂ , from left to right, bright field, live (calcein AM) and dead (EtD-1). (b) Control sample of hepatocytes cultured on untreated glass. Morphology of the hepatocytes cultured on the micro-arrays correlate with the morphology in the control samples. Live/dead analysis shows that the hepatocytes have a higher overall viability on the micro-arrays than on the untreated glass. Scale bars are 150 μm	125
Figure 4.5-3	– Fluorescent microscopy images of primary rat hepatocyte arrays cultured with the Dolomite device showing live/dead analysis. (a) Micro-array live/dead analysis after 24 hours incubation at 37°C, 5% CO ₂ , from left to right, bright field, live (calcein AM) and dead (EtD-1). (b) Control sample of hepatocytes cultured on untreated glass. Morphology of the hepatocytes cultured on the micro-arrays correlate with the morphology in the control samples. Live/dead analysis shows that the hepatocytes have a higher overall viability on the micro-arrays than on the untreated glass. Scale bars are 150 μm	126
Figure 4.5-4	– Primary hepatocytes cultured for 24 hours inside the microfluidic device using the Chamber design. (a) Shows hepatocytes attached to collagen dots, (b) shows a magnified area showing detail of cells cultured on the pattern. (c) and (d) show the same culture of cells fluorescing due to calcein-AM staining; intense fluorescing of the cells indicates viable cells. Scale bars are 500 μm for (a) and (c), 200 μm for (b) and (d)	128
Figure 4.6-1	– EROD assay on the Dolomite device showing the average intensity of resorufin fluorescence emitted by single cells over time. The EROD assay indicates the related quantity of metabolised resorufin due to cytochrome P450. An increase in fluorescence intensity correlates to an increase in resorufin production. Each data point is an average value of randomly chosen single cells within the array. Each data point represents an average of reading from three cells.	129
Figure 4.6-2	- EROD assay performed in a petri dish with hepatocytes. Three regions of interest (ROI) were selected as shown in the microscope image. The respective intensity over time is shown for each ROI is plotted on the left hand side of the figure. Scale bar is 100 μm	130
Figure 4.6-3	- EROD results on four chamber device. Three regions of interest (ROI) were selected as shown in the microscope image. The respective intensity over time is shown for each ROI and is plotted on the left hand side of the figure. Scale bar is 100 μm . ..	131
Figure 5.3-1	– 3D renders of COMSOL geometry and mesh. (a) 3D wireframe render of a lobule electrode with 60 μm spacing embedded to the bottom surface of a defined fluidic volume (1.1 x 1.1 x 0.1) mm. The electrodes are infinitely thin to simplify the meshing. (b) 3D mesh of geometry shown in (a) areas of high mesh density was visible in the corners of the lobule geometry and at the ends of the electrode arms. The total meshed tetrahedral elements was 235571.	136
Figure 5.3-2	– Simulation results of a single electrode lobule using 60 μm spacing between electrodes. (a) Slice plot 10 μm above the surface of the electrodes showing the electric field distribution, (b) shows a close up of the top-right hand side of the electrodes. A red line shows the data used to plot the electric field distribution 1 μm next to the edge of the electrodes. The electric field has shown to increase linearly as the distance between the electrode arm and counter electrode decreased. At the end of the electrode arm the electric field is 211 kV/m, then the electric field drops sharply before picking up to 70 kV/m at the edge of the counter electrode.	138
Figure 5.3-3	– Numerical simulation of electric field by applying 10 V peak-to-peak at 10 MHz for a cell of the lobule array. (a) The distribution of the normalised electric field at 10, (b) 30 and (c) 100 μm from the electrode surface. Scale is in electric field strength (kV/m). Volume simulated is 1.1 x 1.1 mm, 100 μm in depth.	138
Figure 5.3-4	– Electric field strength over the 100 μm volume measured at the tip of the electrode arm shown in Figure 5.3-2. The electric field was shown to decrease exponentially as the distance from the electrode surface increased.	139
Figure 5.3-5	– Numerical simulation of ∇E^2 (V^2/m^3 , \log_{10} scale) in a single cell from the lobule electrode array. Positive DEP force direction is displayed by the $\log_{10}(\nabla E^2)$ by slices through the x-y axis of the model. A rainbow light scale represents the electric	

field gradient distributed through the model. DEP force direction is indicated by blue arrows both normalised in the x-y view and as a log in the isometric view. In addition black ribbons represent paths that particles would take when experiencing DEP forces as displayed in the isometric view. (a) shows a 10 μm slice through the model, (b) 30 μm and (c) 100 μm . The maximum ∇E^2 induced is 16.7 and minimum is 5.8 V^2/m^3 , \log_{10} scale. The electric field is applied with 10 V peak-peak, permittivity is that of water at 80. 140

- Figure 5.4-1 – The system setup and operation for patterning liver like structures within an agar gel with a paper substrate. (a) Warmed 1% agar solution with randomly distributed cells at 37 °C was pipetted into volume designated by the gasket. The Peltier warmed the glass substrate on which the electrodes are situated and enclosed with a cover. (b) Hepatic cells were captured by positive DEP forces (*FDEP*) induced by a non-uniform electric field. (c) Once patterning was completed the Peltier was switched to cooling mode dropping the temperature of the agar to 18 °C curing the gel. Once the air temperature reached 25 °C the AC field was switched off. Agar 1% solution enters gel phase at this temperature.²²⁴ (d) The cells patterned by the DEP forces are not held in place by the cured agar. The paper substrate containing a biomimetic micro liver is used to manipulate the patterned cells into a culture system..... 143
- Figure 5.4-2 – Micro liver patterning protocol. (a) Photograph showing the system assembly with wetted paper rings. (b) IR image of warmed pipette with 10 μl of cell agar solution to be pipetted into the volume of the gasket. (c) Photograph post-patterning with cured micro liver pattern being removed from the electrodes. (d) Photograph of a cured micro liver being moved to a 9-well plate. Scale bars are 5 mm. 145
- Figure 5.5-1 – Time sequence of images for patterning liver cells (C3A) with a non-uniform DEP force field under the DEP voltage of 10 V peak to peak at 10 Mhz. (a) The cell patterning electrodes had 10 μl of cell pipetted onto the surface which are randomly distributed before DEP forces are induced. (b) Image shows cells being manipulated one second after the AC field was induced. Cell being to align to the areas of high electric field strength created at the electrodes. (c) This image shows patterning 15 seconds after DEP forces are induced. (d) This image shows the patterning after two minutes of patterning. Cell have aggregated at the areas of high electric field strength forming a biomimetic lobule pattern. 148
- Figure 5.5-2 – Micro liver pattern handing of patterned C3A cells by DEP forces in agar with a paper substrate. (a) C3A cells patterned in biomimetic liver lobules pattern transferred successfully from electrodes to a petri dish. (b) Patterned C3A cells which the bond of the agar to the paper broke causing the agar to fold over itself, however the pattern is still intact despite this. 149
- Figure 5.5-3 – Viability of C3A lobule like structures in agar over a 72 hrs period as well as controls. Images are a composite of both live cells (FITC) and dead cells (Rho) images. The first column shows fluorescence images of patterned C3A cell in a lobule structure. Cell aggregation increased over the 3 days and high viability (80%) is maintained. Proliferation was slow compared to the 2D control but an increase in cell density was evident from pattern ratio data. Viability in of the control sample is shown in the second column which compares favourably with the patterned C3A cells. The final column shows the 2D culture viability which also compares well to both the patterned and control samples. Cell proliferation was observed to be higher than that of the agar encapsulated C3A cells. Cell density was observed to double after 48 hrs and triple by 72 hrs. The starting cell count for the samples was 1×10^5 cells. Scale bars are 100 μm 151
- Figure 5.5-4 – Pattern ratio of patterned cells as a function of time over 3 days of culture. Live pattern ratios were observed to increase with time, dead ratios increased after 48 hours before decreasing at 72 hours. The electric-field was induced for two minutes (10 MHz, 10 Vpp) at 37 °C following the optimised protocol. The normalised control threshold as expected is 1 ± 0.035 . The pattern ratio for live and dead cells is very similar after 24 hrs. The live pattern ratio increases steady up to a 1.9 ± 0.4 after 72 hrs. While the ratio increased after 48 hrs for dead cells after 72 hrs the ratio is lower than that of live cells (1.4 ± 0.3). Error bars represent standard deviation of the mean (n = 4). 152
- Figure 5.5-5 – Albumin secretion a liver-specific function for hepatocytes was selected as a marker to assess the functionality of the patterned micro liver-like cultures. The concentration of the albumin secreted by the cells in patterned, control and 2D samples over 72 hrs culture was assessed by human albumin ELISA shown in Figure 12. Patterned C3A cells had increased albumin secretion after 48 hrs of

culture compared to the control and monolayer control. The control samples show a relatively stable production over the first two days before decreasing. The albumin concentration observed in the 2D culture after 24 hours was higher than the patterned and control samples before gradually decreasing similar value by day 3. Data represent the mean \pm STD for four independent repeats. The (**) indicates statistical increase in albumin protein of patterned cells relative to control and 2D cultures at day 2, $p < 0.01$ (ANOVA). 154

Figure 6.2-1 – Schematic description showing tissue engineering process from computer-aided design (CAD), to cell culture scaffolds produced by a 3D printer. Reproduced from reference ¹⁸⁸ 158

Figure 6.3-1 – Experimental setup for real-time analysis of zebrafish using the micro analysis platform. a) Photograph showing the interior of the incubator b) with μ AP, reservoir and lighting system. The mp-x pump control unit was placed on the shelf below (not pictured). C) Schematic illustrating the fluidic connections of the system and off-chip connections and hardware actuating the 3D printed zebrafish trapping device. 160

Figure 6.3-2 – 3D rendered images of designed used for biocompatibility of 3D printed materials with zebrafish embryos. A) Discs for inserting into a 24-well plate, engraved here with HD3500 label (15 mm in diameter, 1 mm thick). B) 24-well plate based on flat-bottomed Corning plates available commercially.²⁸³ C) Single-well culture device with lid. D) Cross-section of single well culture device. Scale bars are 20 mm. 161

Figure 6.4-1 – Assessment of microenvironmental conditions inside the chip. Time-lapse images of developing zebrafish embryos collected every 30 minutes over 52 hours. Embryos were loaded on a chip at a volumetric flow rate of 2 ml/min. Subsequently the chip was perfused at a rate of 0.5 ml/min for up to 72 hours. Green dotted circles indicate healthy zebrafish embryos, red dead zebrafish embryos and cyan hatched zebrafish embryo. Scale bar is 1 mm. 164

Figure 6.4-2 – Assessment of viability of zebrafish embryos cultured inside the chip. a) Microphotograph showing zebrafish embryos developed over 48 hours with a flow rate of 0.5 ml/min. Zebrafish developed and were viable. b) Microphotograph 4 hours after switching off the volumetric flow. One hatched zebrafish larva escaped a trap and remained in the channel, a 100% mortality rate of embryos was observed. Scale bar 1 mm. 165

Figure 6.4-3 – Development of zebrafish embryos in 3D printed material VisiJet Crystal and VisiJet S300 support wax: a) Cumulative survival of zebrafish embryos, '3D nowax' indicates 3D printed wells with no support material present, '3D wax' indicates support wax had been present in the well and had been removed pre-experiment. B) Hatching success of embryos held with 3D printed materials. 167

Figure 6.4-4 – Development of zebrafish embryos in HD3500+ printed VisiJet Crystal wells: Culture of zebrafish was conducted within 3D printed samples with and without wax support. Control samples consisted of wax support material melted on the bottom of 24-well plates and untreated 24-well plates. Cell death occurred in zebrafish within the 3D printed no wax samples within 24 hours. Embryos in the wax coated 3D printed wells followed at 47 hours. Wax and untreated samples developed normally. 168

Figure 6.4-5 – Survival of zebrafish cultured with 3D printed materials. Zebrafish at 1.5 hpf were incubated with washed HD3500+ and Viper Pro samples, as well as unwashed samples. As expected unwashed samples caused cell death within 24 hours, cell death for washed samples was deferred to 52 hours. Survival rates of washed samples dropped to 70-75% within 4 hours and maintained at 70% for 22 hours, dropping again at 27 hours to 65%. By 47 hours of incubation washed sample survival had dropped to 5%. Confirmation of 0% survival was visualised at 52 hours. Control and ABS samples showed normal development and maintained a survival rate of 85-100% throughout the experiment. (n=4) 169

Figure 6.4-6 – Morphology analysis at 27 hours incubation of zebrafish with 3D printed materials. Stereomicroscopy images of dechorionated zebrafish embryos immobilised in agar: a) Control zebrafish embryo cultured in a 24-well plate development was normal. B) Image of zebrafish cultured with Watershed (Viper Pro) material. Development has been stunted, appears 2-3 hours behind control, darkening of yolk sac and roughing and widening yolk extension.²²⁷ C) Image of zebrafish cultured with VisiJet Crystal (HD3500+) printed disc. Development has been stunted by 5 hours, still in the 25-somites stage. Eyes and brain have not developed, pigmentation was not present, unusual yolk sac and yolk extension shape all show retardation. 170

Figure 6.4-7 - Survival rate and hatching success of 24 hpf zebrafish cultured with 3D printed materials: a) Cumulative survival rate of zebrafish over a 48 hour incubation period.

Watershed unwashed samples caused cell death within 25 hours of incubation. VisiJet Crystal controls shows a steady reduction of survival, washed samples however have increased survival, b) Cumulative hatching success of zebrafish embryos over a 48 hour incubation period. Watershed unwashed hatching rate was 0%. Washing of VisiJet Crystal samples improved hatching success to 15% compared to 5% for unwashed samples. Hatching of control samples was 80%. (n=4).....171

- Figure 6.4-8 – Morphology changes during incubation with 3D printed materials of 72 hpf zebrafish: a) Stereomicroscopy of hatched zebrafish embryo control showing normal morphology development. B) Zebrafish after 48 hours of incubation with washed VisiJet Crystal samples. These fish are grossly normal, but show signs of developmental delay, hypopigmentation, heart edema, blood pooling and reduced yolk extensions. Scale bars are 500 μ m.172
- Figure 6.4-9 - Zebrafish incubated within a 3D printed single well of ABS for 72 hours: a) Control sample, b) Zebrafish incubated with ABS, no visible defects are present. Scale bar 500 μ m.173
- Figure 6.4-10 – Stereomicroscopy images of zebrafish embryos cultured on untreated 3D printed wells. Unfertilised embryos were sorted out at 6 hour post fertilisation (hpf), then were manually transferred into the wells. After 18 hour of incubation time, embryos from VisiJet Crystal and Watershed printed wells were died while most of embryos from Dreve Fototec printed wells were still alive. However, they experienced cell death after 24 hour of incubation.174
- Figure 6.4-11 - Stereomicroscopy images of zebrafish embryos cultured on solvent rinsed 3D printed wells. Unfertilised embryos were sorted out at 6 hour post fertilisation (hpf), then were manually transferred into the wells. Wells were rinsed by solvents for up to two minutes. Embryos cultured in 99% isopropanol rinsed and 70% ethanol rinsed wells experienced 100% mortality after 66 hours incubation. Embryos from 99% ethanol rinsed wells were still alive but their embryogenesis were significantly delayed.....175
- Figure 6.4-12 – Embryo survival percentages of different treatments over incubation time. Embryos from 99% ethanol, 70% ethanol and 99% isopropanol treated wells survived for up to 91, 66 and 66 hours respectively.175
- Figure 6.4-13 - Stereomicroscopy images of zebrafish embryos cultured on solvent rinsed 3D printed wells. Unfertilised embryos were sorted out at 6 hour post fertilisation (hpf), then were manually transferred into the wells. Wells were soaked in solvents for 24 hours. 50% embryos cultured in 99% ethanol soaked VisiJet Crystal wells experienced mortality after 48 hours of incubation. Meanwhile in 99% ethanol soaked Dreve Fototec wells, all embryos survived, the hatching rate was up to 48%.176
- Figure 6.4-14 - Embryo survival percentages of different materials after 99% ethanol soaking over incubation time. Embryos from VisiJet Crystal printed wells experienced 100% mortality after 72 hours incubation. Apart from unfertilised embryos, all embryos from Dreve Fototec printed well survived after 72 hours incubation.....177
- Figure 6.4-15 – Intersegment vessels (ISV) analysis morphology on hatched zebrafish larvae cultured from a) control petri dish and b) Dreve Fototec printed wells. After 72 hours of incubation in Dreve Fototec printed wells that soaked in 99% ethanol, larvae hatched and ISV were completely developed, in line with those cultured from control petri dish.....177
- Figure 7.4-1 – Photographs showing results of multi-jet modelling (MJM) fabricated fluidic system. (a) The base of the system shown here splits the flow from a central vertical channel into six spate channels ending in connecting nozzles. This bottom piece could be connected to a 3D printed enclosure for liver lobule-like tissue constructs to provide nutrients and analytes. (b) Connected system using interlocking pins. The top cube chambers could act as medium reservoirs for adding analytes to the system. Scale bars are 10 mm.183
- Figure A-1 – PDMS mould design. The lid is fabricated from polycarbonate. The base is fabricated from aluminium.....185
- Figure A-2 - Computer aided design (CAD) design of clamp system with relation to the 4 chamber microfluidic chip (a) shows the Perspex top with channel positioning. (b) shows the aluminium bottom with cross section.186
- Figure A-3 – Designed to attach microbore valves securely to a flat surface, minimising movement of the interconnecting tubing between the pumps and the device. Rubber feet were attached to each of the corners to allow it to grip the microscope stage.186

Figure B-1 – Schematic of cover design used for the liver lobule-like patterning system.
Measurements are in mm..... 187

Figure C-1 – Schematic of design for a stackable interlocking fluidic system. Measurements are in
mm..... 188

Acknowledgements

I wish to thank Professor Jonathan Cooper for inviting me to do a PhD on that sunny afternoon when I bumped into him on Kelvinway. Without this fateful meeting as well as his unwavering support, knowledge and advice throughout, this thesis would not have been possible. Additionally, I wish to thank my international collaborators Professor Michael Louis Shuler (Cornell University, Ithaca, USA) and Prof. Donald Wlodkowic (RMIT University, Melbourne, Australia) .

My most sincere thanks go to Dr. Julien Reboud who has been understanding and insightful to the highest degree and for keeping me sane during the long-hours of experiments, analysis and writing. To Dr. Anoop Menachary, this extends equally for going beyond the call of duty in answering my questions, even when no time was left. I would also like to thank Dr. Rab Wilson for his numerous insightful discussions, support and technical knowledge that borders on wizardry. I highly acknowledge Paula Miller (Cornell University) for her extremely thorough teachings in the art of cell culture and Dr. Mandy Esch for her expertise in organ-on-chip technology.

Special thanks go to: Jin Akagi and Feng Zhu (Auckland University), Dr. Maaïke E. Schutte (LGC, London, UK), Dr. Elizabeth Patton (MRC, Edinburgh, UK) and Dr. Alicja Zarowna-Dabrowska for all of their help and expertise in the technical and experimental aspects of my work. In addition I would like to thank: Dr. Andrew Glidle, Dr. Huabing Yin, Dr. Christopher Syme, Christian Witte, Trevor Waldmeyer, Ewan Russell and all of the technicians from the James Watt Nanofabrication Centre and Mechanical Engineering Workshop. I extend thanks to all of the members of the group that have made working in the Rankine Building labs an unforgettable experience.

An essential contribution of this work was the funding from both EPSRC and Unilever, I wish to thank them for keeping me fed and sheltered during the course of this work. Additionally I wish to thank the Royal Society of Edinburgh and the University of Glasgow for financially supporting my international research collaborations.

For close friends that have supported me throughout this thesis, some of which are no longer in my life, thank you. To all the friends I made along the way, both inside and outside of science (at times around it, climbing up rocks, jumping off walls etc etc), both near and far (USA, New Zealand, Germany, Spain, Switzerland, Australia) thank you. It's been an incredible journey and your part in it has made it something more than I could have ever imagined.

My penultimate acknowledgement goes to my family: to Shirley for putting me up when times were rough and keeping a chipper outlook; Ruairidh and Shona for always making things worthwhile; my Mum for the endless encouragement; my Dad for putting up with me stressing out during my write up and my Grandfather, Rodney Jones for getting me into science in the first place.

Last but not least, Elena Mecheva, for your love and support when I needed it the most.

Authors Declaration

“I declare that, except where explicit reference is made to the contribution of others, this dissertation is the result of my own work and has not been submitted for any other degree at the University of Glasgow or any other institution”.

Niall Patrick Macdonald

List of Abbreviations

3T3	3-day transfer, inoculum 3×10^5 cells (NIM/3T3 fibroblast cells)
Au	Gold
ABS	Acrylonitrile butadiene styrene
ADME	Absorption, distribution, metabolism, and excretion
AFP	Alpha fetoprotein
AMS	Accelerator mass spectrometry
ASPCA	American Society for the Prevention of Cruelty to Animals
ATCC	American Type Culture Collection
BioMEMS	Biological microelectromechanical systems
BUVA	British Union for the Abolition of Vivisection
C3A	Hepatocellular carcinoma cells (HepG2/C3A hepatocyte cell line)
C ₄ F ₈	Octafluorocyclobutane
CAD	Computer aided design
CAE	Computer-aided engineering
CHO	Chinese Hamster Ovary cell line
CM	Clausius Mossotti
CNC	Computer numeric controlled
CO ₂	Carbon dioxide
DEP	Dielectrophoresis
DILI	Drug-induced liver injury
DMEM	Dulbecco's modified Eagle medium
DMSO	Dimethyl sulfoxide
ECM	Extra cellular environment
EGFP	Enhanced green fluorescent protein
EMEM	Eagle's Minimum Essential Medium
EPA	Environmental Protection Agency
EtOH	Ethanol
EU	European Union
EWOD	Electrowetting-on-dielectric
FET	Fish embryo toxicity test
FDA	Food and Drug Administration
FDM	Fused deposition moulding
FITC	Fluorescein isothiocyanate
HBSS	Hank's Balanced Salt Solution
HD3500+	3D Systems HD3500 Plus professional 3D printer
HDPE	High density polyethylene
Hfp	Hour post fertilisation
HMDS	Hexamethyldisilazane
HPDFO	High Power Density Focusing Optics
IACUC	Institutional Animal Care and Use Committees
ICATM	International Cooperation on Alternative Test Methods

ISV	Intersegmental vessels
IPA	Isopropyl alcohol
JaCVAM	Japanese Center for the Validation of Alternative Methods
JWNC	James Watt Nanofabrication Centre
LGC	Laboratory of the Government Chemist
LOC	Lab-on-a-chip
MCF7	Michigan Cancer Foundation-7 (Breast cancer cell line)
MRC	Medical Research Council
MJM	Multi-jet modelling
NaOH	Sodium hydroxide
NAS	National Academy of Sciences
NMR	Nuclear magnetic resonance
PBPK	Physiologically based pharmacokinetic models
PBS	Phosphate buffered saline
PC	Polycarbonate
PD	Pharmacodynamics
PDMS	Polydimethylsiloxane
PEG	Polyethylene glycol
PET	Positron emission tomography
PETA	People For the Ethical Treatment of Animals
PK	Pharmacokinetics
PLA	Poly(lactic acid)
PMMA	Polymethyl methacrylate
PTFE	Polytetrafluoroethylene
REACH	Registration, Evaluation, Authorisation and Restriction of Chemicals
Rho	Rhodomine
ROI	Region of interest manager
RSPCA	Royal Society for the Prevention of Cruelty to Animals
SLA	Stereolithography
SF ₆	Sulphur hexafluoride
Ti	Titanium
USP	United States Pharmacopeia
UV	Ultra-violet
Viper Pro	Viper Pro SLA System

1 Introduction and review of literature

1.1 Animal testing and the need for alternatives

Modelling is a key aspect of engineering design. It allows for a complex system to be separated into modular systems and understand how they integrate into the whole. This is accomplished with graphical 3D modelling in architecture, mathematical modelling of chemistry and biological phenomenon, physical working models in mechanical engineering and prototypes circuits on breadboards in electronics. These models allow the engineer designing or investigating the system, insight and increased awareness in building an effective device and discover interactions. For the most part, these models can be developed using computers and will give accurate and precise results.

Modelling of biological interactions however remains a difficult task. Understanding of DNA, cells, viruses and other biological systems have been revealed in great detail, however the interaction of these different factors particularly *in vivo* (within the living) is at present unelucidated.¹ The effect that pharmaceuticals have on the body varies from person to person, biological implants can cause immuno-responses and other environmental effects which can have negative effects on the human body.

Drug testing is a long expensive process taking 12 to 15 years and \$100 of millions in development costs.² It is estimated that only 1 in 10, 000 new compounds tested are successful.³ Early detection of toxicity and efficacy is tested however many drugs still fail at Phase II and III testing; currently only 1-10 drugs exit human trails as approved drugs.⁴

An example is fialuridine, identified as a potential treatment for the hepatitis B virus infection. Unfortunately during clinical trials it led to the death of 5 out of 15 patients due to fulminant liver failure.⁵ This was mainly due to animal testing failing to discover these hepatotoxic effects and was considered unusual at the time. However, it is has become increasingly observed that animal studies do not offer the security and quality of information that is believed by the scientific community.⁶ Of all animal studies it is only chimpanzees that hold any credible correspondence to human effects in regard to toxicity, carcinogenicity and teratogenicity. There are many differences in humans to mice for example where the biological separation is about 120 million years of evolution.⁷ For example, a recent study by *Seok et al* observed that the genomic responses to different acute inflammatory stresses are

not present in current mouse models. In addition to improvements in the current animal model systems, their results urged research to focus on translational medical research rather than relying on mouse models for studying human inflammatory diseases.⁸

Economic and ethical factors are also a factor in the need for alternatives to animal testing. Government research centres and universities are granted hundreds of millions of dollars for animal related studies demonstrating the expense and reliance on external funding.⁹ The cost of one genetically modified mouse can be up to \$100, 000 for a custom specimen. Additionally the treatment of animals in these studies and their upkeep has been an area of dispute by various organisations and groups.¹⁰

Strong opposition against animal testing particularly for cosmetics has been voiced by animal rights groups including the British Union for the Abolition of Vivisection (BUVA)¹¹, People For the Ethical Treatment of Animals (PETA), American Society for the Prevention of Cruelty to Animals (ASPCA) and the Royal Society for the Prevention of Cruelty to Animals (RSPCA).

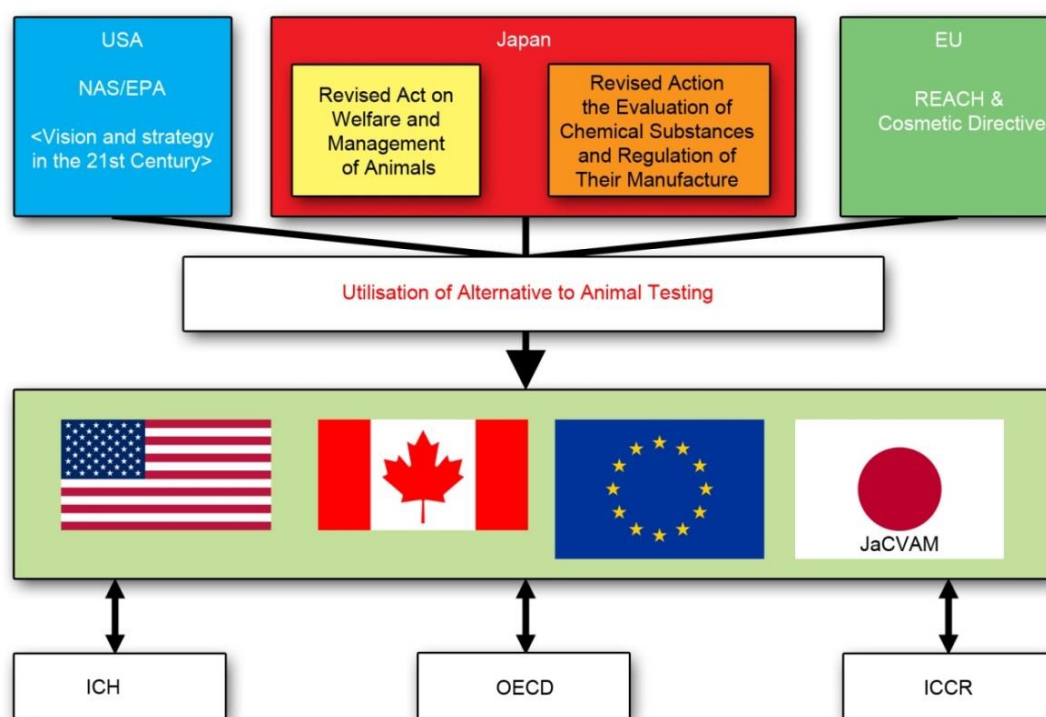


Figure 1.1-1 – International Cooperation on Alternative Test Methods (ICATM): On April 27, 2009 the U.S., Canada, Japan and EU signed a memorandum of cooperation that could reduce the number of animals required for consumer product safety testing worldwide. The agreement will yield globally coordinated scientific recommendations on alternative toxicity testing methods that should speed their adoption in each of these countries, thus reducing the number of animals needed for product safety testing.¹² ICH: The International Conference on Harmonisation of Technical Requirements for Registration of Pharmaceuticals for Human Use. OECD: The Organisation for Economic Co-operation and Development has a Test Guideline program that deals with chemicals. ICCR: The International Cooperation on Cosmetics Regulation (ICCR) is an international group of cosmetic regulatory authorities from the U.S. (FDA), Japan (Ministry of Health, Labour, and Welfare), the EU (EC, DG Enterprise), and Canada (Health Canada).

On the global scale the International Cooperation on Alternative Test Methods (ICATM), on April 27, 2009 the U.S., Canada, Japan and European Union (EU) signed a memorandum of cooperation that could reduce the number of animals required for consumer product safety testing worldwide illustrated in Figure 1.1-1. The agreement will yield globally coordinated scientific recommendations on alternative toxicity testing methods that should speed their adoption in each of these countries, thus reducing the number of animals needed for product safety testing.¹²

Groups included in this are the National Academy of Sciences (NAS) and Environmental Protection Agency (EPA) in the USA and Japanese Center for the Validation of Alternative Methods (JaCVAM) in Japan. In the EU, the Regulation on Registration, Evaluation, Authorisation and Restriction of Chemicals (REACH) was put into force on 1st June 2007. It streamlines and improves the former legislative framework on chemicals of the EU. In addition, the European Commission passed the 7th amendment to the EU Cosmetics Directive which has banned all animal testing of cosmetics since 2004 and as on 11th March 2009 a “testing ban” was put in place for cosmetic ingredients as well as a “marketing ban” on such products regardless of the country of origin. The EU put into effect a complete ban on the sale of cosmetics developed through animal testing in March 2013.¹³ This ban applies to all products within the EU regardless of the place of production. Many countries worldwide however enforce animal testing for cosmetics by law. The implications of this mean that cosmetics companies are shifting their markets in order to avoid the EU ban issue.¹⁴

1.2 The 3R's of animal testing

One of the driving factors of this sector of non-animal alternatives is the three Rs (3Rs). This includes that of replacement (with non-animal models), reduction (of animal numbers), and refinement (to decrease animal suffering) of laboratory animal use. The 3Rs were first proposed by *Russell and Burch* (1959), and have since become almost universally accepted as a fundamental to good laboratory animal practice.¹⁵

In addition to the 3R's legislation of animal ethics committees, such as Institutional Animal Care and Use Committees (IACUC) in the United States, assure that the numbers of animals proposed for use in scientific experiments are justified and reasonable. Animal studies must be designed to accomplish experimental aims with minimal use of animals.¹⁶ Suggestions to reduce the number of animals include: (1) rational selection of group size (pilot study, power analysis); (2) careful experimental design; (3) maximizing use of each

animal; (4) minimizing loss of animals; and (5) statistical analysis (maximum information from minimum number of animals).¹⁷ The identified problem with this approach however is that pilot studies and power analysis can overcompensate for animal numbers.¹⁸

1.3 Alternative methods to animal testing

1.3.1 Human volunteering

Human volunteering involves the use of humans voluntarily performing *in vivo* testing of existing and new drugs. Human micro-dosing, is a technique for studying the behaviour of drugs in humans through the administration of doses so low ("sub-therapeutic") they are unlikely to produce whole-body effects, but responses can be studied on the cellular level.¹⁹ It has been established that efficiency gains, as well as ethical and practical advantages in addition to reduction in animal use make it a useful tool.²⁰ Compared with animal testing, human volunteering can provide meaningful data as metabolism pathways and scale are relevant.¹⁹ Current methods for non-invasive imaging of the effect drugs and compounds have *in vivo* include: accelerator mass spectrometry (AMS), Nuclear magnetic resonance (NMR) spectroscopy and Positron emission tomography (PET).²¹ A combination of *in vivo* human and *in vitro* human cell testing has been presented as a plausible method to reduce the need for animal testing.^{22, 23}

1.3.2 Cell line drug testing

In vitro assays are a well employed technique that can utilise bacterial, yeast, protozoan, mammalian or human cell cultures and exist for a wide range of toxic and other endpoints, including skin corrosion/irritation, phototoxicity, eye corrosion/irritation, skin absorption, skin sensitisation, carcinogenicity and systemic toxicity.²⁴

The first recorded use of cell culture dates back to the 16th century and Sir William Harvey. He noticed that myocardium kept in the palm of his hand covered in his own saliva could remain contractile for extended periods of time.²⁵ Several important advancements in cell based studies can be identified since then and have been well documented in a review on cell lines for toxicity studies by *Allen D. et al.*²⁶ The first continuous cell line began in 1951 known as HeLa in remembrance of Henrietta Lacks from which the cervical cancer immortal cell line were derived.²⁷ Concerns about cells losing functionality due to the immortalised state focused research into stabilising cell and tissue culture *in vitro*. Eagle and Levintow in 1961 made the first systematic investigation of essential nutritional requirements of cultured cells.²⁸ Several years later in 1969 Augusti-Tocco and Sato established the first immortalised cell line to retain differentiated traits of the original

tissue.²⁹ As well as the adapted mouse nerve cells, other cell lines were established at this time including skeletal muscle and liver cell lines. Present day there are a vast number of different established cell lines. It is currently stated that The American Type Culture Collection (ATCC) has over 4,000 cell lines ranging over 150 different species.

Cell line drug testing is the primary alternative to animal testing. These are biochemical assays carried out *in vitro* based on biochemical assays. Individual organ tissues can be studied and conditions are strongly constricted improving repeatability. The range of methods of *in vitro* testing for cosmetics and drugs is vast and can be studied in more depth in these reviews and documents^{11, 24, 30}. It also allows these tests to avoid the ethical and high-cost issues of animal testing when investigating early stages of new compounds.²⁶ Further, if adverse effects are determined *in vitro*, reduction in the numbers of animals being unnecessarily screened can occur as well. Changes in policy and improvement in toxicity testing technology has reduced animal testing from 8988 to 344 animals from 2004 to 2009 within the EU. However animal studies outside of the EU still number as much as 15000 and 27000 animals for cosmetic testing alone.¹³ Exchanging *in vivo* animal testing directly for *in vitro* alternatives is regarded as a positive step towards replacement, however complete replacement requires further research.^{11, 23}

1.3.3 Mathematical modelling of pharmacokinetics

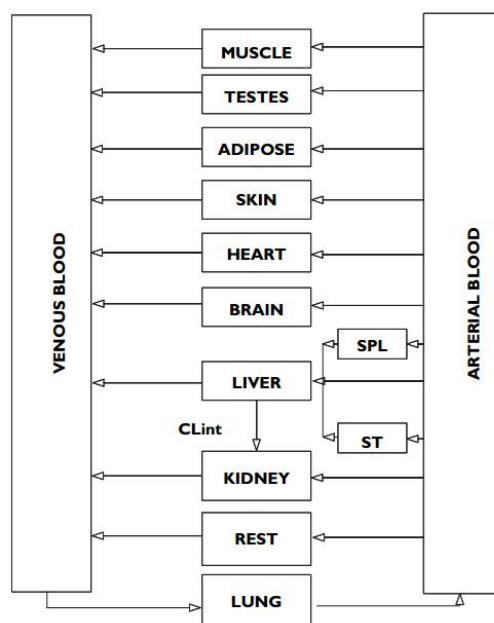


Figure 1.3-1 - An example of a physiologically based pharmacokinetic model. The compartments represent tissues and organs; connecting arrows represent blood supplies; ST is stomach; SPL are splanchnic organs; and CL_{int} is intrinsic hepatic clearance. Reproduced from reference³¹.

In addition to microdosing and cell culture studies computational models and algorithms are employed. The standard models for such studies are pharmacokinetics (PK) and

pharmacodynamics (PD), both branches of pharmacology. The former is dedicated to the determination of the fate of substances administered externally to a living organism,³² the latter is concerned with the mechanisms of drug action on the organism.³³ PK modelling is primarily concerned with analysis of pharmacokinetics and pharmacology for absorption, distribution, metabolism, and excretion, (ADME) to describe the disposition of a pharmaceutical compound within an organism; an extensive review by *Lin et al* provides further details.³⁴ The most comprehensive pharmacokinetic models are based on physiological considerations as shown in the example in Figure 1.3-1. Physiologically based pharmacokinetic models (PBPK) are compartmental in nature. This differs from traditional PK as each section representing an organ or tissue is based on medical data. Volumes, physical dimensions, residence times and other factors are included in the model. This model was first development in 1937 by Teorell³⁵, regarded as “father of pharmacokinetics”³⁶. His model was later developed further to include biophase compartment and concentration–effect transducer, by Segre in 1968³⁷. Pharmacology now relies heavily on predicating the effects of drugs through use of PK and PD modelling. Drug testing with PBPK models is not the only application, they are also utilised for disease progression and therapeutic response³³.

Generally, the five major steps in PBPK model development include (1) specifying general model structure, (2) specifying tissue model, (3) writing model equations, (4) defining model parameterization, and (5) simulations and/or parameter estimation.

However, the complexity of a pharmacokinetic model depends on the level and quality of information available and on its purpose³¹. It is also of concern that the quality of the modelling itself can lead to biased results and that there remains a shortage of prospective examples that verify that this technique is as good in clinical practice as in theory³⁸. Current models have critical elements missing such as the exchange of metabolites from one cell type to another, the three-dimensional extracellular matrix environment that provides chemical and mechanical cues, the physiological liquid-to-cell ratios in a tissue/organ, and the physiological shear stresses from fluid flow are all missing; therefore, authentic cellular behaviour is limited.³

The ideal model would be able to biomimetically represent animal and human organs within an *in vitro* device. This would allow the reliance on animal studies during drug trials to be lessened significantly and suitably improve success rates in clinical trials.

1.4 Liver tissue and cells for toxicity testing

The liver is the primary organ responsible for detoxification, protein synthesis, and production of biochemicals necessary for digestion in the body; the unique structure of the liver is illustrated in Figure 1.4-1. Due to the unique vascular, secretory, synthesis and functional features of the liver and their role in the metabolic elimination of most drugs, the liver is the major target of toxicity studies.³⁹ Additionally, drug-induced liver injury (DILI) is the most common cause of withdrawal of approved drugs from the pharmaceutical market.⁴⁰ This is due to poor prognosis and idiosyncratic nature of DILI which makes this reaction a major safety issue for drug development. For these reasons the liver is of particular interest to cosmetics and toxicity studies. Assay studies are now routinely performed using hepatocyte cells for *in vitro* studies.⁴¹

Hepatocytes are the main cell type in the liver and are responsible for detoxification of blood, removal of bacteria and other harmful substances. Hepatocyte function strongly impacts on the pharmacokinetics, side-effects and toxicity of drugs^{42, 43} and hence are a powerful tool for toxicity testing. The lobule was first discovered by Kiernan in 1833 Figure 1.4-2.

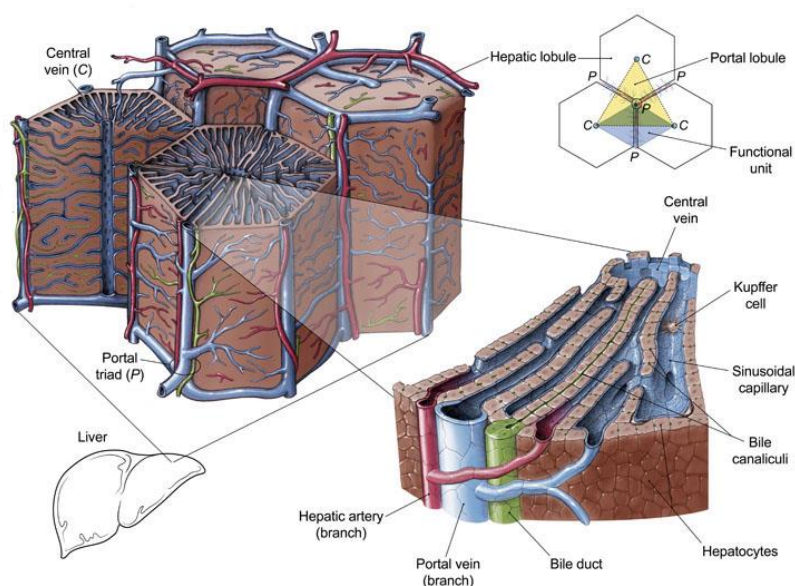


Figure 1.4-1 – The liver is the largest internal organ in the human body weighing approximately 1500g. It performs over 500 metabolic functions, resulting in the synthesis of products that are released into the blood stream or that are excreted to the intestinal tract (bile). The portal tract supplies the vast majority of blood which is low O₂ content from the gastrointestinal tract as well as from the spleen, pancreas and gallbladder. The second blood supply is the hepatic artery; a high pressure O₂ saturated supply. The building blocks of the liver are hexagonal structures, hepatic lobules that are composed almost primarily of hepatocytes with in most cases 3 portal triads in the corners. Sinusoidal canals formed by the spaces between the hepatocytes are approximately 8-10 μm in diameter, orientated in a radial direction from the central vein. Sinusoids are lined with endothelial cells and Kupffer cells which have a phagocytic function. On the opposite sides of the hepatocytes are bile canaliculi (1 μm diameter). Bile produced by the hepatocytes is transported away in the opposite direction from blood flow to the main bile duct and finally the gallbladder⁴⁴. Image reproduced from reference.⁴⁵

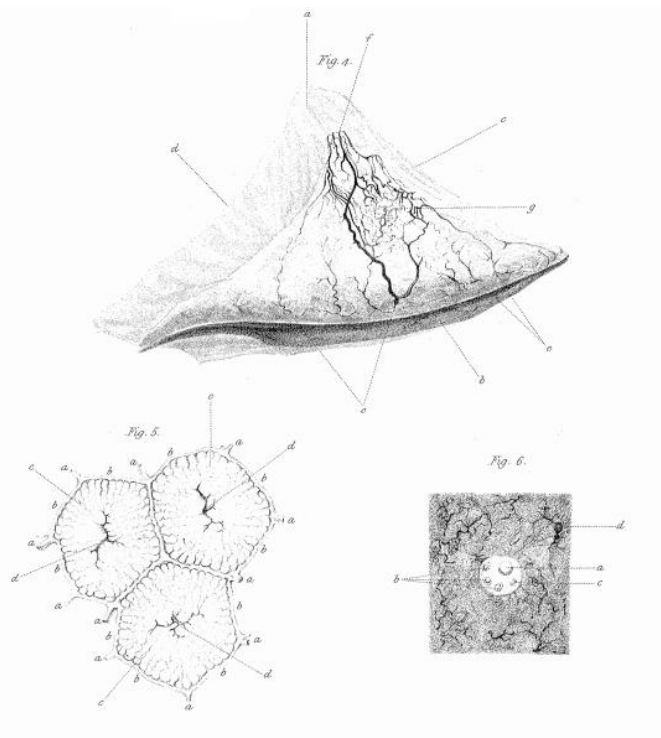


Figure 1.4-2 – Classic lobule sketches by Francis Kiernan. Fig 5 of this illustration in particular shows the structure of the liver lobule with a hexagonal like geometry (c) identifying the hepatocyte plates and (d) the central vein. Reproduced from ⁴⁶

Since the first isolation of hepatocytes by Berry & Friend in 1969 hepatocytes have seen universal acceptance by the scientific community.⁴⁷ Over the last 40 years human and various animal hepatocytes have been isolated for used in a diverse range of fields.⁴⁸ Human hepatocytes are heavily utilised by pharmaceutical companies in metabolism studies for toxicokinetics and are an accepted standard by the EC as of 2011.¹¹ *In vitro* studies⁴⁹ as well as in conjunction with PBPK modelling provide considerable evidence that predictive data is more accurate than animal testing on rats or dogs.⁵⁰ A retrospective analysis of 50 drugs has also shown hepatocytes to be as predictive as animal studies.⁵¹ They are at present the closest *in vitro* model to the liver but are phenotypically unstable, have a limited life-span outside of *in vivo* conditions and exhibit large inter-donor variability.³⁹

Primary hepatocytes are obtained from a whole liver or fragments and when fresh, exhibit most functions of a healthy liver. They will only survive for a few hours in suspension and must attach to a substratum to survive longer.⁵²⁻⁵⁴ A detailed review on conditions required to improve hepatocyte survival has been covered by *Tueschl et al.*⁵⁵

1.4.1 Other liver cell models

Alternative cell models of hepatocytes are precision cut tissue slices which are about 250 μm in thickness (≈ 10 cells). These retain the 3D structure of the liver and other cell types

(endothelial cells, stellate cells, Kuffer cells, pit cells, bile duct cells) but have a very limited 1-2 day shelf-life.⁵⁶ Hepatocyte-like cells derived from stem cells are emerging as a new potential alternative source of hepatocytes also.⁵³

1.4.2 Hepatocyte cell lines

Alternative to primary hepatocytes are a number of hepatoma cell lines that are derived from hepatocytes using oncogenic immortalisation or from tumours. These include HepG2(HepG2/C3A), Hep3B, PLC/PRF₃ Huh7, HBG and HepaRG. Compared to hepatocyte metabolic rates, P450 enzymes activity, urea and albumin secretion and other factors these cell lines do not display the same levels. However, some lines such as the HepG2 cells secrete the major plasma proteins and hepatitis B surface antigen despite having lost substantial liver specific functions.⁵⁷ The modified HepG2/C3A is a clonal derivative of Hep G2 that was selected for strong contact inhibition of growth, high albumin production, high production of alpha fetoprotein (AFP) and ability to grow in glucose deficient medium allowing higher drug-metabolising activities.⁵⁸

However, all of these models carry drawbacks such as low differentiated state in most of the hepatic cell lines usually used in static culture, unpredictable availability, and genetic polymorphism for human primary hepatocytes⁵³.

1.5 Model *in vitro* systems

1.5.1 Introduction

In vitro models of biological tissues are critical in the reduction of animal testing, assessing new compounds and improving the understanding of human physiology. Unfortunately the advantage of *in vitro* testing is paradoxically the main drawback. *In vitro* models are simple and hence do not replicate the complex systems present in the human body. As these models do not mimic the reality of physiological factors the results can be skewed and misinterpreted leading to false conclusions^{59, 60}. However as the complexity increases so does the number of interacting parts of the model such as including more cell types⁶¹, which can lead to unpredictable behaviour⁶². Hence, in turn this can cause an unclear response to stimuli and hence less robust measurement when compared with a simple model. This problem can be met however with the use of artificially engineered microenvironments for *in vitro* studies. The challenge here lies in how to design, build and test *in vitro* model systems that allow for biomimetic models. This can be achieved by utilising integrated, micro engineered *in vitro* platforms: organs-on-chips.⁶³

1.5.2 Lab-on-a-chip devices (LOC)

It has long been observed that the microenvironment cells inhabit *in vivo* can affect their behaviour.⁶⁴ Tissue engineering scaffolds composed of porous polymer scaffold can act as substrates for attachment⁶⁵ as illustrated by Figure 1.5-1.

Studies have also shown that the chemistry, cell-cell proximity, and the mechanical properties of the substrate are cultured *in vitro* affects their phenotype.⁶⁶ Organs-on-chip are a class of microdevices for *in vitro* tissue culture that feature a physiologically relevant, engineered micro environment. Currently only 1 in 10 drugs that enter human trails exit as approved drugs. Microdevices modelling human organs could reduce this to 1 in 4 which would yield important economic and social benefits.¹

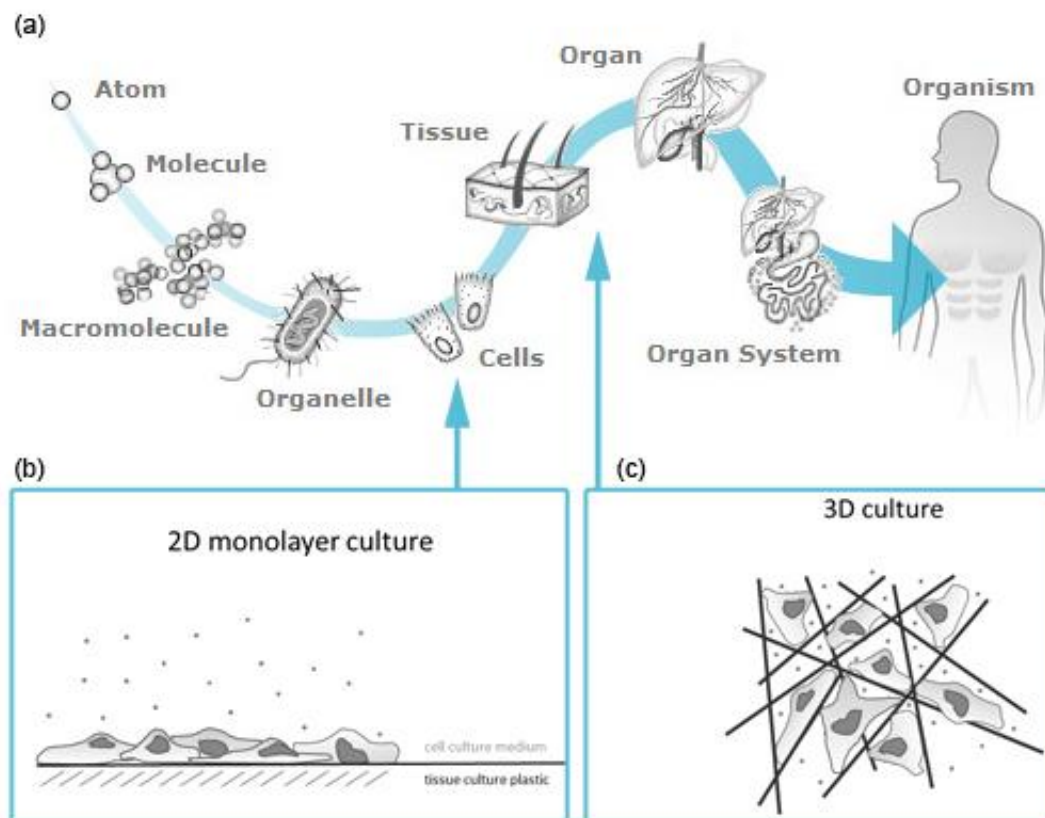


Figure 1.5-1 – 2D vs 3D cell culture, (a) represents the progression from a single atom through to a full organism. (b) 2D static cell culture is the current industry standard for toxicity testing. The environment is constantly changing as nutrients in the media are depleted and metabolites accumulate. (c) 3D cell culture offers a practical alternative to natural tissue models^{67,68}. These systems provide an environment in which one or more cell types can be encouraged to form tissues-like constructs, often using natural or synthetic scaffolds, such as collagen, alginate, polyethylene glycol hydrogels and nanofibres to provide structural support to the growing tissue construct. Scaffolds can also provide - through modification or by virtue of their natural composition - growth factors and other proteins to replicate the biochemical cues offered by the extracellular matrix (ECM) in native tissues. Figure formed through reproduction of images from.^{69,70}

The fields for such engineering include biological microelectromechanical systems (bioMEMS)⁷¹, microfluidics⁷² and biomimetics.⁷¹ Devices are often referred to as “chips” due to the strong basis on microchip technology to build multiple parallel chips, chambers, gradient networks, pumps, valves and integrated electrical and biochemical sensors. The term “organ” is used because of micro engineered, micro environmental stimuli that are derived from organ-level functions.

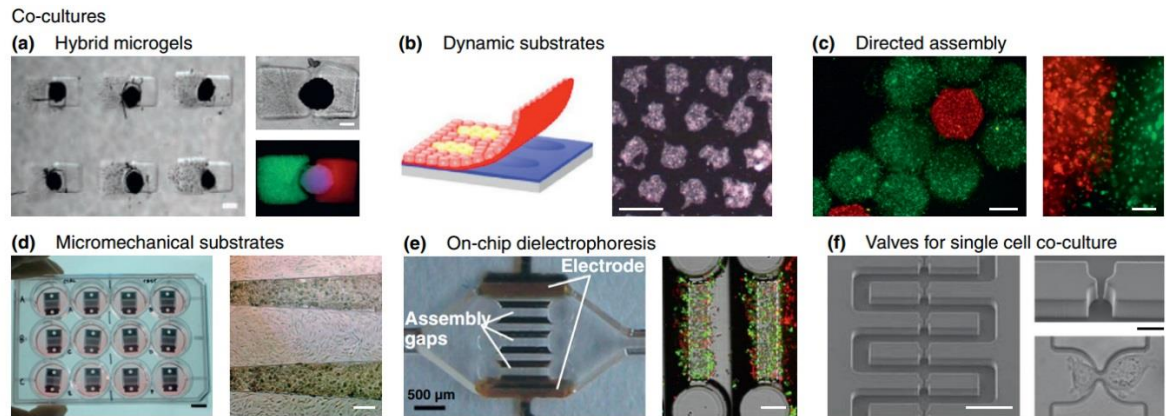
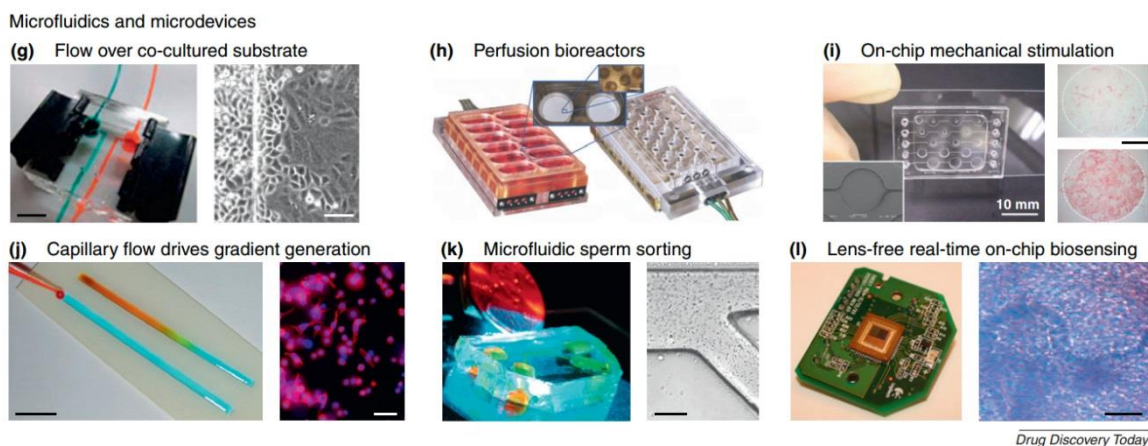


Figure 1.5-2 - Enabling technologies for on-chip tissue models. (a) Patterned microenvironment regulates differentiation of embryoid bodies. Scale bars 300 μm . Source: Qiet al.⁷³, (b) Dynamic substrate enables co-culture harvesting. Scale bar 1 μm . Source: Tsuda et al.⁶¹, (c) Directed assembly of cell-laden hydrogels for generating hierarchical tissue constructs. Scale bars 500 μm (left), 100 μm (right). Source: Zamanian et al.⁷⁴, (d) Micromechanical substrates enable micrometer-resolution cell positioning and co-culture. Scalebars 10 mm (left), 250 μm (right). Source: Hui and Bhatia et al.⁷⁵, (e) Microfluidic cell culture chambers with integrated electrodes to assemble liver sinusoids by dielectrophoresis. Scalebars 500 μm (left), 200 μm (right). Source: Schütte et al.⁷⁶, (f) A microfluidic channel with an array of valves for single cell co-culture. Scale bars 100 μm (left), 20 μm (right). Source: Frimat et al.⁷⁷

In order to build organ-on-chip devices many approaches are employed including microfabrication techniques such as photolithography, soft lithography, micro contact printing and micromolding.⁷⁸ There are extensive recent reviews detailing the vast range of techniques in use that hold great potential for synthesising tailored cellular microenvironments with high spatiotemporal control over the mechanical and biochemical cues to regulate cellular behaviour.⁷⁹⁻⁸⁵

1.5.3 Microfluidics

Microfluidics is the study of systems that manipulate or process small amounts of fluids within geometries measuring tens to hundreds of microns.^{72, 86, 87} The first publication describing the use of microfluidic systems was in 1992 by A Manz for use in electrophoresis based separations.⁸⁸ There are extensive reviews on the use of microfluidics for a wide range of bio medical applications including drug discovery^{89, 90}, stem cell biology^{91, 92}, cancer biology and experimental oncology⁹³, cell culture and processing^{89, 94-97}, and probing cellular behaviour such as angiogenesis, migration and cell-cell interaction⁹⁸⁻¹⁰⁰, even at the single cell level.¹⁰¹



Drug Discovery Today

Figure 1.5-3 – Microfluidics and microdevices (g) Flow of growth factor directs the migration of one cell type into the other within a co-culture. Scale bars 5 mm (left), 100 μm (right). Source: Kaji et al.¹⁰² (h) Multiwell plate with an array of perfusion bioreactors for 3D liver tissue culture. Source: Domansky et al.¹⁰³ (i) Pneumatic microfluidic chip for the differentiation of stem cells under mechanical stimulation. Scale bars 10 mm (left), 1 mm (right). Source: Sim et al.¹⁰⁴ (j) Capillary-flow-driven gradient generation within a fluid stripe for synthesizing gradient biomaterials to regulate cellular behaviour such as spreading. Scale bars 100 mm (left), 100 μm (right). Sources: Hancock et al.¹⁰⁵ (k) A microfluidic device for separating motile and non-motile sperm. Scale bar 200 μm . Sources: Cho et al.¹⁰⁶ (left), and Wu et al.¹⁰⁷ (right), (l) CMOS chip from webcam used to detect cardiomyocyte beating within a cell-based biosensor. Source: Kim et al.¹⁰⁸

On-chip devices can apply enhanced dynamic control over the microenvironment of cells to provide nutrients and dissolved gasses (Figure 1.5-3h)¹⁰³ and by using sheer-stress can mechanically stimulate them (Figure 1.5-3i)¹⁰⁴. Microchannels have been immobilised onto co-cultured substrates while perfusing specific nutrients to influence cell migration (Figure 1.5-3g)¹⁰² An interesting use of microfluidics has been to mimic an *in vivo* process: detecting smells.¹⁰⁹ It is also useful in micro-particle sorting such as sperm cells (Figure 1.5-3k).¹⁰⁶ Microfluidics in tandem with other bioMEMS techniques allows the development of complex devices for tissue and biomaterials research.⁷⁹

1.5.4 Microfluidics Theory

Fluids in microfluidics system behave differently largely due to scaling laws. Volume laws when scaled to the microscale in Lab-on-a-chip (LOC) systems become largely unimportant.¹¹⁰ Surface forces become dominant instead such as viscosity and surface tension.¹¹¹ This can be shown by a low Reynolds number as defined in:

$$R_e = \frac{\rho VL}{\mu} = \frac{VL}{\nu} \quad (1)$$

Here ρ is the density of the fluid, V is the mean velocity of the object relative to the fluid, L is the travelled length of the fluid, μ is the dynamic viscosity of the fluid and ν is its kinematic viscosity.¹¹²

Hence within microfluidic devices if the viscosity of the liquid is higher than or equal to the fluidic velocity ($\nu \geq V$), the Reynolds number will be low.

1.5.5 Liver on-a-chip devices

A multitude of tissues models have been developed through academia and industry; biomimetic devices that emulate the sub-systems of organs or biological processes. Modelled organs include the spleen¹¹³, lung¹¹⁴, interconnected neurons¹¹⁵, intestinal villi¹¹⁶ and the liver.¹¹⁷ In terms of animal testing the liver is of particular interest as hepatotoxicity is a major side effect of many chemicals and drugs that are administered over prolonged periods of time. Acute liver toxicity is the cause of almost half of all drug withdrawals which highlights the need for more efficient, reliable, accurate and inexpensive tools for testing liver toxicity.¹¹⁸ The liver is the principal site of xenobiotic metabolism as well as the most common organ where toxicity manifests itself,¹¹³ and thus is the organ of choice to perform the first primary screening of metabolism.³⁰

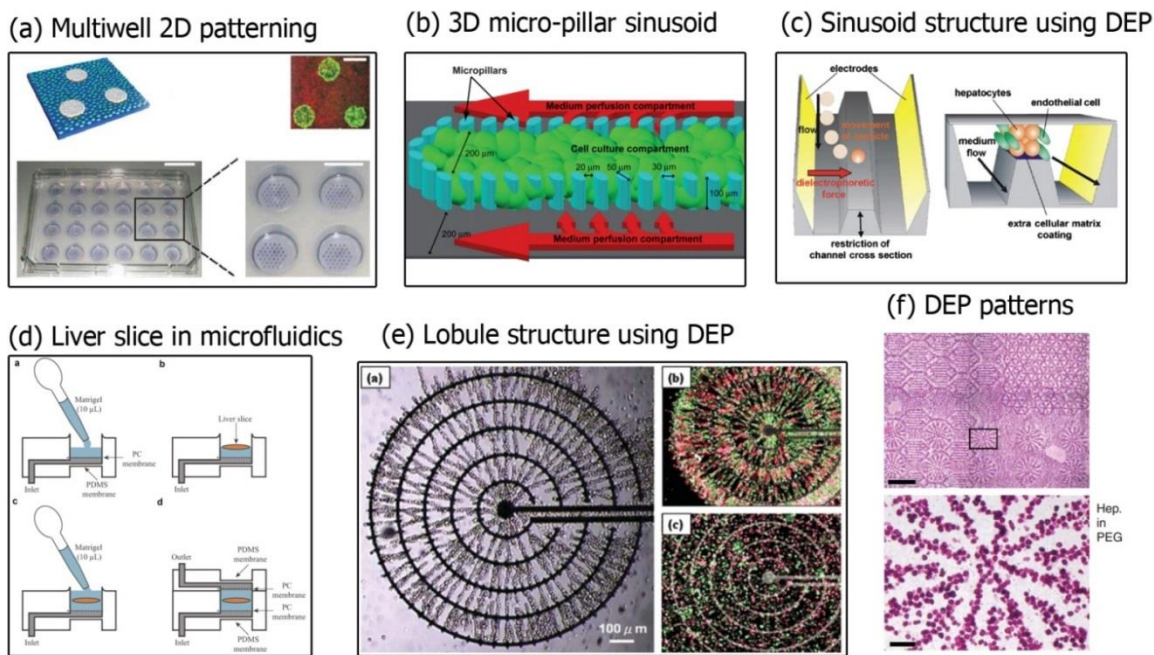


Figure 1.5-4- Liver on-chip models (a) Photograph of a 24-well device with repeating hepatic microstructures (37 colonies of 500- μm diameter in each well), stained purple by MTT. Scale bars, 2 cm and 1 cm for enlargement. Phase-contrast micrographs of micropatterned cocultures, primary human hepatocytes are spatially arranged in B500- μm collagen coated islands with B1,200 μm centre-to-centre spacing, surrounded by 3T3-J2 fibroblasts. Scale bars, 500 μm . Source Khentani and Bhatia¹¹⁹. (b) Sinusoid like structures to promote cell-cell interaction. An array of 30 x 50 μm pillars separated the channel into 3 compartments: a central cell culture compartment and 2 side media perfusion compartments. Source: Toh *et al.*¹²⁰. (c) Sinusoid structure through dielectrophoresis. Concept of the HepaChip. Hepatocytes (orange) and endothelial cells (green) are arranged in a sinusoid-like fashion. The cell chamber features two electrodes on the outer channel walls for dielectrophoretic cell assembly, extra cellular matrix support in the cell seeding area and allows for an organ-like perfusion of the culture. Source Schütte *et al.*⁷⁶. (d) Intact liver tissue integrated on-chip for *in vitro* metabolism and toxicity testing. Source: Midwoud *et al.*¹²¹. (e) Lobule pattern on-chip constructed with DEP. Source: Ho *et al.*¹²². (f) Rat hepatocytes patterned in various biomimetic microstructures within a PEG hydrogel. Source: Albrecht *et al.*¹²³

Current tools involving liver cell lines to quantify toxicity all suffer from major limitations. Key metabolic functions found in the human liver are not reproduced in 2D *in vitro* cultures and animal models.¹²⁴ As cyro-preserved human primary hepatocytes have poor viability, the critical challenge is to maintain them at a level that allows them to retain their metabolic activity and phenotype. More detailed information regarding on-chip solutions for liver tissue or cells for metabolism, drug discovery and toxicity studies can be found in recent reviews^{69, 78, 117}.

1.6 Dielectrophoresis

1.6.1 Introduction

Dielectrophoresis allows for the controllable, selective and accurate manipulation of bioparticles.^{125, 126} Unlike electrophoresis which is concerned with the ratio of particles compared to their mass¹²⁷, dielectrophoresis relies on their dielectric properties.¹²⁸

Dielectrophoresis (DEP) systems can either be operated in a droplet based manner by

dropping liquids directly onto system electrodes or by utilising flow-through of buffer laden with particles of interest integrated with the DEP system. It is expected for DEP systems in either case to produce sufficient force to overcome gravitational, drag, electrothermal, intra-particle and surface-particle resistive forces to guide particles to desired regions. The bio-applications for DEP have been demonstrated for a range of bio-applications including: transportation, concentration¹²⁹, separation¹³⁰, patterning¹²³ and characterisation of bioparticles such as cells.¹³¹ It has also been employed for cell lysis¹³² and investigating the response of cells to drugs and other stimuli.¹³³

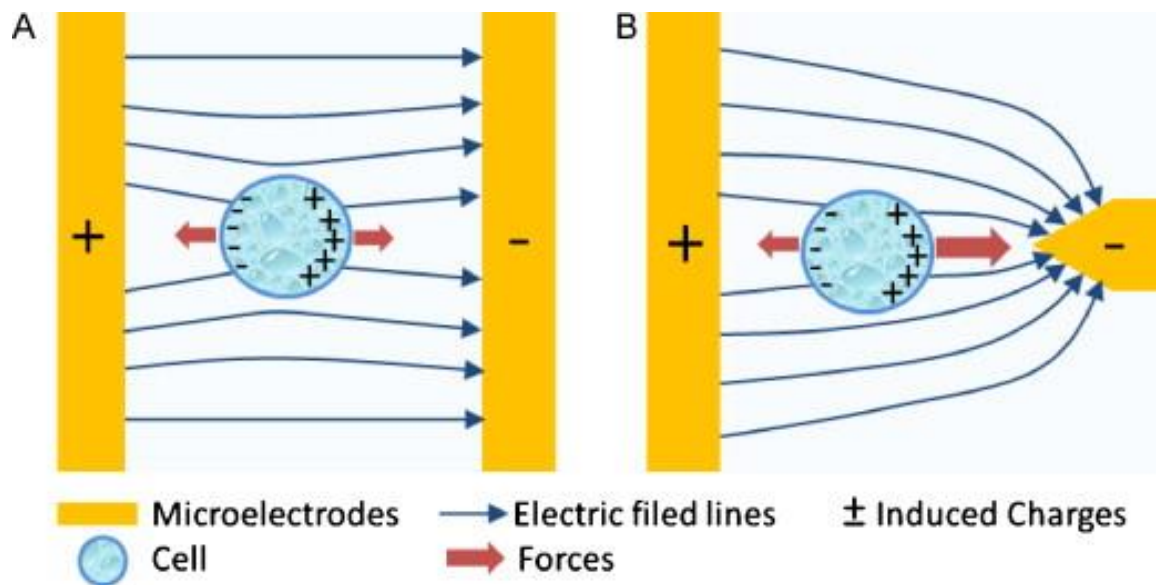


Figure 1.6-1 – Response of a polarisable particle to (A) uniform and (B) non-uniform electric fields. The electric field lines are bent towards the cell provided that the conductive buffer is less polarisable than the cells. A net force is exerted on the particle within a non-uniform electric field and is pushed towards the maxima of the electric field gradient. Reproduced from reference.¹²⁶

1.6.2 Theory

First defined by Pohl¹³⁴ in 1978, DEP is a phenomenon in which a force is exerted on a dielectric particle when it is subjected to a non-uniform electric field. Polarisable particles such as cells will experience dielectrophoretic forces when suspended in a suitable medium and subjected to an inhomogeneous electric field¹³⁵. This can be used to manipulate small particles including cells into patterns due to the non-uniform electric field they experience. The time-average DEP force (acting on a spherical particle) takes the form

$$F_{DEP} = 2\pi R^3 \epsilon_m \text{Re}[f_{CM}] \nabla E^2 \quad (2)$$

where ε_m is the *absolute* permittivity ($\varepsilon_r \varepsilon_o$) of the surrounding medium, R is the particle radius, $Re[f_{CM}]$ is the real part of the Clausius-Mossotti factor (3) related to the effective polarizability of the particle, E is the amplitude (rms) of the electric field, ε_p^* and ε_m^* represent the complex permittivity of the particle and medium respectively and ∇ represents the gradient operator.

the factor f_{CM} is the well-known Clausius-Mossotti factor defined as

$$f_{CM} = \left(\frac{\varepsilon_p^* - \varepsilon_m^*}{\varepsilon_p^* + 2\varepsilon_m^*} \right) \quad (3)$$

The complex permittivity of a lossy dielectric is defined as

$$\varepsilon_p^* = \varepsilon_o \varepsilon_p - j \frac{\sigma_p}{\omega} \quad (4)$$

where j is the imaginary vector $\sqrt{-1}$ and ω is the angular frequency of the applied AC field.

$Re[f_{CM}]$ defines the sign of the DEP direction and hence the direction of the force which is dependent on the frequency of the electric field. When the particle is more polarisable than the medium, $Re[f_{CM}]$ is >0 and positive dielectrophoresis occurs. The resulting force pulls particles to the maxima of the electric field gradient. If the particle is less polarisable than $Re[f_{CM}]$ is <0 then particles are repelled to the minima of the electric field gradient.

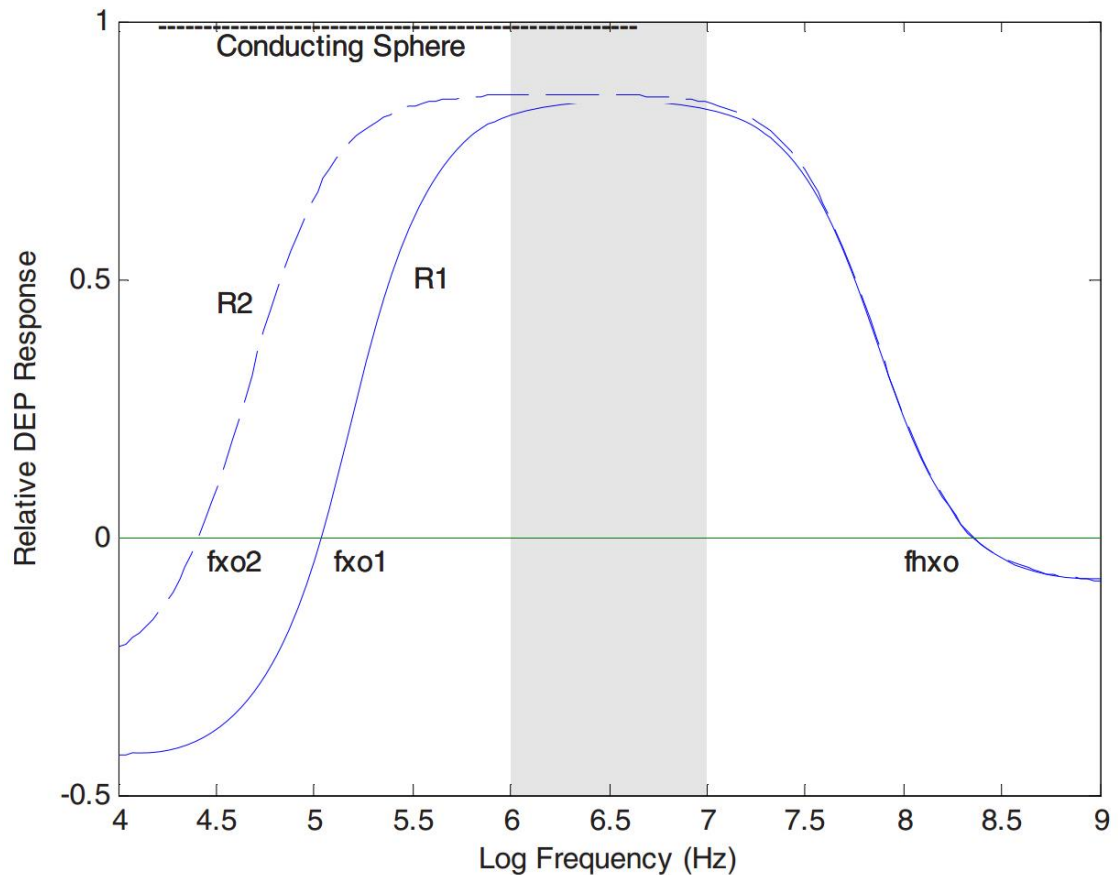


Figure 1.6-2 – Graph illustrating relative DEP response in relation to frequency (Hz). The solid line is the DEP response modelled for a viable cell normalised against the DEP response for a sphere composed of the same electrolyte as the cell cytoplasm. As the frequency is increased the cell's DEP behaviour approaches that of the conducting sphere, making the transition from negative to positive DEP at the “cross-over” frequency f_{xo} . The dashed line shows the DEP response for a larger cell (radius $R2 > R1$). The cross-over frequency f_{xo} is affected by cell size, however the cross-over at higher frequency f_{hxo} is not effected by cell size. All other dielectric factors remain constant. The highlighted band indicates the frequency band of 1-10 MHz, here the relative DEP response is the most positive. In this work this frequency band was selected as it was only of interest to achieve positive DEP forces. This was because the electrode design required cells to be attracted to the electrode edges and not be repelled which would be the case for negative DEP. Additionally, the DEP response for positive DEP is stronger than that of negative DEP. Thus as the frequency range selected was 1-10 MHz, which is greater than the cross-over frequency f_{xo} of any cell line used in this work, the cross-over frequency was not of concern. Adapted from reference.¹²⁸

Using equations (2) and (3) the expected DEP behaviour of cells with regard to frequency can be modelled for a large range of frequencies.¹³⁶ Figure 1.6-2 shows the typical response of modelled cells due to DEP forces, clearly illustrating the findings of Höber.¹³⁷ He showed that by increasing the frequency, the dielectric properties of a cell with an intact non-conducting membrane approaches that of a conducting sphere. In this example two model cells of different cell radius make the transition from negative to positive values of DEP response with respective “cross-over” frequencies f_{xo1} and f_{xo2} . While f_{xo} is affected by cell size, Figure 1.6-2 shows that as the relative DEP response is inverted from positive to negative values at higher frequencies the frequency f_{hxo} does not. This shows that at higher frequencies dielectric polarisations are dominant. Thus cells under the influence of frequencies of 1-10MHz as indicated by the grey band in Figure 1.6-2 will

only experience a positive DEP response regardless of cell size. This is also true for conductivity of the suspending medium. Increasing the conductivity (mS/m) will increase the frequency f_{x0} however for frequencies in the range of 1-10MHz the cross-over f_{hx0} is not sensitive to the medium conductivity.¹²⁸

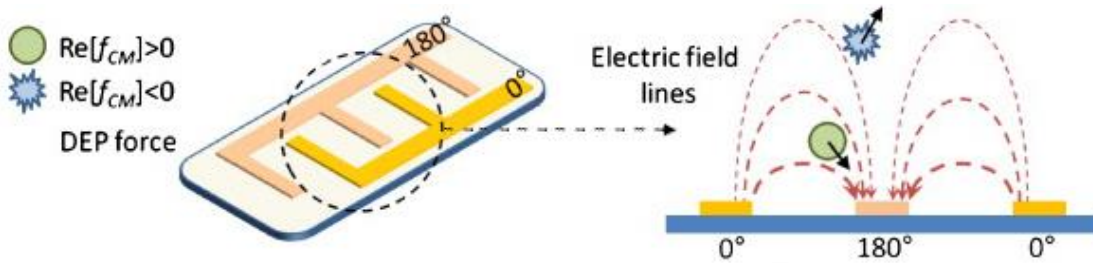


Figure 1.6-3 – A non-uniform electric field created by a metallic microelectrode patterned on a substrate. When the $Re[f_{CM}]$ is >0 cells are attracted to the electric-field maxima, when $Re[f_{CM}]$ is <0 cells are repelled to the electric-field gradient minima. Reproduced from reference.¹²⁶

1.6.3 Joule heating

Joule heating (also referred to as ohmic heating due to the relationship with Ohm's Law) is the effect of thermal energy transfer from electrical domains due to an electric potential (E) being applied across a substance with a finite conductivity (σ). This can be described by the Joule heating equation

$$Q = \sigma |E|^2 \quad (5)$$

Where Q is the heat generated per volume (Wm^{-1}).¹³⁸

Strong electric fields required for DEP forces can incur significant Joule heating to occur.¹³⁹ Heat generated within a droplet dissipates by thermal conduction through the area of contact with the substrate, hence the surface to volume ratio controls heat rejections. Therefore it follows that scaling down the electrode dimensions (10 μm) and employing microdroplets (10 μL) will reduce heating. Provided the buffer used for DEP is of low conductivity and an insulating dielectric, Joule heating will not incur significant temperature changes in the DEP patterning volume.

1.7 Small model organisms

1.7.1 Introduction

An emerging alternative to current *in vitro* cell culture is the use of models based on smaller organisms. These models have become widely used throughout research groups the world over. These organisms include fruit flies (*Drosophila Melanogaster*)¹⁴⁰, nematodes or roundworm (*Caenorhabditis elegans*)¹⁴¹, and zebra fish (*Danio rerio*).¹⁴² Each organism possess distinct advantages and disadvantages in relation to laboratory expense, reproduction time, genetic accessibility, efficiency of screening methods and relation to higher organisms.¹⁴³ For example fruit flies have been shown to be powerful models in neurotoxicology research¹⁴⁰ and drug discovery. In this regard nematodes have been used in neurotoxicology also as well as genetic toxicology, environmental toxicology, as well as other high-throughput experiments.¹⁴¹

Table 1.7-1 - Attributes of some key animals used to model human disease. Note in particular the high cost of mice and rat models and the large range of molecular biology tools available for zebrafish research. Source:¹⁴⁴

Attribute of disease model	Model organism			
	Fly	Zebrafish	Mouse	Rat
Practical issues				
Husbandry infrastructure	\$	\$	\$\$\$	\$\$\$
Cost per animal per year	\$	\$	\$\$\$	\$\$\$
Characterized inbred strains	+	-	++++	+++
Outbred laboratory strains	+	+++	++	++
Anatomical similarity	-	+	++	++
Molecular or genetic similarity	+	++	+++	+++
Pathological similarity	-	++	+++	+++
Storage; for example, freezing sperm	No	Yes	Yes	Yes
Molecular biology tools				
Transgenesis*	++	++	++	++
Targeted gene modification*	+	-	++++	+
Transient <i>in vivo</i> assays*	++	++++	+	+
Allelic series from TILLING*	+++	++++	++	+
Feasibility of large-scale screens ^f	++++	+++	++	+
Affordability of large-scale screens ^f	++++	+++	+	-
Sequencing progress [§]	+++	++	+++	++
Annotation progress [§]	++	++	++++	++
Cell-biology tools				
Cell lines and tissue culture	++	+	++++	+
Antibody reagents	++	+	++++	++

*Reverse-genetics approach; ^fforward-genetics approach; [§]genome sequence; -, not relevant, or not a strength; \$, \$\$, \$\$\$ and +, ++, +++, relative cost (\$) and strength (+) of the model in each category; +++, outstanding strength of the model; TILLING, targeting induced local lesions in genomes.

While these models are useful a range of factors including evolutionary proximity and anatomical relevance must be considered when selecting a model for human disease and toxicity. Mammals such as rats or sheep have more similar physiology than that of invertebrates for example, with organ sizes more in commensuration with humans making them useful in developing surgical therapeutics.¹⁴⁴

1.7.2 Zebrafish as a model organism

Zebrafish have similar qualities to other small organism models, their advantages being numerous¹⁴² but unlike the previous models are more closely related to humans due to being vertebrates, hence offering an alternative to larger animal models. The primary advantages of zebrafish are their small size, optical transparency, genetic accessibility, rapid development and external fertilisation.¹⁴⁵ There has been much development in the use of zebrafish to understand human development, disease, and toxicology as well as environmental toxicology.¹⁴² Zebrafish have a long history as having first being investigated in the 1950's with early investigations into using the chemical toxicity and carcinogens.¹⁴²

Zebrafish as a small model organism

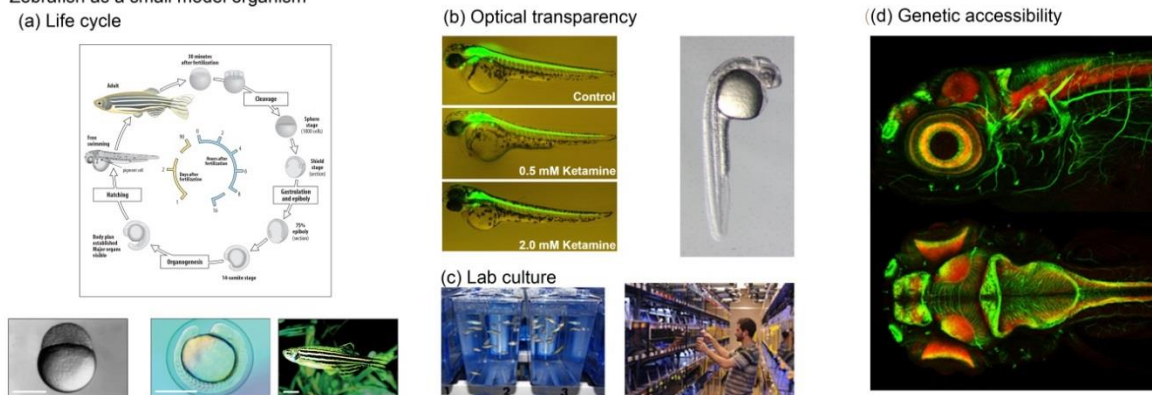


Figure 1.7-1 – (a) Zebrafish life cycle – After fertilisation the cells of the embryo rapidly divide during the cleave stage. This then leads to the sphere stage after a further 2 hrs, then the shield stage at 6 hrs total. By 16 hrs the pronephros forms during the somite stages. Organogenesis occurs over the next 8 hrs; the body plan becomes visible and major organs develop. After about 48 hrs hatching start to occur of larvae swimmers during which time fins, mouth, pigment and teeth develop. The first signs of bone development occur mark the end of embryogenesis. By 90 hrs the larvae are now full developed adult zebrafish. Scale bars are 0.5 mm and 1 mm respectively. (b) Zebrafish, like humans, have a backbone and many genes in common with humans. In one laboratory test, the addition of the chemical ketamine—a pediatric anesthetic—lowers the fish’s heart rate and reduces the number of neurons (nerve cells), shown in the slide as short, vertical lines coming down from the horizontal spinal cord¹⁴⁶ (c) Photographs showing zebrafish culture facilities. Zebrafish culture and husbandry is most commonly done by hand. (d) 4 day old zebrafish embryo labelled with SV2 and acetylated tubulin antibodies showing axon tracts(green) and neuropil(red)viewed from lateral(top) and dorsal(bottom) orientations. Source: UCL¹⁴⁷.

This was advanced further into genetic studies and human disease modelling by George Streisinger *et al* regarded as the “founding father” of zebrafish research. There are a large number of reviews detailing *in vitro* assay techniques and methods using zebrafish.^{142, 145, 149}

The key aspects of zebrafish research are that they are currently the only vertebrate model able to bridge the cell-based and mammalian model gap and are well suited to high-throughput screening. Zebrafish studies have shown xenobiotic metabolism and biotransformation of certain drugs and compounds important to toxicity assessment. This information is important in filling the gaps in ADME, drug transporters, harmonisation of

protocols and scaling knowledge.¹⁵⁰ The greatest barrier to more intensive use of zebrafish screening is automation and scaling of laboratory equipment.¹⁵¹

1.7.3 LOC devices for small organism manipulation

In order to miniaturise and increase the efficiency of toxicity testing using such models LOC technology can be employed. Developments in this area have led to devices capable of manipulating *C.elegans* nematodes to observe age-related phenotypic changes¹⁵² and controlling the temperature on opposite sides of a living *D. melanogaster* fruit fly embryo.¹⁵³ DEP has also been employed to manipulate and trap nematode *Panagrolaimus davidi* embryos within a LOC device.¹⁵⁴

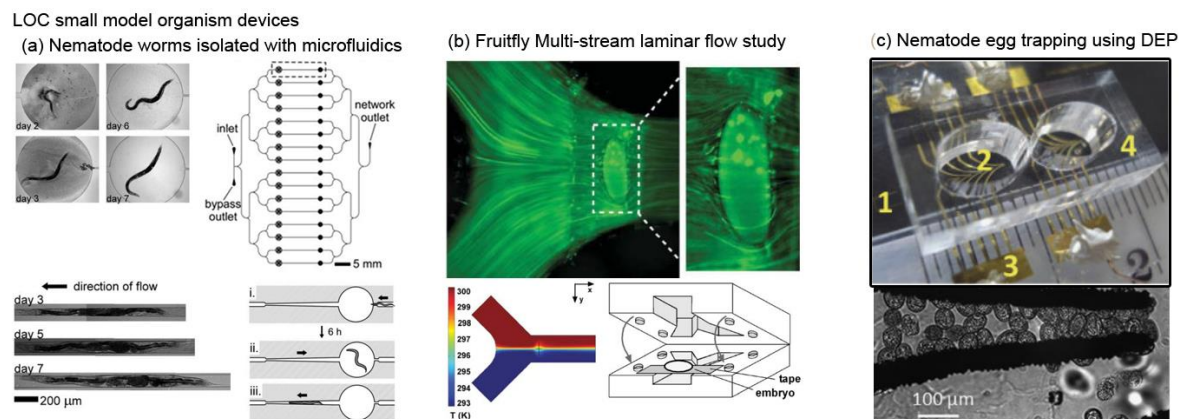
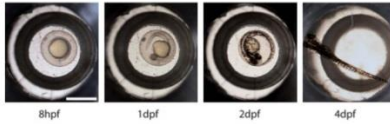
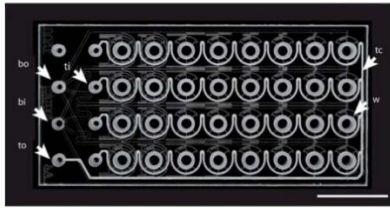


Figure 1.7-2 – Examples of LOC devices for manipulation of small model organisms. (a) Images of *C. elegans* inside the LOC device. The microfluidic system immobilised the worms and allowed study over the 9 day life-cycle. Source: Hulme *et al.*¹⁵² (b) This device relies on laminar flow of two streams of liquid with different temperature using rapid-prototyping technique polydimethylsiloxane (PDMS) to control the micro environment of a living *D. melanogaster* fruitfly embryo. Source: Lucchetta *et al.*¹⁵³. (c) Assembled DEP manifold with an array of microelectrodes and a microculture PDMS chamber: The eggs trapped along the surface of microelectrodes under the DEP force at 20 MHz. Source: Khoshmanesh *et al.*¹⁵⁴.

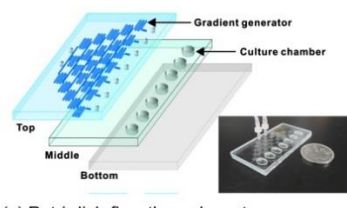
Zebrafish automation for high-throughput screening has seen various technologies developed. Work by Wielhouwer *et al* has shown that culture of wild zebrafish embryos over 5 days on-chip is possible. The device is capable of culturing up to 100 embryos in a space no larger than a credit card.¹⁵⁵ Further to this, toxicity testing has been demonstrated on chip by Yang *et al* using a gradient generating microfluidic device in order to expose single embryos to test compounds.¹⁵⁶ Lammer *et al* have shown that the fish embryo toxicity test (FET) can be made to operate as a flow through system.¹⁵⁷ In terms of automation, a fully integrated system to sort embryos has been demonstrated by Graf *et al*¹⁵⁸ as well as a 3-axis imaging system by Pardo-Martin *et al.*¹⁵⁹ Automated loading of embryos using microfluidic trapping has also been shown by Wlodkowic *et al* for use in toxicity assays.¹⁶⁰

LOC devices for zebrafish manipulation

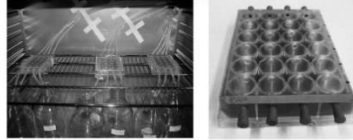
(a) Zebrafish culture on-chip



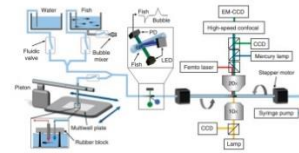
(b) On chip toxicity testing



(c) Petri-dish flow through system



(d) Zebrafish manipulation system



(e) Microfluidic Trapping Array

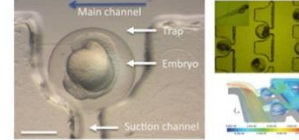


Figure 1.7-3 – (a) Layout of the biochip, an example of a 32-well chip. Embryos cultured in the biochip. Consecutive photos of the same embryo developing in the same well (1.8 mm internal diameter) of a 32 well biochip. Each picture is framed by a circular hole in the metal clamp that holds the lid in place. Source: Wielhouwer *et al*¹⁵⁵. (b) A three-layer PDMS microfluidic chip to create gradients of test drugs to the embryos. Source: Yang *et al*¹⁵⁶. (c) 24-well plate system for FET tests using zebrafish embryos. Source:¹⁵⁷. (d) Schematic of zebrafish manipulation and imaging platform. Source:¹⁵⁹. (e) Zebrafish embryos trapped on a microfluidic chip by use of steady fluid flow for LOC based studies. Scale bar 0.5 mm. Source: Akagi *et al*.¹⁶⁰

1.8 Rapid prototyping technologies

1.8.1 Introduction

A major obstacle impeding the manipulation of zebrafish embryos on chip is the relatively large diameter (≈ 1 mm) and mass (≈ 1 mg) leading to high inertial forces and gravitational-induced sedimentation.¹⁵⁸ In addition to this traditional BiMEMS fabrication methods of photolithography are difficult and expensive when building devices in the region of mm height channels¹⁶¹. Rapid prototyping (RP) and manufacturing technologies allow researchers to generate physical parts in a short period (hours or days), directly from designs created via computer-aided design (CAD), computer-aided engineering (CAE), and computer-aided manufacturing (CAM) programs¹⁶². There are a wide range of technologies that allow for high resolution fabrication of devices in these dimensions including X-ray lithography and LIGA (Lithographie, Galvanoformung, Abformung meaning Lithography, Electroplating, and Moulding in English).^{163, 164}

Rapid prototyping (RP) process using a 3D printer

(a) Design created with CAD software to form a tessellated model.

(b) Conversion to .stl format/polyhedrization, introduction of CAD file in RP machine

(c) Automatic layer-by-layer prototype manufactured using CAD geometry



Figure 1.8-1 - Schematic description of the rapid prototyping (RP) process using the HD 3500+ MJM system from 3D Systems, Inc. Abbreviations: CAD, computer-aided design; stl, standard tessellation language; MJM, Multi-jet-modelling. Scale bar 10 mm.

However, these require extensive clean facilities and are very expensive to run.¹⁶⁴ Cheaper more accessible technologies exist in the form of computer numeric controlled (CNC) mechanical micro-milling^{165, 166}, desktop digital craft cutting¹⁶⁷, water jet machining¹⁶⁵, and laser based direct micromachining in quartz, glass or plastic substrates^{163, 168-170}. Further information on additive manufacturing for tissue engineering¹⁷¹ and in biomedical engineering¹⁶² can be found in reviews by *Melchels et al* and *Lantada et al* respectively.

Prototyping methods up to 200 μm resolution have been reported¹⁶⁵ using CNC; this method leaves surface roughness and debris during cutting which is a problem. Laser cutting resolution varies on the laser technology with simple carbon dioxide (CO_2)-lasers achieving up to 3 μm ¹⁷² while advanced ultra-violet (UV)-lasers such as excimer lasers and frequency-doubled solid-state laser systems achieving 1 μm ¹⁶⁹. However, these systems only allow for the fabrication of 2.5D structures which in turn using multiple layers which in turn can be bonded to form 3D microfluidic devices or as moulds for use in softlithography¹⁶⁰.

1.8.2 Stereolithography (SLA)

Stereolithography (SLA) is an additive manufacturing method employing UV laser light and UV sensitive photopolymers illustrated in Figure 1.8-2. It was invented and patented by Charles W. Hull in 1984.¹⁷³ A beam of UV laser light is reflected to the surface of the liquid photopolymer resin forming layers of hard cured resin.^{174, 175} Each slice of the model is fabricated by scanning the laser across the surface, before the build platform is lowered (typically 50-150 μm) for the next layer. This process bonds the new layer to the previous layer below. As the process is repeated the model gradually is lowered into the resin until the model is complete, where the platform is then raised revealing the finished model.

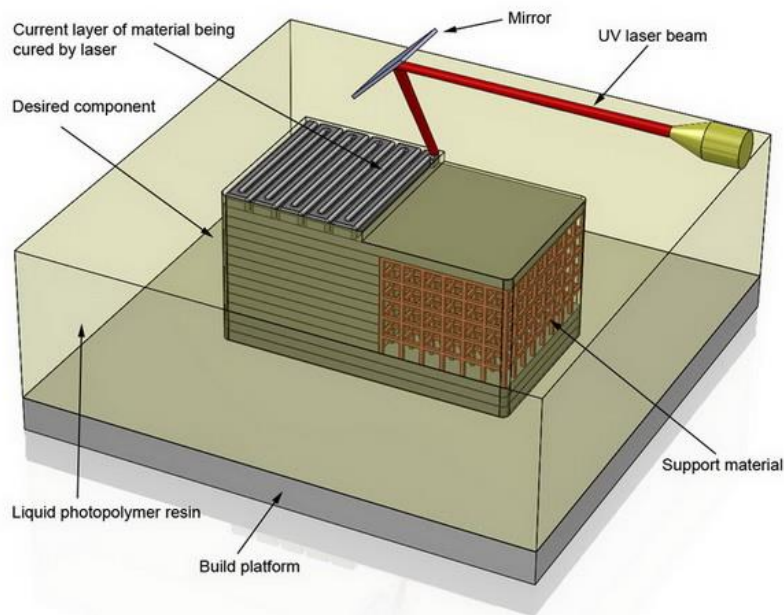


Figure 1.8-2 - 3D rendering illustrating the basic operational components of stereolithography. Stereolithography is an additive manufacturing method employing UV laser light and UV sensitive photopolymers. A beam of UV laser light is reflected to the surface of the liquid photopolymer resin forming layers of hard cured resin. Each slice of the model is fabricated by scanning the laser across the surface, before the build platform is lowered (typically 50-150 μm) for the next layer. This process bonds the new layer to the previous layer below. As the process is repeated the model gradually is lowered into the resin until the model is complete, where the platform is then raised revealing the finished model. Reproduced from reference.¹⁷⁶

SLA systems do not use a support material, instead they use a support scaffold that must be manually removed following completion. Models are then post-cured in a UV oven. To date stereolithography can achieve resolutions of up to 50 μm with the Viper Pro system with 25 μm layers in both opaque and transparent materials.¹⁷⁷

1.8.3 Fused Deposition Modelling (FDM)

Fused deposition moulding (FDM) is a form of extrusion based additive manufacturing technology pictured in Figure 1.8-3. This form of additive manufacturing was invented by Scott Crump in 1989¹⁷⁸, this method is popularly called “3D printing”. The method involves the extrusion of heated thermosetting polymer drops through a nozzle onto a motorised platform.¹⁷⁹ Material extruded by a heated nozzle deposits lines into the build platform tracing out each layer. On completion of each layer the build platform is lowered (typically in the range of 250-300 μm), for the next layer to be deposited. This process bonds to the new layer as the polymer is in a molten state. A second nozzle is often used to deposit a support material for overhanging features as shown in Figure 1.8-3. Support material is removed from the finished model either by hand or by dissolving it in an alkaline water bath.

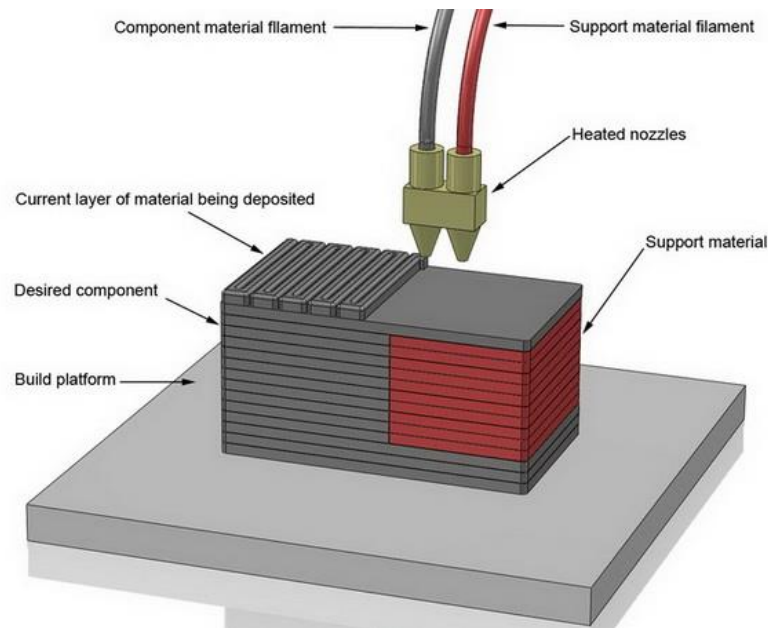


Figure 1.8-3 – 3D rendering illustrating the main components required for fused deposition moulding (FDM). Material extruded by a heated nozzle deposits lines into the build platform tracing out each layer. On completion of each layer the build platform is lowered (typically in the range of 250-300 μm), for the next layer to be deposited. This process bonds to the new layer as the polymer is in a molten state. A second nozzle is often used to deposit a support material for overhanging features. Illustration reproduced from reference.¹⁷⁶

Various polymers are used, including acrylonitrile butadiene styrene (ABS), polycarbonate (PC), polylactic acid (PLA), high density polyethylene (HDPE), PC/ABS, and polyphenylsulfone (PPSU).¹⁸⁰ Additionally 3D bioprinting using FDM machines use hydrogels loaded with cells¹⁸¹ to form 3D printed organs.

1.8.4 Multi-jet-modelling (MJM)

Multi-jet modelling (MJM) also known as polyjet technology is a form of (FDM) illustrated in Figure 1.8-4.¹⁸² The materials used are either thermopolymers or liquid photopolymers which require an additional UV source during printing.¹⁸³ Both methods use an array of linearly arranged nozzles similar to an inkjet printer; this allows jetting heads to spray tiny droplets of melted liquid material which cool and harden on impact to form the solid object over a larger area than FDM. Slices of the model are fabricated as the nozzles scan in the x-y axis; both material for the model itself is deposited as well as support materials as required. Completed models require no further post-printing treatment to cure the polymer.

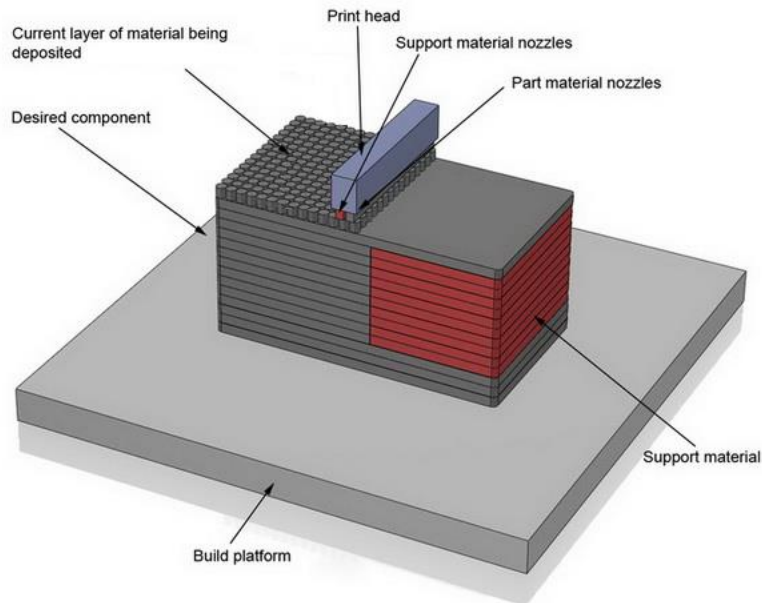


Figure 1.8-4 – 3D rendered schematic illustrating the major components of MJM modelling. Multi-jet modelling (MJM) also known as polyjet technology is a form of fused deposition modelling (FDM). The materials used are either thermopolymers or liquid photopolymers which require an additional UV source during printing. An array of linearly arranged nozzles similar to an inkjet printer spray tiny droplets of melted liquid material which cool and harden on impact to form the solid object. Slices of the model are fabricated as the nozzles scan in the x-y axis; both material for the model itself is deposited and support materials as required. Completed models require no further post-printing treatment to cure the polymer. Illustration reproduced from reference.¹⁷⁶

Resolutions of 25 μm and 16 μm thickness are achievable with this system allowing for very finely detailed models. Opaque and transparent models are possible with MJM.^{182, 183}

1.8.5 Current applications in biomedical engineering

At present the use of 3D printing in biomedical engineering has been limited, mostly to simple microfluidic devices¹⁸⁴⁻¹⁸⁶, medical imaging¹⁸⁷ and scaffolds for cells¹⁸⁸. This has been due to the opaque nature of basic 3D printing materials and the difficulty in removing support structures required for creating channels within a 3D object. Removing support material from channels fabricated using FDM and SLA fabricated devices can be problematic if the device is sealed. In addition the resolution of 3D printers has been unable to fabricate the required finish for manipulating small organisms on chip without incurring unintended damage to the samples or interfering with the fluidic dynamics.

1.9 Theoretical summary and preamble of experimental work described herein

This research focuses on developing LOC systems to improve *in vitro* testing for ADME and toxicity studies. Pressing factors from economic, legal, scientific and ethical vectors require that further replacement of animal testing to be developed. The current state-of-the-art is capable of research in the areas of metabolism, drug discovery and toxic effects of various compounds. However, the complex interactions that take place *in vivo* are not currently well enough modelled either through LOC devices or computer simulations to replace mammalian testing.

Firstly, work focused on the use of hepatocyte patterning on microfluidics; the principle being to build a high-throughput screening LOC device using human hepatocytes for ADME screening of toxic compounds. A microfluidic system was designed using 4 chambers and use of micro-patterning to create arrays of hepatocytes on a chemically treated glass substrate. In order to assess the effectiveness of this system the metabolic functionality of the hepatocytes was measured using an off the shelf assay.



Figure 1.9-1 – Lab-on-a-chip (LOC) device for high-throughput screening of human hepatocytes. (a) Photograph of experimental setup and LOC device installed with fluidic connections and valves. (b) Schematic of microfluidic chamber design with micro-patterns.

Secondly, an innovative micro liver fabrication platform for use in toxicity studies was devised, designed, constructed and tested. This system employed the use of dielectrophoresis patterning of cells (HepG2/C3A) to form liver lobule like arrays within a hydro-gel. This pattern was framed by a paper ring which allowed the patterns to be transferred to culture dishes. The progress of this work has led to two conference papers.

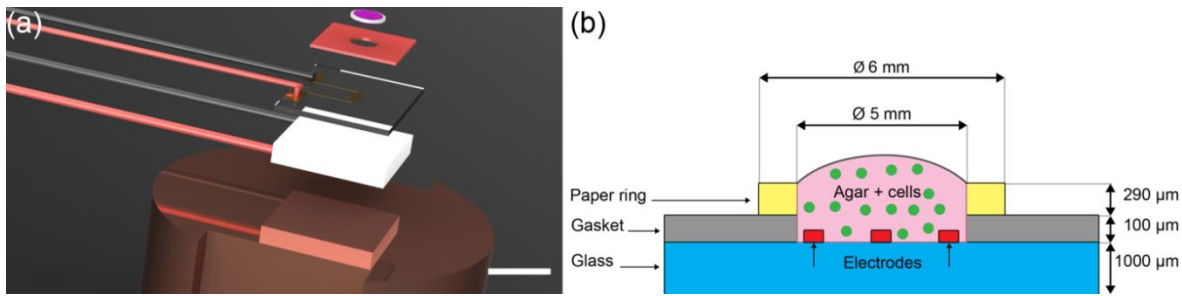


Figure 1.9-2 – Dielectrophoresis system for the patterning of liver cells (HepG2/C3A) to form liver lobule like arrays within a hydro-gel. (a) Scale 3D render of the patterning system. Scale bar is 10 mm. (b) Schematic showing the design of the patterning volume.

Thirdly, the design of a miniaturised zebrafish automatic analysis platform was designed, fabricated and constructed. This involved the use of both SLA and MJM rapid prototyping techniques to fabricate a monolithic zebrafish trapping and analysis chip. The investigation of the biocompatibility of these chips was conducted. This work has been presented in a conference paper.

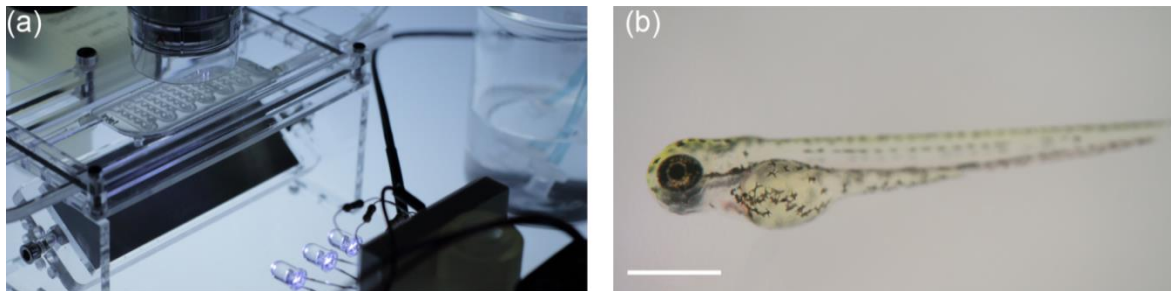


Figure 1.9-3 – Micro analysis platform for on-chip zebrafish development studies. (a) Photograph of the analysis platform with fluidic connections, USB microscope, light source and installed 3D printed chip. (b) Microscope image of a healthy zebrafish after 72 hrs of development with a 3D printed material. Scale bar is 1 mm.

2 Materials and Methods - Microfabrication

2.1 Abstract

This chapter describes the materials and methods used for microfabrication in this thesis. Due to the range of fabrication methods used in this thesis the materials and methods have been separated into two separate chapters. For each, following the description of materials, a general overview of methods and characterisation methods used in the thesis are presented.

The remainder of the chapter is separated into 2 sections covering methods for developing multi-chamber microfluidic devices and dielectrophoresis micro liver-like patterning system. Each section describes specific methods followed immediately with a short results and discussion.

2.2 Introduction

This thesis was concerned with designing, prototyping and testing *in vitro* devices to augment and reduce animal testing. Through the course of the project a number of different devices, techniques and experiments were designed. This chapter covers the general methods and materials used for work described within this thesis as well as details including fabrication of microfluidic devices for cell culture, electrode fabrication for dielectrophoresis, cell culture as well as data collection methods.

Unless stated all fabrication methods were developed and conducted by the author. Microfabrication processes were carried out in the James Watt Nanofabrication Centre (JWNC). Device manufacturing was conducted by the mechanical workshop at the School of Engineering, University of Glasgow. Cell culture experiments took place in the following laboratories: Laboratory of the Government Chemist (LGC), London, UK; Biomedical Engineering, University of Glasgow, Rankine Building, Glasgow, UK; Biomedical Engineering, Cornell University, Ithaca, USA.

2.3 Materials

2.3.1 Cell culture

Cell lines HepG2, HepG2/C3A (C3A), NIM/3T3 fibroblast (3T3), Chinese Hamster Ovary (CHO), MCF7, were acquired from ATCC, UK. Fresh primary rat hepatocytes were obtained from LGC Standards, UK. All chemicals were supplied by Sigma-Aldrich, UK unless otherwise stated. Eagle's Minimum Essential Medium (EMEM) for HepG2 cell lines was supplied by ATCC, UK and EMEM was supplemented with 10% foetal bovine serum.

Primary rat hepatocytes were cultured according to suppliers instructions and cultured in Leibovitz-(L-15) medium (GIBCO) supplemented with 1 μ M dexamethasone, 25 mM HEPES (4-(2-hydroxyethyl)-1-piperazineethanesulfonic acid), 0.1 μ M insulin, 8 mM D-glucose and 0.1 mM gentamicin. Cell culture medium for cell lines 3T3, CHO and MCF7 was Dulbecco's modified Eagle medium (DMEM) containing nutrient mixture F-12 (DMEM/F12, GIBCO, UK) supplemented with foetal bovine serum (FBS), L-glutamine, penicillin and streptomycin. Trypsin 0.25%, dimethyl sulfoxide (DMSO) and phosphate buffered saline (PBS) were used in cell culture.

2.3.2 Cell Assays

7-ethoxyresorufin and resorufin were obtained from Invitrogen, now Life Technologies, UK for Ethoxyresorufin-o-deethylase (EROD) assays. All other reagents were obtained from Sigma-Aldrich. QuantiChrom™ Urea Assay Kit and BCP Albumin Assay Kit were obtained from BioAssay Systems, Hayward, USA. Albumin Human ELISA kit (ab108788) was obtained from Abcam, Cambridge, UK. Trypan Blue Solution, 0.25% and LIVE/DEAD® Viability/Cytotoxicity Kit, for mammalian cells were obtained from Life Technologies, UK.

2.3.3 Cell Patterning in hydrogel with paper substrate

Low gelling temperature agarose (Type IX-A: Ultra-low Gelling Temperature) for cell culture was obtained from Sigma-Aldrich. Petri dishes, 6, 24 and 96-well plates, sterile single use pipettes, Eppendorf tubes, and microscope slides were obtained through Fisher Scientific, UK. Whatman No. 114 (USA) filter paper was obtained through Sigma-Aldrich. Nescofilm was obtained from Alfresa Pharmaceutical Corp, Osaka, Japan. To perform dielectrophoresis a 50 MHz TG5011 LX1 frequency generator (Thurlby Thandar Instruments Ltd, UK) was employed. Temperature control was maintained manually using a pair of Peltier coolers (MULTICOMP - MCPE-071-10-13 -, 19.1 W, 1639748) supplied

by Farnell controlled by a dual-rail current supply EX 354D 280 W (Thurlby Thandar Instruments Ltd, UK). Passive cooling solutions were met by a selection of heatsinks namely heatsink 6.8 °C/W (36-0292) from Rapid Electronics, UK and Zalman CNPS7000a-CU from Zalman, USA. Heat connection was made by thermal paste (36-0400) again from Rapid Electronics, UK.

2.3.4 Microfabrication

Standard mechanical grade silicon thickness 500 µm, 4 inch wafers were supplied by University Wafer, USA. Additionally, gold (Au) and titanium (Ti) wire for resistive heating evaporation deposition were supplied by the JWNC and were obtained from Goodfellows UK.

2.3.5 Microfluidics

Tubing for microfluidics, 0.030"OD PTFE tubing was supplied by Cole-Parmer Instrument Company, Venon Hills, Illinois, USA. Hypodermic needles and BD syringes used were supplied by Agar, UK and Fisher Scientific, UK. 2010 and 2041 Elvacite polymethyl methacrylate (PMMA), with molecular weights of 80k and 345k respectively, was obtained from Lucite International Inc. S1818 photoresist, AZ-4562, AZ400K and Microposit Cd-26 developer were obtained from Shipley company Inc. Opticlear was obtained from National Diagnostics, USA. Acetone was obtained from Fisher Scientific. Trichloro(1H,1H, 2H, 2H – perfluorooctyl)silane 97%, isopropyl alcohol (IPA) and ethanol (EtOH) for various fabrication and cleaning steps.

Commercially available PEG-trichlorosilane containing between 9 and 12 ethylene glycol units (MW=600) was supplied by Gelest, Inc. USA. Dried collagen fibre (type I from calf skin) and acetic acid were used for micro dot printing.

2.4 General Methods

The following methods describe general methods used over the course of this thesis. Specific methods and results corresponding to microfluidics, dielectrophoresis and 3D printing are listed following this summary.

2.4.1 Cell culture

All cell lines were cultured in a HERA cell 150 incubator (Thermo Scientific) and maintained at 37 °C with 5% CO₂. All handling of cells was completed inside of an ESCO biology safety cabinet (Class II). All items taken into the hood were sterilised with 70% EtOH. Pipette tips, paper, agar solution and tools were sterilised by autoclave (Prestige

Medical Series 2100) 126 °C for 11 minutes. Centrifugation steps were completed using a Thermo Scientific Heraeus Biofuge Primo and Pico 21 for 15 or 50 ml tubes or Eppendorf tubes respectively. Reagents were heated using a SUB6 Grant water bath.

2.4.2 Cell counting

Cell counting and viability was performed using an improved Neubauer Haemocytometer (Fisher Scientific UK) by mixing 1:1 trypan blue with cell suspension. The resulting solution was pipetted (10 µl) into the first chamber; cells were counted within the centre 5x5 grid (0.1 mm³), this was repeated in the second chamber.

2.4.3 Cell viability

The live/dead kit viability kit was used to assess the health of the C3A cells by simultaneously staining the living and dead cells. The distinction was made by the green-fluorescent calcein-AM (494/517 nm) staining the membranes of all cells indicating intracellular esterase activity and the red-fluorescent ethidium homodimer-1 (EthD) (528/617 nm) to indicate loss of plasma membrane integrity¹⁸⁹. Cell cultures were washed with PBS prior to staining. Samples containing 5 µM calcein-AM, 10 µM EtD-1 solution in PBS were foil wrapped. Live/dead stain was added and cultured at 37 °C for 45 minutes. Both inverted and confocal microscopy was used with this viability kit.

2.4.4 Long-term cell storage

Tubes of 10⁶ cells per 1 ml of 10% dimethyl sulfoxide (DMSO) and 90% FBS were frozen down progressively for future experiments. 12hrs at -20 °C, followed by -80 °C for 2 days finally placed at -173 °C in liquid nitrogen. Primary hepatocytes and HepG2/C3A cells were stored using this method.

2.4.5 Statistical analysis

Analysis of variance (ANOVA) was used to analyse data and significance was considered $p < 0.05$.

2.4.6 Microfabrication

2.4.6.1 General processes

Fabrication of micron dimension features was performed using well established methods of microfabrication.^{190, 191} This process required the design of a mask for use in photolithography to perform pattern transfer. In photolithography, a substrate, spin-coated with a thin layer of photo-sensitive polymer (photoresist) was exposed to a UV (ultra-violet) light source through the designed mask. Photolithography for all microfabrication

was performed on a Suss Microtec MA6 mask aligner (MA6) in the JWNC. Depending on the photoresist type the exposed polymer areas become more (positive) or less (negative) soluble with developing solution. Regardless of the chosen method the pattern in the mask was transferred to the photoresist; patterned photoresist then acted as a mask for further processes, etching or metallisation.

2.4.6.2 Soft lithography (PDMS)

Soft lithography was performed to fabricate microfluidic devices using etched silicon masters to form PDMS devices the selected method was replica moulding. This allowed the duplication of the morphology present on the silicon masters using the curable prepolymer PDMS. This was due to the PDMS device fabrication technique being a non-photolithographic strategy based on replica moulding to fabricate micro dimension structures. Positive resist was used for these devices when using a silicon master in order to fabricate a mould with positive features, thus forming a negative cast of the features within the PDMS. Provided the PDMS does not contain solvent, the typical shrinkage of PDMS casts is less than 3% on curing.^{192, 193} A schematic of the fabrication procedure can be found in Figure 2.6-1.

2.4.6.3 Dielectrophoresis electrodes (metallisation)

The fabrication of micro electrodes required the design of brightfield masks for pattern transfer to photoresist. As metallisation of micron dimension electrodes was required a negative resist was employed. This was because the metallisation process unselectively deposits material on the sample. Thus post-metallisation the areas where metal was not required needed to be removed. The use of a negative photoresist allowed for this process as the areas exposed polymerised and remained after development.

2.5 Characterisation

2.5.1 Scanning electron microscopy (SEM)

All scanning electron micrographs were taken using a Hitachi S-3000 SEM operating at 8.51 kV. Before loading into the SEM samples were coated with Au/Pd using an in-house sputter coater operating at 15 mA for 2 minutes.

2.5.2 Absorption spectroscopy

Measurements for albumin and urea assays were taken with use of a BioTek ELx808 plate reader. The assays were performed according to the manufacturer protocols, emissions

read at 450 nm and 520 nm accordingly. Data was acquired using the supplied software package Gen5™.

2.5.3 Fluorescence microscopy - cells

2.5.3.1 Inverted microscopy

The majority of fluorescence microscopy was carried out on a Zeiss D.1 Axio Observer. A mercury lamp (HBO 100) was used to excite fluorophores, and was filtered using fluorescein isothiocyanate (FITC) (XF100-2) and Rhodamine (Rho) (XF101-2) filters; excitation at 475 and 525 nm, emission at 535 and 565 respectively. The objectives on the scope were: Zeiss EC Plan-NEOFLUAR x5, x10 and x20. Images were captured using an Andor tech iXOn EM+ microscope camera with a 60N-L 1.0x collar. Images were collected using the ImageJ software package¹⁹⁴.

2.5.3.2 Confocal microscopy

Confocal microscopy images were taken using a Zeiss LSM 510 Meta Confocal Microscope using 488 nm Argon laser excitation. A long pass 510 ± 20 nm filter was used for calcein detection with 543 nm HeNe laser excitation and a long pass filter 585 ± 20 nm were used for EtD-1 detection. Confocal microscopy allows photos to be collected at a specific height which is advantageous in metabolism studies. As metabolites are formed by the cells, they will quickly diffuse into the medium. By employing a confocal microscope metabolites could be detected in specific volumes around the cells as they were produced.

2.5.4 Osmolarity, conductivity and pH measurements

Osmolarity of solutions was measured using an Advanced Micro Osmometer 3300 calibrated using standard solutions of 850, 290 and 50 mOsm/kg supplied by Advanced Instruments, UK. Conductivity was measured using a Jenway 4071 conductivity meter (288-8199) obtained from RS, UK. pH measurements were taken using a Hanna Instruments pH meter and calibrated using solutions of 4, 7 and 10 pH (Fisher).

2.5.5 Thermal measurements

Thermal imaging was taken using a Ti 25 Fluke thermal camera from Fluke, Norwich, UK. Direct thermal readings were taken from devices using a thermocouple CM1200T (IEC 584-3)T from Caltex Industrial(H.K.) Ltd, Hong Kong.

2.6 Multi-chamber microfluidic devices

All master wafers for microfluidic devices were fabricated using the James Watt Fabrication Centre (JWNC), University of Glasgow, Glasgow, UK. Processes were followed according to established JWNC protocols unless otherwise stated. The process is illustrated in Figure 2.6-1.

2.6.1 Design

Design of microfluidic acetate masks were drawn using CorelDraw X5 (Corel Corporation, Ontario, Canada) and printed by JD Photo Tools, UK (the smallest feature size was 100 μm).

2.6.2 Cleaning

Silicon wafers were submerged in acetone and sonicated for 10 minutes in order to clean the wafers **Figure 2.6-1(a)**. This process was repeated in methanol (100%) and isopropanol (100%). Finally the wafers were washed in de-ionised (DI) water and dried in a stream of compressed air.

2.6.3 Resist spinning

Following wafer cleaning resist spinning was performed **Figure 2.6-1(b)**. For this process the positive photoresist AZ-4562 was used. AZ-4500 series photopolymers are capable of spinning layers in excess of 3 μm and hence are suitable for making thick layers of photoresist. This is vital to protect the wafer during the etching process. Before applying photoresist, hexamethyldisilazane (HMDS) primer was spun on the silicon wafer at 4000 rpm for 5 seconds. AZ-4562 was then applied to the wafer by filtered syringe and spun at 4000 rpm for 30 seconds to achieve a thin film. Then, the substrate was soft-baked for 5 minutes at 95°C on a vacuum hot-plate.

2.6.4 Photolithography

Using an acetate mask attached to quartz glass the design was transferred to the AZ-4562 **Figure 2.6-1(c)**. This was performed using an optical photoaligner (MA6) to expose the substrate with UV light (30 mW) for 16 seconds in hard contact mode. In hard contact mode the sample was in direct contact with the photomask, the main advantage being that no projection optics are required between the object and image.¹⁹⁵

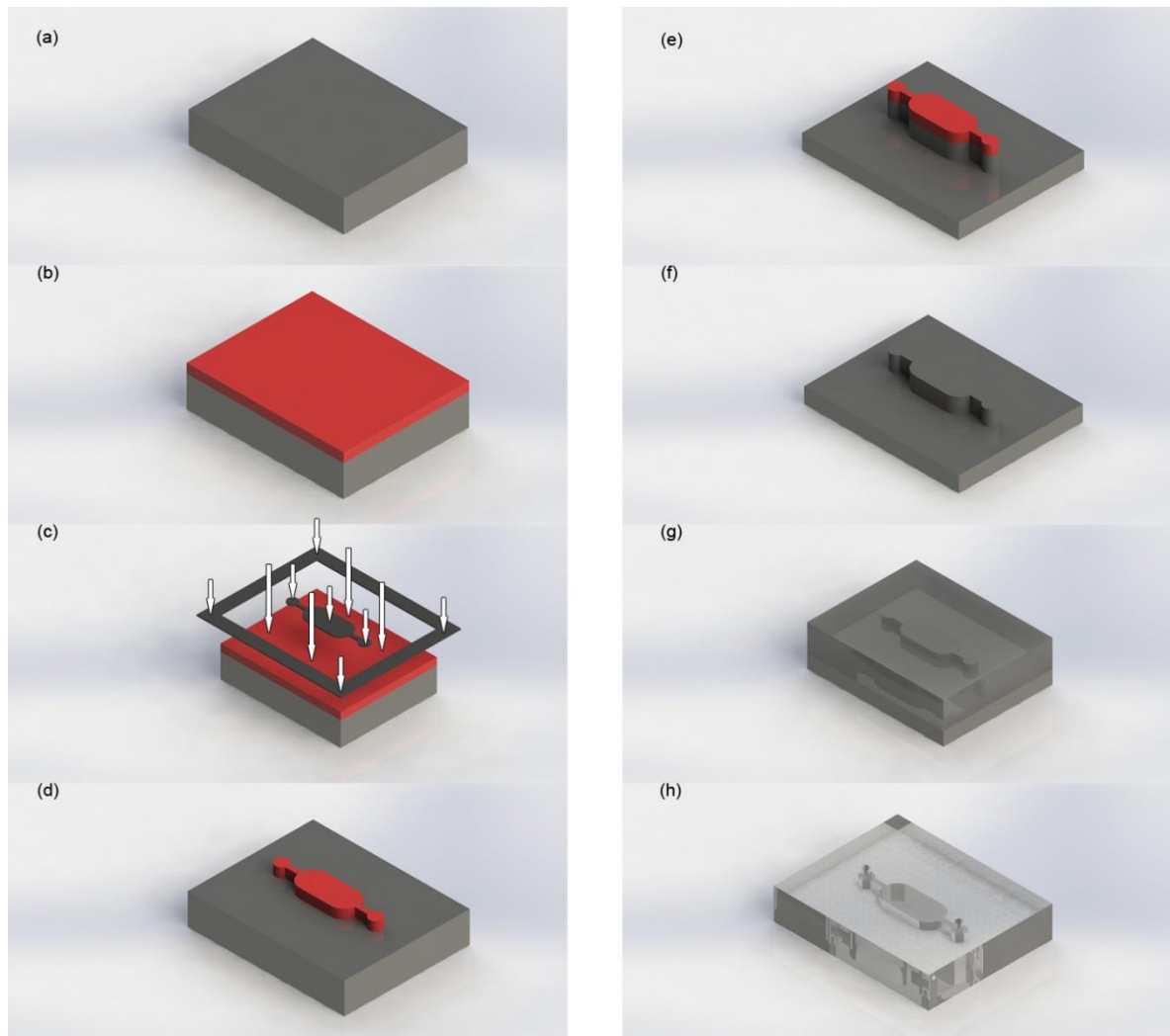


Figure 2.6-1 - Schematic of fabrication procedure: (a) - Cleaned Silicon wafer; (b) - AZ-4562 spun onto the surface of the silicon wafer to make a $6.2 \mu\text{m}$ layer; (c) - Exposure of UV radiation to transfer the mask pattern to the polymer; spun onto the glass substrate; (d) - Development of AZ-4562 to remove areas exposed leaving a positive structure of the pattern; (e) - Etching using an STS multiplex inductively coupled plasma (ICP) machine to a depth of $100 \mu\text{m}$; (f) Cleaning of remaining AZ-4562 using organic solvents and ultrasonics; (g) Soft lithography moulding of PDMS using the silicon etched pattern; (h) Completed PDMS microfluidic chip removed from the silicon master and prepared for use by cutting connections using an appropriate punch.

2.6.5 Development

Removal of the exposed areas was conducted by resist development Figure 2.6-1(d). The wafer was submerged in a solution of (1:4) A-Z developer to DI water for 3 minutes.

Following development, the wafer was rinsed in DI water and air dried. The wafer was finally exposed to oxygen plasma at 100 W for 2 minutes in an oxygen barrel asher (Gala Instruments Plasmaprep 5).

2.6.6 Etching

The final step in fabricating a deep microfluidic channel master was etching Figure 2.6-1(e).¹⁹⁶ The patterned substrate was etched using an STS multiplex inductively coupled plasma (ICP) machine. This machine etches using the Bosch process^{197, 198}, which can be

briefly described as consisting of sequential etching and passivation steps using an appropriate gas chemistry in each step, sulphur hexafluoride (SF_6) for etching, octafluorocyclobutane (C_4F_8) for passivation.¹⁹⁸ The full list of parameters are described in Appendix . Etching of a silicon master used alternated SF_6 and C_4F_8 gases for 50 minutes at an etch rate of 2 μm per minute sustained for a 100 μm deep pattern within the silicon master. After etching, the fabricated silicon master Figure 2.6-1(f) was washed successively for 5 minutes in an ultrasonic bath in reagent grade acetone, methanol, IPA and DI water respectively and was then air dried.

2.6.7 Soft lithography

Transparent microfluidic channels were then fabricated by soft lithography technique using the master described in 2.6.1 - 2.6.6.^{199, 200} The channels were cast in PDMS, a transparent silicone elastomer and then cut from the master Figure 2.6-1(g). The silicon master was first silanised with 1% trichloro(1H,1H, 2H, 2H – perfluorooctyl) silane solution for at least 1 hour under vacuum. Silanisation functionalises the surface of the wafer to discourage the adhesion of PDMS to the silicon.

PDMS base pre-polymer monomer and curing agent were mixed at a ratio of 10:1, the PDMS was thoroughly mixed by hand with a stirring stick to ensure a uniform consistency.²⁰¹ The wafer was then placed in a PDMS mould to ensure a thickness of 5 mm and flat top surface. The design of the mould can be found in Appendix A. This allows for a more consistent seal when placed in the device clamp. To remove air bubbles from the PDMS the mould was put under vacuum for 20 minutes. To accelerate curing of the PDMS the mould was placed in an oven for 2 hours at 60 °C. Once cured the PDMS was peeled gently from the mould and cut to shape using a scalpel and metal ruler Figure 2.6-1(f).

2.6.8 Microfluidic connections

The next fabrication step of the microfluidic device consists of making connections between the PDMS channels and supplying tubes. This process involved making holes in PDMS channels with blunt metal needles (26G), inserting blunted 23G needles (BD Microlance, Becton, Dickinson and Company, New Jersey, USA) into the holes and connecting the channels via blunt needles with 0.030"OD PTFE tubing and syringes. The experimental setup consisted of syringe pumps (Basi, MD-1001, 2701 Kent Avenue, West Lafayette, IN, USA) up to four) connected to a 3-way valve (2421 Omnifit 3-way hex valve, Diba Industries Ltd, Cambridge, UK)²⁰³

2.6.9 Piezoelectric printing

The process used for fabricating micropattern arrays was developed by *Alicja Zarowna et al.*²⁰⁴ Collagen dot printing was performed by *Alicja Zarowna* and the author in the School of Life Sciences, University of Glasgow. The following describes the methods required to fabricate these patterns.

2.6.9.1 Sample preparation

Glass slides (1 mm thick) were washed for 5 min in an ultrasonic bath successively with reagent grade acetone, methanol and isopropanol. Next, glass slides were washed in Piranha solution for 10 min (7:1 proportions of Sulphuric Acid to Hydrogen Peroxide (30%)). Slides were then rinsed in RO water and blown dry with nitrogen.

Cleaned glass slides were treated in an oxygen plasma chamber at 200 W for 5 minutes. The slides were then treated with 1% v/v PEG-trichlorosilane in anhydrous toluene for 2 hours under vacuum.

After modification, slides were rinsed in fresh toluene, blow dried under a nitrogen gas stream and cured at 100 °C for 2 hours. Modified samples were stored in desiccators for further use.

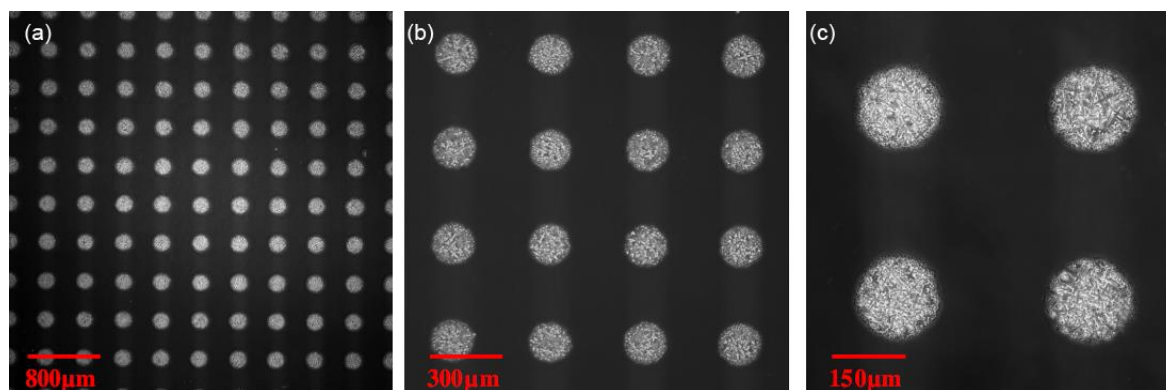


Figure 2.6-2 – Piezoelectric printing – Microscopy images showing a 150 μm diameter collagen dot array printed on PEG treated glass substrate shown at (a) x5 (b) x10 and (c) x20 magnifications.

2.6.9.2 Collagen printing

First, 15 mg of dry collagen from calf skin type I, was dissolved in 15 ml of 0.1M acetic acid. After complete collagen dissolution, the pH was adjusted to physiological level of 7.4 with 10% sodium hydroxide (NaOH) solution. After pH adjustment final concentration of collagen estimated as 0.9 mg/ml. A range of collagen patterns were printed with a PerkinElmer® printer location in the School of Life Sciences, University of Glasgow. The micropattern arrays used in this work were 25 columns x 23 rows, 20 x 10 and four 10 x 5 arrays with 3 mm spaces between each. All patterns used 150 μm diameter dots. An

example of one layer of dots printed in the central part of a polyethylene glycol (PEG) treated glass slide, covering surface of 1 cm^2 is shown in Figure 2.6-2.

All collagen patterns, except control samples, were cross-linked with high power UV lamp (100 mW/cm^2) for 30 minutes, and with heat ($37 \text{ }^\circ\text{C}$) for 1 hour. After cross-linking printed samples were washed twice in PBS and sterilised under standard UV light in a fume hood for 15 minutes. Sterilised samples were stored in the fridge until further use.

2.7 Dielectrophoretic patterning micro liver system

2.7.1 Electrode design principle

The human liver consists of two lobes which are irregular in shape and divided by the falciform ligament Figure 2.7-1(a). In mammals the hierarchical structure of these lobes finally end in 10^5 to 10^6 functional units called lobules.⁴⁶ In cross-section the hepatocytes are seen to be arranged in plates of one to two cells thick, organised radially around the central vein in cords as illustrated in Figure 2.7-1(b) separated by sinusoids.

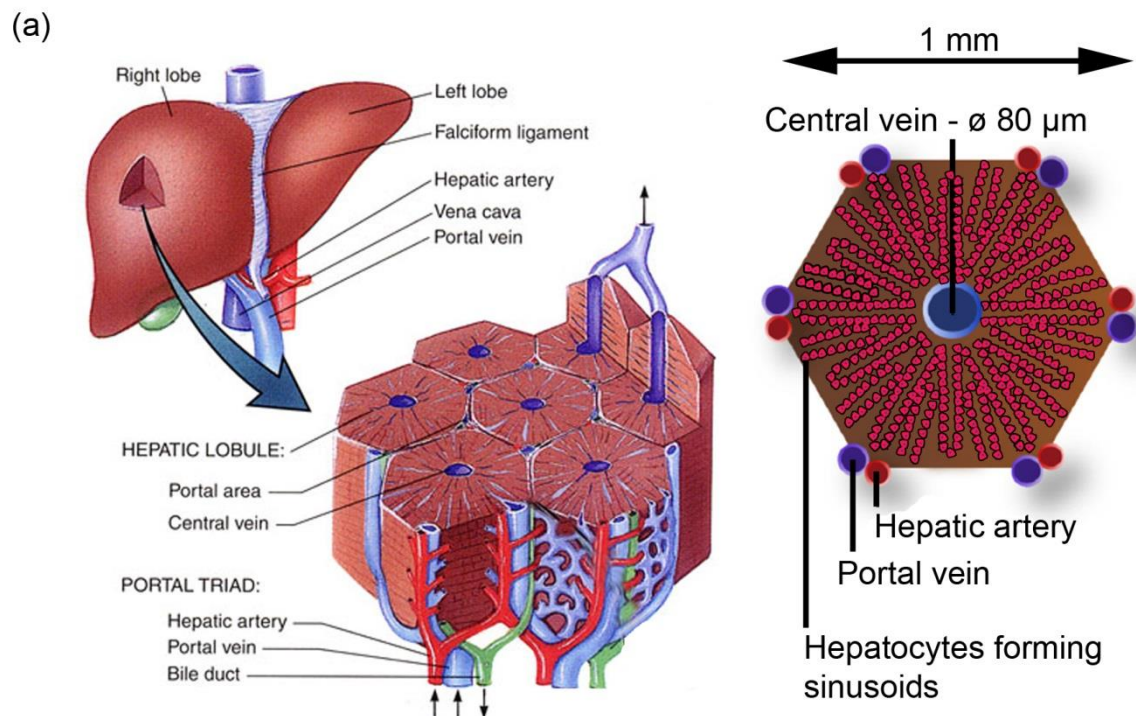


Figure 2.7-1 – Human liver basic physiology. (a) The liver is the largest gland in the body and receives blood from two main sources the hepatic portal vein and the hepatic artery. The liver is composed of small units, which can be described in a number of ways. One of the common descriptions is the “classic lobule”⁴⁴. Approximately the lobules are hexagonal in cross-section, with the central vein ($80 \mu\text{m}$ diameter) in the centre surrounded radially by sinusoids constructed of hepatocytes. Liver cross-section illustration reproduced from reference²⁰⁵.

The sinusoids in the liver are vascular spaces lined by fenestrated endothelial cells.

Compounds within the blood are exchanged with the hepatocytes as blood passes through

the endothelial layer.²⁰⁶ This branching structure is connected to a central vein enlarges the total volume in contact with the organ, aiding mass transport to the hepatocytes in the lobules. Enzymes present within the hepatocytes act on compounds flowing into the liver where there are metabolised. By using anatomical data^{207, 208} to develop the electrode arrangement, a biomimetic design was developed.

The design is illustrated in Figure 2.7-2(a); the inner branches of the electrodes (**red**) are connected to an alternating current (AC) supply, the outer connection (**black**) to the ground line. The design uses 19 lobules giving the array dimensions of 5 x 4.6 mm. This array size was chosen to allow it to fit within the diameter of a 5 mm gasket. Reasoning for this was that it had to fit within a paper ring, 5 mm inner, 6 mm outer diameter. This is because individual wells of industry standard 96-well plates are typically 6.86/6.35 mm (top/bottom) in diameter, hence 6 mm was chosen as the diameter for the paper ring.²⁰⁹

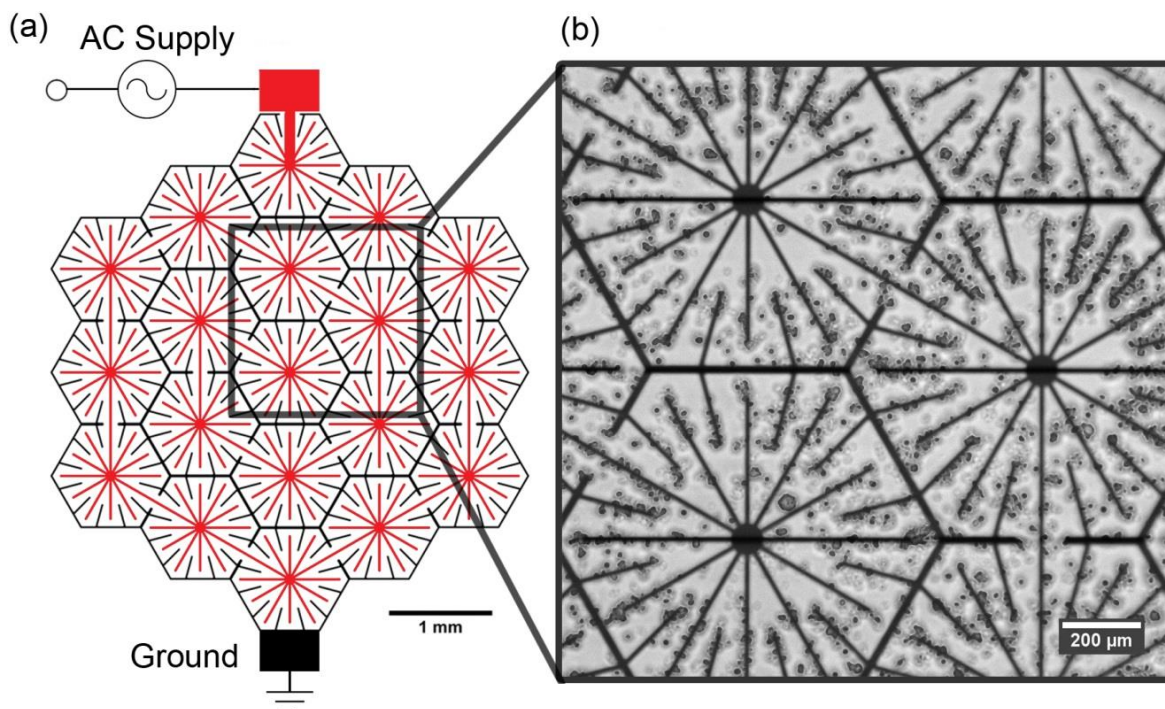


Figure 2.7-2 – Microelectrode design for inducing DEP forces to pattern cells into a micro liver lobule array. (a) Using a biomimetic electrode design hepatocytes are patterned into an array 19 lobules in size using DEP forces. The largest gap is 60 μm between the electrodes. The thickness of the electrodes is 10 μm. (b) Microscope image showing C3A liver cells being held in place by DEP forces to form liver lobule like structures. Scale bar is 200 μm.

Standardised research machines such as plate readers and microscope stages are engineered to hold and read results from 96-well plates. This choice of dimensions allowed for immediate compatibility with standard assay readers and microscopes. Therefore the array could not be larger than 5 mm in diameter. A microscope image shown in Figure 2.7-2(b) is an example of cell patterning using this design. Cells are attracted to the edges of the electrodes where the electric field is strongest. The voltage drop across the electrodes

is insignificant due to the high conductivity of the material (Au). Table 2.7-1, a lobule like array consisting of 19 lobule structures was designed to generate an electric field Figure 2.7-3. The lobule hexagonal prism that forms the lobule structure is shown in Figure 2.7-3(a), a sketch illustrating the electrode design detail is shown in Figure 2.7-3 (b). The electrode width was chosen to be 10 μm thick because this allowed for a gap between the hepatocyte cords being patterned.

Sinusoids in the liver are typically of the diameter of 10 μm .²¹⁰ The central point of the design was designed to be 80 μm in diameter corresponding to the diameter of the centrilobular vein.²¹¹ The width of the lobule was designed to be 1 mm, the sides 500 μm , also with relation to anatomical data.²¹¹

Table 2.7-1 – Typical values of dimensional quantities from physiological conditions of the human liver

Description	Value	Source
Width of a single lobule	1 mm	211
Length of edge of a lobule	500 μm	211
Diameter of the centrilobular vein	80 μm	211
Number of lobules (human liver)	1-1.5 $\times 10^6$ lobules	212
Number of hepatocytes (per lobule)	1 $\times 10^5$ cells	212
Width of sinusoids	10 μm	210

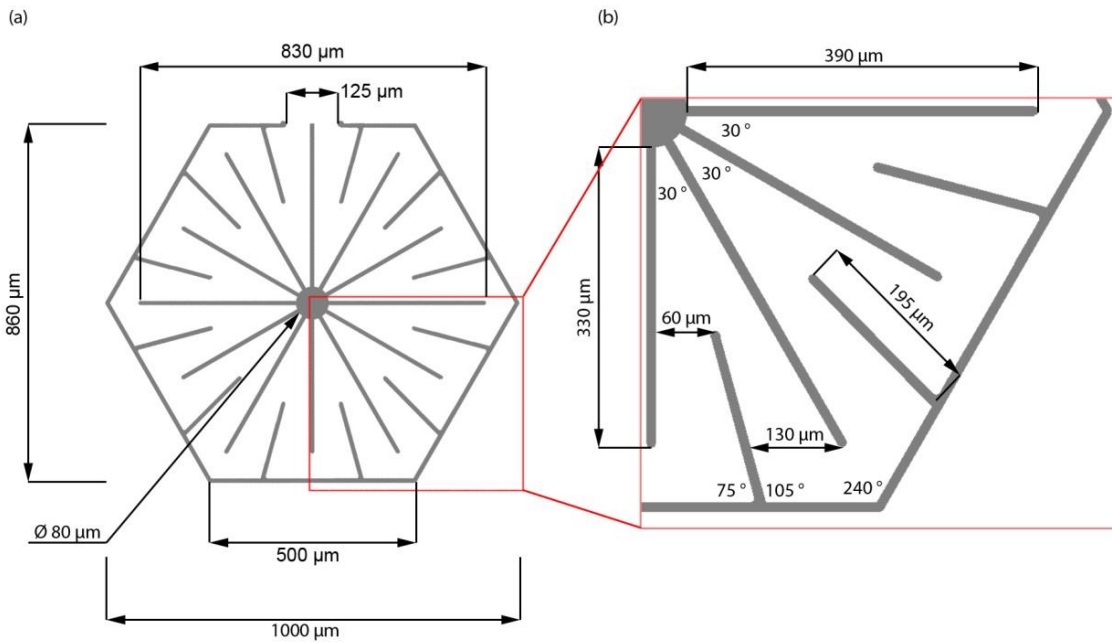


Figure 2.7-3 – Schematic of a single electrode lobule unit. (a) Shows the centre lobule of the array indicating major feature dimensions. (b) Detail showing a quarter of the lobule unit fine dimensions of the design are indicated. Electrodes are 10 μm in width.

Each liver lobule electrode arm is 10 μm thick spread out radially from the centre circle every 30 ° for a total of 12 arms. The inner circuit was connected by joining the electrodes through an extended arm branching off from the centre. This connection spiralled round from the outside to the inside where the connection terminates. For the counter electrode the design used the edges of the lobule design to connect to the electrodes. The connections were made in the same manner and follow the design round until the centre lobule where it terminates. Three variations to this design were made shown in Figure 2.7-4. All stated anatomical values were considered as constants for the lobule design. This only left the separation between the inner and outer electrodes as a variable. Designs with 30, 50 and 60 μm gaps were used.

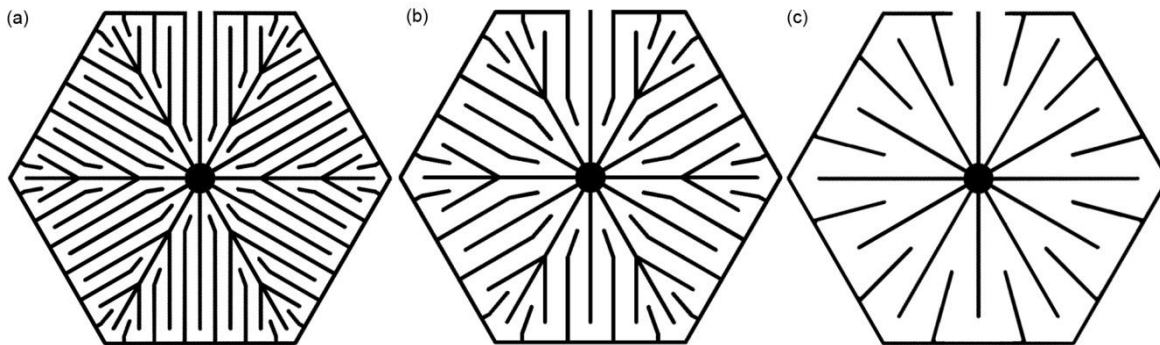


Figure 2.7-4 – Schematics illustrating the 3 electrode lobules used. Each was designed to fit within the anatomical restrictions of considered constants. The variable changed was the minimum distance between the inner and outer electrodes. Distances used were (a) 30 μm (b) 50 μm and (c) 60 μm. All lobules were 1 mm in width.

2.7.2 Fabrication of electrodes for dielectrophoresis

The fabrication process used for the electrodes in this work follow the well-defined photolithographic techniques.¹³⁶ All dielectrophoresis devices were fabricated using the JWNC.

2.7.2.1 Design

Electrodes were designed using L-Edit, Tanner EDA, USA. Due to the small size of features for electrodes (10 μm) a chrome mask was selected. This ensured a high quality and pattern

reproduction during lithography. The mask was fabricated in house using a Vistec EBPG5 HR 100 Electron Beam Lithography tool situated in a Class 10 clean room.

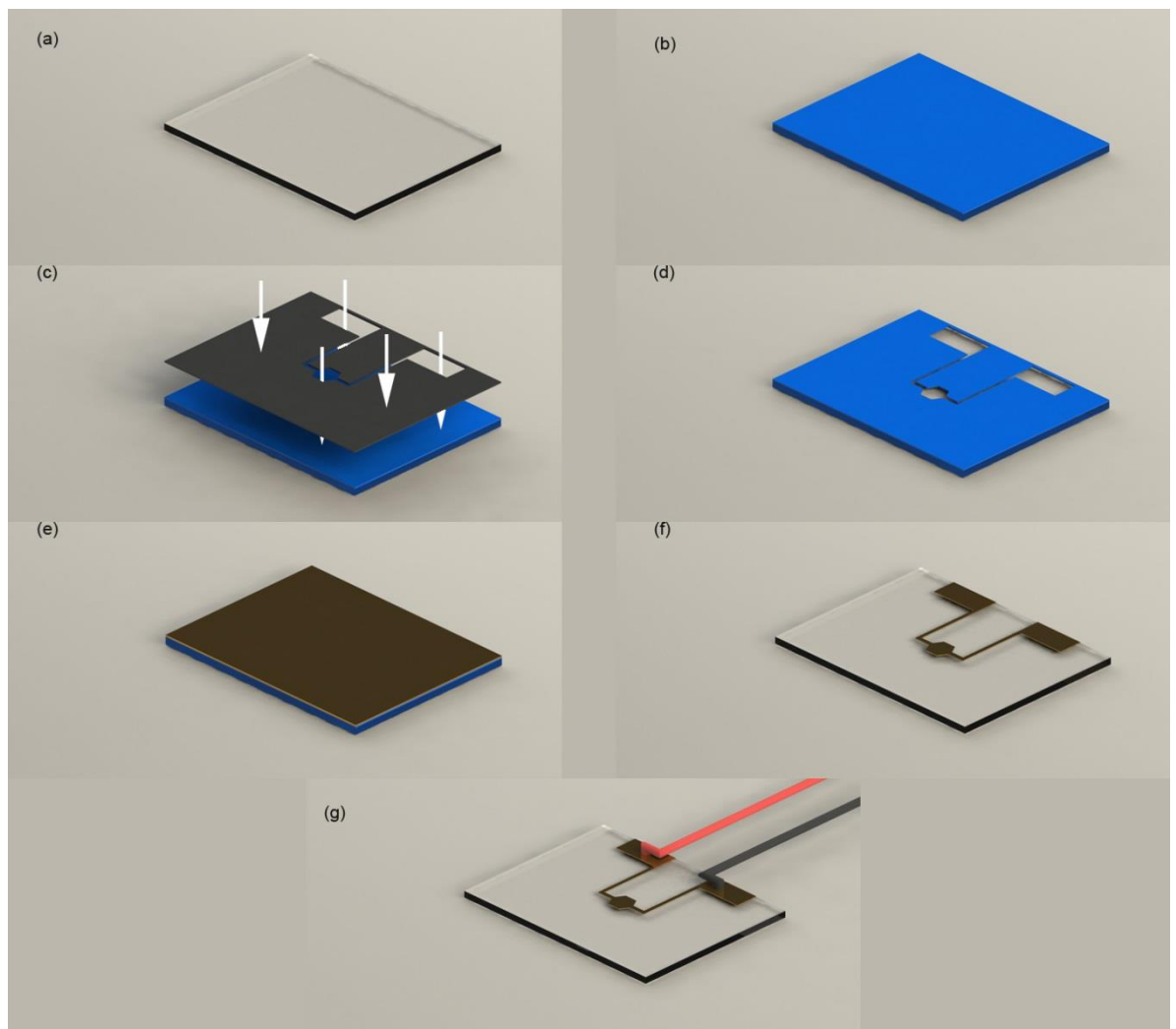


Figure 2.7-5 – Process for fabricating electrodes for dielectrophoretic patterning (a) Cleaned glass slide by Opticlear and organic solvents using ultrasonics; (b) Spinning of S1818 resist (negative photopolymer) followed by soft-baking at 95 °C for 5 minutes; (c) Exposure using lithography and chrome mask to polymerise areas to be removed; (d) Developed S1818 showing exposed glass in the pattern of the mask; (e) Metallisation through use of metal evaporator to deposit Ti and Au (10 nm, 100 nm), the Ti layer improves adhesion of Au to the glass; (f) Lift-off, removal of excess Ti and Au by removing remaining S1818; (g) Completed electrodes with wires soldered to make connections to the signal generator.

2.7.2.2 Cleaning

Glass slides (0.5 mm thick) were cut into 30 x 25 mm samples and rinsed in DI water to remove debris. To thoroughly clean the glass samples were immersed in Opticlear and sonicated for 5 minutes. Following rinsing with DI water, the samples were sonicated in acetone, methanol and finally IPA for 5 minutes each. Samples were then removed and air dried Figure 2.7-5(a).

2.7.2.3 Resist Spinning

Samples were spun individually with S1818 resist at 4000 rpm for 30 seconds Figure 2.7-5(b). S1818 was applied to the samples via 0.45 μm filtered syringe. Following spinning samples were immediately soft-baked at 95 °C for 3 minutes. This step was critical in achieving correct photolithography transfer as shall be described in Section 2.7.2.8.1

2.7.2.4 Photolithography

Samples were individually exposed using 2 inch chrome masks using the optical photoaligner (MA6) as detailed in 2.4.6. Exposure was performed with UV light (30 mW) for 5 seconds in hard contact mode Figure 2.7-5(c) as described in 2.4.6.1.

2.7.2.5 Development

Removal of exposed areas is achieved using Micro Developer in a 1:1 ratio with DI water Figure 2.7-5(d). Samples were submerged in developer and agitated for 1 minute and 10 seconds. Samples were then rinsed in DI water and air dried.

2.7.2.6 Titanium and gold metallisation and lift-off

The metallisation process was completed using a Plassys MEB 400S Electron Beam Evaporator Figure 2.7-5(e). Typically up to 4 samples would be coated at a time, depositing 10 nm of Ti (titanium) and 100 nm of Au (gold). The Ti was used as an adhesion layer as Au adhesion to glass is poor.²¹³ Unwanted metal was removed from the substrate by submerging the samples in acetone at 50 °C for up to 12 hrs. As this was a large layer of Au being deposited it could take an overnight soak in reagent grade acetone to fully remove the resist and metal from the substrate Figure 2.7-5(f).

2.7.2.7 Connections

To complete the fabrication of electrodes, solid core wires were cut and soldered to the electrode pads Figure 2.7-5(g). This was completed by pressing the wire to the electrode connection pads while heating the wire from above (pliers were needed as to not burn ones hands) then dropping a thread of solder into the wire. This ensured a strong electrical and

structural connection. The wires had micro 2-pin female molex connector fitted as to improve connection to the rest of the system.

2.7.2.8 Results and discussion

2.7.2.8.1 Optimisation of soft-baking temperature

During the soft-baking stage it was critical that the S1818 was subjected to the correct temperature for the allotted time. Failure to do so resulted in poorly cross-linked polymer which in turn did not polymerise in the desired fashion when exposed to UV radiation as Figure 2.7-6 demonstrates.

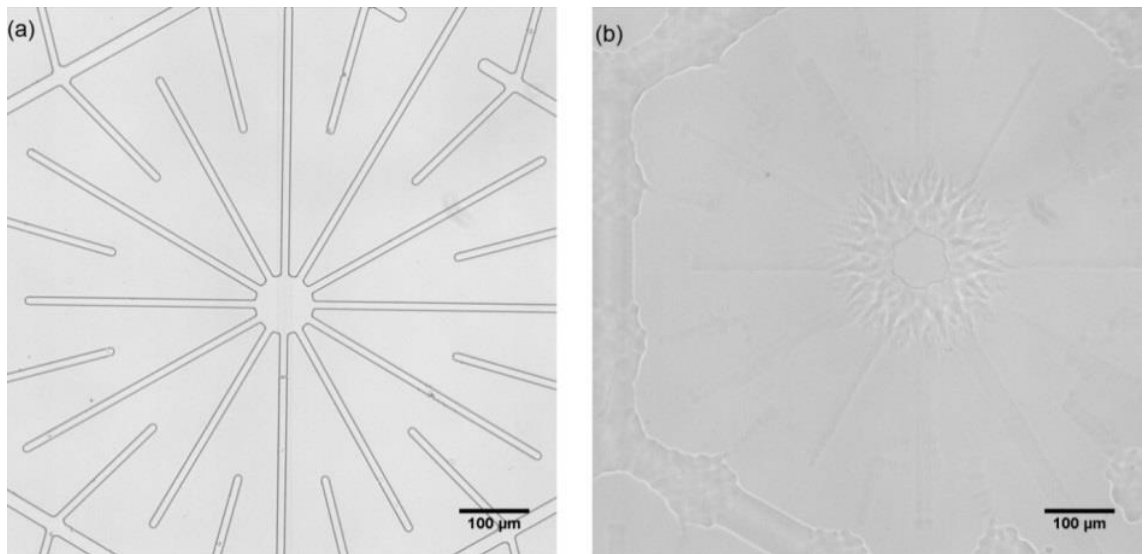


Figure 2.7-6 – Incorrect soft-baking - Microscope image showing identically processed samples with the exception of soft-bake temperature (a) 110 °C (actual 94 °C) and the (b) 95 °C (actual 75 °C). The features were barely visible when the development process was completed.

2.7.2.8.2 Effect of over-exposure

The time for which the S1818 layer was exposed to the UV radiation was also critical. Here it can be seen that when the exposure was increased to 7.5 seconds the pattern, “bulges” and does so even more at 15 seconds. Figure 2.7-7 below demonstrates the effects of this change in parameters.

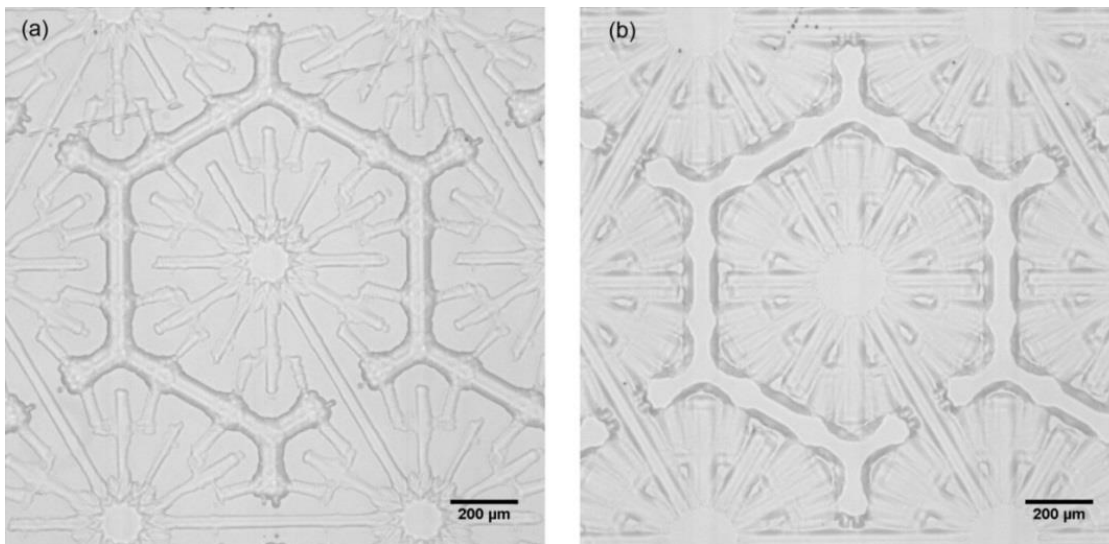


Figure 2.7-7 - Influence of exposure time on structures – Microscope image showing a sample exposed for 7.5 seconds (a) and 15 seconds (b). The structure has bulged out losing the definition of the pattern.

2.7.2.8.3 Fabrication and electrode selection

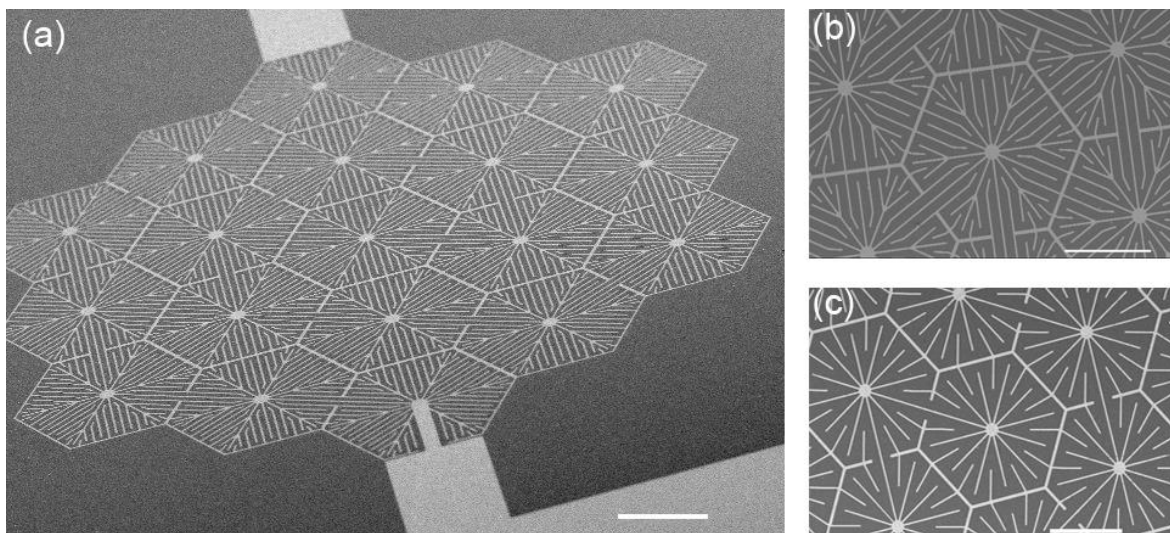


Figure 2.7-8 – SEM images of fabricated electrodes designed for dielectrophoresis patterning of cells. Each image shows the result of different spacing between the electrodes. (a) Angled view showing the complete array with 30 µm spacing. Scale bar 1 mm (b) Top down view of electrodes with 50 µm spacing. Scale bar 500 µm. (c) Top down view showing electrodes with 60 µm spacing. Scale bar 500 µm.

SEM images showing electrodes fabrication results Figure 2.7-8(a)-(c). Each of the 3 different electrode spacing designs (30, 50 and 60 µm) was shown to be successfully fabricated. It was observed in patterning experiments using the 3 different designs that each was capable of arranging cells into lobule like arrays as shown in Figure 2.7-9. The electrode design with 60 µm spacing was shown give the most defined visual pattern compared with the 30 and 50 µm spacing designs. To aid with conformation of patterning and alignment during pattern efficiency analysis, the 60 µm design was selected.

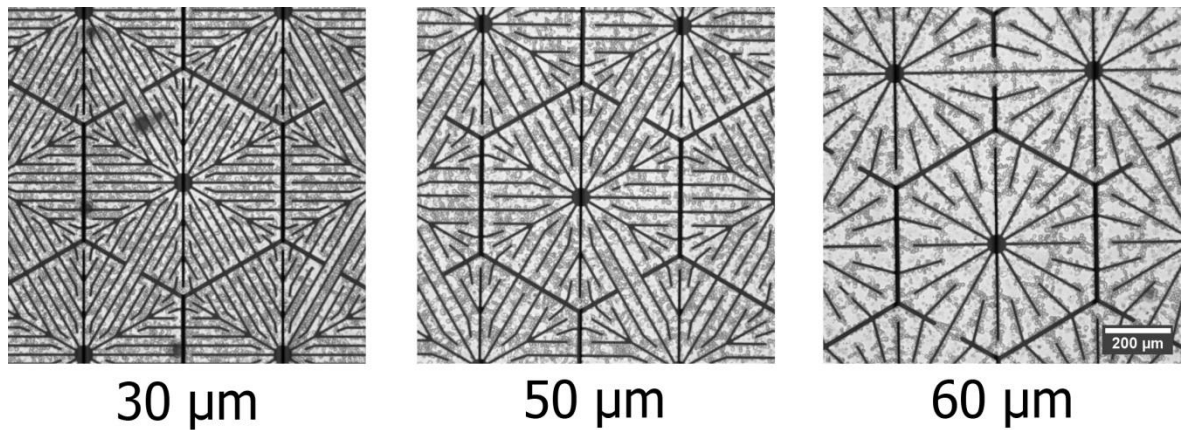


Figure 2.7-9 – Microscope images of electrodes show C3A cells patterned by DEP forces under the same conditions. (a) Spacing of 30 μm resulted in patterning however visualisation of the pattern proved difficult. (b) Spacing of 50 μm also resulted in patterning with improved visualisation of the pattern. (c) Spacing of 60 μm resulted in patterning and further improved visualisation. Scale bar 200 μm .

2.7.3 Hydrogel and Paper substrate Preparation for cell patterning

2.7.3.1 Cell culture and media

Human liver cell line, HepG2/C3A was maintained according to supplier instructions at 37 $^{\circ}\text{C}$ with 5 % CO_2 , in Eagle's Minimum Essential Medium (EMEM) as described in Section 2.3.1. Antibiotics are used prophylactically in cell culture maintenance however, it has been observed that they cause disruption of cellular functions including cell morphology, cellular degeneration and cell death.²¹⁴ Hepatocytes have been observed to have reduced metabolic function when cultured with penicillin, a commonly used antibiotic in cell culture.²¹⁵ As toxicity studies using hepatic cell lines are reliant on reproducible data from protein synthesis, antibiotics were not used in this work.

2.7.3.2 Cell preparation for DEP manipulation

C3A cells were harvested from 70% confluent cultures and detached from the surface of 25 ml culture bottles using 0.25 % trypsin-EDTA . This was diluted with 5 ml of warmed (37 $^{\circ}\text{C}$) EMEM and then pipetted into a 15 ml centrifugation tube. Cells were centrifuged for 3 minutes at 1500 rpm (312 g) to form a soft cell pellet. Waste media was gently removed from the tube using pipetting, the final solution being removed using a 200 μl pipette in order to reduce the transfer of extra ions into the final solution. The pellet was then pipetted with 5 ml of DEP buffer (9% sucrose, 0.3% dextrose, 3 mM HEPES in DI H_2O ; conductivity 13 mSm^{-1} at 37 $^{\circ}\text{C}$, pH 7.4, osmolality 300 mOSM). A low conductivity was selected to maximise the dielectrophoretic forces exerted on the cells.²¹⁶ The suspended cells were then spun down again at the same settings; this process was repeated 3 times. Finally 200 μl of DEP buffer was then added to the cell pellet to yield a cell concentration

of 2.5×10^6 cell/200 μ l. This concentration was selected to provide 125×10^5 cells/10 μ l which was the designed volume used to fabricate the micro liver.

2.7.3.3 Agar gel preparation

Low-gelling agar was dissolved by boiling with DEP buffer to give a final agar concentration of 2% (wt/vol). Batches of this buffer were sterilised by autoclave to ensure sterile conditions for the cells. This agar solution was maintained at 37 °C in a water bath until required. A pre-warmed (37 °C) Eppendorf 1.5 ml tube was used to mix 1:1, agar 2% solution with 2.5×10^6 cell/ml concentrate DEP buffer; yielding a 1% agar solution of 1.25×10^6 cell/ml with DEP buffer. This final solution was kept at 37 °C before use in DEP-based cell-patterning experiments.

2.7.3.4 Results and Discussion

2.7.3.4.1 Agar and paper substrate handling

Agar moulding results using a 0.5 mm thick silicon gasket with 6, 5 and 3 mm punched holes are shown in Figure 2.7-10. Agar 0.5% (wt/vol) removed from the punched gasket, agar was observed to be structurally unstable. Figure 2.7-10 (b) Agar 1% (wt/vol) removed from the punched gasket, straight edged discs of agar were observed. Agar 1% was selected as a suitable concentration for three reasons.

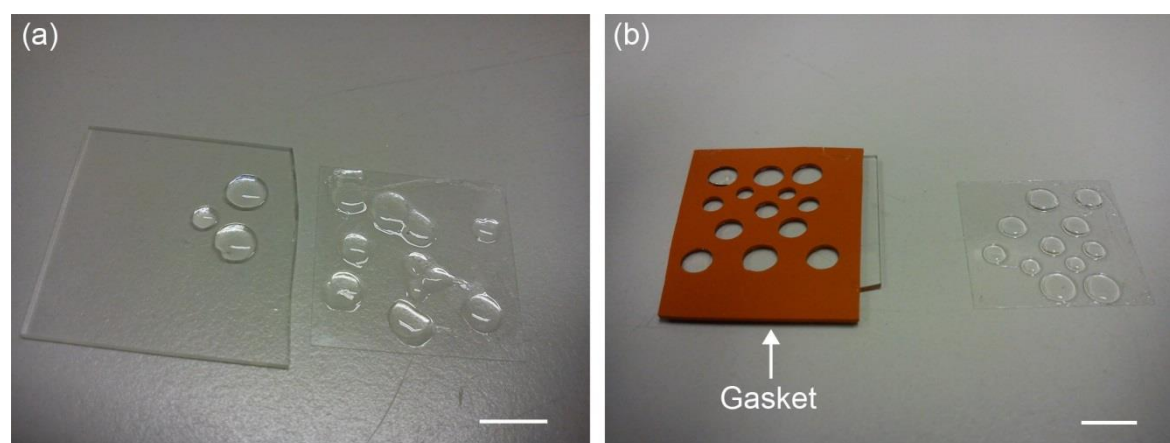


Figure 2.7-10 – Agar moulding results using a 0.5 mm thick silicon gasket with 6, 5 and 3 mm punched holes. (a) Agar 0.5% (wt/vol) removed from the punched gasket. Agar was observed to be structurally unstable. (b) Agar 1% (wt/vol) removed from the punched gasket. Straight edged discs of agar were observed.

Firstly, agarose is a naturally derived hydrogel from seaweed that provides large-pore, macroreticular networks by thermoreversible gelation. Agar has been shown to provide a suitable tissue engineering ECM for mammalian cells²¹⁷ and agar scaffolds for HepG2 liver cell culture.²¹⁸ It was selected for the biocompatibility, porosity allowing the diffusion of nutrients and gases to cells and physiologically suitable sol phase temperature (> 30 °C).

Secondly 1% (wt/vol) agar has been observed to allow positive DEP patterning while maintained at 25-37 °C. Fibroblast cells were observed by *Albrecht et al* to pattern closely to the original photomask design. They hypothesised that this micro-scale organisation had a multifactorial role in chondrocyte behaviour compared to 2D model cultures.¹²³ This was considered with regard to cell-matrix interaction and direct cell contact which have been identified as major factors in emergent tissue properties.²¹⁹

Thirdly post-gelation 1% (wt/vol) agar was found to be strong enough to maintain the shape of 3, 5 and 6 mm holes punched in a 0.5 mm silicon gasket press between a microscope slide and coverslip as shown in Figure 2.7-10. Agar 1% (wt/vol) was observed to attach to the edges of the paper ring substrate without detaching or ripping.

Successful results using a paper ring substrate 6.2 mm OD, 5 mm ID to remove cured agar with patterned cells using DEP are shown in Figure 2.7-11. Shown in Figure 2.7-11 (a) the Computer aided design (CAD) drawing of 6.2 mm OD, 5 mm ID circles. Figure 2.7-11 (b) Laser cut paper rings cut from paper using the CAD design. (c) Successful removal of a paper ring used as a substrate to manipulate thin discs of agar with patterned cells using DEP. All scale bars are 5 mm. Experiments using lower concentrations of 0.8, 0.5 and 0.25% resulted in the gel not attaching to the paper ring.

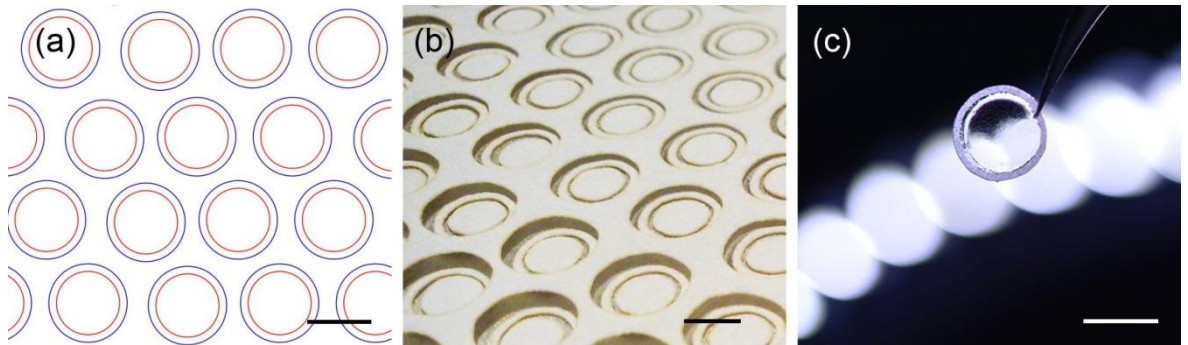


Figure 2.7-11 – Paper handling results. (a) Computer aided design (CAD) drawing of 6.2 mm OD, 5 mm ID circles. (b) Laser cut paper rings cut from paper using the CAD design. (c) Paper ring used as a substrate to manipulate thin discs of agar with patterned cells using dielectrophoresis (DEP). All scale bars are 5 mm.

2.7.3.4.2 Medium conductivity

Optimal parameters for DEP patterning of cells includes low medium conductivity as Joule heating can be induced.²¹⁶ Joule heating as described in Section 1.6.3 ($q = \sigma E^2$) increases both with electric field strength and conductivity. To reduce the effect of heating by Joule heating the conductivity of the medium should be as low as possible. The Clausius Mossotti (CM) factor also described in Section 1.6 is affected by conductivity, decreasing CM will increase the DEP forces. Experiments were conducted using voltages

of 10 Vpp and a frequency of 10 MHz. The electrodes were heated by the Peltier (+0.28 A) to a temperature of 26 °C a conductivity of 41 mSm⁻¹ for example was found to increase the temperature of the patterned solution to 40 °C where as a conductivity of 13 mSm⁻¹ would bring the temperature to 36 °C. The lowest achievable conductivity while offering non-toxic conditions was found to be 13 mSm⁻¹ and was used for all experiments.

2.7.3.4.3 Cell concentration and preparation

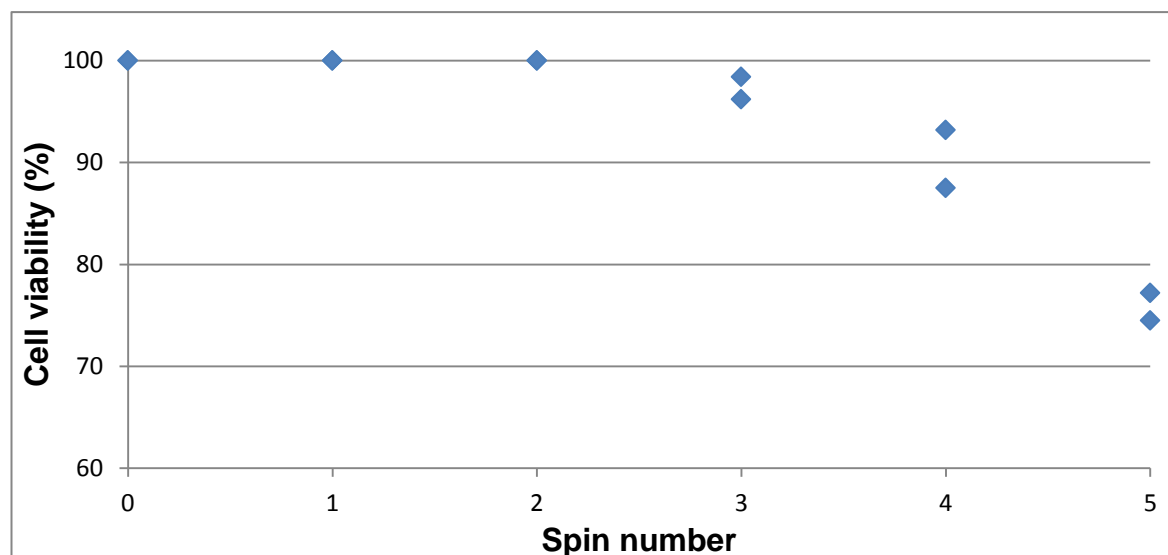


Figure 2.7-12 – Cell viability due to wash steps in DEP buffer. Cell concentration was 1.0×10^6 cells/ml. Cell viability was assessed through Trypan blue staining and cell counting. There is a significant drop off after 4 wash steps therefore 3 steps was selected as the optimal number of wash steps.

Data from literature states that a liver lobule contains 10^5 cells, of which 60-65% are hepatocytes.²¹² Thus using the cell concentration used corresponds to approximately 2 liver lobules. Viability and cell count were checked before and after the centrifugation. The drop in viability due to 3 spins was not significant as shown in Figure 2.7-12 therefore this was the selected number of wash steps. Washed cells were transferred to a 1.5 ml Eppendorf tube and placed in a 37 °C water bath.

2.7.3.4.4 Agar definition temperature and conductivity

Conductivity of the DEP buffer agar solution against time was investigated in relation to temperature. The results shown in Figure 2.7-13 show a linear decrease in temperature from 41 °C onwards, a faster cooling rate was observed from 45 °C to 41 °C. This is reflected in the conductivity which sees a rapid decrease from 21 mSm⁻¹ to 17 mSm⁻¹. Conductivity is stable from 43 to 36 °C (12 minutes) after which it started decrease reaching 13 mSm⁻¹ at 32 °C. This showed that the conductivity of 1% agar solution mixed with 13 mSm⁻¹ at 37 °C was 4 mSm⁻¹ higher than that of the buffer. This conductivity was low enough still to provide strong positive DEP forces.²¹⁶ The dip in conductivity at 33 °C indicated that the agar had entered the transition regime (gelation stage) which was not

expected as the agar was designed to begin curing at 30 °C. However it has been shown by *Tang et al* that the addition of sucrose to agar increases the gelation temperature.²²⁰ They observed that a 10% concentration of sucrose in agar increased the gelation temperature by 3-5 °C which is in agreement with the results found here. As the temperature of the system was designed to be maintained at 37 °C for DEP patterning this had no significant effect on the system.

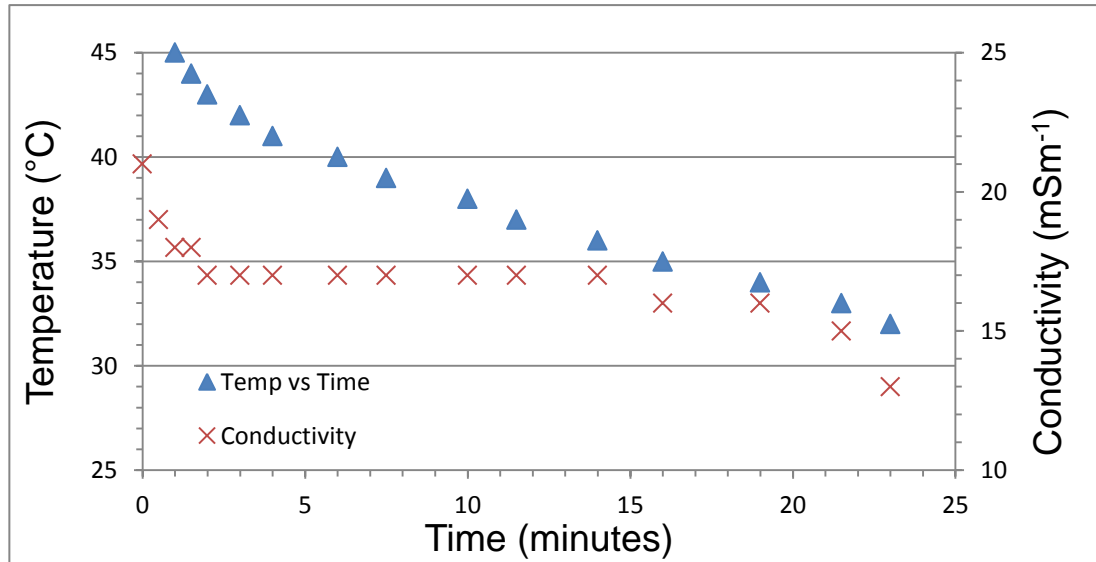


Figure 2.7-13 – Graph showing the relationship of temperature (°C) and conductivity (mSm⁻¹) of 13 mSm⁻¹ DEP buffer mixed 1:1 with 2% agar solution (resulting in 1% agar solution) allowed to cool at room temperature (25 °C).

2.7.4 System Design

The system design is illustrated in Figure 2.7-14. Electrodes for patterning and serving as a control were placed on their respective Peltier coolers. A layer of thermal paste was placed between the Peltier and copper heat sink to promote thermal conduction to the heat sink. Repeated patterning operations generated more heat than could be dissipated by over heat sinks available hence the Zalman CNPS7000a-CU was selected. The 3D printed cover was employed to reduced evaporation during the patterning process, detailed in Appendix B.

An exploded 3D rendered model of the system can be seen in Figure 2.7-14(a) and a cut away view in Figure 2.7-14 (b). The copper heat sink was the base of the system which was connected to the Peltier reversibly with thermal paste. A drop of deionised (DI) water was pipetted onto the surface of the Peltier acting as a thermal interface with the bottom of the electrodes.

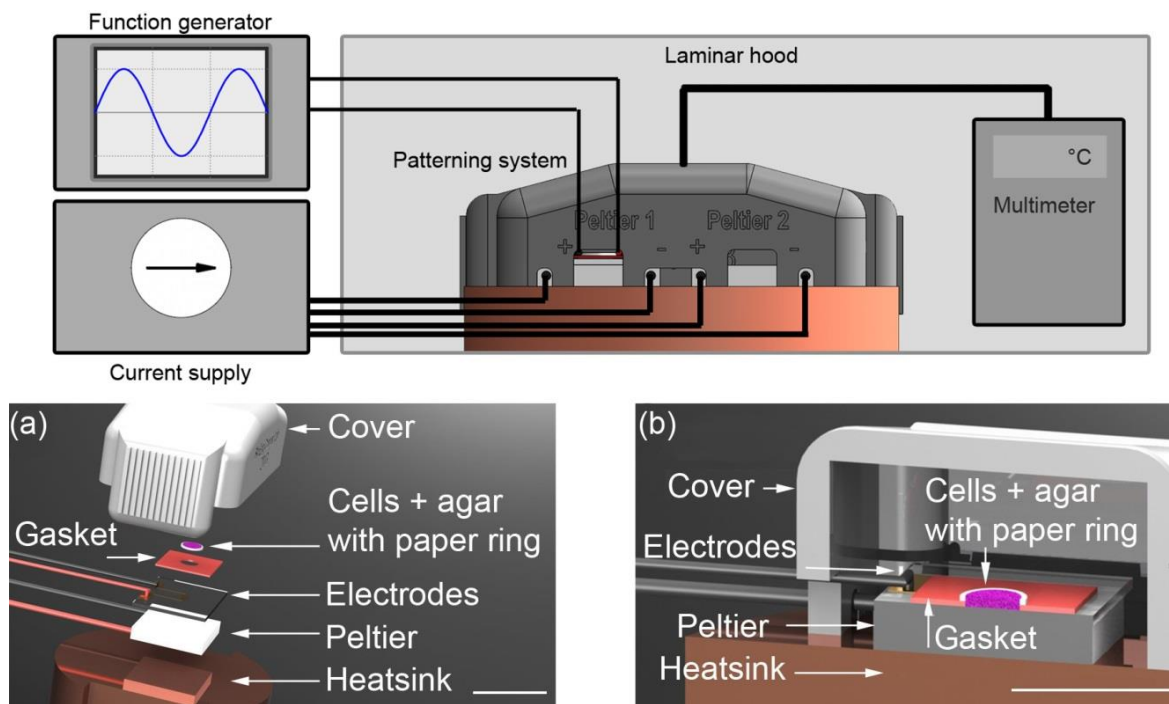


Figure 2.7-14 – Physical setup of the patterning system: Illustration at the top shows the patterning system placed inside a laminar hood along with a multimeter for air temperature readings via thermocouple. An infrared camera (not pictured) was also used for surface temperature measurements. The function generator and current supply were located outside of the laminar hood. Below are two 3D model renderings of the micro liver patterning system at 1:1 scale and realistic material properties. (a) Exploded view shows the patterning system design. The base is a copper heat sink on which the Peltier was reversibly attached using thermal paste. Glass with microfabricated electrodes for DEP patterned are placed on top on the Peltier loosely interfaced with DI water. To define the volume of the agar cell solution a 100 μm gasket was pressed onto the electrode with a 5 mm hole cut in the centre. A 6 mm laser cut paper ring was placed around the perimeter of this hole. Agar cell solution to be patterned was pipetted into this volume. A 3D printed cover was placed over the top enclosing the system during the patterning process. (b) Cut-away view illustrating the system. The insertions for electrical connections through the cover can be seen to the left of the Peltier. Scale bars are 15 mm.

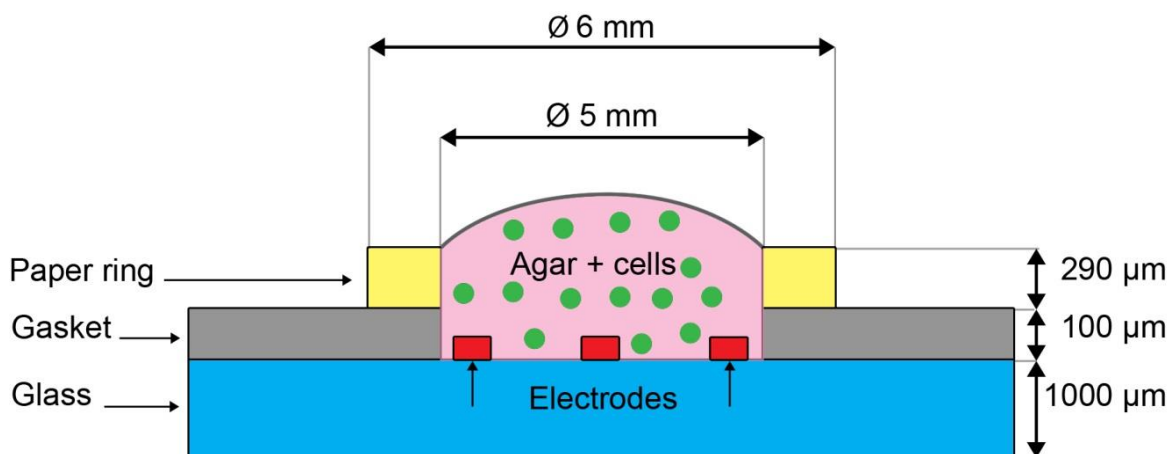


Figure 2.7-15 – Illustration showing the design of the patterning volume. A Nesofilm gasket (100 μm) was pressed onto the surface of glass substrate with DEP electrodes. Around the circumference of this gasket a 5 mm ID, 6.2 mm OD paper ring previously soaked in 2% (wt/vol) agar was placed. This defined a 7.7 μl volume for electrode patterning. The paper ring was soaked to stop the wicking of 1% agar DEP buffer cell solution into the paper.

Shown in Figure 2.7-15 the top of the electrodes had a 100 μm gasket made from Nesofilm with a 5 mm diameter hole cut in the centre. This defines the volume of the agar cell solution to be patterned. Around the circumference of this gasket a 5 mm ID, 6.2 mm OD

paper ring previously soaked in 2% (wt/vol) agar was placed. This defined a 7.7 μl volume for electrode patterning. The paper ring was soaked to stop the wicking of 1% agar DEP buffer cell solution into the paper. The agar cell solution was pipetted into this volume for patterning; it was found that a volume of 10 μl was suitable for a consistent result in that the agar did not becoming dehydrated during the patterning process.

2.7.4.1 Patterning variable optimisation

Before cell patterning experiments for C3A cells (10 – 15 μm in diameter) the frequency domain was evaluated for the appropriate AC signal for DEP manipulation. Cell mixed with DEP buffer and agar to make a 1% (w/v) solution was pipetted onto the electrodes by the volume defined by the gasket. It was expected that the range of 1 MHz to 10 MHz to provide positive DEP phenomenon as described in Section 1.6.2. Then the AC signal was varied over a range of 1 MHz to 10 MHz as well as the peak to peak voltage from 1 to 10 V_{pp} to observe positive DEP phenomenon. Additionally this frequency range is ideal for mammalian cells as this balances the maximal CM factor magnitude (Section 1.6.2) with minimal induced transmembrane potential.²¹⁶ *Gray et al* showed that the transmembrane potential decreased for frequencies over 50 MHz by a factor of two compared to 1 MHz.²²¹ However, the real part of the CM factor decreases significantly for frequencies higher than 50 MHz meaning that the range of 1-10 MHz is optimal for mammalian cells. The voltage ranges were limited by the signal generator used in this work. Confirmation was made of positive DEP forces in this range.

Experimental results showed that electric-field induced negative DEP appeared at sub-kHz frequencies, positive DEP was generated at fields over sub-MHz frequencies. These observations are in agreement with previous studies of DEP cell based patterning.^{123, 222} ,

The range of currents to supply the Peltiers used for temperature changes in the patterning volume was restricted to 0.2 – 0.28. This provided a range of temperatures from 32-36 °C. The top range was selected as the temperature required by the cells was 36.5 to 37.5 °C. The bottom value was selected as the agar gel enters the gelling phase at 30-32 °C.

2.7.4.2 Micro liver patterning efficiency

To assess the patterning efficiency, images of the micro liver samples fabricated with this system were analysed using a geometrical quantification method detailed below.

2.7.4.2.1 Mask template generation

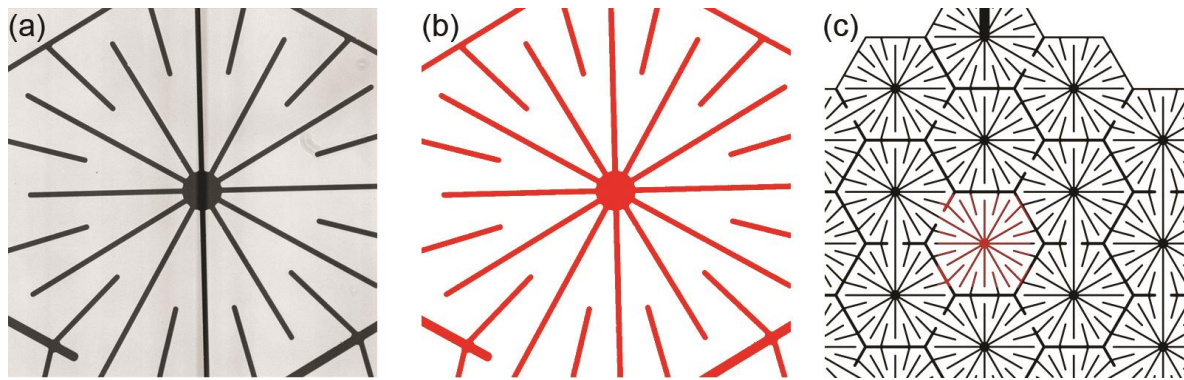


Figure 2.7-16 – Process of mask generation. (a) Microscope image (Z.D1 at x10) taken of electrodes. (b) Microscope image adjusted with threshold to reduce the image to black and white only isolating the electrodes from the image, coloured here in red. (c) Electrodes imported as a layer into Photoshop on top of the electrode design. The electrode array was adjusted until it scaled correctly with the reference electrode image from (b). Electrode thickness is 10 μm .

The electrode array design was opened in Photoshop where a reference image of the electrodes taken with the same microscope (Z.D1 at x10) Figure 2.7-16(a). This image had the threshold adjustment applied reducing it to black and white. The electrodes were then removed from the background, this can be seen in Figure 2.7-16(b) where the electrodes have been coloured red. To scale the electrode array design, this threshold electrode image was used to scale the design to the correct dimensions shown in Figure 2.7-16(c).

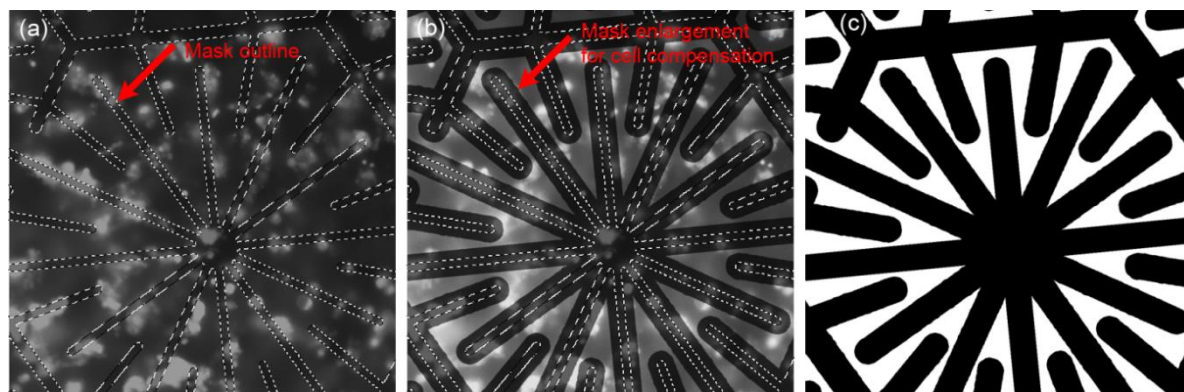


Figure 2.7-17 - Mask processing. (a) Scaled electrode array previously shown in Figure 2.7-16(c) was aligned manually with a microscope image of patterned cells in agar by dielectrophoresis (DEP). (b) The aligned electrodes then have a 23 pixel stroke applied, increasing the thickness of the electrodes by adding extra pixels to the perimeter of the electrodes. This compensates for the designed effect of cells attaching to the edges of the electrodes. (c) Finally the mask is completed by merging the electrodes and stroke effect.

Having completed this step, the fluorescent image to be analysed was opened in Photoshop, where the scaled electrode design was superimposed onto the image on another layer shown in Figure 2.7-17(a). By manually aligning the mask to patterned cell image the electrode design was matched to the cell pattern in the microscope image. However the mask only covers the cells attached to the top of the electrodes, the design also included cells attaching to the edges of the electrodes as the electric field is strongest in these locations.¹²⁸ Therefore the whole mask layer then had a 23 pixel stroke effect added to the

pattern. This number was selected because the average cell diameter was measured to be 23 pixels (± 7 pixels). This effect adds 23 extra pixels to the perimeter of the electrodes making them effectively larger hence including cells attached to the edges of the electrodes as shown in Figure 2.7-17(b). Once complete, the mask was flattened and saved before being exported as a .tif file (minus the microscope image) as shown in Figure 2.7-17(c).

2.7.4.2.2 Mask ROI generation

The .tif mask for the fluorescent images to be analysed was then opened in ImageJ. Here the bit depth was reduced to 8-bits, default threshold was applied and finally the image was forced to binary. The mask was dark field hence the negative (white) areas of the mask are selected and were stored in the region of interest manager (ROI). This area represents the positive mask where the cells are to be patterned, a green outline was given to this mask Figure 2.7-18 (b).

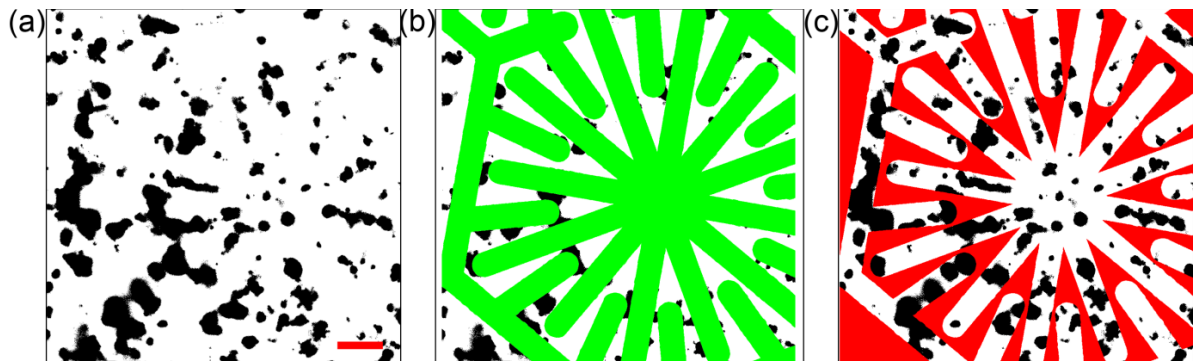


Figure 2.7-18 – Image analysis using ImageJ. (a) Processed image of live cells after 72 hrs culture. Threshold and binary processing has been done on this image. Cells aggregates are black. (b) The processed cell pattern image superimposed with a positive mask (green), covering the area in which cells are designed to be patterned. (c) This image shows the same processed image but with the negative mask (red) superimposed. This is represented by the inversion of the electrode mask from (b) covering the area where cells should not be. Scale bar is 100 μm .

The whole image was then inverted, so that the negative areas where the cells are not designed to be patterned was selected and stored in the ROI. This area was filled red to represent the negative mask Figure 2.7-18 (c). The area covered by each mask would be saved and added together to ensure the whole area had been captured. The total should be 1006008 pixels for a 1004 x 1002 image.

2.7.4.2.3 Image analysis

Fluorescent images of micro liver structures (Z.D1 x10) were imported into ImageJ. These images were then switched to 8-bit depth, thresholded using default settings and binary processed as shown in Figure 2.7-18 (a). Patterned cells are represented as black, while white areas represent cell free areas. The example show is of a cell pattern cultured for 72

hrs. For each image the area in pixels with value 1 would be measured using the positive and negative masks. Using the formula below the patterning ratio was calculated:

$$\text{Pattern Ratio} = \frac{(A_{Im+}/A_{M+})}{(A_{Im-}/A_{M-})} \quad (6)$$

Where A_{Im+} represents the total area of pixels counted in the image using the positive mask, A_{Im-} represents the area outside of this, the negative area. A_{M+} and A_{M-} represent the same mask used for the image but with 100% area filled for each case.

A_{Im}/A_M represents the amount of area of the mask covered by the cells. Successful patterning was represented by the a ratio > 1 , (ie more of the area of the electrodes are covered by cells than that outside of the electrodes), while poor to no patterning has a ratio of ≤ 1 . This ratio can be affected by cell concentration however the cell concentration was consistently made to be 1.25×10^6 cells/200 μ L for patterning experiments.

This process was computed for both live and dead fluorescent images.

The mean value of up to 3 images from each sample was calculated using Excel. Control ratio was calculated by averaging the control patterning ratio values for each data set.

2.7.4.3 Results and discussion

2.7.4.3.1 Voltage optimisation

The pattern ratio calculated from the method in 2.7.4.2 and viability of patterned cells as a function of voltage are shown in Figure 2.7-19. It was observed that both live and dead pattern ratios increased with voltage. The electric field was induced for two minutes (10 MHz) at 37 °C . Viability of the patterned cells was observed to be constant as the voltage was increased.

Viability of the cell patterns was confirmed to be 80%. The pattern ratio for voltages of 7 and 8 Vpp was incalculable using the geometric method described in 2.7.4.2 for these voltages. This was because the agar gels had broken during handling thus the pattern was not flat. The error bars for the threshold values arise from the manual alignment of the patterns and random pattern sample selection from the array. Software aided alignment, increased sample size and consistent sampling from patterns would reduce these errors.

It was observed that the ratio of dead cells was higher than that of live cells for all voltages. It is hypothesised that this is because of cells making direct contact with the electrodes. As the simulation results in Section 5.3 show, the electric field is strongest at the electrode edges. The electric field strength at the very edges where the electrodes and counter electrodes are close proximity are in the region of 100 kV/m. It has been observed by *Glasser and Fuhr* that the edges of the electrodes producing an electric field of 58 kV/m increased the temperature by 2 °C.²²³ The measured surface temperature of the patterning volume was 37 °C for these experiments, however as heating was induced by Peltier heaters from below the heat dissipation by the electrodes may have been impaired.

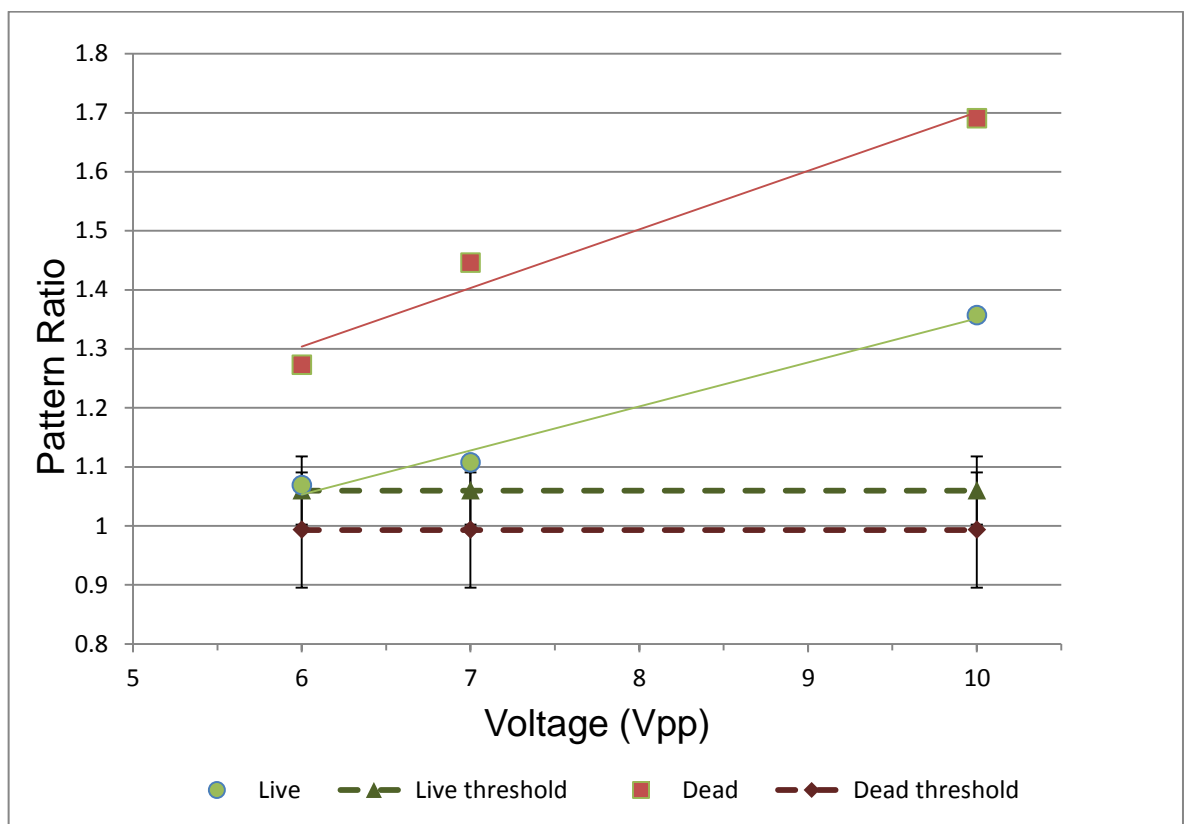


Figure 2.7-19 – Pattern ratio and viability of patterned cells as a function of voltage. Both live and dead pattern ratios were observed to increase with voltage. The electric-field was induced for two minutes (10 MHz) at 37 °C. Viability of the patterned cells was observed to be constant as the voltage was increased. Error bar represents standard deviation of the mean (n = 3).

The voltage used effects the strength of the electric field and thus DEP action on the cells. Ideally the voltage used should be high in order to maximise patterning velocity; this equates to the greatest tolerated applied potential. The rationale is that the transmembrane voltage (V_{tm}) is proportional to applied voltage (V). However, patterning time (t_{pat}) varies by V^{-2} meaning that $V_{tm} \times t_{pat} \propto V^{-1}$ which is a linear measure of total exposure, will minimise exposure at greater applied voltages.²¹⁶ With the setup used the maximum

voltage was 10 Vpp which allowed for maximal patterning time without reducing cell viability.

2.7.4.3.2 *Temperature optimisation*

Control and optimisation of system temperature was critical for successful patterning because of two factors. Firstly mammalian cells ideally are maintained in conditions no greater than 37 °C due to physiological factors. Secondly for the agar in this work to remain in the sol phase a temperature of at least 32 °C must be maintained. These factors restrict the temperature range for the patterning system to 32-37 °C. This range was investigated for patterning reproduction by powering the Peltiers using currents of 0.2, 0.25 and 0.28 A; this induced temperatures of 32, 34 and 37 °C respectively.

The pattern ratio and viability of patterned cells as a function of temperature at the surface of the patterning volume is shown in Figure 2.7-20. Temperature values were measured by infrared camera immediately after removing the cover. Both live and dead pattern ratio were observed to increase with temperature. The electric-field was induced for two minutes (10 MHz, 10 Vpp). Viability of the patterned cells was shown to be stable at 80% across this temperature range. Error bar represents standard deviation of the mean (n = 4).

Patterning ratios for both live and dead were observed to increase with temperature. This is because the agar is entering the gelation stage at lower temperatures.

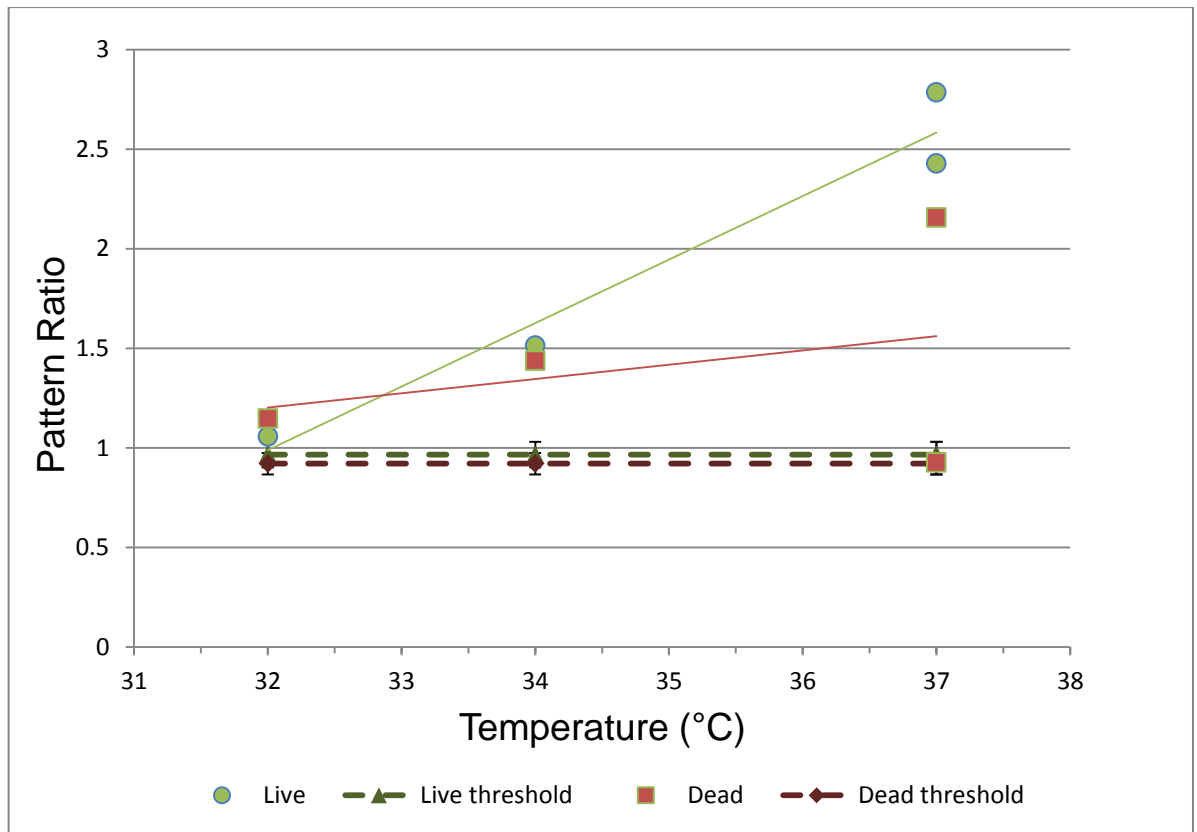


Figure 2.7-20 – Pattern ratio and viability of patterned cells after 24 hrs of culture as a function of temperature at the surface of the patterning volume. Temperature values were measured by infrared camera immediately after removing the cover. Both live and dead pattern ratio were observed to increase with temperature. The electric-field was induced for two minutes (10 MHz, 10 Vpp). Viability of the patterned cells was shown to be stable at 80% across this temperature range. Error bar represents standard deviation of the mean (n = 4).

Results presented by *Nordqvist and Vilgis* showed that temperature change of 5 °C (37 °C to 32 °C) increased the elastic modulus from 200 Pa to 5000 Pa for 1% agar (wt/vol).²²⁴ As observed in Figure 2.7-20 the pattern ratio for both live (1.2) and dead (1.15) cells at 32 °C was only marginally higher than the threshold (0.92±0.05). The pattern ratio for live (2.79) at 37 °C was three times greater than that of the ratio at 32 °C. The lower pattern ratio at 32 °C was because of the increase in viscosity of the agar as it entered the gelling stage. Due to the higher pattern ratio and maintained high cell viability the temperature of 37 °C (0.28 A) was selected for cell patterning.

2.7.4.3.3 Frequency optimisation

The results of the temperature changes near the surface of a drop of agar as a function of electric field frequency are shown in Figure 2.7-21. Measurements were made using an infra-red camera (± 0.09 °C). The black solid line represents the temperature when no AC signal is applied, only the Peltier is heating the system (+0.28 A) to 36 °C. The average temperature over this frequency range was 37.13 °C \pm 0.47.

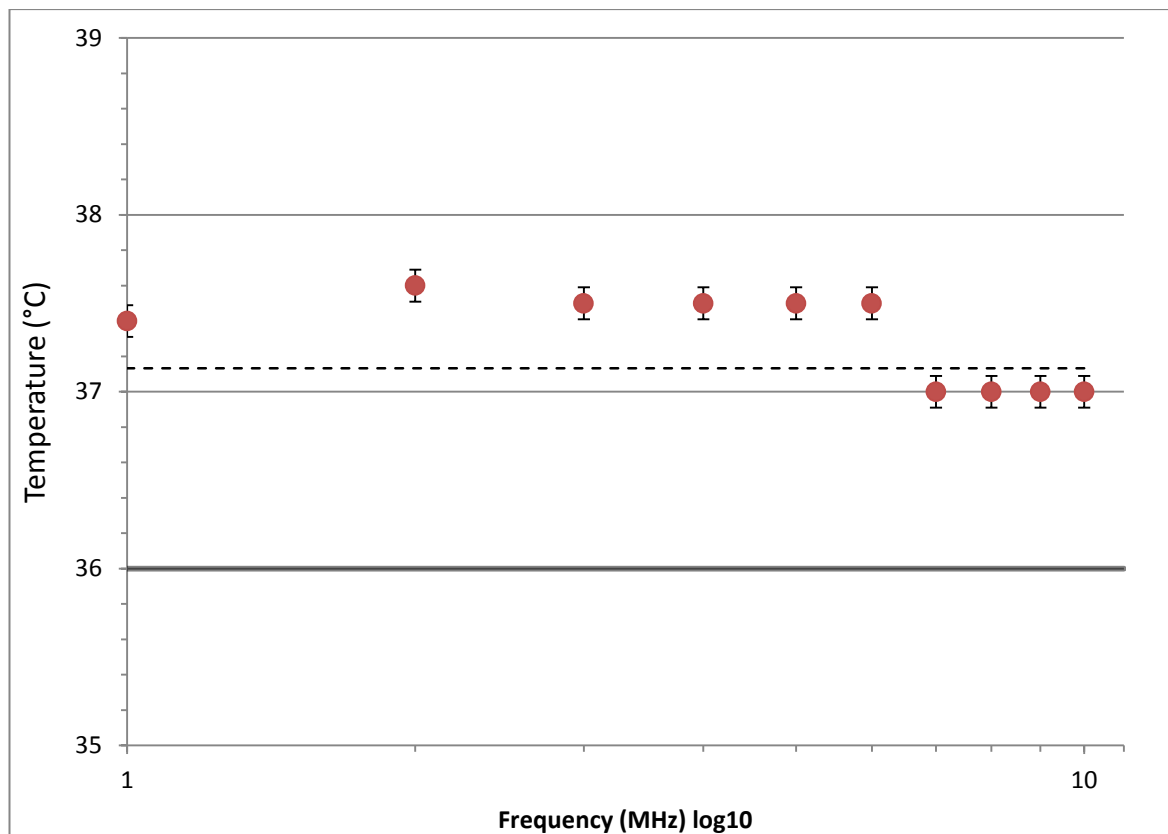


Figure 2.7-21 – Temperature near the surface of the a function of electric field frequency. Measurements were made using an infra-red camera (± 0.09 °C). The black solid line represents the temperature when no AC signal is applied, only the Peltier is heating the system (+0.28 A) to 36 °C. The average temperature over this frequency range was 37.13 °C ± 0.47 . The measured solution was 1% agar, voltage during this sweep was 10 Vpp, buffer conductivity 13 mSm⁻¹. As a result, over this frequency sweep only a 1.24 °C ± 0.33 increase in temperature was detected.

The measured solution was 1% agar (wt/vol) mixed with DEP buffer, voltage during this sweep was 10 Vpp, buffer conductivity 13 mSm⁻¹. As a result, over this frequency sweep only a 1.24 °C ± 0.33 increase in temperature was detected. The frequency for patterning cells was required to induce maximal positive DEP effects as stated in Section 1.6. This was experimentally confirmed by varying the frequency between 1-50 MHz, which identified 1-10 MHz as the optimal range. The crossover frequency took place at about 15 kHz, these results are in agreement with similar studies which also observed that the crossover frequency of HepG2 cells (parent cell line of the HepG2/C3A cell line) to be 15 kHz.²²⁵

However, as the desired temperature of the system was 37 °C an investigation into any possible heating was required. Strong electric fields can cause heating in liquids due to Joule heating; however surface to-volume ratios control heat rejection thus scaling of electrode dimension and droplet volumes reduce heating significantly.²²² This is a major advantage of using microstructures for DEP patterning as there is a very low temperature increase. It has been reported by *Glasser et al* that an average increase of 2 °C in and outside of the cell can be expected at high-frequencies (MHz-range). It was observed that

the temperature increase show in Figure 2.7-21 for frequencies in the range of 8-10 MHz induced a 1 °C rise. Combined with the heating from the Peltier cooler the surface temperature was observed to be 37 °C. This was the ideal temperature for the system due to the physiological requirements of the cells and to maintain the agar in the sol phase during patterning.

Additionally, the patterning ratio and viability of cells over this frequency range was investigated. The pattern ratio and viability of patterned cells as a function of frequency is shown in Figure 2.7-22. Both live and dead pattern ratios were observed to increase with frequency. The electric-field was induced for two minutes (10 Vpp) at 37 °C . Viability of the patterned cells was to shown increase as the frequency was increased. This range of frequencies were selected due to the results observed in Figure 2.7-21. The temperature remained constant from 3-6 MHz indicating that the viability would remain constant over this range. The range of 7-10MHz again was constant while 1MHz and 2 MHz differed. Therefore the selected frequencies for tests were 1, 2, 5 and 10 MHz.

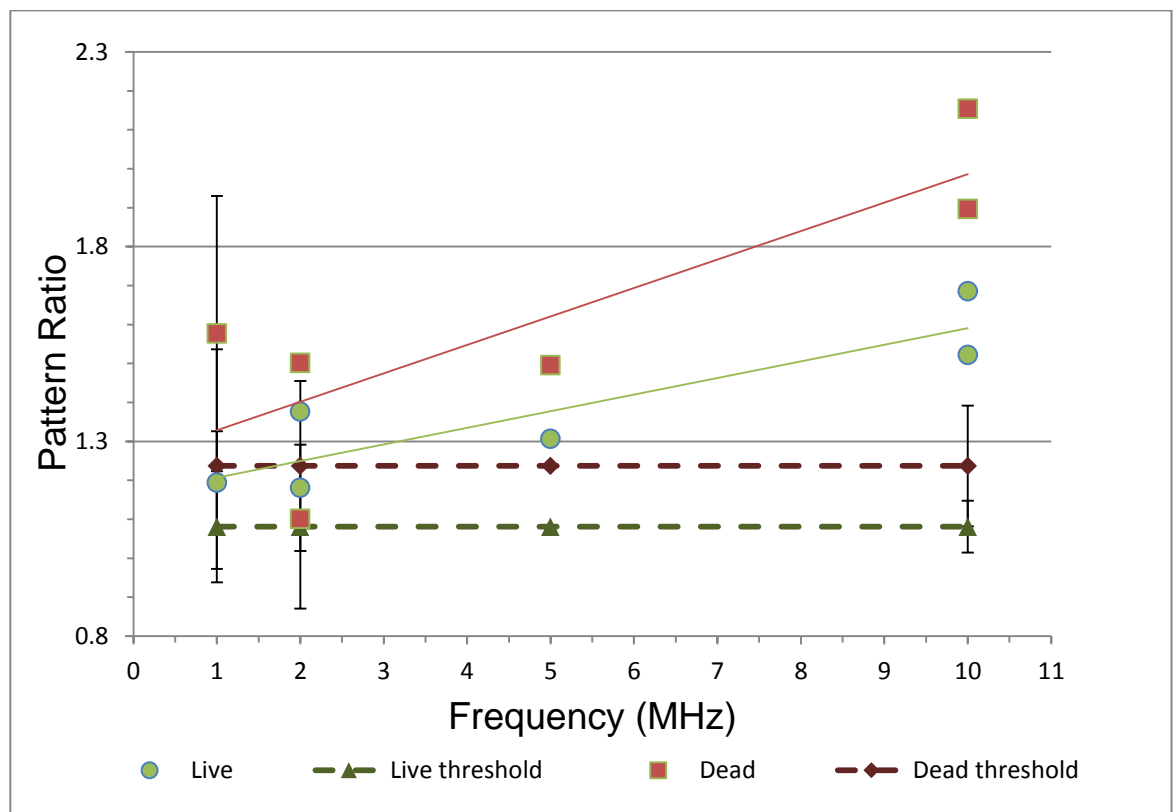


Figure 2.7-22 – Pattern ratio and viability of patterned cells as a function of frequency. Both live and dead pattern ratios were observed to increase with frequency. The electric-field was induced for two minutes (10 Vpp) at 37 °C . Viability of the patterned cells was shown to increase marginally as the frequency was increased. Error bar represents standard deviation of the mean (n = 3).

It was observed that the pattern ratio increased with frequency. This is due to the increase in the real part of the CM factor as discussed previously in Section 1.6. It is hypothesised that the increase in the pattern ratio with frequency for the dead cells was due to the increased positive DEP response. Higher numbers of cells were drawn to the edges of the electrodes which as described previously in Section 2.7.4.3.1 have the highest electric-field strength (100 kV/m^{-1}) in the array. However, the overall viability increased with frequency from 60% viability at 1MHz to 80% at 10MHz. This effect of viability increasing with frequency has been observed by *Glasser and Fuhr*. Over a range of 0.5 MHz to 15 MHz a viability increase from 20% to 75% was shown for electric-field strengths of 80 kV/m^{-1} .²²³ This effect is well understood as the transmembrane potential decreases with increasing frequency.²²¹

2.8 Conclusions

In this chapter the materials and methods used in this thesis have been presented. The techniques used for fabricating microfluidic devices for on chip cell culture have been described. In addition the fabrication of electrodes for dielectrophoresis for cell pattern has been described.

The results from optimisation of the dielectrophoretic liver lobule-like patterning system has been presented and discussed. Fabrication methods were found to be optimal using S1818 photoresist using a 5 second UV exposure. Electrodes designed to pattern hepatocytes into lobule-like patterns were fabricated using these parameters; results of metallisation were found to be suitable for dielectrophoretic patterning. Parameters for successful patterning of liver-like lobule patterns within 1% agar (wt/vol) with a paper substrate were found to be 10 Vpp, 10 MHz, 37 °C (0.28 A) for 2 minutes. Viability was found to be high using these parameters and patterning was observed to be represented of the original electrode design. Methods - Rapid Prototyping

3 Materials and Methods - Rapid prototyping and zebrafish

3.1 Abstract

This chapter describes the materials and methods for zebrafish handling, additive manufacturing methods for microfluidic devices and laser cutting. Further details on microfabrication methods can be found in Chapter 2. The methods for 3D printing microfluidic devices are followed immediately with a short results and discussion.

3.2 Introduction

This thesis was concerned with designing, prototyping and testing *in vitro* devices to augment and reduce animal testing. Through the course of the project a number of different devices, techniques and experiments were designed.

Unless stated all fabrication methods were developed and conducted by the author. 3D printing was conducted by the mechanical workshop at the School of Engineering, University of Glasgow and laser cutting of filter paper at the MAKLab, Glasgow. Additionally, rapid prototyping was performed in the mechanical workshop and BioMEMs laboratory, Auckland University, Auckland, New Zealand. Zebrafish experiments were carried out at the BioMEMs Laboratory, Auckland University, Auckland, New Zealand and Medical Research Council (MRC) Human Genetics Division, Edinburgh, UK.

3.3 Materials

3.3.1 Zebrafish

Wild-type zebrafish *Danio rerio* (AB line) were obtained from Zebrafish International Resource Center (Oregon, Eugene, USA). Experiments using leukaemia integration 1a transgenic zebrafish line (fli1a:EGFP) expressing enhanced green fluorescent protein (EGFP) in the vasculature throughout the development of zebrafish embryos were performed at the School of Medical Sciences, University of Auckland, Auckland, NZ. Adult zebrafish were kept in a 14 hour light, 10 hour dark cycle fish facility and fed twice daily with artemia and once daily with dry feed. Zebrafish embryos were obtained from random pair-wise mating and natural spawning. Collected embryos were maintained in embryo medium E3 and rinsed to remove debris and dead embryos. Embryos were cultured at the optimal temperature of 28.5 ± 0.5 °C in E3 medium and developmentally

staged as described earlier^{226, 227} as well during microfluidic culture experiments. Animal research was conducted with approval from The University of Auckland Animal Ethics Committee (approval ID R661/1).

Zebrafish experiments were also conducted at the Medical Research Council Human Genetics Unit, Edinburgh, UK. Zebrafish line Edinburgh wild type, UK. Animal research was conducted with approval from The University of Edinburgh Ethics Committee.

3.3.2 Rapid prototyping materials

VisiJet® Crystal and VisiJet® S300 Support Material supplied by 3D Systems, Australia. WaterShed XC 11122 supplied by Somos, Australia. Dreve Fototec 7150 Clear was supplied by Dreve Otoplastik GmbH, Germany. 3D printing Acrylonitrile butadiene styrene (ABS) 655 cm³ rolls were obtained from Solutions 2 Enterprise, UK. Poly-methyl methacrylate sheet (PMMA/Acrylic) in 3, 4.5 and 6 mm thicknesses were supplied by PSP Plastics Ltd, Auckland, New Zealand for laser cutting.

S300 support material was removed using a Thermotec 2000 oven supplied by Contherm, New Zealand and E 60H Elmasonic bath, Elmasonic, Germany. MF1 pump head, PVC calibrated tubing (1.02 mm ID) and Gilson Minipuls evolution were supplied by Gilson Inc, Middleton, USA for cleaning microfluidic chips. 1/16" polyurethane tubing was supplied by Cole-Parmer Instrument Company, Illinois, USA.

P1500 and P2000 sandpaper was supplied by Norton Saint Gobain, Paris, France and Diamond paste, 9 µm was supplied by Boride, Traverse City, US for polishing microfluidic chips.

3.4 General Methods

3.4.1 Additive Manufacturing

In this work three rapid prototyping machines were used. The Hewlett-Packard(HP) DesignJet (University of Glasgow, Scotland, UK), 3D Systems HD3500 Plus (Auckland University, New Zealand) and Viper Pro (Plastic Design Technology, Auckland, New Zealand) additive manufacturing machines. Each printer uses different processes to form 3D printed objects, the details of which are listed below in Table 3.4-1. All printers were selected from the current professional market pictured in Figure 3.4-1. It was important to only use current off the shelf technologies in order meet the goal of reducing the need for expensive microfabrication facilities for microfluidic devices.

The HD3500 Plus professional 3D printer (HD3500+) used multi-jet modelling (MJM) method to fabricate microfluidic devices and culture dishes with VisiJet Crystal material. The Viper Pro SLA System (Viper Pro) used the stereolithography (SLA) method to fabricate microfluidic devices and culture dishes using Watershed 11122XC and Dreve Fototec 7150 Clear. The HP DesignJet 3D printer used the fused deposition moulding (FDM) method to fabricate culture dishes and prototype elements for experimental setups.

Models were printed and processed according to the operating manuals as per machine using the appropriate software unless otherwise stated.

3.4.1.1 3D design

2D and 3D CAD drawing was completed in SolidWorks 2011 x64 (Dassault System SolidWorks Corp, Concord, MA ,USA), completed .stl files were verified using SolidEdge (Siemens PLM Software, UK). Completed .stl files were then processed by HP Designjet 3D Software Solution for the HP DesignJet, ProJet® Accelerator Software for the HD3500+, and 3DManage™ and 3DPrint™ for the Viper Pro.

3.4.1.2 Post processing – HP DesignJet

Devices printed using the DesignJet HP cleaned using the HP Removal kit system. This required the parts to be left in a water bath at 60 °C with a mixture of sodium: percarbonate, carbonate and bicarbonate with DI water. Once the cycle was completed (3-12 hrs depending on model size) they were removed from the solution, rinsed in water and dried with paper towel.

3.4.1.3 Post processing – Viper Pro

Devices printed using the Viper Pro system were processed by Plastic Design Technology, Auckland, New Zealand.

3.4.1.4 Post processing – HD3500+

Devices printed using the HD 3500+ were detached from the printing tray by being placed at 4 °C for 2 minutes. This caused the support wax to harden making it easy to remove the models from the tray by hand. Models were then placed in an oven (Thermotec 2000, Contherm, New Zealand) at 70 °C causing the wax support to melt. Depending on the thickness of wax support material and geometry 15-30 minutes was sufficient to remove the bulk of the wax. To accelerate the process a small spatula or cocktail stick was used to remove larger areas of softened wax after 5 minutes.

Table 3.4-1 – List of additive manufacturing machines used in this project with main specifications.

Machine	Manufacturer	Technology (print mode)	Accuracy (μm)	Layer thickness (μm)	Material
HD3500+	3D Systems	MJM (HD)	50	32	VisiJet Crystal (USP Class VI), VisiJet S300
		MJM (UHD)	25	29	
		MJM (XHD)	25	16	
Viper Pro	3D Systems	SLA	25	50	Watershed 11122XC Dreve Fototec 7150 Clear
DesignJet	Hewlett Packard (HP)	FDM	120	254	ABS

Once the majority of the wax support had been removed models were submerged into canola oil and sonicated using an ultrasonic bath (E 60H Elmasonic) at 55 °C for 10 minutes. Models were then removed from the ultra-sonic bath and allowed to cool at room temperature to allow optical transparency to return to the model. Following this, models were rinsed in warm soapy water. For optimal transparency, particularly of larger models, they would be placed in an oven at 60 °C for 10 minutes. The oven was then switched off and allowed to cool for 1 hour letting the models cool slowly. If cooled rapidly the thermo-polymer VisiJet Crystal would form misty, crack like defects in the model impairing the optical quality.



Figure 3.4-1 – Photographs of 3D printers used in this thesis. (a) The HD3500 Plus professional 3D printer (HD3500+) used multi-jet modelling (MJM) method to fabricate microfluidic devices and culture dishes with VisiJet Crystal material. (b) Viper Pro SLA System (Viper Pro) used the stereolithography (SLA) method to fabricate microfluidic devices and culture dishes using Watershed 11122XC and Dreve Fototec 7150 Clear. (c) HP DesignJet 3D printer fused deposition moulding (FDM) method to fabricate culture dishes and prototype elements for experimental setups. All scale bars are 0.5 m.

3.4.2 Laser cutting

3.4.2.1 PMMA

Prototyping and fabrication was performed using a non-contact, 30 W CO₂ laser cutting system equipped with High Power Density Focusing Optics (HPDFO)TM (Universal Laser Systems, Scottsdale, AZ, USA). Parts were cut in various thicknesses of PMMA 3, 4.5 and 6 mm thicknesses.

3.4.2.2 Filter Paper

Laser cutting of paper was completed using a GCC Laserpro Spirit Laser engraving / cutting machine. The cutting of the filter paper would cause it to stick to the substrate due to additives in the paper. Thus 200 µm aluminium would be placed underneath the filter paper; then when completed scrapped off gently using a metal ruler. Low power and an increase of the outer diameter were used to ensure the correct sizing of the paper rings. In addition, to ensure that that paper did not lift during the cutting due to the air jet cooling the flow rate of the cooling was reduced to the minimum setting.

3.4.3 Imaging and data analysis of zebrafish

For studies carried out at BioMEMS Auckland, general stereoscopic images of embryos grown on chip-based devices were obtained using the Leica MZ7.5 stereomicroscope from Leica Microsystems, Wetzlar, Germany. Stereoscopic fluorescence images were taken using a Nikon SMZ1500 from Nikon, Japan. For studies completed at MRC, Edinburgh, general stereoscopic images were collected with a Nikon SMZ1500 and Nikon E5400 Coolpix camera from Nikon, Japan. Data analysis of collected images was completed using the Leica Application Suite (LAS)(Leica Microsystems) and ImageJ.¹⁹⁴

3.5 Additive manufacturing for microfluidic devices

3.5.1 Chip Design

The monolithic microfluidic chip was designed and modelling using SolidWorks 2011 CAD package. Fabrication was completed according to the methods described in Section 3.4.1.4. The design of the microfluidic serpentine embryo array device was adapted for printing using the HD3500+ on XHD (750 x 750 x 1600 DPI (xyz); 16 µ layers) with VisiJet Crystal to achieve 16 µm layers and Viper Pro using Watershed 11122XC (Watershed) material Figure 3.5-2. A lid was designed to be 500 µm thick allowing for optical clarity and also allowed for material to be removed during the polishing process to

be non-detrimental. The design of different nozzle designs to achieve a fluidic seal with tubing is shown in Figure 3.5-1. These designs were based on the range of fluidic connectors distributed by Cole-Parmer (Small barbed fittings kit. 30612-03).

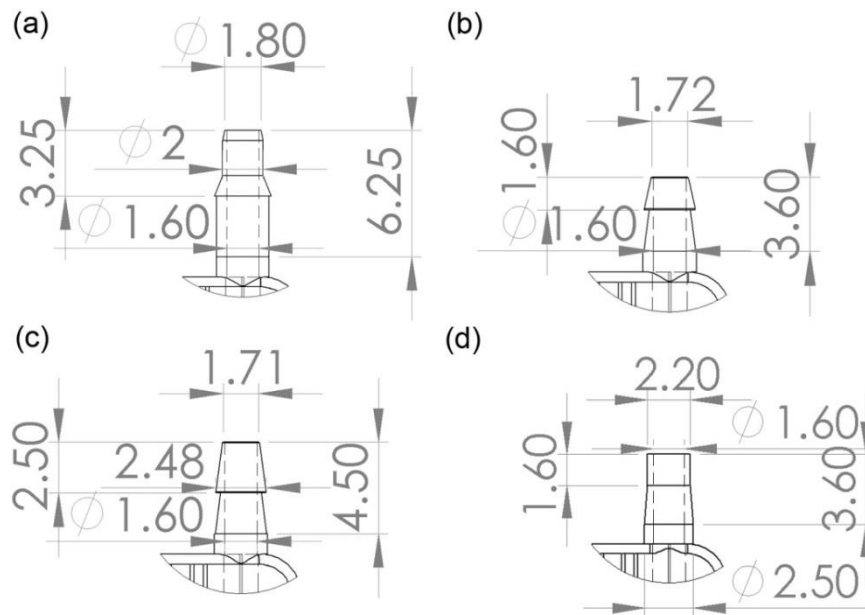
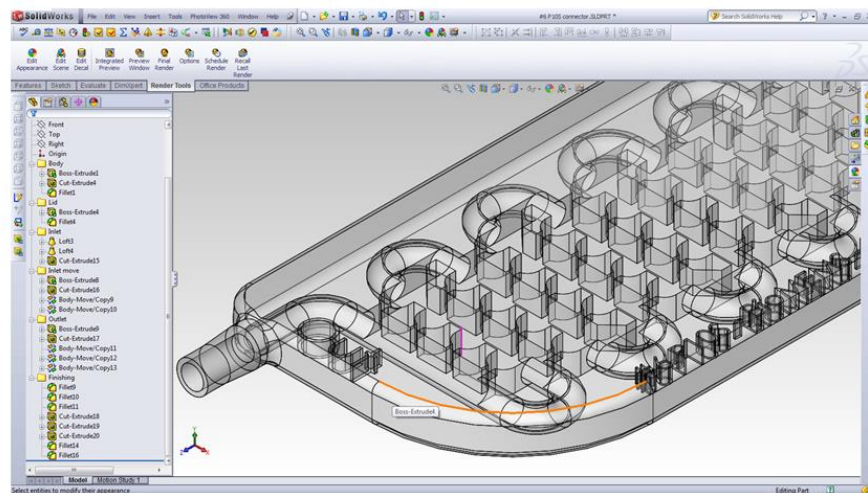


Figure 3.5-1 – 2D CAD sketches of four connector types designed for the 3D printed chip. a) Large connector with a 1.9 mm ID and 2.0 mm OD b) same shape as 1a but with a 1.6 ID and OD of 1.8 mm. c) Different shape and design with a more flanged top ID 1.6 mm OD 1.8 mm d) Final design with a ID 1.6 mm and OD 2.2 mm. 300 μ m thick sidewalls stopped the connectors from breaking off from repeated connections to the tubing.

a)



b)

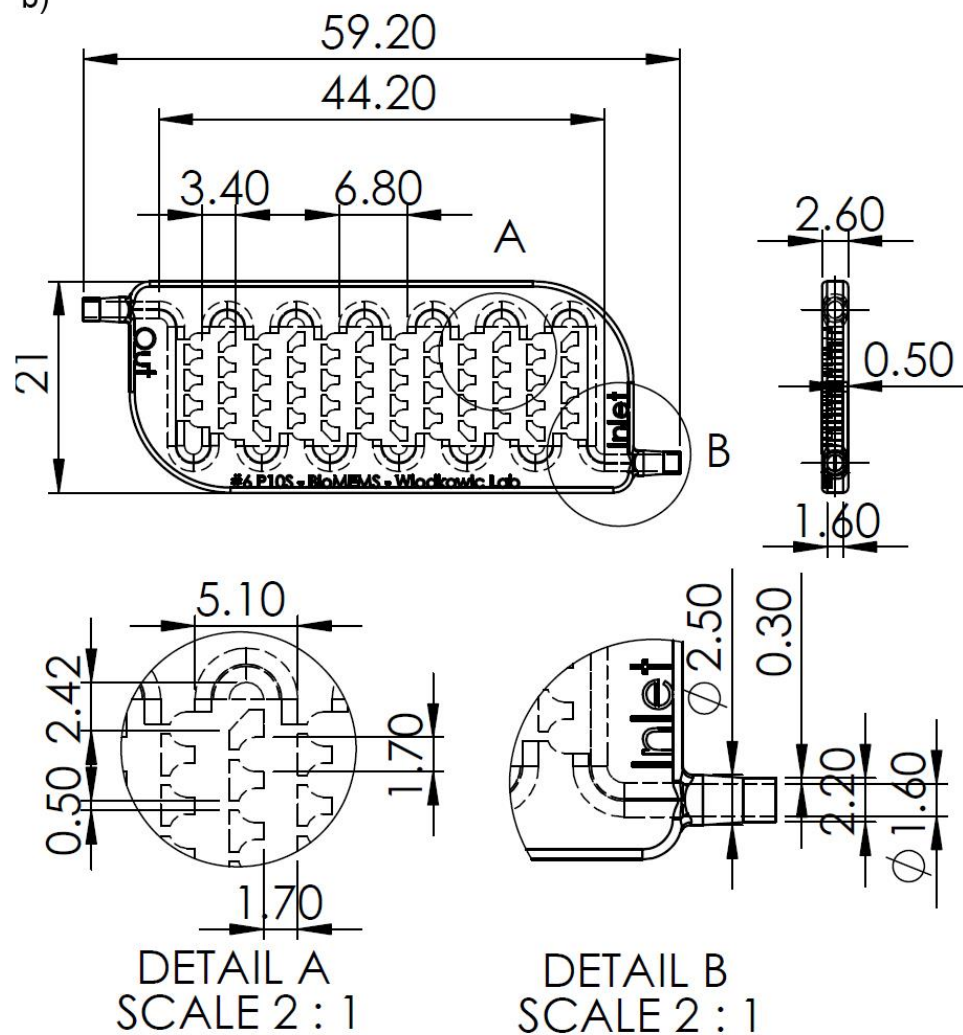


Figure 3.5-2 – Image showing design of microfluidic embryo array chip for automatic trapping and immobilisation of zebrafish embryos. (a) SolidWorks CAD package used to design the chip. (b) 2D rendered image showing the x-y profile of the chip. Detail A shows the trapping area and Detail B shows the connector. This is a monolithic design as the lid and connectors are included in the fabrication process and hence are not added to the device in a later stage of manufacture.

3.5.2 Post processing of microfluidic chips

The method for post-processing microfluidic chips printed using the HD 3500+ required additional steps as shown in Figure 3.5-3 to the description in 3.4.1.4. Following detachment from the printing tray by placing it at 4 °C for 2 minutes Figure 3.5-3(a), chips were then placed in an oven at 70 °C causing the wax support to melt. It was advantageous to angle the chips vertically aiding liquid wax to flow out of the channels Figure 3.5-3(b).

Once the majority of the wax support had been removed chips were submerged into canola oil and sonicated using an ultrasonic bath at 55 °C for 10 minutes Figure 3.5-3(c). Canola was selected due to having a low viscosity than that of the wax; wax would separate and collect at the surface of the oil. To remove wax from channels a peristaltic pump with was connected to the inlet channel using 1/16" polyurethane tubing.

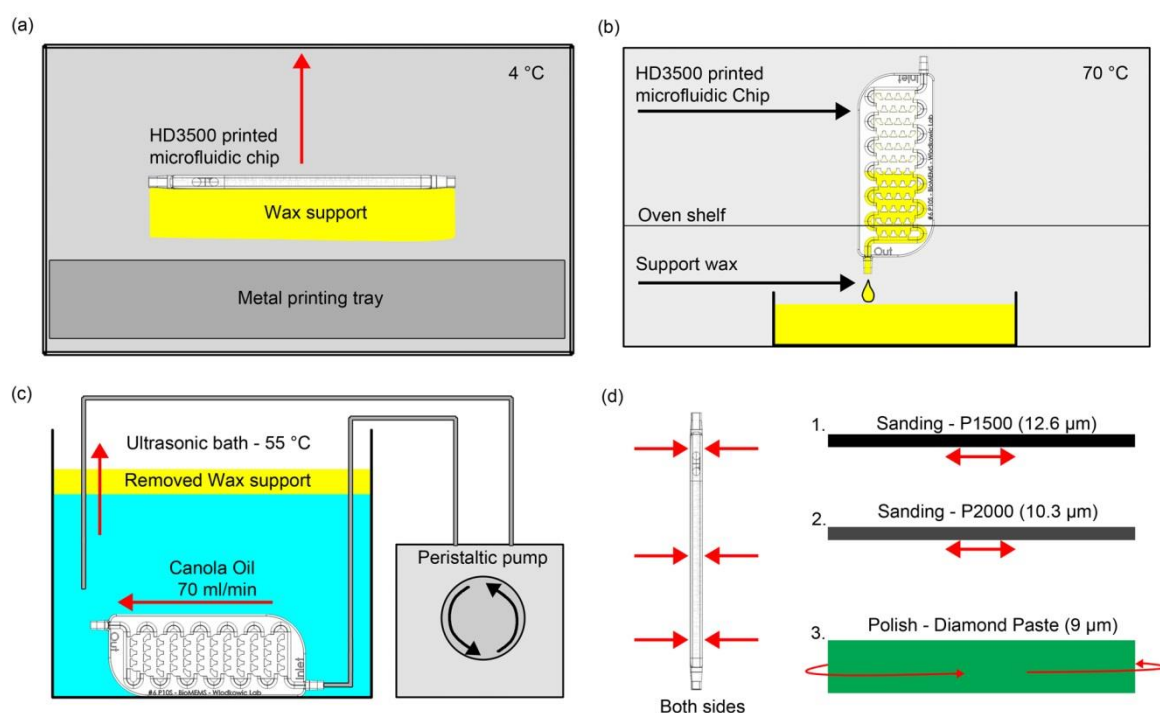


Figure 3.5-3 – HD3500+ printed monolithic microfluidic device post processing steps – This figure shows the development process required to fabricate 3D printed devices using an HD3500+ pictured in the centre (a) The device was removed from the metal printing tray. This requires cooling to allow the support wax to detach from the tray. (b) Printed devices were then placed upright in an oven at 70 °C allowing the bulk of the support wax to melt and drain out of the material. To remove remaining material the devices were placed in an ultrasonic bath at 55 °C, filled with cannoli oil. Fluidic channels were cleared of support material by connecting 1/16" polyurethane tubing flexible tubing to the connections and using a peristaltic pump melted wax was flushed out for 5 minutes. This was performed in both directions to aid removal; (4) Optical quality of the device was improved by high-grit sandpaper P1500, followed by P2000 and finally buffed using 9 μm polishing paste and soft, cylindrical modelling head using a head. The device was finally washing in warm soapy water to remove residual polish and pumped through with DI water to complete the process.

Using the max flow rate at 70 ml/min oil would be pumped through the chip for 5 minutes with sonication in both directions Figure 3.5-3(c). This removed almost all wax from the interior channels of the chip.

Following cooling chips were rinsed in warm soapy water. Channels were then rinsed with soapy water using the pump for 5 minutes to flush out oil and remaining wax.

In order to achieve a higher optical quality polishing of the 3D printed model surfaces was required illustrated in Figure 3.5-3(d). By using successive use of fine grit P1500 and P2000 followed by diamond paste polishing, 9 μm (BORIDE, Traverse City, MI, USA) with high-quality modelling heads using a hand dremel.

3.5.3 Micro Analysis Platform (μAP) Design and Construction

In order to integrate imaging functionality, positioning of the microfluidic chip and lighting system the μAP was designed and built as shown in Figure 3.5-4. The base of the platform was laser cut using 6 mm poly-methylmethacrylate sheet 4.5 mm was used for the chip holder and spacers, 6 mm for the metal reflector, all other PMMA parts were cut from 3 mm sheets.

The chip holder was detachable from the platform to aid chip preparation. The stand for the MS34B-R2 Dino-Lite was designed in SolidWorks and printed using the HD3500+ on HD mode (375 x 375 x 790 DPI (xyz); 32 μm layers). This allowed the 5 megapixel polarisation Dino-Lite microscope (AD7013MZT Dino-Lite Premier microscope, AnMo Electronics Corp, Taiwan)²²⁸ to be securely attached to the platform for live zebrafish imaging.

Finally the platform was assembled using M2x10, M2x12, M3x10 and M3x16 bolts and nuts. A laptop installed with DinoCapture 2.0 was used to capture time-lapse microphotography.

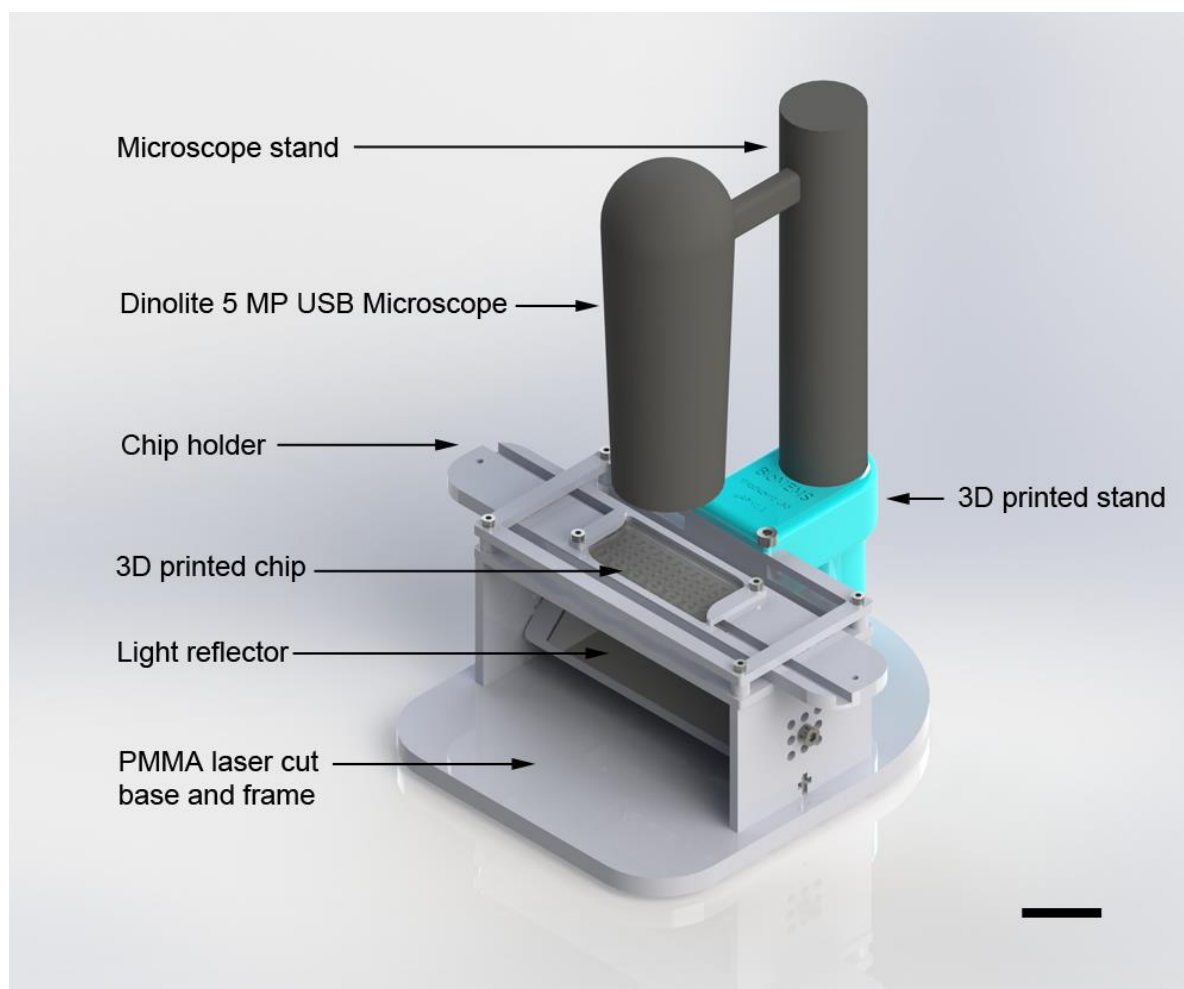


Figure 3.5-4 – 3D rendered image of the micro analysis platform. The system consisted of a PMMA laser cut frame connected with nuts and bolts. A polished steel metal light reflector was attached by two 3M bolts allowing for rotation around the axis. This allowed for adjustment of the bottom lighting solution. The 3D printed chip was held in place by a laser engraved PMMA piece with small clips to keep the chip fixed when tubing was attached. A 3D printed stand was attached to the PMMA base to which the microscope stand could be fitted securely with a screw bolt (not rendered). Scale bar is 20 mm.

3.5.4 Results and discussion

3.5.4.1 Surface quality of 3D printed materials

It was observed that the surface finish of the VisiJet Crystal, printed by the HD3500+ models were rough with distinctive visual qualities Figure 3.5-5. SEM image in Figure 3.5-5(a) shows a close up of an engraved “D” the thickness of the “D” being 200 μm . No wax support material was used in this model. However debris material is present in the engraved area designed to be 500 μm deep. Stitching lines seen as horizontal lines tracking across the surface, were observed on the surface of the “D” as this surface was in contact with the printed base. The printed edge of the “D” exposed shows layers of a material 16 μm thick. A close up of this edge in Figure 3.5-5(c) shows the organic and irregular

surface texture of the printed layers. No holes or gaps in the material were observed indicating that the material is suitable for retaining fluids. Thread line structures can be seen protruding from the surface of the material in the region of 100 nm in diameter.

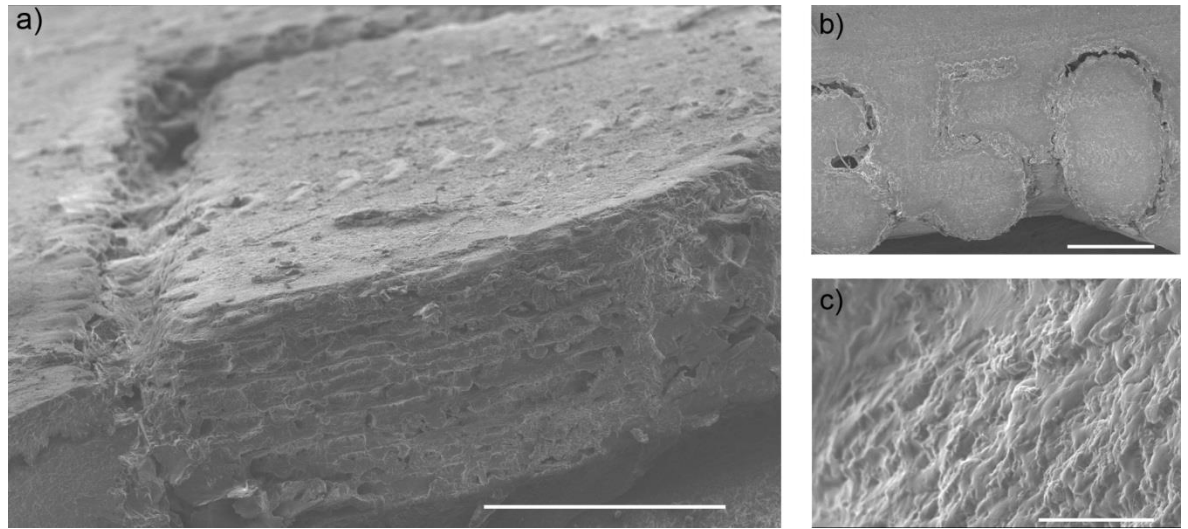


Figure 3.5-5 – SEM images of HD3500 printed discs with VisiJet Crystal material. (a) Image of printed engraved “D” from a side on perspective. Scale bar 500 μm . (b) Top view of printed engraved text reading “350”, stitch marks are observed across the surface. Scale bar 1 mm. C) Close up of “D” showing texture of layers used to form the model. Scale bar 20 μm .

Models printed by the Viper Pro using Watershed material are shown in Figure 3.5-6. The SEM image in Figure 3.5-6(a) shows the engraved letters ‘Vip’ in the surface of the disc. The dot of the ‘i’ has merged with the top right hand feature of the ‘V’. The designed spacing between them is 280 μm . This illustrates the limitations in close-proximity of small features of printing with Viper Pro. Shown in Figure 3.5-6(b), the layers from each build step are visible. Each layer blends with neighbouring layers in a smooth finish, ridges are seen when the layers meet. Compared to the surface characterisation of the HD3500+ printed VisiJet Crystal the finish is smooth with little or no debris. Further examination inside of the surface shows that the surface quality has a texture in the nm range Figure 3.5-6(c).

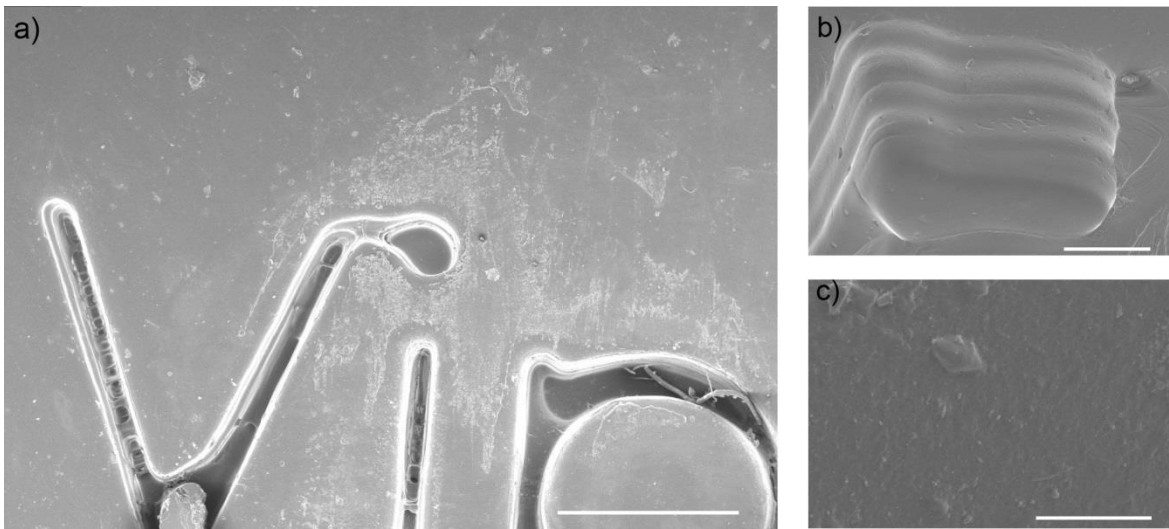


Figure 3.5-6 – SEM images of Viper Pro printed discs with Watershed material: A) Low magnification image showing engraved lettering. B) High magnification of interior of engraved letter. C) High magnification of engraved letter.

A comparison of surface quality of the VisiJet Crystal printed by the HD3500+ and Watershed by the Viper Pro is shown in Figure 3.5-7. The Watershed was observed to have a smoother surface finish than the VisiJet Crystal. Edges of the Watershed disc were rough compared to the rest of the surface. Randomly distributed marks and chips can be seen on the surface. The VisiJet Crystal in addition to the stitch marks had a lined texture on the edges of the disc.

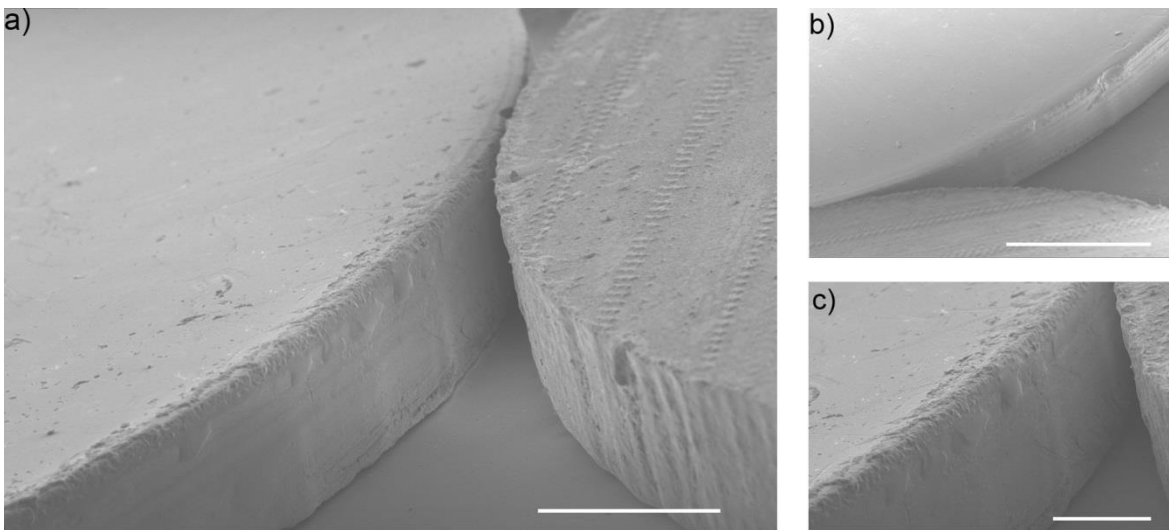


Figure 3.5-7 – Comparison of SEM images of Watershed and VisiJet Crystal surface profiles. A) Watershed (left) next to VisiJet Crystal (right) printed disc. Watershed had a smooth surface profile with rough edges. VisiJet Crystal had a rougher surface with stitch lines every 500 μm , edges were sharper than the Watershed but lines appeared in the sidewalls of the disc. Scale bar 1mm. B and C) higher magnification showing detail. Scale bars 2 mm and 500 μm respectively.

3.5.4.2 Fabrication and optical quality of microfluidic chips

Assessment of the optical quality and feature reproduction of both VisiJet Crystal and Watershed materials was investigated. This was an important consideration as optical transparency was critical to develop the chips for optically based assays. Microfluidic zebrafish trapping devices were fabricated with the HD3500+ (VisiJet Crystal) and Viper Pro (Watershed) systems shown in Figure 3.5-8. The chips were printed as monolithic models the smallest relevant feature of the model was the suction channel between the zebrafish traps. The suction channel designed to be 500 μm in width was reproduced by the HD3500+ using XHD mode averaging 506 \pm 8 μm .

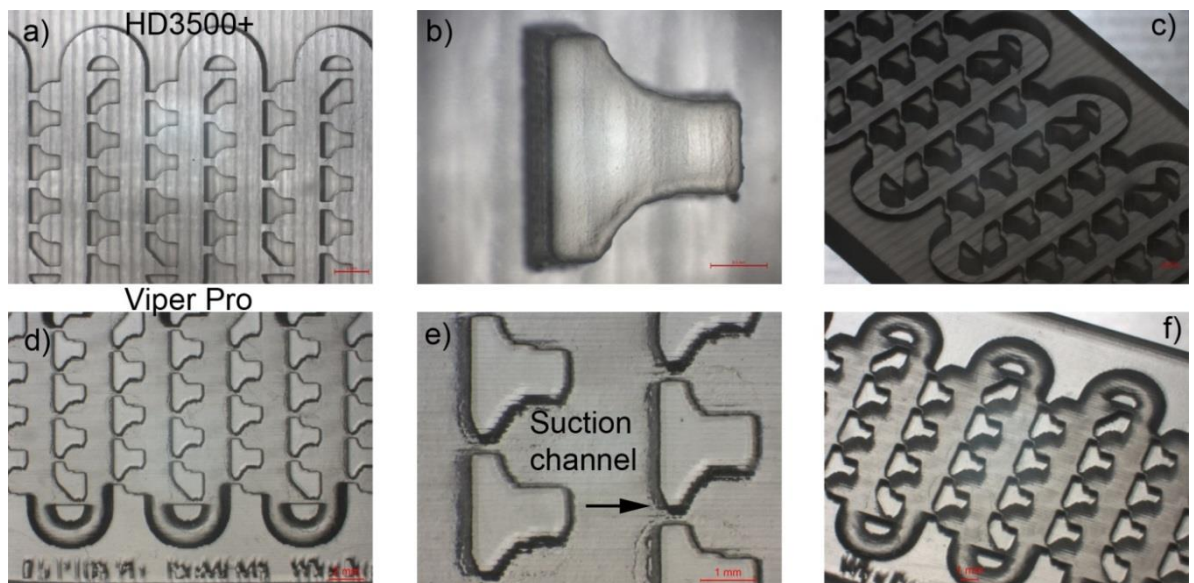


Figure 3.5-8 – Stereomicroscopy of 3D printed zebrafish traps. A-C) Uncovered HD3500+ fabricated zebrafish trap model showing definition of trapping features and channels. Scale bars are 2, 1 and 1 mm respectively. D-F) Enclosed Viper Pro fabricated zebrafish trap model, showing definition of trapping features and channels. Scale bars are 2, 1 and 1 mm respectively.

When reproduced by the Viper Pro it averaged 370 \pm 39 μm . Stitch marks can be seen running vertically through the material repeating every 1 mm Figure 3.5-8(a), this was present on the opposite side of the traps. This was a required part of the printing process providing increased friction between the bottom of the model and the printing tray. Traps and channels were produced with few defects by the HD3500+ as can be seen in Figure 3.5-8(a-c). Models produced by the Viper Pro showed a scanline pattern running through the model horizontally, repeating every 100 μm Figure 3.5-8(d-e). Trap reproduction had a rougher finish due to the scanning nature of the SLA system Figure 3.5-8(e).

The HD3500 Plus professional 3D printer (HD3500+) was selected to develop monolithic 3D printed chips for zebrafish sorting. This printer was selected for two reasons. 1) It had the technical specification which allowed accurate parts in the micro meter range in the x-y

axis (25-50 μm) and z-axis (16-32 μm). The HD3500+ can be selected to print at three different resolutions: High definition (HD) 375 x 375 x 790 DPI (xyz), 32 μ layers; Ultra high definition (UHD) 750 x 750 x 890 DPI (xyz), 29 μm layers and Extreme High Definition (XHD) 750 x 750 x 1600 DPI (xyz); 16 μm layers. Minimum feature size for the zebrafish device was in the order of 500 μm meaning that the HD3500+ could achieve the designed features ; 2) Transparent material VisiJet Crystal allowed for optically transparent parts to be fabricated facilitating *in vitro* observation by microscopy.

The Viper Pro SLA System (Viper Pro) shown in was also selected for fabricating monolithic zebrafish trapping devices. Properties that made the Viper Pro suitable for this project were: 1) Accuracy in the x-y (25 μm) and z-axis (50 μm) made it possible to build the minimum features of the zebrafish device (500 μm). 2) The Viper Pro can use a range of different materials, including the clear photopolymer, Watershed 11122 XC (Watershed).²²⁹ Watershed has a clear engineered plastic finish making it ideal for fabricating microfluidic devices for zebrafish trapping.

3.5.4.3 Effect of chemical exposure on optical quality

The VisiJet Crystal material used in this work was highly sensitive to organic solvents. Exposure to acetone dissolves the material, while methanol and IPA in high concentrations will cause the material to whiten. This effect was also present when exposed to EtOH however in a low enough concentration 50% or below, there appeared to be no negative effects on the optical quality. Figure 3.5-9 demonstrates the effects of 40, 50 and 60% EtOH with DI water on optical quality respectively.

Photopolymers are typically composed of three components: a photosensitive compound, a base resin, and an organic solvent. It is accepted that trace amounts of solvents will be present after polymer cross-linking as described in a study by Ye *et al.*²³⁰ They observed that the photopolymer BisGMA/TEGDMA would rapidly decrease in mechanical strength for concentrations of ethanol greater than 50 wt %, which confers with the results found in this study.

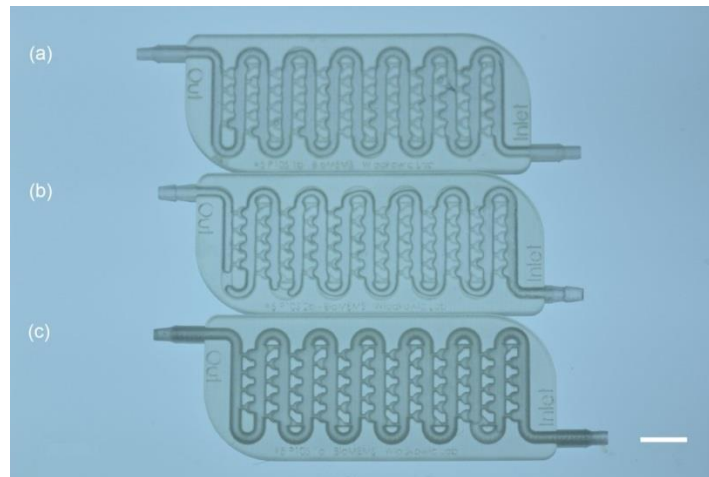


Figure 3.5-9 – Effect of EtOH on optical quality of VisiJet Crystal material – This figure shows 3 chips with identical fluidic channels but with different connectors. Each had EtOH:DI water of varying concentration pumped through them with a peristaltic pump, (a) 40%, (b) 50% and (c) 60%. The optical quality of the channels has remained unaffected in (a) and (b) but in (c) the EtOH has reacted with the VisiJet Crystal polymer, darkening the channels. With increased concentrations of EtOH the material distorts further to the point of being opaque white. Scale bar 10 mm.

3.5.4.4 Nozzle design optimisation

HD3500+ fabricated nozzles in VisiJet Crystal using the designs Figure 3.5-1 are shown in Figure 3.5-10. Features of the nozzles were reproduced within the accuracy of the machine $\pm 25 \mu\text{m}$. All designs provided sufficient fluidic seals at high flow rates (70 ml/min).

Nozzle 1a shown in Figure 3.5-10(a) was shown to be the most robust of the three designs. It used a 2.8 mm flange and 2.6 mm neck. Nozzles 2a and 2b Figure 3.5-10(b)-(c) used a 2.5 mm flange with 2 mm neck and repeatedly broke after removing tubing from the 3D printed chips.

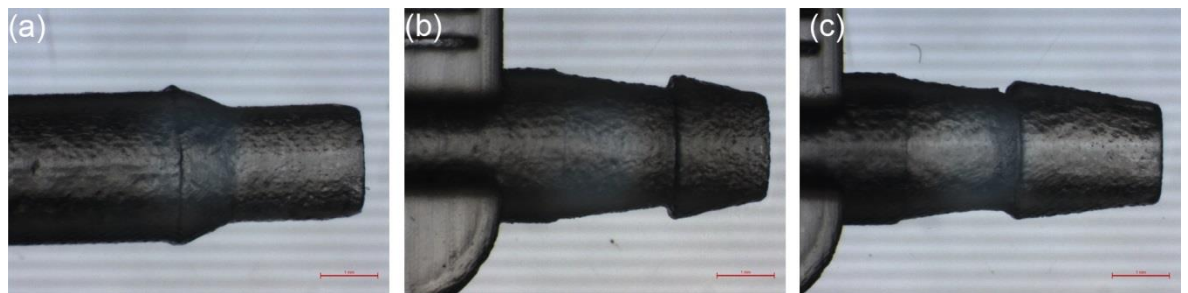


Figure 3.5-10 – Stereomicroscopy photographs of three nozzle designs fabricated using the HD3500+ with VisiJet Crystal. Inner diameter was kept constant throughout the designs (a) Nozzle 1a (b) Nozzle 2a (c) Nozzle 2b

However the 1a nozzle design was also prone to breaking due to repeat disconnections from tubing. A simplified design without a flange neck shown in Figure 3.5-11, this design was found to provide a fluidic seal at 70 ml/min and not break through repeated reconnections of tubing.

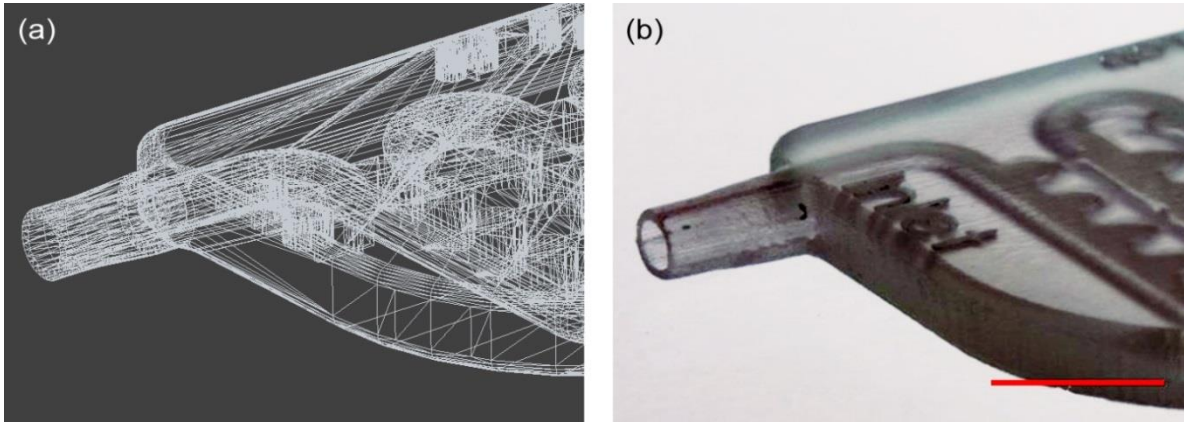


Figure 3.5-11 – Design of the final nozzle – (a) Computer render of the device with the nozzle showing triangle edges. (b) Photograph of the device with final nozzle design fabricated using the HD3500+ with VisiJet Crystal. Scale bar 500 μm .

3.5.4.5 3D model resolution parameter adjustment

3D models designed in Solidworks were exported for printing with the HD3500 Plus and Viper Pro. The resolution of the file (.stl) depended on the tessellation of the surfaces of the model which in turn affected the outcome of the 3D printed model. This can be adjusted by altering the deviation which controls whole-part tessellation and the angle which controls smaller detail tessellation. Lower numbers of deviation and angle generate higher accuracy models but are larger in size and slower to generate.

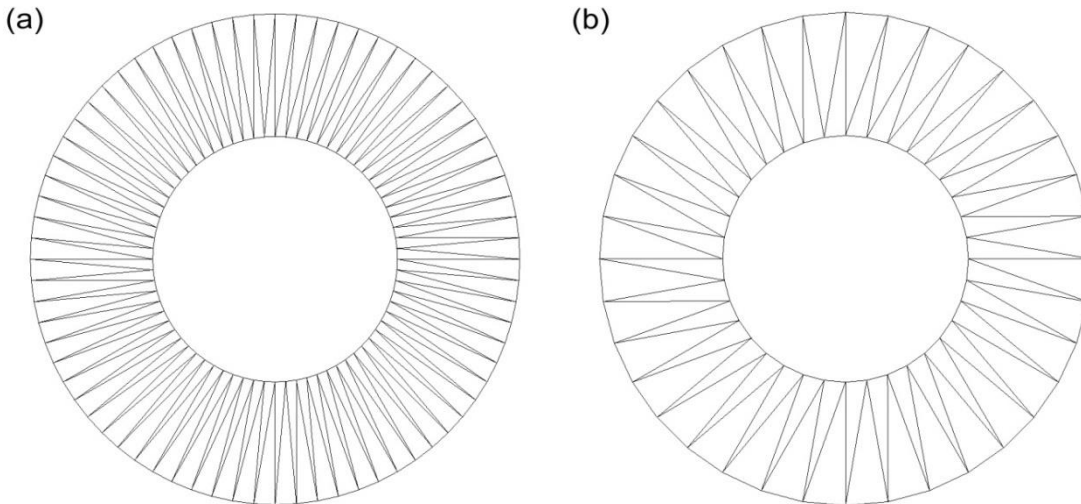


Figure 3.5-12 - Changes to tessellation by altering the angle and deviation tolerances. The figure shows wireframe rendered 3D cylinders (OD, ID = 3, 1.5 mm) after processing to .stl format for printing. (a) Resolution parameters - deviation tolerance 0.002, angle tolerance 5. Tessellation resolution was high formed by 576 triangles and resulting file size of 28884 Bytes. (b) Resolution parameters - , deviation tolerance 0.0129, angle tolerance 10. Tessellation resolution was low having only formed the model with 288 triangles and resulting in a file size of 14484 Bytes. This resulted in flat spots for representing curves in the model.

Essentially, faceting, or flat spots on the finished file would appear if the resolution was low. By inspecting the finished file using SolidView the .stl was checked for faceting and to ensure the part appeared as designed by looking for excessive flat spots on curves and contours. An example of this can be seen in Figure 3.5-12.

The effect of changes in resolution by altering angle and deviation of MJM printed parts was investigated Figure 3.5-13. For changes of angle, the deviation remained constant at 0.02 and for deviation, the angle had a constant of 10. These values were selected to give a high quality mesh while leaving room for increased tessellation. Measurements of the resulting model (a cylinder 3 mm long, OD 3 mm, ID 1.5 mm) from MJM printing showed that even with course deviation there was little variation in the model. Changes in the angle caused inaccuracy in the ID by $1.54 \text{ mm} \pm 0.06 \text{ mm}$, as the angle decreased.

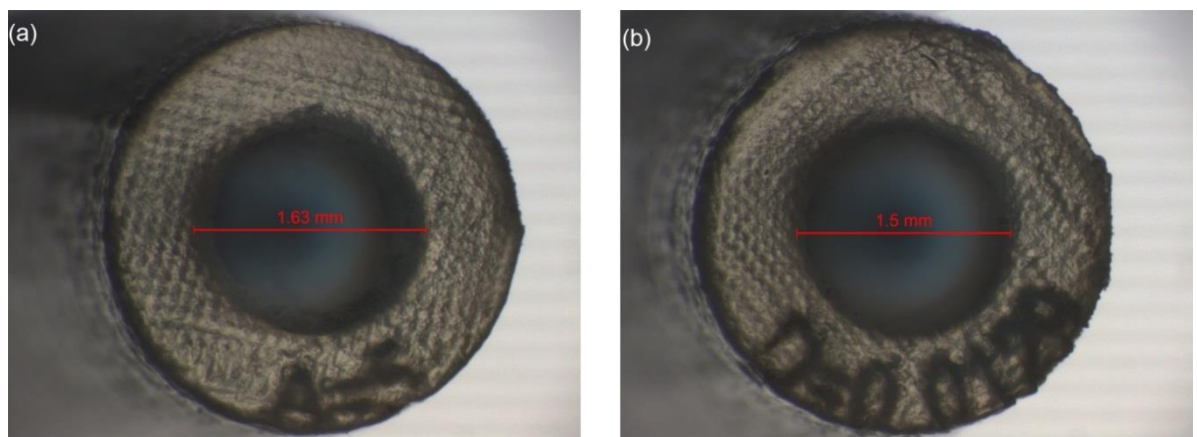


Figure 3.5-14 – Effect of changes in resolution by altering angle and deviation of MJM printed parts – (a) Micrograph showing top surface of a 3D printed cylinder (OD, ID = 3, 1.5 mm). Deviation constant is 0.02, the angle has been changed to 5. This has resulted in a finer surface finish but has over smoothed the opening of the cylinder to make the ID 1.63 mm, rather than the designed 1.5 mm. (b) using the same design, here the angle has remained at 10, the deviation is 0.0129. The surface quality is lower than when lower angle values are used but the ID was measured to be 1.5 mm as designed.

It was found that the change in angle tolerance had more effect on the accuracy of the model compared to changes in deviation. The values of 0.002 for deviation and 5 for angle tolerance respectively created models with a tessellation resolution able to represent curves suitable for the microfluidic chips and hence were selected for all .stl exports.

3.5.4.6 Non-processed vs. polished

The improvement of optical quality by polishing using the method described in Section 3.5.2 was applied to microfluidic chips printed by the HD3500+ and Viper Pro. Chips printed by the HD3500+ responded positively to the polishing process allowing for the removal of the stitch marks created during fabrication Figure 3.5-15(a)(c). Compared to the HD3500+ printed samples, Viper Pro chips were more optically transparent. Scanlines

from fabrication were visible however running through the model horizontally Figure 3.5-15(b). Polishing of the Viper Pro model improved the optical quality marginally, however the scanlines remained.

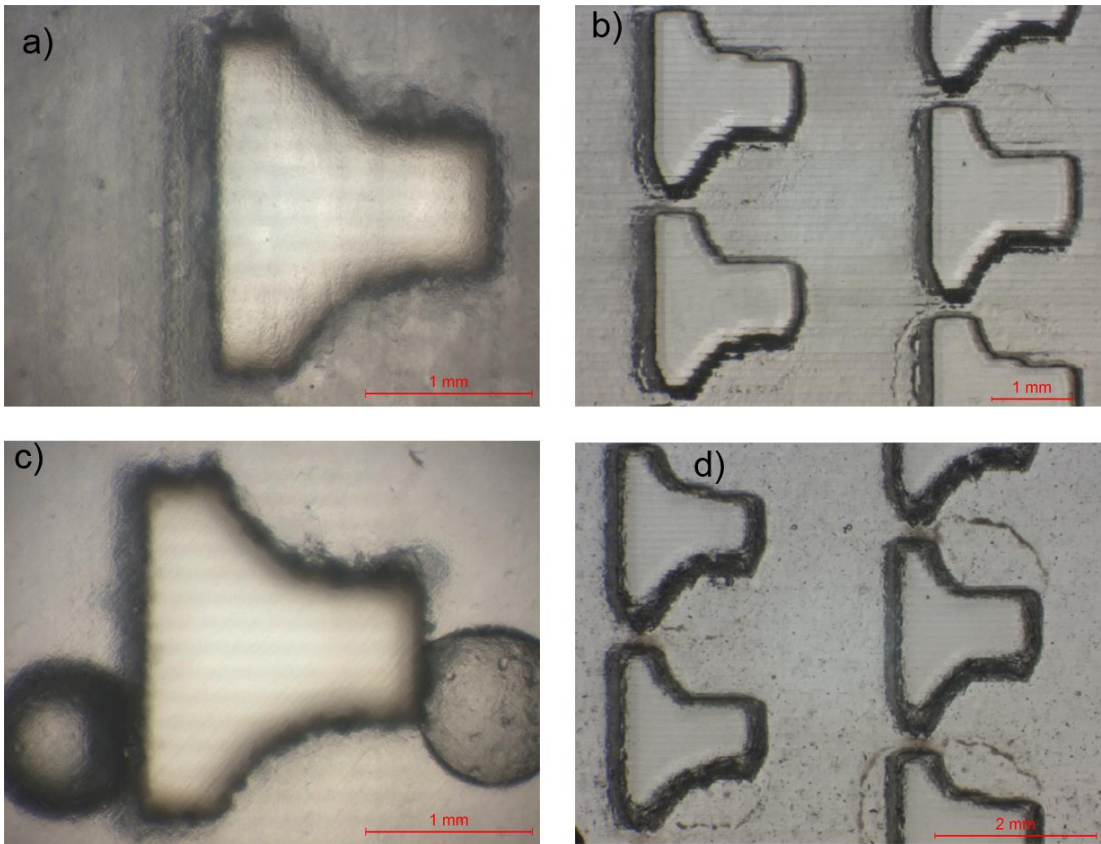


Figure 3.5-15 – Stereomicroscopy of 3D printed chips before and after polishing. A and C) HD3500+ printed chip showing the feature used to create the zebrafish trap. A stitch line is visible on the edge of the trap which was then removed in C) by polishing. Water was injected into the channels to demonstrate the optical quality expected during zebrafish analysis. Faint horizontal lines are visible through the trap pillar which are internal to the printing process and hence not removable. The clarity of the chip was improved significantly by polishing. B and D) Viper Pro printed chips showing 3 trapping areas before polishing B) Scanlines are visible at this stage. D) Polishing removed the stepped visualisation of the features however the scanlines remain. Polishing of the Viper Pro produced traps did not improve optical quality significantly.

3.5.4.7 Difference in optical quality with fluorescent zebrafish

Assessment of polished HD3500+ and Viper Pro fabricated chips was performed. Both were loaded with transgenic zebrafish embryos for imaging Figure 3.5-16. For these experiments transgenic *fli1a:EGFP* larva at 54 hour post fertilisation (hpf) were loaded into 3D printed chips with E3 medium. The zebrafish larva in each chip was anaesthetised for the experiment. The optical transparency of the chip and larva allowed for convenient microscopic visualisation of the characteristic patterns of intersegmental vessels (ISV). Chips fabricated with the HD3500+ shown in Figure 3.5-16(b) demonstrated that the EGFP fluorescence of ISV could be visualised through the monolithic printed chip.

The image taken of the fluorescent zebrafish within the HD3500+ chip compares favourably with the control image Figure 3.5-16(c). An image using the same conditions of a transgenic zebrafish within a Viper Pro fabricated chip is demonstrated in Figure 3.5-16(a). The scanlines formed during fabrication disrupt the clarity of the image and make the ISV indistinguishable from the rest of the tail. It was concluded that the HD3500+ was more suitable for fabricating chips conducting visual based assays such as the angiogenesis assay.¹⁶⁰

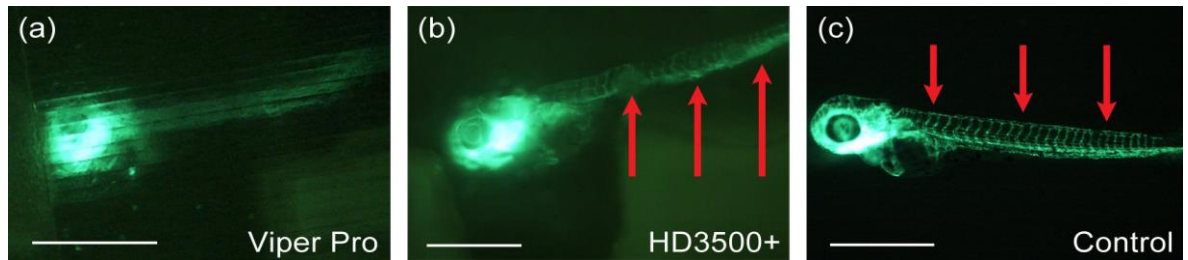


Figure 3.5-16 – On-chip visualisation of transgenic zebrafish line with different 3D printed materials. a) Fluorescent image of a zebrafish within a Viper Pro printed chip. The scanlines created during printing impede the visualisation of the zebrafish. The ISV were indistinguishable from the tail, only the eye of the zebrafish was recognisable. **b)** Fluorescent image showing a transgenic zebrafish larva within a HD3500+ printed chip. Red arrows indicate ISV in the tail of the zebrafish. Developing patterns of ISV were clearly visible at low magnification. **c)** Image of a zebrafish control sample in a petri dish clearly showing the ISV. Scale bars are 1 mm.

3.6 Conclusions

In this chapter the fabrication methods of 3D printed embryo array technology has been described and the conditions used for handling of zebrafish embryos. Additive manufacturing of microfluidic devices and post-processing development was presented and discussed. Both multi-jet modelling (MJM) and stereolithography (SLA) processes were explored for this application. Monolithic microfluidic chips printed with the HD3500+ using VisiJet Crystal were fabricated to have optical quality and fluidic sealing suitable for visualisation and trapping of zebrafish embryos; the optical quality allowed for suitable detail to perform future angiogenesis assays. The Viper Pro chips printed with Watershed material was found to be unsuitable for these purposes but allowed for brightfield imaging and trapping. Fabrication results compared favourably to other forms of rapid prototyping such as laser cut PMMA devices and PDMS moulded microfluidic devices of the same design. Both processes allowed for fabrication of monolithic, optically transparent devices with features in the 100 μm range requiring minimal post-processing.

The following chapters will discuss the application of these methods and from Chapter 2 for developing *in vitro* toxicity testing platforms to reduce animal testing.

4 Microfluidic devices for the culture of hepatocytes on micro-arrays

4.1 Abstract

This chapter shall discuss the development of microfluidics devices with the integration of micro-arrays. The objective of this work was to develop a high-throughput platform for the culture of primary hepatocytes. Motivations for this work are that primary liver cells have been proven to be an excellent indicator of toxicity and are in agreement with the 3R's of animal studies discussed in Chapter 1. The reproducibility of the cell array as well as cell viability was studied. As primary cells are more difficult and expensive to obtain, a model cell line 3T3 fibroblast cells, were employed to test patterning efficiency. This immortalised cell line enabled the optimisation of conditions for cell patterning and maintenance. Following optimisation with this cell line, primary cell rat hepatocyte micro-arrays were studied. Integration of micro-array patterns for culture of hepatocytes was tested with three different microfluidic devices. The metabolic functionality of primary hepatocytes cultured on micro-arrays within microfluidics was tested using the 7-ethoxyresorufin-O-deethylase assay (EROD).

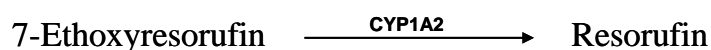
4.2 Introduction

The microenvironment in which cells are cultured affects cellular processes including proliferation, differentiation and the expression of phenotype-specific functions.²³¹ The way that cells interact with their surroundings is defined by their environment including the extra cellular environment (ECM), neighbouring cells and soluble factors. Previous studies on the maintenance of primary cells, specifically hepatocytes in this work, have shown to rely on cell-cell communications and ECM composition.^{219, 231} The culture and testing of *in vitro* primary hepatocytes have been observed to be a suitable platform for toxicity assays.^{41, 232-234} In addition, successful fabrication of micro patterning and surface engineering techniques using photolithography and robotic protein printing has been demonstrated for hepatocytes.^{204, 235} It was demonstrated by *Bhatia et al* that through successful engineering of the microenvironment using substrate patterning, the functionality of cultured primary hepatocytes was improved.

This included key liver functions: albumin secretion, urea synthesis and cytochrome P450 activity.⁷⁵

Cytochrome P450 is the official title for a larger superfamily of enzymes (specifically haem-thiolate proteins) involved in the metabolism of a wide variety of both exogenous and endogenous compounds.²³⁶ This includes the metabolism of oxidative metabolism of steroids, fatty acids, prostaglandins, leukotrienes, biogenic amines, pher-omones and plant metabolites. The rationale for the interest in this group of enzymes is that they are the primary site of metabolism for drugs, chemical carcinogens, mutagens and other environmental contaminants.²³⁷ While there are over 50 enzymes in this family and are present in cells throughout the body (located on the smooth endoplasmic reticulum), the highest concentration is found in the liver and small intestine. The liver is very active in metabolising foreign compounds and often the primary site of exposure to toxins making hepatocytes a target for investigation of P450 activity.²³⁸ Investigation of P450 activity in single hepatocytes has been shown to be detectable *in vitro* through resorufin fluorescence intensity.²³⁹

Hepatocytes are the primary source of cytochrome P450 enzymes in the liver, hence the functionality of these enzymes is indicative of the hepatocytes ability to metabolise toxic compounds. A method of measuring the metabolic functionality of hepatocytes with regard to P450 activity is the 7-ethoxyresorufin-O-deethylase (EROD) assay.²³⁹ This assay measures the activity of isoform cytochrome P450 1A2 enzymes present in hepatocytes as they catalyse the deethylation of 7-ethoxyresorufin to resorufin:



The formation of resorufin is measured in the cell culture medium by optical fluorescence microscopy with excitation at 530 nm and emission at 590 nm. Observed fluorescence intensity of metabolised resorufin by hepatocytes is representative of cell functionality. It has been demonstrated by *Hammond et al* that toxicity studies employing the EROD assay using *in vitro* human hepatocyte cultures to be a reflection of direct action of toxic substances.²³⁹ This is a comparable method compared with studies on whole animals where measurements are complicated by adsorption, transport and other secondary effects. This makes the EROD assay an appropriate method to measure the functionality of hepatocytes cultured on a micro-array within microfluidics.

4.2.1 Integration of micro-array technology with microfluidics

Microfluidics as described in Section 1.5.2 offers advantages over static conditions for cell culture which are desirable for the toxicity testing of compounds which include, reduced volumes of reagents, size, controlled flow-rates and delivery of reagents.⁷² In relation to the 3R's of animal testing described in Section 1.2, microfluidics offers a solution. Primary hepatocytes of human or animal origin must be harvested fresh to maintain specialised functions relating to drug toxicity testing such as P450 enzymes.⁵⁵ By integrating microfluidic devices with micro-arrays, high-throughput liver toxicity screening can be achieved. Typically static culture conditions using 96-well plates have a culture surface area of 32 mm² per culture group.²⁰⁹ The microfluidic culture area for the devices used in this work range from 86 mm² total area (575 individual culture groups) to 7.5 mm² total area (50 individual culture groups). Thus the functionality in terms of culture area is increased which in turn decreases the number of experiments required, therefore the number of donor livers demanded for toxicity studies. This therefore reduces the loss of animal lives required for liver based toxicity assays.

The integration of microfluidics with micro-arrays for culturing hepatocytes allows for physiologically relevant ECM for attachment and a continuously perfused cell culture medium supplying nutrients and removing resultant metabolic by-products. The combination of microfluidics and micro patterns has been demonstrated by *Kane et al*²⁴⁰ for the culture of primary hepatocytes. By using photolithography techniques and soft-lithography an array of polydimethylsiloxane (PDMS) chambers were clamped reversibly with collagen treated areas within the chambers for hepatocyte attachment. Combining microfluidic conditions with a micro-array to create a high-throughput device for toxicity testing is the goal of the work presented in this chapter.

4.2.2 Aims of this chapter

The aims of the work presented in this chapter were to further and confirm the use of micro-arrays (collagen dots on a PEG treated surface) as a suitable culture substrate using 3T3 fibroblast cells. Develop microfluidic devices suitable for the integration of micro-arrays to create a high-throughput device for toxicity testing. Establish the viability of primary hepatocytes cultured on micro-arrays within microfluidic devices. Finally, establish the functionality of cultured hepatocytes with microfluidic devices on micro-arrays by observation of P450 enzyme activity through application of the EROD assay.

4.3 Materials

Cell types 3T3 and primary hepatocytes are described in Section 2.3.1. Cell culture mediums DMEM and L-15 are detailed in Section 2.3.1. Microfluidic materials are described in Section 2.3.5 as well as the fabrication materials of PDMS microfluidic devices in Section 2.6.

4.4 Methods

3T3 cells were cultured at 37 °C and 5 % CO₂ in DMEM. Fresh primary rat hepatocytes were prepared according to suppliers instructions detailed in and cultured in L-15 medium also at 37 °C and 5 % CO₂. As described in Section 2.6.9, micro pattern arrays of 150 µm dots of collagen, 25 x 23, 20 x10 and multiples of four, 10 x 5 were fabricated onto polyethylene glycol (PEG) treated glass, along with control samples PEG on glass and non-treated glass. All substrates were cut to 1.5 x 2.5 cm slides. These samples were washed twice with PBS (pH 7.4) and sterilised using UV radiation within a Class II biosafety cabinet for 15 minutes. Samples were then placed in 6-well plates and seeded with cell suspension at a density of 2.5 x 10⁵ cells/cm². Cell types (hepatocytes and 3T3) were handled in the same fashion. Cell viability was assessed using fluorescent confocal microscopy with a live/dead stain as described in Section 2.4.3.

4.4.1 Dolomite microfluidic device for on-chip analysis of hepatocyte arrays

Firstly, the possibility of using microarrays for hepatocyte toxicity analysis within a microfluidic device was assessed. This was accomplished by using a commercially available system and fresh rat hepatocytes. Microarray patterns (26 x 24 array of 150 µm collagen dots) covering an area of 1.5 x 2.5 cm cultured in microfluidics were compared within petri-dish conditions for viability and response to the EROD assay.

4.4.1.1 Assembly

On-chip analysis of hepatocyte arrays was conducted using the micro reaction chamber by Dolomite Microfluidics UK (Resealable Chip Interface, P/N 3000306, Dolomite Microfluidics, Royston, UK)²⁴¹ shown in Figure 4.4-1(a). Two microfluidic connectors were also sourced from Dolomite (4-way linear M1 connector)²⁴² shown in Figure 4.4-1(b). The microfluidic chamber was supplied by Dolomite (main chamber 6.33 x 7 mm), fabricated in 2 mm thick poly(methyl methacrylate) (PMMA) with 100 µm deep etched channels. The main volume of the chamber was 88.6 µL. The design is illustrated in

Figure 4.4-1(c). Pumps, syringes and needles used to inject fluids into the system are described in Section 2.3.5. The 25 x 23 micro pattern array of 150 μm collagen dots on the glass substrate (29.8 x 22.3 x 3 mm) was placed into the resealable device with the PMMA etched chamber on-top, the device was then sealed.

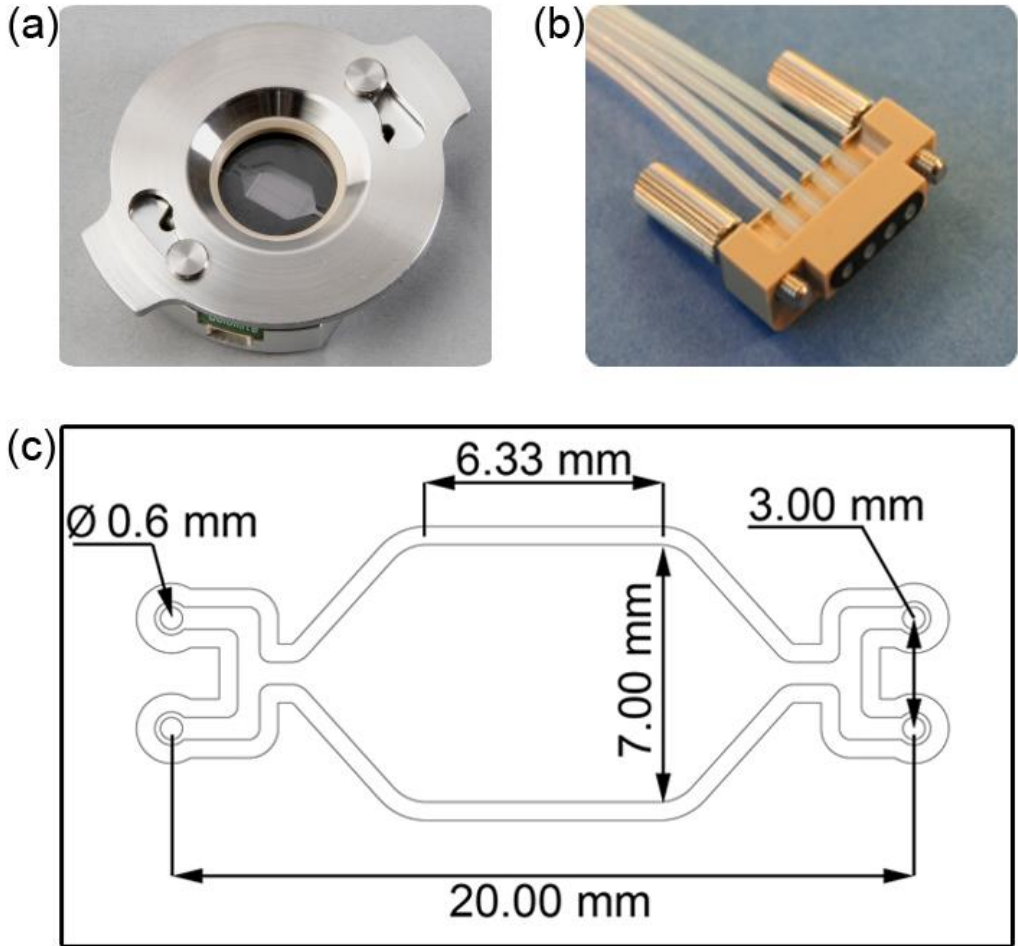


Figure 4.4-1 – Photographs and diagram illustrating the Dolomite resealable device used for analysis of on-chip micropattern arrays of hepatocytes. (a) Photograph showing the Dolomite resealable device, twisted clockwise to release the lid and anti-clockwise to seal. A PDMS gasket (100 μm) placed around the channels seals the chip to the selected base substrate. This is illustrated by the outer line of the chamber design shown in (c). (b) Photograph of the 4-way linear fluidic connector by Dolomite. Only two connections were used in these experiments as the chamber only has two inlets. (c) Schematic of the Dolomite two-inlet, two-outlet microreaction chamber. A PDMS gasket 1 mm wide and 100 μm thick follows the edge of the design to provide a seal to the chosen substrate (glass with micropatterned collagen dots).

4.4.1.2 Connections and Operation

The micro-array of 150 μm collagen dots (25 x 23) were rinsed in phosphate-buffered saline solution (PBS) before being assembled into the Dolomite microfluidic device. The completed device was assembled inside a fume hood, the fluidic connections are illustrated in Figure 4.4-2. Two disposable 5 ml syringes were connected to the tubing of the Dolomite, one for injection of L-15 cell culture medium. Tubing and chamber were

sterilised with 70% ethanol (EtOH) (v/v) prior to setup. The tubing was then primed with PBS before fresh rat hepatocytes (6×10^5 cells/ml) were seeded onto the micro-array within the microfluidic device using a syringe and incubated for 2 hours (37°C , 5% CO_2). Control samples of microarrays, PEG treated glass and collagen glass were also incubated for comparison. After 2 hours, cell medium was slowly injected into the microfluidic chamber to rinse all non-adhered cells from the device. Microfluidic cultures were performed for 24 hours using a pump set to a flow rate of $0.1 \mu\text{L}/\text{min}$, (37°C , 5% CO_2).

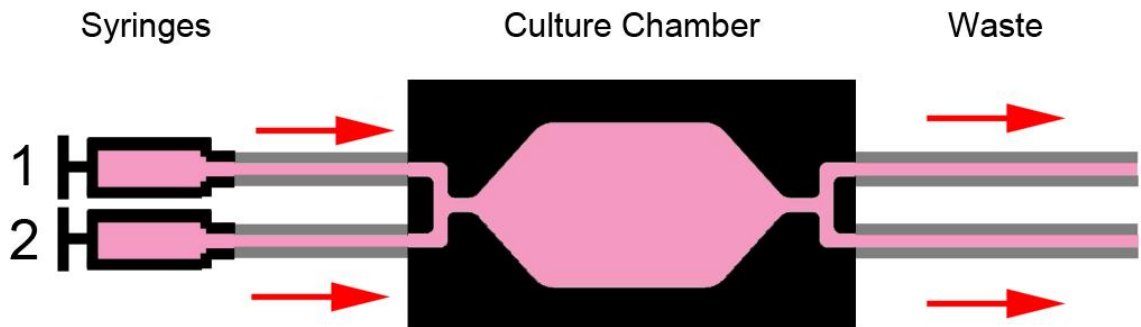


Figure 4.4-2 – Illustration of microfluidic connections for the Dolomite microfluidic device. Two disposable syringes were connected to the inputs of the microfluidic chamber used for injecting cells, medium and assay reagents. Waste fluids was be collected by Eppendorf tubes.

4.4.1.3 7-ethoxyresorufin-O-deethylase (EROD) assay in Dolomite device

The 7-ethoxyresorufin-O-deethylase (EROD) assay was used to measure the activity of the enzyme cytochrome P450 in the primary rat hepatocytes cultured for 24 hours on the micro-arrays. Cell culture medium was removed from samples before replacing with fresh medium containing $20 \mu\text{M}$ 7-ethoxyresorufin and $40 \mu\text{M}$ dicumarol. The fluorescence intensity was recorded every minute for 30 minutes using a confocal microscope with HeNe laser excitation at 543 nm. The emission was observed at 590 nm using a long pass filter (585 ± 20 nm). The fluorescence intensity (arbitrary units) within defined regions of cells in the field of view was analysed using ImageJ software.¹⁹⁴

4.4.2 Microfluidic devices for cell culture and analysis on micro pattern arrays

For further investigation of hepatocyte cultures, two designs were made to enclose micro pattern arrays. A large single chamber device was first designed to use a 20×10 array of $150 \mu\text{m}$ dot patterns covering an area of 20 mm^2 . Secondly a second microfluidic device was designed for a smaller array (10×7) arrays covering an area of 4.2 mm^2 . This design used 4 chambers to enclose 4 individual arrays.

4.4.2.1 Clamp Device Design

The designed microfluidic system is shown in Figure 4.4-3. This system used a clamp like system to press multiple layers of the device to create a fluidic seal. It consisted of an aluminium bottom plate with a machined engraving large enough to fit a 2.5 x 1.5 mm glass slide Figure 4.4-3(a). Glass slides substrates were for micropattern arrays of collagen dots. A microfluidic chamber or chambers fabricated in PDMS as shown in Figure 4.4-3(b) was pressed onto the glass slide. Alignment with the micro patterns on the glass slide was made by hand and reversibly pressed in place. To seal the channel a Perspex top was used to sandwich the PDMS microfluidic channels and be screwed into the aluminium base. This design allowed for a simple resealable microfluidic system. The reason for this choice of design was that the collagen micropatterns were sensitive to typical bonding techniques such as UV exposure that would destroy the pattern. It also allowed for the microfluidic device to be removed and cleaned easily for repeated experiments with new micropattern samples.

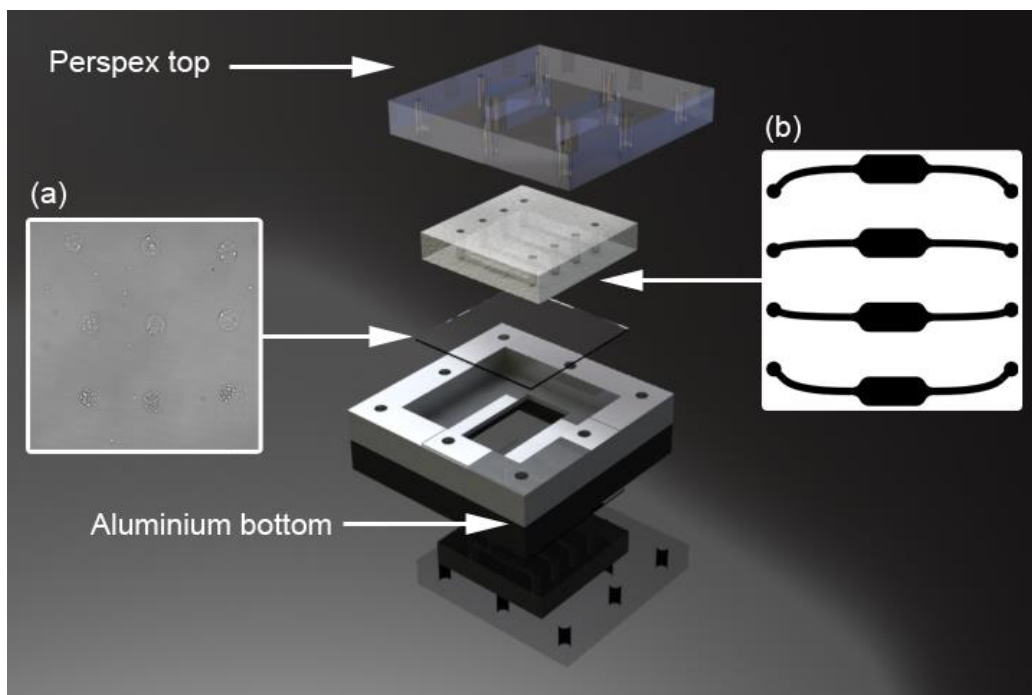


Figure 4.4-3 – Microfluidic biochip device for toxicity testing – This figure shows both a 3D rendered image of the device as well as schematic of the channel design and a microscope image of the protein micro-arrays. The device consists of a milled Perspex top, PDMS with four soft-lithography mould microfluidic chambers, PEG treated glass slide with 4 printed protein micro-arrays and an aluminium bottom. The device was clamped together with the use of eight M3 screws. (a) shows a microscope image of the printed collagen pattern; (b) shows the microfluidic chamber design.

4.4.2.2 Fabrication of microfluidic channels

As described in Section 2.6 microfluidic channels were fabricated through a combination of microfabrication techniques and PDMS soft-lithography.

4.4.2.3 Single chamber culture device design

The microfluidic chamber was designed to enclose a microarray in the same manner as the Dolomite designed chip. The design of the chip used in the LGC manufactured by Dolomite Ltd was used as a design template. Results shown in Section 4.5.3 of *in vitro* cell patterning and viability indicated that the main area (6.33 x 7 mm) of the Dolomite chamber was suitable for purpose. Thus the new design chamber was 6.5 x 5 mm, 100 μm deep with two inlets and one outlet as shown in Figure 4.4-4(a). The main volume of the chamber is 3.25 μL . This allowed for the injection of assay reagents without unplugging the connections needed for cell medium supply.

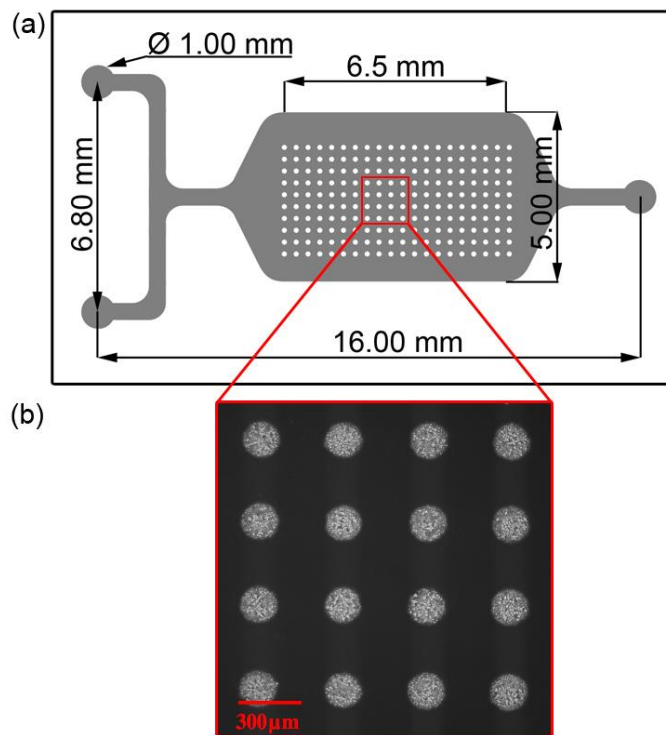


Figure 4.4-4 - Single chamber microfluidic device for culture of cells on collagen micropattern arrays. (a) Schematic of microfluidic channels. The main chamber was 6.5 x 5 mm, the depth of the channels was 100 μm . Channels for inlets and the outlet were 500 μm in width. Inlet and outlet connections were 1 mm in diameter. The two inlet design allowed for the injection of two different fluids without disconnecting the system. Superimposed in the chamber is a 20 x 10, 150 μm dot array. This array was fabricated on a glass substrate and aligned by hand to fit into the chamber during assembly of the device. **(b)** Microscopy image showing a 4 x 4 portion of an array of collagen dots printed onto a PEG treated glass slide. Scale bar is 300 μm .

The reduction of the chamber width was to maintain the height to channel width ratio so that the chamber would not collapse (1:50). This is a well-documented issue of fabricating microfluidic channels and chambers in polydimethylsiloxane (PDMS).¹⁹² Micropattern arrays (20 x 10; 150 μm dots) were designed to fix within this chamber a close up of printed arrays can be seen in Figure 4.4-4(b). This allowed for a 1 mm error in alignment of the array into the chamber which was possible by hand. The PDMS chip was made by soft-moulding using a silicon master fabricated using photolithography and dry etching as described in. A full schematic describing the integration with the clamping device with the microfluidic chamber device is illustrated in Appendix A.

4.4.2.4 Single chamber setup and operation

The PDMS chip was fabricated using the methods from Section 2.6 and cleaned using methanol and isopropyl in an ultra-sonic bath for 5 minutes each. The microfluidic clamp, tubing and valves were washed in 70% EtOH before use. Fluidic connections are illustrated in Figure 4.4-5. Cells were removed from culture, centrifuged and added to 1 ml of degassed growth medium appropriate for the cells typically a concentration of 1×10^6 cells/ml which was kept in an incubator (37 °C, 5% CO₂). Within a laminar hood the microfluidic device was sealed with the micropattern array using the clamping device. Connections using blunted needles and tubing were then connected to the PDMS chip and to syringes. The device was then assembled and rinsed with PBS for 10 minutes.

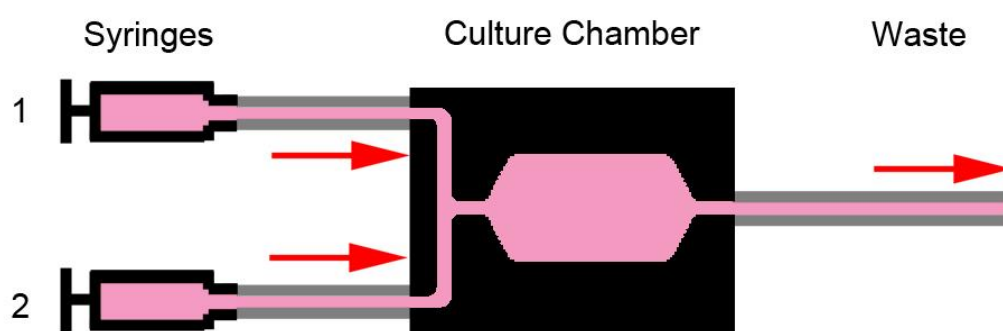


Figure 4.4-5 – Illustration of microfluidic connections for the single chamber microfluidic device. Two disposable syringes were connected to the inputs of the microfluidic chamber used for injecting cells, medium and assay reagents. A single channel is used to dispose of waste fluids collected by Eppendorf tubes.

Abcellute preserved rat hepatocytes were cultured in the PDMS device. Of the preserved cells, 7×10^6 cells were activated with a 76% viability (using a Trypan Blue stain). As the cells will only live for about 4 to 5 days, only 2 experiments were carried out in the microfluidic device, the rest of the cells were frozen down as detailed in Section 2.4.4 or used in Petri dish based experiments. The cells were then injected manually by syringe into

the microfluidic chamber. The device was then left in the incubator (37 °C, 5% CO₂) for 1 hour to allow the cells to adhere to the surface of micropattern array. After this the syringe attached to the device was attached to a syringe pump and placed inside the incubator. A flow rate of 0.1 µL/min was selected and left to culture for 24 hours.

4.4.2.5 Four chamber culture device design

The microfluidic device was designed in CorelDraw X3 (Corel Corporation, Ontario, Canada) and SolidWorks 2011 (Dassault Systemes SolidWorks Corp, Concord, MA, USA) CAD packages. Subsequent prototyping and fabrication of PDMS devices was performed using photolithography, etching and soft-lithography as described previously in Section 2.6. This chip was designed to be used with the clamping system Figure 4.4-3 to allow the use of micro-patterns on glass shown in Figure 4.4-6(a). The technical drawings of the device are shown in Appendix A. Four identical chambers were designed to allow for the simultaneous testing of different concentrations and/or different compounds within the same device. Each chamber had one outlet and one inlet with channels 500 µm wide, the depth of each chamber was 100 µm.

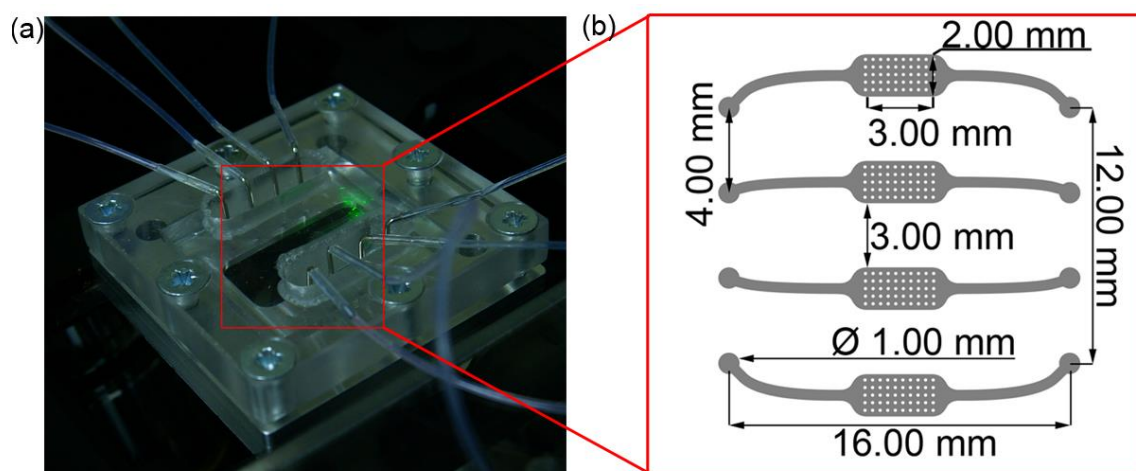


Figure 4.4-6 – Design of 4-chamber microfluidic device to enclose micro pattern protein arrays. (a) Photograph showing the microfluidic device assembled and setup with fluidic connections on a microscope stage. (b) Schematic illustrating the microfluidic chambers and dimensions. Micro-arrays can be seen in the chambers (10 x 5, 150 µm dots). A full technical drawing of the design can be found in Appendix A.

The main chamber volume was 0.6 µL. The chambers main area was 3 x 2 mm designed to allow for a 10 x 5 array of 150 µm dots per chamber. The chamber area was reduced from the previous design (6.5 x 5 mm) to allow 4 chambers to fit within the clamping device. The reason for this was to be able to test multiple compounds or a range of concentrations simultaneously on one device. Microfluidic chambers with one inlets and one outlet were designed Figure 4.4-6(b). The previous design used two inlets to allow for injecting of

assay fluids without disconnecting the medium and cell fluidic connection. In practice as the single chamber system did not use external valves, the introduction of air bubbles was frequent. By using external valves as shown in Figure 4.4-9, the introduction of air to the system was reduced.

4.4.2.6 Four chamber setup and operation

The device was setup on the Zeiss confocal microscope stage within an incubator system to maintain 37°C throughout the experiment. The device was connected to 4 external syringe pumps using disposable 5 ml syringes polyurethane tubing with an internal diameter of 100 µm through 3 way valves before finally being connected to the device. Each chamber had a waste tube, with a 1 ml Eppendorf tube with a hole punched through the top. The device was setup inside a microscope cell culture system. Valves were mounted a custom-made stage to minimise connection movement and hence pressure changes and introduction of air into the system. Details of the design can be found in Appendix A. Devices were primed with 70% EtOH to help wet the PDMS and reduce the effect of nucleation and persistence of air bubbles. This was followed by sterile PBS, then warmed growth medium to provide the correct pH of 7.4. The experimental setup consisted of syringe pumps (Basi, MD-1001, 2701 Kent Avenue, West Lafayette, IN, USA) up to four) connected to a 3-way valve (2421 Omnifit 3-way hex valve, Diba Industries Ltd, Cambridge, UK)²⁰³ attached to a bread board Using 0.030"OD PTFE tubing (Cole-Parmer Instrument Company, Venon Hills, Illinois, USA) valves were connected to the microfluidic chip with blunted 23G needles (BD Microlance, Becton, Dickinson and Company, New Jersey, USA). The complete system was enclosed within a heating system (Pecon Gm5H, Germany) as can be seen in Figure 4.4-9.

Steps required to setup this device were identical to the methods described in Section 4.4.2.4 until the point of cell seeding. For each of the four chambers, cells were injected manually by syringe into the microfluidic chamber using individual syringes through a 3-way valve. Valves were mounted on a custom made bread board to aid transportation from the laminar hood to the incubator and microscope setup. Cells were first injected into the 3-way valve using a 5 ml disposable syringe, flowing from 1 to 2 Figure 4.4-7(a).

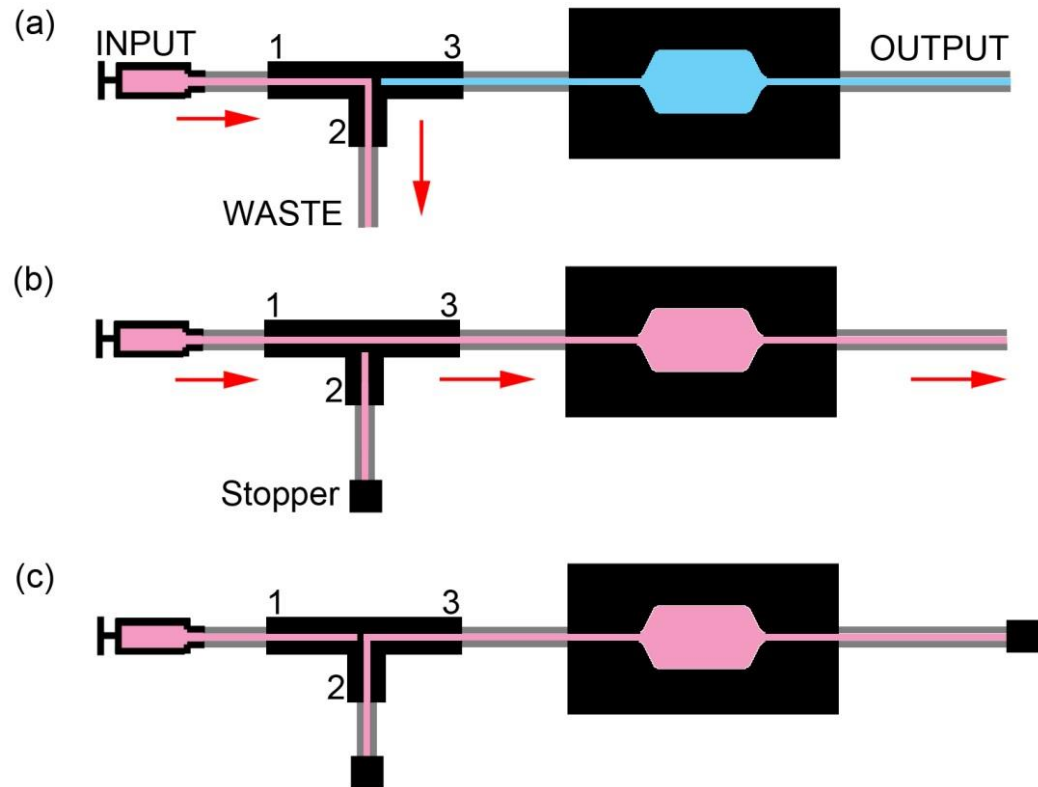


Figure 4.4-7 – Illustration showing the general operation of the 4 chamber microfluidic device, this process is applicable to each chamber. (a) Cells were first injected gently into the 3-way valve using a 5 ml disposable syringe, flowing from 1 to 2. The system was previously primed with the same protocol with phosphate-buffered saline solution (PBS) illustrated as blue filled areas. Once no bubbles were visible at the waste outlet the valve was switched to flow from 1 to 3. (b) Cell solution was then injected into the chamber with waste flowing to the output. On filling the chamber, the flow was stopped and a stopper was inserted into the tubing on connection 2. (c) The valve was then switched to close the input (syringe) from the chamber. The system was then sealed, as a stopper was then placed in the output tubing (connection 2).

The system was previously primed using the same protocol with phosphate-buffered saline solution (PBS) illustrated as blue filled areas. Once no bubbles were visible at the waste outlet the valve was switched to flow from 1 to 3 Figure 4.4-7(b). Cell solution was then injected into the chamber with waste going to the output. A stopper was inserted into the tubing on connection 2. The valve was then switched to close the input (syringe) from the chamber, now connection 2 was connected to 3 Figure 4.4-7(c). A stopper was then placed in the output tubing of the chamber sealing the system. The device was then left in the incubator (37 °C, 5% CO₂) for 1 hour to allow the cells to adhere to the surface of micropattern array. After this the four syringes attached to the device were attached to a syringe pumps and placed inside the incubator. A flow rate of 0.1 μL/min was selected and left to culture for 24 hours. A complete diagram of the fluidic connections for operation of this system can be seen in Figure 4.4-8 and photographs of the setup are shown in Figure 4.4-9.

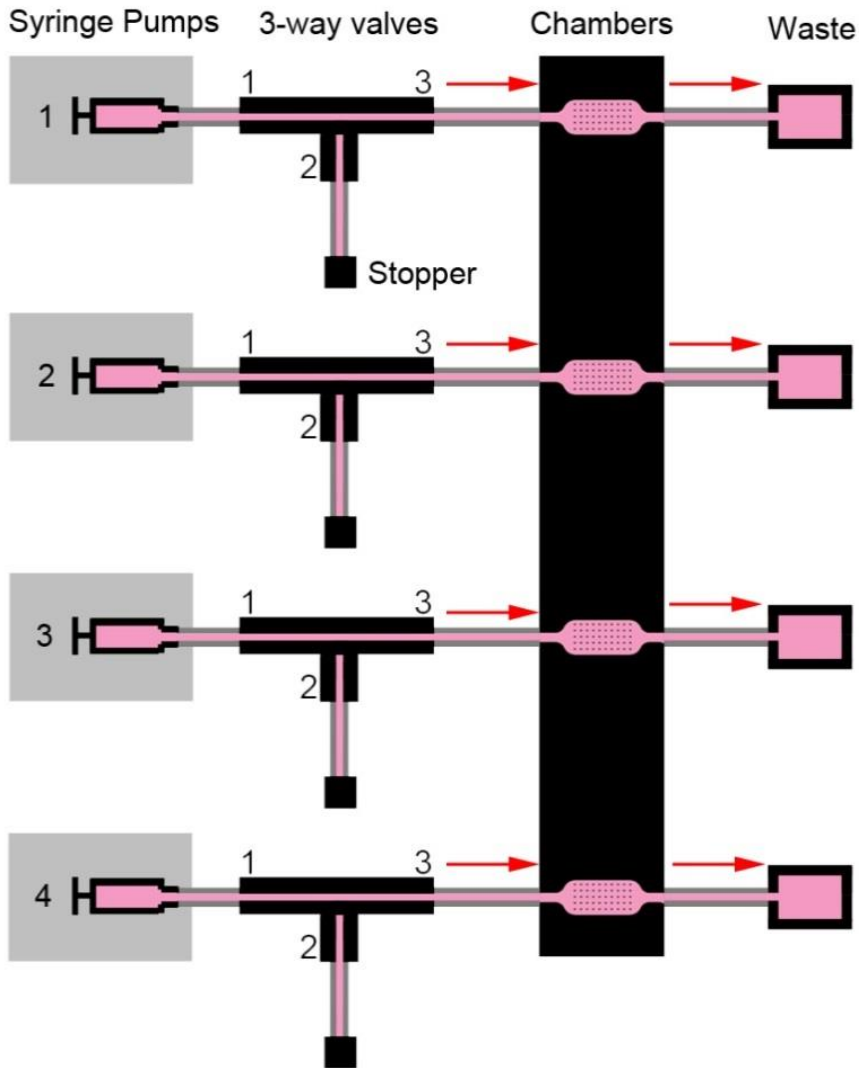


Figure 4.4-8 – Illustration showing the fluidic setup used for culturing cells using the multiple chamber culture device. The system consisted of 4 syringe pumps each connected to a separate 3-way valve by PTFE tubing. The valves were in turn connected to the chambers of the microfluidic device, terminating in a waste collection Eppendorf tube. The illustration shows the system in cell culture operation using a flow rate of 0.1 $\mu\text{L}/\text{min}$ (direction of flow indicated by red arrows), therefore the valve is opened to allow flow from port 1 to 3 of the 3-way valve. A stopper is inserted into the tubing of port 2 to seal the tubing to aid in the reduction of air into the system.

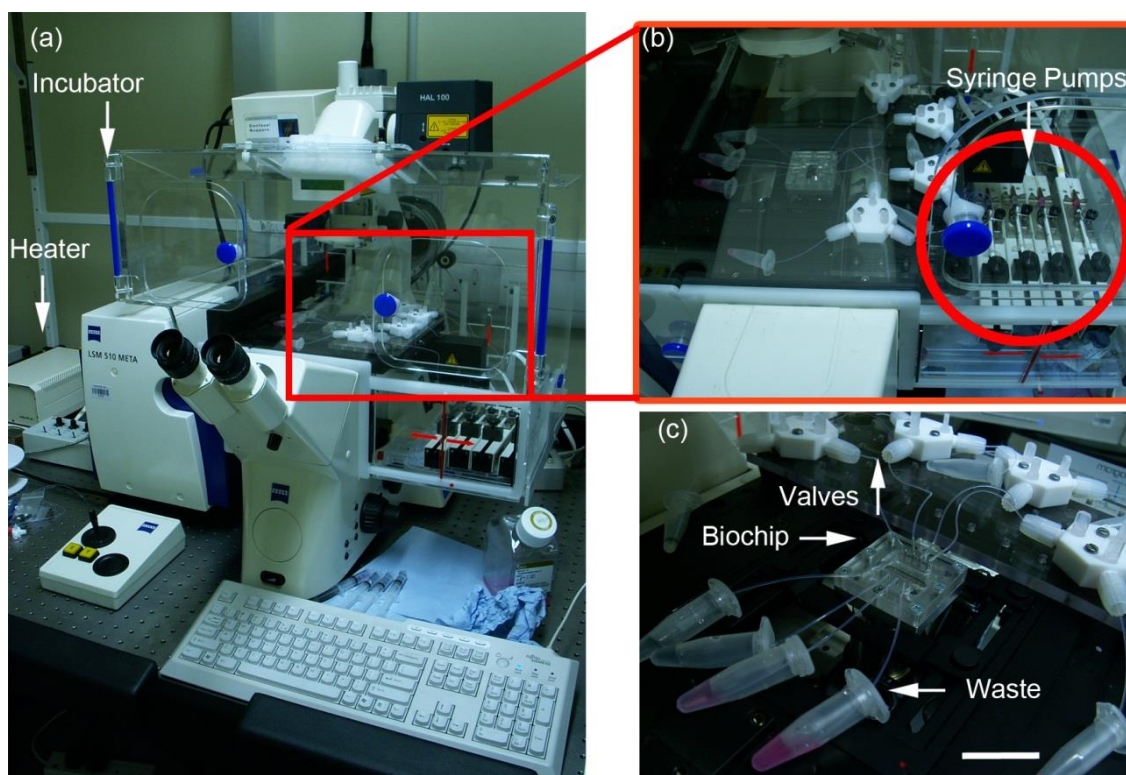


Figure 4.4-9 – Microfluidic device experimental setup using a confocal microscope with incubation enclosure. (a) Photograph showing the confocal microscope Zeiss LSM 510 Meta with incubator enclosure and heater. (b) The highlighted area shows enclosed within the incubator housing syringe pumps to provide flow for the biochip connected to 3-way valves; (c) Photograph shows the biochip assembled and connected to 3-way valves and waste collection Eppendorfs. Scale bar is 40 mm.

4.4.3 7-ethoxyresorufin-O-deethylase (EROD) assay in microfluidic devices

The ethoxyresorufin-o-deethylase (EROD) measures cytochrome P450-1A2 levels through the metabolism of 7-ethoxyresorufin (7-ER) to resorufin. Both compounds can be detected by fluorescence. Cytochrome P450 monooxygenases (CYPs) are a superfamily of enzymes involved in the biotransformation of a wide range of both endogenous and exogenous compounds.²³⁹ These enzymes play important roles in the metabolism of many drugs and in the activation of a variety of chemical toxicants and carcinogens in both humans and animals

To perform the assay HBSS containing 20 μM 7-ER and 40 μM dicumarol was prepared. This was added to wells directly to cell samples in wells and within the microfluidic device. The fluorescence was measured by confocal microscopy for 30 minutes at a constant temperature of 37 $^{\circ}\text{C}$ (excitation 530 nm; emission 585 nm).

The hepatocytes cultured on micro-pattern arrays within microfluidics were then used to test the enzyme cytochrome P-450 (CYP) 1A1 present in these cells to assess the metabolic functionality. This enzyme is capable of activating pro-carcinogenic polycyclic hydrocarbons and halogenated aromatic hydrocarbons into mutagenic compounds. The EROD assay was completed on both the device and petri dish which provided a detectable resorufin response in both cases.

4.4.3.1 Calibration

Before running an EROD assay a calibration of the system was required shown in Figure 4.4-10. To achieve this, seven different concentrations of resorufin were measured to provide a calibration curve to compare the EROD results with. A standard curve with resorufin concentrations of 0, 0.01, 0.05, 0.1, 0.5, 5 and 10 μM was prepared by adding 5 μL of 200 \times resorufin stock to 995 μL Hank's Balanced Salt Solution (HBSS). The dilutions and required are shown in Table 4.4-1. A sample of each concentration was pumped into a chamber of the device and the fluorescence at excitation 530 nm and emission 585 nm measured using the confocal setup.

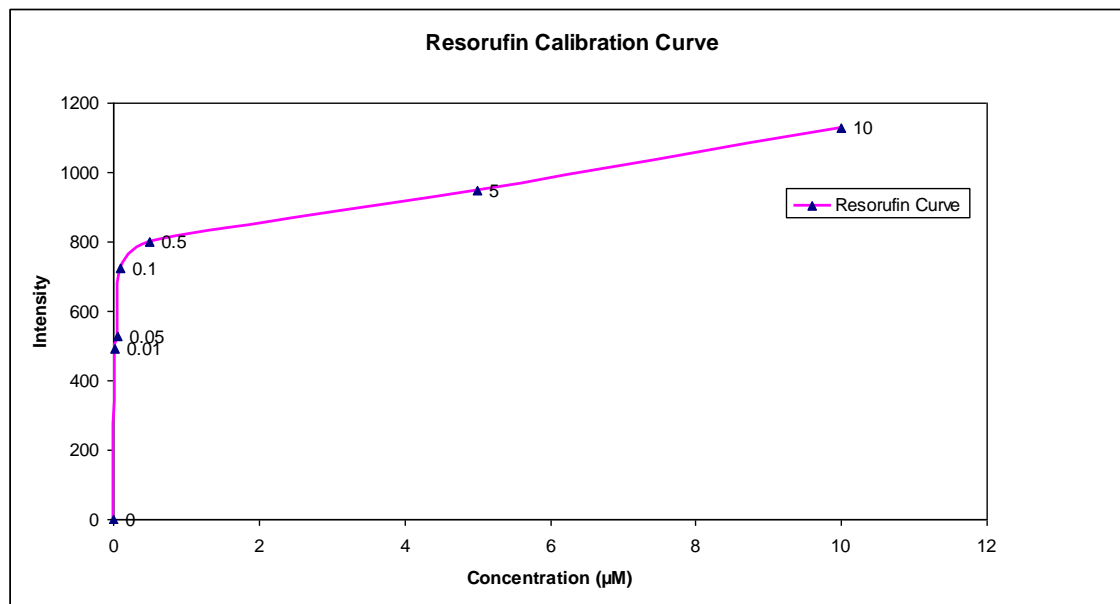


Figure 4.4-10 - A standard curve with resorufin concentrations of 0, 0.01, 0.05, 0.1, 0.5, and 10 μM needed to compare and interpret results from the EROD assay. Excitation 530 nm and emission 584 nm.

Table 4.4-1 – Resorufin concentrations for calibration

Final concentration in HBSS	200× Stock concentration in DMSO	Volume of stock resorufin	Volume DMSO (μl)
10 μM	2 mM	20 μL 5 mM	30
5 μM	1 mM	10 μL 5 mM	40
0.5 μM	100 μM	5 μL 1 mM	45
0.1 μM	20 μM	10 μL 100 μM	40
0.05 μM	10 μM	5 μL 100 μM	45
0.01 μM	2 μM	5 μL 20 μM	45

4.4.3.2 Microfluidic assay procedure

Following the successful culture of primary hepatocytes within the single chamber device using the microfluidic device, the experiment was set up on a confocal microscope complete with heating unit for temperature control to maintain viability Figure 4.4-9. Reagents were prepared as described in Section 4.4.3.1. Resorufin was used prior to experiments to test the delivery time (from syringe to chamber) to the chambers. A flow rate of 20 μL/min was found to have a delivery time of 1 min. The microfluidic chamber was first washed with PBS before starting the assay. To perform the assay 100 μL of HBSS containing 20 μM 7-ethoxyresorufin and 40 μM dicumarol was injected into the microfluidic chamber with the micro-array cultured hepatocytes. After 1 minute the fluorescence was measured for 30 minutes (image taken every 2 minutes) using the confocal setup at a constant temperature of 37 °C (excitation 530 nm; emission 585 nm). Analysis was completed using ImageJ and Lecia LSM5 series software.

4.5 Results and discussion

4.5.1 Fibroblast arrays

Firstly experiments were conducted to confirm the reproducibility of cells attaching to micro pattern assays of collagen dots. 3T3 fibroblasts were seeded onto micro-array patterned substrates and attached to the collagen protein. Following incubation for 2 hours in the cell culture incubator, cells attached to the protein patterns. Unattached cells were washed away with a pipette twice with the appropriate cell culture medium. Areas of PEG were devoid of 3T3 cells. Using an average seeding density of 2.5×10^5 cells/cm², and cultured for 24 hours the results of which are shown in Figure 4.5-1. It was observed that

3T3 cells attached selectively to the collagen dots and were repelled by the PEG treated surfaces. This proved that micro-arrays of collagen dots on PEG surfaces promote cell proliferation within the designed pattern. Cell patterns were maintained for up to 5 days before the level of proliferation caused enough overgrowth to bridge the gap between dots. The results showed that PEG surfaces have a stability and resistance to cell attachment Figure 4.5-1 (c).

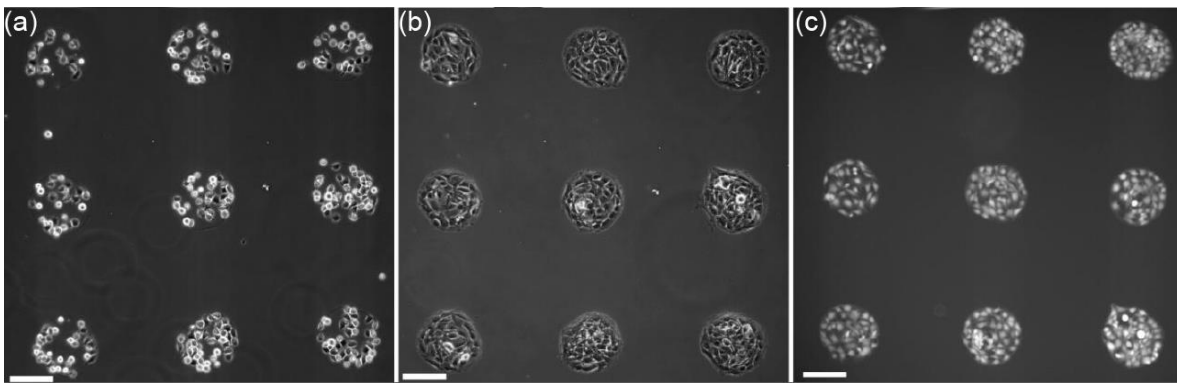


Figure 4.5-1 – 3T3 fibroblast array on a micro-array of printed collagen (0.9 mg/ml) with a cell seeding density of 2.5×10^5 cells/cm². Phase contrast images of cells on patterns after (a) 2 hours; (b) 24 hours; (c) fluorescence image of cells from (b) using calcein AM. Fluorescence emitted from cells shows viability of cells attached to the micro-array. Images taken by Zarowna-Dabrowska. Scale bars are 150 μ m.

Reliable cell patterns could be achieved for up to 5 days before the pattern was compromised. Printed collagen dots used in this work were 150 μ m in diameter making them among the smallest realised using this method of printing.²⁴³ The characterisation used for this process has been investigated in more detail by Zarowna-Dabrowska *et al*²⁰⁴. They observed that these dots offer enough surface area for small numbers of cells to attach and proliferate. A similar patterning system reported by Bhatia *et al.* observed results that hepatocytes islands less than 490 μ m elicited higher levels of hepatic function (albumin secretion and urea synthesis).²¹⁹ Thus the collagen dots designed micro-arrays in this work were in the ideal diameter range for enhanced hepatic functions of primary hepatocytes.

4.5.2 Hepatocyte arrays

As the results from 4.5.1 and Zarowna-Dabrowska *et al*²⁰⁴ showed, collagen arrays printed using a PerkinElmer Piezoarray spotter were suitable for 3T3 cell patterning. This conformation led to the investigation of using these arrays for primary rat hepatocyte arrays using the same technique.

As shown in the bright field image of Figure 4.5-2(a) cells have attached spread only on the collagen dots and are repelled by the PEG treated surface. Control cultures in untreated glass

have spread randomly across the surface of the glass as shown in Figure 4.5-2(b). Observation after 24 hours of culture showed that the hepatocytes exhibited features representative of viable specimens.^{235, 240} This includes distinct nuclei and nucleoli, polygonal morphology, anisokaryosis and a large number of binucleate cells. These features are visible in the bright field images shown in Figure 4.5-2(a) and (b).

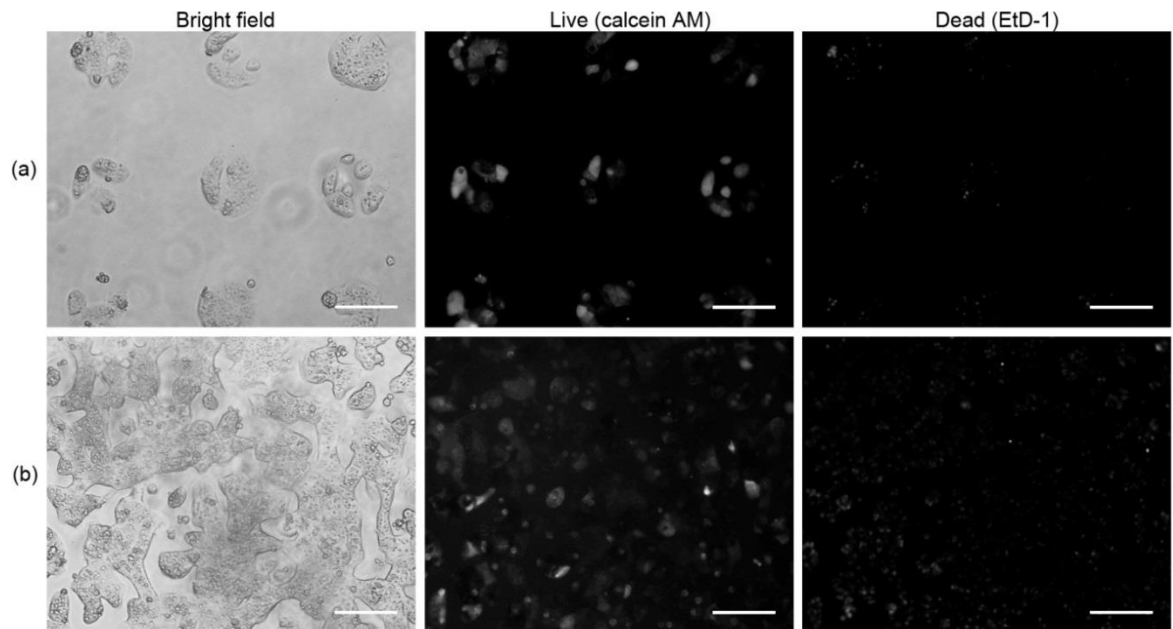


Figure 4.5-2 – Fluorescent microscopy images of primary rat hepatocyte arrays showing live/dead analysis. (a) Micro-array live/dead analysis after 24 hours incubation at 37°C, 5% CO₂, from left to right, bright field, live (calcein AM) and dead (EtD-1). (b) Control sample of hepatocytes cultured on untreated glass. Morphology of the hepatocytes cultured on the micro-arrays correlate with the morphology in the control samples. Live/dead analysis shows that the hepatocytes have a higher overall viability on the micro-arrays than on the untreated glass. Scale bars are 150 μm.

The results of live/dead analysis are shown in Figure 4.5-2(a) and (b) in the live (green) and dead (red) images respectively. Quantification of viability for the micro-array (number of live cells/[number of live cells + number of dead cells]) confirmed a higher viability of (95%) compared to the cell viability in the seeding solution (75% with trypan blue stain). Viability of the control sample shown in Figure 4.5-2(b) showed that the viability of hepatocytes grown on glass to be lower than that of the micro-array. Hepatocytes are anchorage dependant cells, their viability is improved by physiologically similar substrates for attachment.³⁹ Collagen is an abundant protein in the liver environment and hence the micro-array of collagen has improved the hepatocyte viability compared with the untreated glass substrate. These results show that viable hepatocyte cells adhered to the micro-arrays and were successfully cultured for 24 hours.

4.5.3 Micro-pattern of cells inside microfluidic channels

The results from Section 4.5.12 showed that PEG treated glass slides with collagen dots printed in an array was suitable for culture of primary hepatocyte cells. Thus microfluidic devices described in where used to culture cells on micro-array substrates. The chips were all placed in an incubator at 37°C, 5% CO₂ to provide the correct temperature for mammalian cells and to compensate for the loss of O₂ and CO₂ in the syringes and the biochip during culture. The flow rate used in the experiments was set at 0.1 μL/min.

4.5.3.1 Dolomite Device

This experiment involved the culture of cells using a Dolomite Resealable Chip Interface microfluidic device described in Section 4.4. This system allowed for the enclosure of the collagen patterned glass to a microfluidic chamber without any bonding steps required, thus making the device both reusable and avoiding the removal of the collagen through bonding techniques to glass by using plasma bonding.²⁴⁴ No screws are required for this design the system seals through a twist and lock mechanism, the device is sealed with a gasket.²⁴¹ In these experiments primary rat hepatocytes cells were seeded into the device for cell pattern formation to investigate the combination of protein micro-array collagen dot and microfluidics.

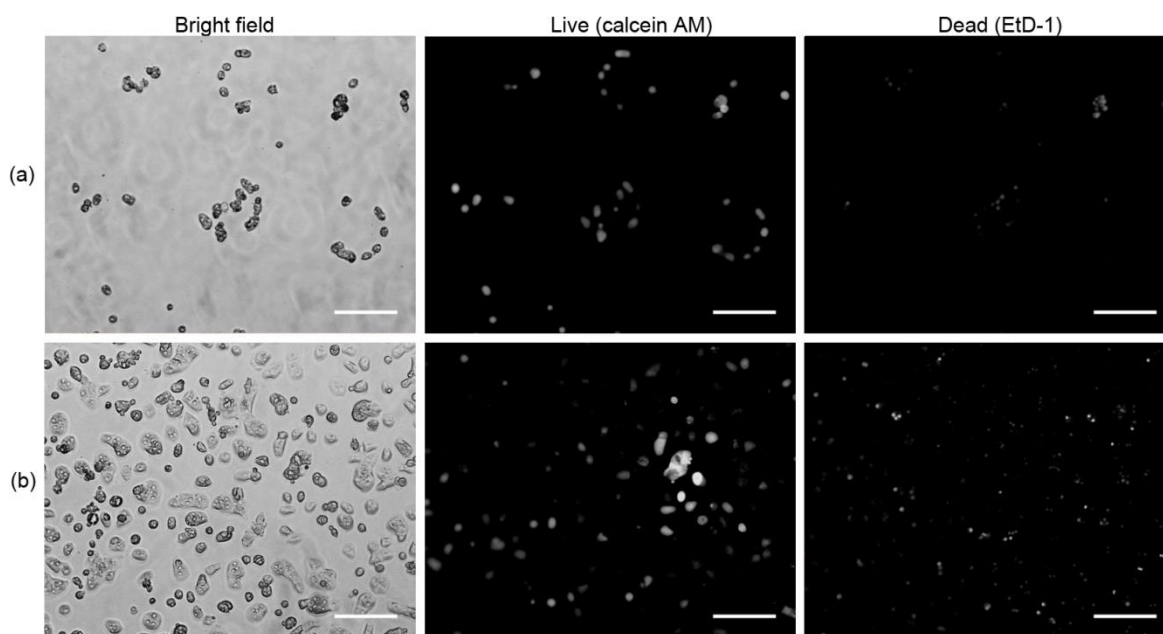


Figure 4.5-3 – Fluorescent microscopy images of primary rat hepatocyte arrays cultured with the Dolomite device showing live/dead analysis. (a) Micro-array live/dead analysis after 24 hours incubation at 37°C, 5% CO₂, from left to right, bright field, live (calcein AM) and dead (EtD-1). (b) Control sample of hepatocytes cultured on untreated glass. Morphology of the hepatocytes cultured on the micro-arrays correlate with the morphology in the control samples. Live/dead analysis shows that the hepatocytes have a higher overall viability on the micro-arrays than on the untreated glass. Scale bars are 150 μm.

The bright field image of Figure 4.5-3(a) shows cells attached and spread only on the collagen dots and are repelled by the PEG treated surface. Control cultures in untreated glass have spread randomly across the surface of the glass as shown in Figure 4.5-3 (b). Compared to results shown in Section 4.5.2 adhesion of cells to the dots was reduced when cultured in the Dolomite microfluidic device. Observation after 24 hours of culture showed that the hepatocytes exhibited features representative of viable specimens.^{235, 240} Distinct nuclei and nucleoli were visible and polygonal morphology however anisokaryosis and number of binucleate cells was reduced. Cells appeared to be more rounded than in petri dish conditions. These features are visible in the bright field images shown in Figure 4.5-3 (a) and (b).

The results of live/dead analysis are shown in Figure 4.5-3(a) and (b) in the live (green) and dead (red) images respectively. Viability of the control sample shown in Figure 4.5-3(b) showed that the viability of hepatocytes grown on glass to be lower than that of the micro-array. Attachment to the micro-array dots appears to have been reduced compared to the results in petri dishes Section 4.5.2. It is possible that the collagen has been washed away through the repeated steps required to culture cells within the microfluidic chamber. Additionally, the use of PMMA as the material for the microfluidic is a nonporous material. These results show that viable hepatocyte cells adhered to the micro-arrays in reduced numbers and were successfully cultured for 24 hours.

4.5.3.2 Single Chamber Device

As the Dolomite Resealable device used in the previous study shown in Section 3.3.4.1, culture of primary hepatocytes was demonstrated successfully with reduced cell adhesion to the patterns. This led to the design of a new PDMS microfluidic chip to allow for seeding of cells on glass slides prepared with PEG and a collagen printed pattern. It was hypothesised that by emulating the dimensions used by the commercial device similar results could be achieved with a custom device. It was also hypothesised that the use of PDMS, which is a porous material, would improve cell viability and potential attachment to the collagen dots.

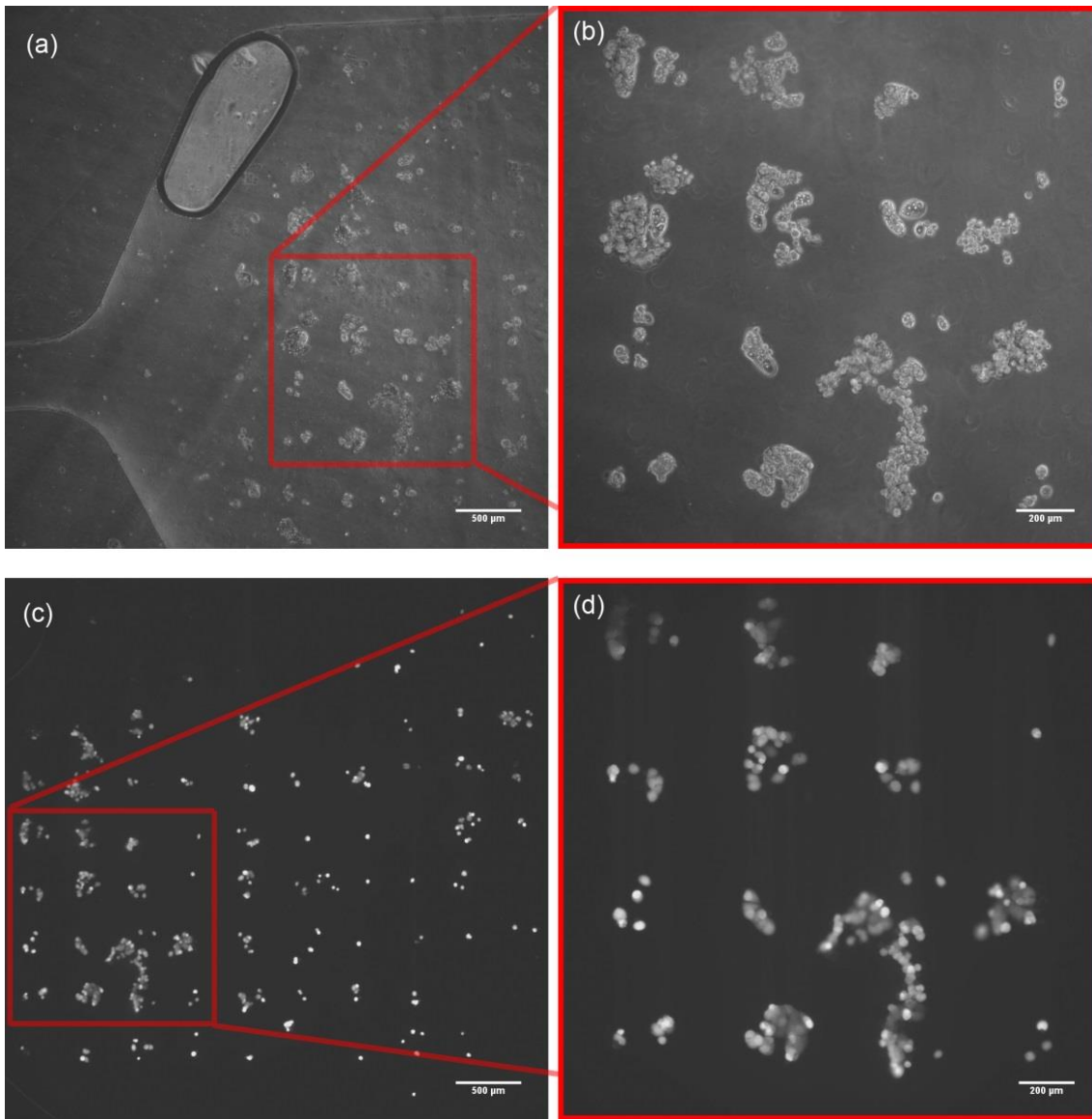


Figure 4.5-4 – Primary hepatocytes cultured for 24 hours inside the microfluidic device using the Chamber design. (a) Shows hepatocytes attached to collagen dots, (b) shows a magnified area showing detail of cells cultured on the pattern. (c) and (d) show the same culture of cells fluorescing due to calcein-AM staining; intense fluorescing of the cells indicates viable cells. Scale bars are 500 μm for (a) and (c), 200 μm for (b) and (d)

The bright field images of Figure 4.5-4(a) and (b) showed that cells attached and spread on the collagen dots and are repelled by the PEG treated surface. However cells made inter-dot contacts as shown in Figure 4.5-4(b). Compared to results shown in Section 4.5.2 adhesion of cells to the dots was reduced when cultured in the single chamber device. Attachment was similar in lack of uniformity when compared to the dot coverage in Section 4.5.3.1. Observation after 24 hours of culture showed that the hepatocytes exhibited features representative of viable specimens as previously discussed. Cells cultured on neighbouring collagen dots were observed to bridge the gap between them. They appeared to be rounded indicating a lack of adhesion to the PEG surface, instead preferring to attach to neighbouring cells.

The results of fluorescent staining by calcein-AM are shown in Figure 4.5-4(c) and (d). Fluorescent staining indicated that the cells had intact cell membranes showing viable cells.

4.6 7-ethoxyresorufin-O-deethylase (EROD) assay in microfluidics

4.6.1 Dolomite device

Results of the EROD assay performed on the Dolomite device are shown in Figure 4.6-1. The average resorufin metabolism for the first 10 minutes was undetectable, by 12 minutes the intensity increased and peaked at 16 minutes. The fluorescence intensity decreased gradually until the end of the experiment.

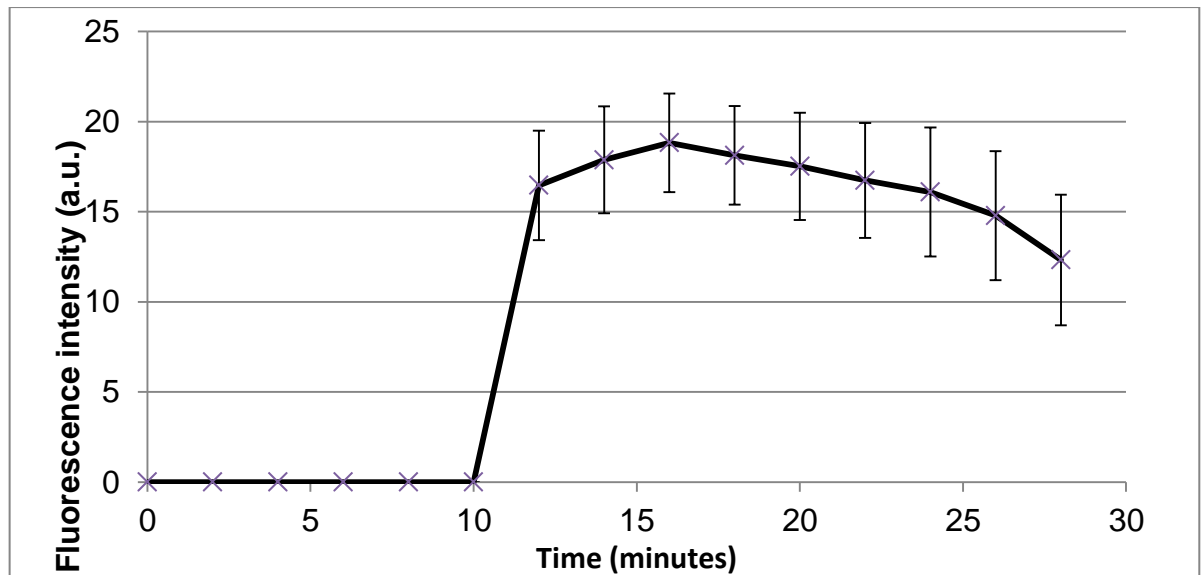


Figure 4.6-1 – EROD assay on the Dolomite device showing the average intensity of resorufin fluorescence emitted by single cells over time. The EROD assay indicates the related quantity of metabolised resorufin due to cytochrome P450. An increase in fluorescence intensity correlates to an increase in resorufin production. Each data point is an average value of randomly chosen single cells within the array. Each data point represents an average of reading from three cells.

4.6.2 Multiple chamber device

The following experiment consisted of conducting the EROD assay on a micro-array of hepatocytes. As a comparison the assay was also performed on hepatocytes cultured inside of a multiwell plate. Results of the EROD assay are shown in Figure 4.6-2. Representative results of P450 metabolism of resorufin, the intensity of which indicates cell function. Higher intensity of fluorescence indicates higher P450 activity. The assays performed in the petri dishes produced a typical curve indicating an average intensity of 100 which using the resorufin curve corresponds to a concentration of less than $0.01\mu\text{M}$ Figure 4.6-2.

However, the assays performed in the microfluidic device yielded a signal four times weaker than the results observed in the Petri dish shown in Figure 4.6-3.

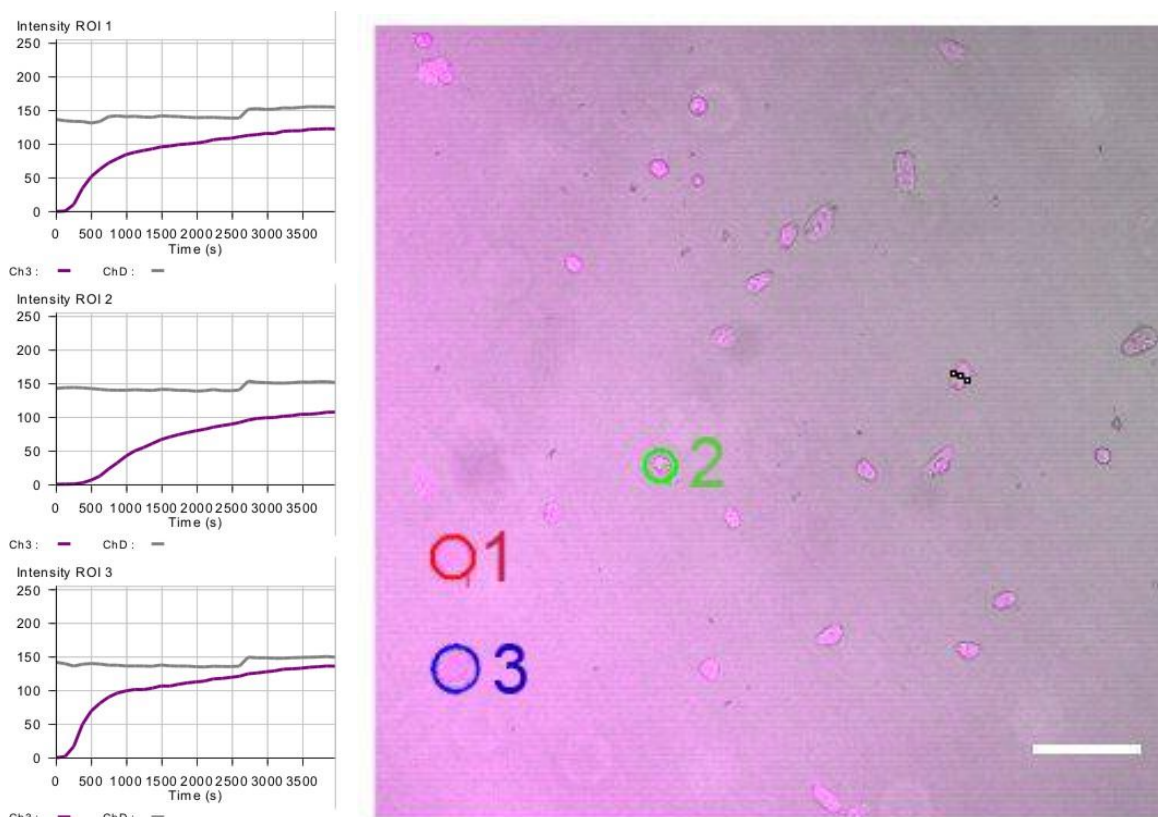


Figure 4.6-2 - EROD assay performed in a petri dish with hepatocytes. Three regions of interest (ROI) were selected as shown in the microscope image. The respective intensity over time is shown for each ROI is plotted on the left hand side of the figure. Scale bar is 100 μ m.

The results here show that the resorufin concentration being produced by the hepatocytes is about half what was produced by that of the petri dish. Attachment of the cells to the micro-array pattern was also shown to be significantly reduced compared to results from petri dish and previous microfluidic experiments. Hepatocytes have poorly attached to the surface of the micro array, distinct nuclei and nucleoli were not visible and polygonal morphology not observed.

The results suggested that micro-pattern arrays fabricated using these methods were not suitable for microfluidic culture. It has been reported that there can be significant differences in P450 enzyme activity between donors (human and animal) and even within an individual.⁴¹ Gomez-Lechon *et al.* stated that, “variability in P450 enzymes is the rule rather than the exception”.⁴¹ The hepatocytes used in both the microfluidic and control EROD assay were from the same batch therefore some variation was expected. The difference in conditions for the hepatocytes was the microfluidic environment.

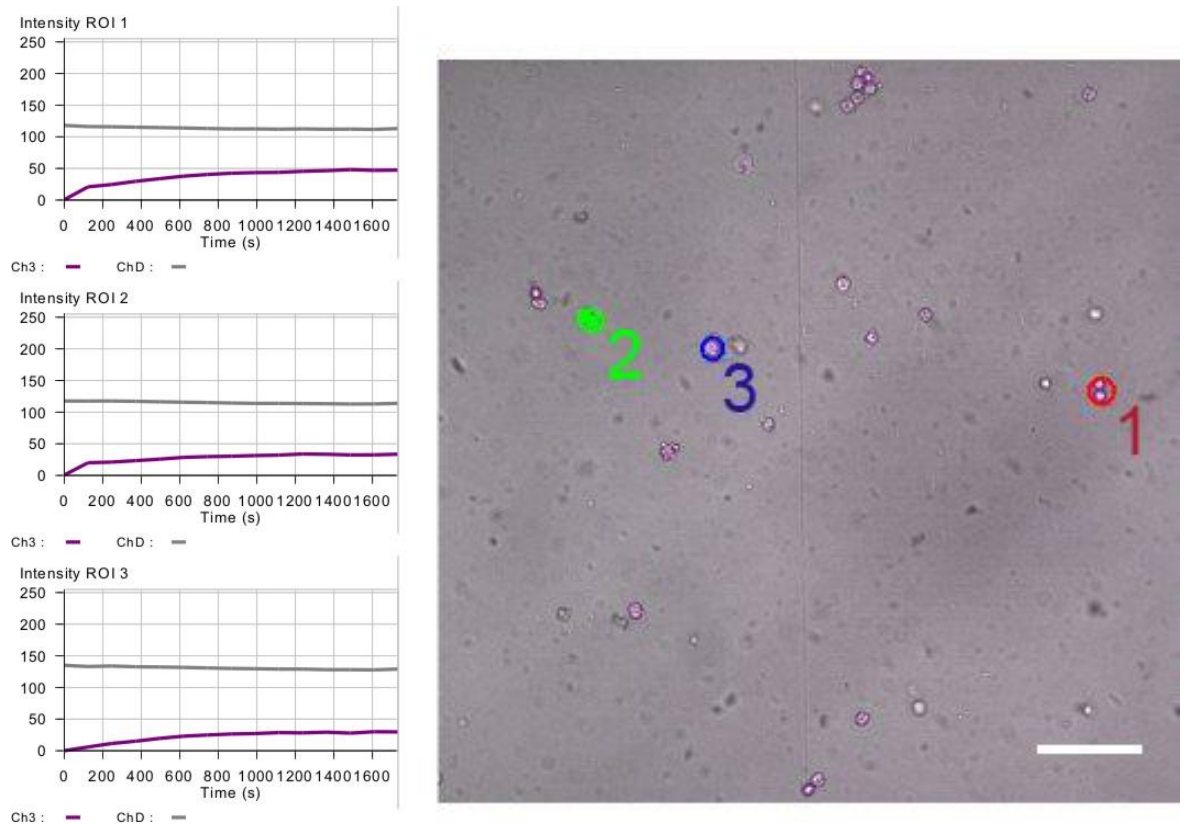


Figure 4.6-3 - EROD results on four chamber device. Three regions of interest (ROI) were selected as shown in the microscope image. The respective intensity over time is shown for each ROI and is plotted on the left hand side of the figure. Scale bar is 100 μm .

The reduction in performance of hepatocytes with microfluidics can be effected by the flow rate and subsequent shear stress. Typically the shear stress found *in vivo* is in the region of 10-50 mPa.¹⁰³ As shown shear stress calculations by *Domansky et al* have shown, flow rates of 0.25 mL/min (0.3 $\mu\text{L}/\text{min}$ within the device channels) should not exceed 30 mPa. Culture results of shear stress and velocity by *Zhang et al* are also indicative of flow rates in the range of 15-60 $\mu\text{L}/\text{min}$ being suitable for hepatocyte culture within a microfluidic device.²⁴⁵ For the experiments conducted in this work the flow rate of 0.1 $\mu\text{L}/\text{min}$ was selected to keep shear stress on the cells low and to refresh the chamber once every hour and will not have affected the cells negatively.

The confluence of the cells will have affected the hepatic functionality. It has been consistently reported that confluent cultures have higher hepatic function than sparse ones, partly due to cadherin interactions.¹¹⁹ However this was the case for both the microfluidic device and control.

Low oxygen levels would also be a cause for a reduction in cell functions due being an essential nutrient for cell culture. However, one of the reasons for selecting PDMS as the material for the microfluidic channels was for the advantageous high diffusivity (4.1×10^{-5}

cm²/sec) and solubility (0.18 cm³) of oxygen in PDMS making it highly suitable for cell-based studies.²⁴⁶

However, it is possible that the manual injection of the cells of seeding was at fault. Both in terms of potentially washing away the collagen printed on the surface of the PEG and also negatively affecting the cell viability. It has been observed by *Toh et al* that seeding flow rates of 0.1 mL/hr (1.7 μL/min) can have a significant impact on cell viability.²⁴⁷ As the hepatocytes were injected into the device manually, the flow rates were potentially > 1.7 μL/min and placed high shear stresses on the cells.

4.7 Conclusions

The use of high resolution collagen dot micro-arrays fabricated by piezoelectric printing for patterning cells within microfluidic systems has been demonstrated. This work has confirmed that cell arrays of 3T3 fibroblast cells and primary hepatocytes using these micro-arrays are stable over a 24 hour period.

Demonstration of primary hepatocyte culture on micro-arrays within a Dolomite microfluidic device was shown to yield viable cells and cell arrays. Two microfluidic devices for micro-array culture as a platform for high-throughput toxicity testing were designed, fabricated and tested. It was shown that micro-arrays of primary hepatocytes were viable and successfully attached to the micro-arrays within the device. Attachment of hepatocytes to the micro-array was reduced however from that of the results observed in Petri dish cultures. Results of EROD assay studies showed a decreased level of P450 activity by four times when hepatocytes were cultured within microfluidic devices compared to Petri dish conditions. Further investigation into the environmental effects reducing the function of P450 enzymes in hepatocytes cultured on micro-arrays within microfluidics is suggested.

5 Micro liver fabrication platform

5.1 Abstract

In this chapter, we develop a successful cell manipulation technique based on dielectrophoresis (DEP), which has been described in detail in Chapter 1. In brief, a biomimetic strategy to provide an *in vivo*-like *in vitro* environment for toxicology testing was designed, prototyped and tested. Employing electrodes designed and microfabrication methods described in Section 2.7.2, DEP forces assembled liver cells into physiologically relevant liver, cord-like hepatocyte structures. Post-DEP patterning, these biomimetic patterns were fixed by agarose hydrogel and manipulated by a laser cut paper ring substrate into conventional 96-well plate cell culture dishes. Observation of these biomimetic micro liver structures showed high viability (80-90%) and an increase in liver specific functions (20%) compared to control samples after 48 hours.

5.2 Introduction

Drug-induced liver injury (DILI) is the most prominent reasons for pharmaceutical products being banned, withdrawn, severely restricted or not approved by governments since the 1950s.²⁴⁸ This underlines the importance of the liver itself as the toxicity centre of the human body and hence is the major target of toxic effects of drugs.^{40, 249}

At present industrially established high throughput hepatocyte test assays employ 2D or 3D tissue culture which are limited to perturbations in pathways of toxicity (PoTs) at the molecular, organelle and cellular levels of hepatocytes.¹¹⁷ Additionally animal testing suffers from phylogenetic distances between animals and humans. There is a critical demand for human biological models to improve the understanding toxicity effects induced by new compounds.²⁵⁰ As over 50% of all withdrawn drugs fail due to acute liver toxicity,¹¹⁸ it would be advantageous to model the human liver as accurately as possible to deliver reliable results.

5.2.1 Dielectrophoresis methods for patterning liver like cell structures

As discussed in Section 2.7.1 the liver is a complex organ, which is challenging to model using a microengineered approach. Approaches to improve the accuracy, precision and relevance of liver models on chip have been made using dielectrophoresis to pattern cells into physiologically relevant structures.^{76, 117, 225}

Work by *Schütte et al* demonstrated a method of developing an artificial liver sinusoid within a microfluidic chamber with DEP.⁷⁶ This involved the trapping of liver cells to protein modified surfaces on chip which could then be supplied with medium carrying nutrients. However this approach does not offer an extra cellular matrix (ECM) for the liver cells to adhere to which has been shown to improve hepatic functionality.²¹⁹

Another approach shown by *Ho et al* used DEP with a microfluidic chip to pattern hepatocyte cell line HepG2 into a lobule like structure.¹²² Further to this they fabricated an array of lobule like electrodes to form a 1 cm² area of 2D patterned hepatocytes in co-culture with human umbilical vein endothelial cells (HUVEC). In general, cell functions in 3D culture rather than 2D culture result in enhanced cell-cell interactions.²⁵¹⁻²⁵³

Approaches by both *Ho et al* and *Schütte et al* employ a disposable, one shot method. Additionally, these approaches are not designed to integrate with current industry methods for toxicity testing standards as the microfluidic chip must be disposed of due to cells attaching to the substrates used. These models have not been designed to be compatible with industry standard multi-well culture plate dimensions for high-throughput screening of drugs and compounds.¹⁰³

Patterning of mammalian cell in agar has been demonstrated by *Albrecht et al* in 2 cm² hydrogel.¹²³ Studies have shown that hepatocyte cell lines retain liver specific functions including albumin secretion, urea synthesis and CYP450 activity when cultured within agarose based hydrogels.^{218, 253} One of the major tests for investigating liver functionality is albumin secretion, a protein primarily synthesised in the liver.²¹⁹

5.2.2 Aims of this chapter

The aim of this work was to build a liver lobule-like tissue construct for toxicity testing that was compatible with industry standard assay methods. Conventional 2D cell cultures grow until confluence unlike cells cultured within agar. Limited proliferation within this microenvironment can control the cell density and thus make toxicity screening tests more

consistent than 2D cultures. This was achieved by employing the system designed and optimised in Section 2.7.4. By using physiological data an electrode design was developed to replicate the hepatocyte cord structure in the liver into an array of liver lobule like structures. The electrode were designed to be fabricated on only one surface in order to simplify the operation of the system which allows the system to be re-useable.

This device resulted in reproducible patterns of liver cells according to the electric field induced by the electrode design, producing an array of lobule like liver sinusoids mimicking the liver structure *in vivo*. Post-DEP the pattern was held by an agar gel providing a 3D environment for the cells and supported by a paper ring substrate. This innovative technique makes use of laser-cut, wet-strengthened, medical grade filter “paper rings”. These enable the removal of the cells, patterned in 3D in the soft gel (agar 1% wt/vol), from the electrodes to be placed in a culture system of choice; a highly parallel microtiter plate. This was selected as these plates are compatible with commercial plate readers which would allow scaling into industry-scale screening.

3D patterning was achieved with 80-90% viability of cells confirmed over 3 days. The increase of albumin protein was observed by ELISA to increase after 2 days of culture (0.8 ± 0.08) compared to controls (0.6 ± 0.04). This showed an increase in the functionality of HepG2/C3A cells patterned into live lobule-like patterns within agar.

5.3 Numerical simulation of dielectrophoresis

In order to test the DEP effect being induced by the electric-field gradients of the lobule array electrodes simulations were conducted. The simulations were carried out using COMSOL Multiphysics (Cambridge, UK) and its AC/DC module²⁵⁴ of simulated steady-state electric fields. Computationally the complete array of 19 lobules proved to be too large a model to work with. Total meshing tetrahedral elements were over 4 475 849 for the complete 19 lobule array proving computationally intensive and could not be successfully meshed. One lobule electrode had 235 571 meshed tetrahedral elements and was successfully meshed. The array is formed from 19 lobule electrodes with minor adjustments to provide connections as shown previously in Section 2.7.1. It stands to reason therefore that simulating one such lobule electrode unit was an accurate representation of DEP forces in one lobule, the results of which would be insignificantly different to other lobules in the array. However this does not interfere with the analysis of the overall electric field prediction and therefore is acceptable for visualising DEP forces.

5.3.1 Meshing and modelling

Figure 5.3-3 shows the simulation of the 60 μm lobule design at 10, 50 and 100 μm slices through the model. The design was embedded in the bottom surface of a cuboid measuring 1.1 x 1.1 mm and 100 μm in depth as depicted in Figure 5.3-1(a). This depth was selected as it is the thickness of the gasket used to define the micro liver patterning volume. The relative permittivity of the solution was chosen to be that of water. For these simulations it is presumed that the volume is a constant homogeneous fluid (DEP buffer and agar solution in a liquid state), hence there are no changes to the relative permittivity. Meshing was computed using the ‘extra fine’ setting providing a mesh consisting of 235571 tetrahedral elements allowing for an accurate numerical simulation of a single lobule electrode illustrated in Figure 5.3-1(b).

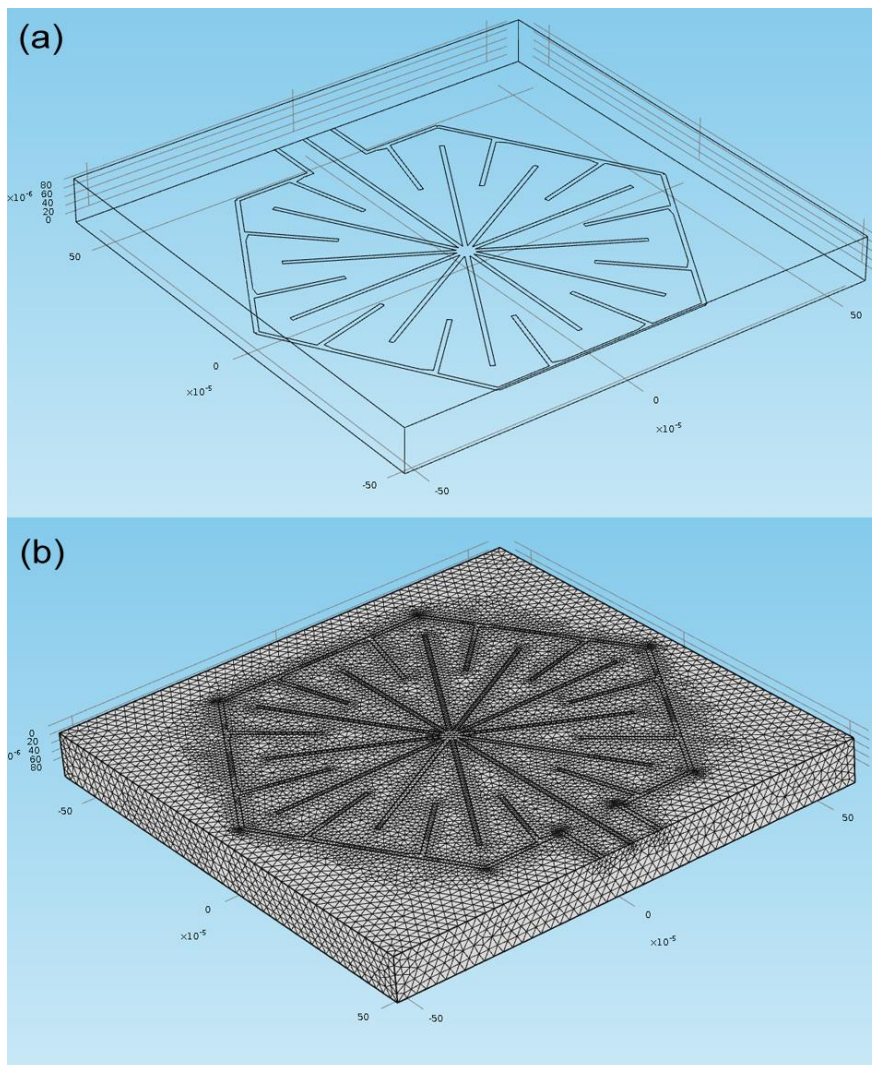


Figure 5.3-1 – 3D renders of COMSOL geometry and mesh. (a) 3D wireframe render of a lobule electrode with 60 μm spacing embedded to the bottom surface of a defined fluidic volume (1.1 x 1.1 x 0.1) mm. The electrodes are infinitely thin to simplify the meshing. (b) 3D mesh of geometry shown in (a) areas of high mesh density was visible in the corners of the lobule geometry and at the ends of the electrode arms. The total meshed tetrahedral elements was 235571.

The DEP force direction was defined in COMSOL by the using the equations:

$$\nabla E^2_x = \left(\frac{d}{dx} (Ex^2 + Ey^2 + Ez^2) \right) \quad (7)$$

$$\nabla E^2_y = \left(\frac{d}{dz} (Ex^2 + Ey^2 + Ez^2) \right) \quad (8)$$

$$\nabla E^2_z = \left(\frac{d}{dz} (Ex^2 + Ey^2 + Ez^2) \right) \quad (9)$$

$$\text{therefore, } \nabla E^2 = \sqrt{(\nabla E^2_x + \nabla E^2_y + \nabla E^2_z)} \quad (10)$$

where, E is the amplitude (rms) of the electric field.

5.3.2 Electric field analysis

The operating AC potential was set to be 10 Vpp at a frequency of 10 MHz. The rendered simulation images in Figure 5.3-2 shows a slice plot of the electric field 10 μm from the surface of the electrodes. A complete lobule is shown in Figure 5.3-2 (a), with the image on the right Figure 5.3-2 (a) showing a close up. The indicated red line indicated shows the line that was used to measure the change in electric field 1 μm away from the electrode edge. The electric field plot is of this line is shown below (0 - 405 μm) from the inside edge of the electrode to the outside edge of the counter electrode. The simulation showed that the electric field is highest at the ends of the electrode arms, peaking at 212 kV/m. As the distance from the end increased, the electric field linearly decreased. Directly across from the end of the electrode arm, the counter electrode edge electric field was in the region of 70 kV/m. These results show that the electrode design causes areas of high electric field strength in the pattern designed and thus pattern cells into cords, 60 μm apart. These cords radially spread around a centre with lower cell patterning.

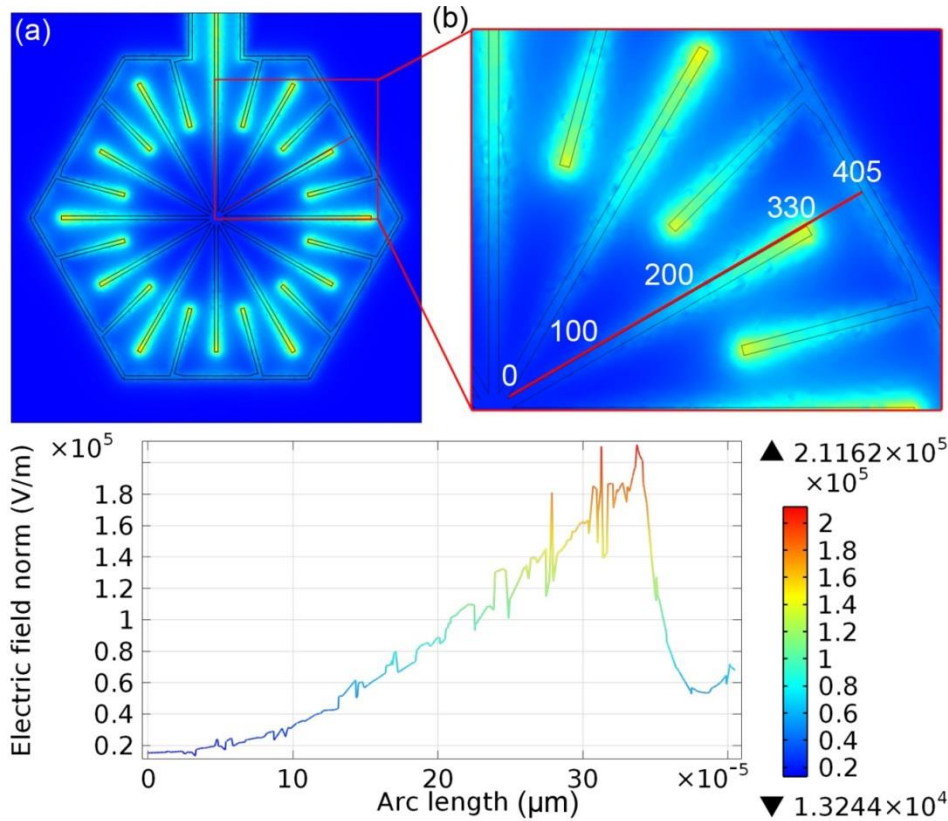


Figure 5.3-2 – Simulation results of a single electrode lobule using 60 μm spacing between electrodes. (a) Slice plot 10 μm above the surface of the electrodes showing the electric field distribution, (b) shows a close up of the top-right hand side of the electrodes. A red line shows the data used to plot the electric field distribution 1 μm next to the edge of the electrodes. The electric field has shown to increase linearly as the distance between the electrode arm and counter electrode decreased. At the end of the electrode arm the electric field is 211 kV/m, then the electric field drops sharply before picking up to 70 kV/m at the edge of the counter electrode.

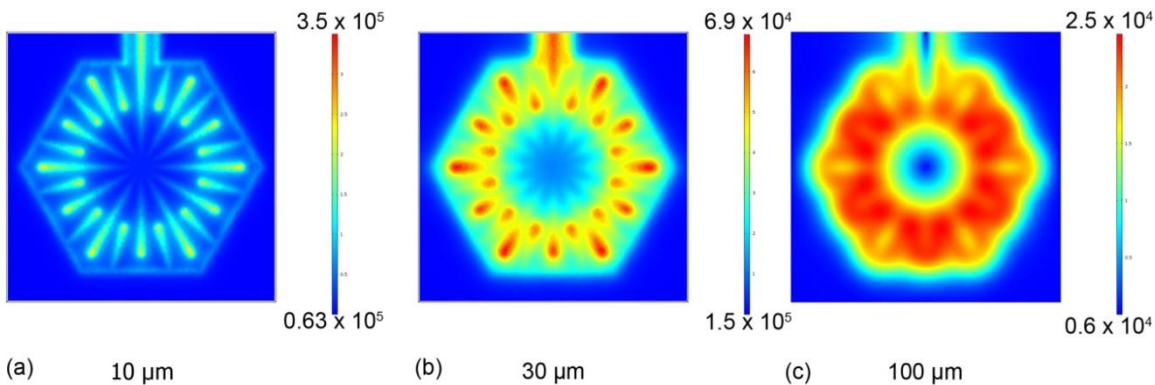


Figure 5.3-3 – Numerical simulation of electric field by applying 10 V peak-to-peak at 10 MHz for a cell of the lobule array. (a) The distribution of the normalised electric field at 10, (b) 30 and (c) 100 μm from the electrode surface. Scale is in electric field strength (kV/m). Volume simulated is 1.1 x 1.1 mm, 100 μm in depth.

As the distance from the electrodes increased, the electric field intensity decreased. Plotted slices of the electric field through the model volume are pictured at 10, 30 and 100 μm from the electrode surface in Figure 5.3-3. The plotted 3D slices through the model show that the intensity of the electric field is highest close (10 μm) to the electrodes as shown in Figure 5.3-3(a). The definition of the electric field correlates to the electrode pattern in this

plot, the field decreased linearly towards the centre of the lobule. The slice taken at the 30 μm shown in Figure 5.3-3(b) indicated that the definition of the pattern decreases as the distance from the electrode increased. The red areas indicate generation of an electric field in the region of 60 kV/m, this due to the ends of the electrode arms. The final slice through the model at 100 μm shown in Figure 5.3-3(c) indicated that the electric field was in the region of 20 kV/m. The plot showed red to orange colouring of the slice indicating that the electric field range is in the range of 15-25 kV/m. The exponential drop in electrical field due to the increasing distance from the electrode over 100 μm in Figure 5.3-4 is shown. Analysis of patterning efficiency in regard to distance from the electrode by *Albrecht et al*²¹⁶ demonstrated that patterning time increased as the distance from the electrodes increased. These results from the simulation of the electric field are in agreement with that of their results.

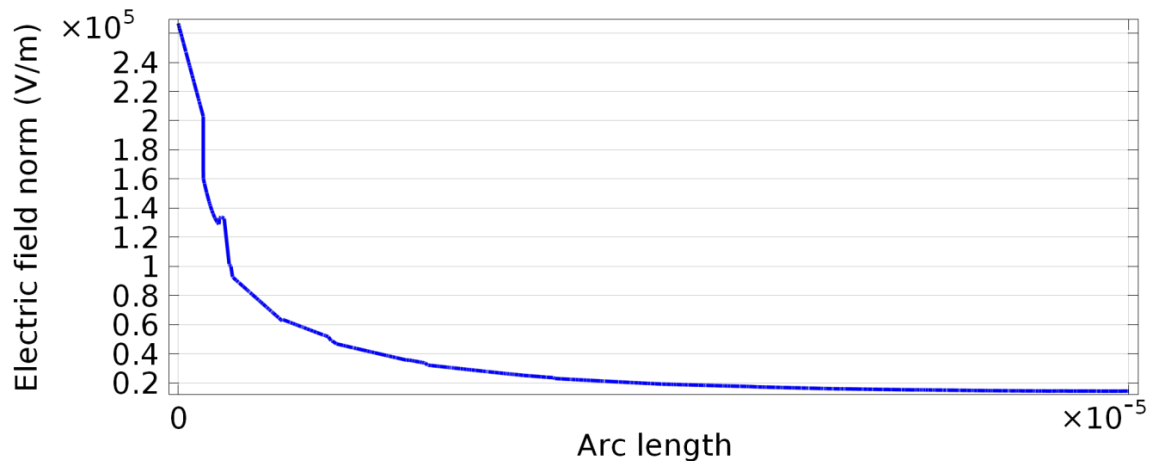


Figure 5.3-4 – Electric field strength over the 100 μm volume measured at the tip of the electrode arm shown in Figure 5.3-2. The electric field was shown to decrease exponentially as the distance from the electrode surface increased.

5.3.3 Positive dielectrophoresis force direction analysis

The system requires that cells are patterned throughout the defined volume by the gasket which was 100 μm thick. As shown by the electric field simulation results in Section 5.3.2, the electric field decreases exponentially as the distance from the electrode surface increases. For distances larger than 200 μm patterning becomes negligible. By selecting a gasket to provide a 100 μm thick gel layer, cells present in the agar DEP buffer solution would be patterned due to the forces created by the electrodes as illustrated in Figure 5.3-5.

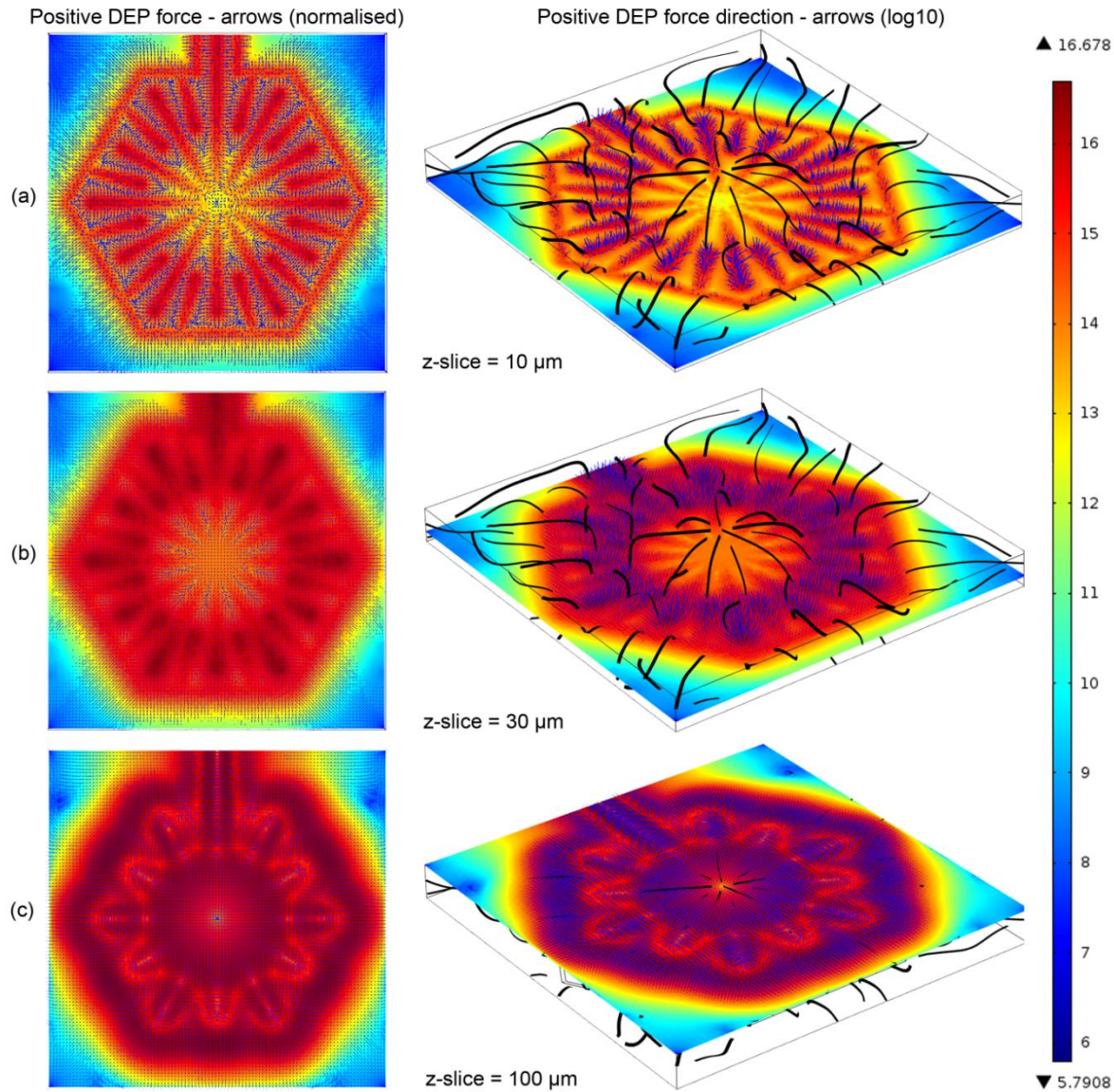


Figure 5.3-5—Numerical simulation of ∇E^2 (V^2/m^3 , \log_{10} scale) in a single cell from the lobule electrode array. Positive DEP force direction is displayed by the $\log_{10}(\nabla E^2)$ by slices through the x-y axis of the model. A rainbow light scale represents the electric field gradient distributed through the model. DEP force direction is indicated by blue arrows both normalised in the x-y view and as a log in the isometric view. In addition black ribbons represent paths that particles would take when experiencing DEP forces as displayed in the isometric view. (a) shows a $10\ \mu\text{m}$ slice through the model, (b) $30\ \mu\text{m}$ and (c) $100\ \mu\text{m}$. The maximum ∇E^2 induced is 16.7 and minimum is $5.8\ V^2/m^3$, \log_{10} scale. The electric field is applied with 10 V peak-peak, permittivity is that of water at 80.

Results plotted from the slice $10\ \mu\text{m}$ from the electrodes surface are shown in Figure 5.3-5(a). The forces are strongest ($13\text{-}16\ V^2/m^3$) close to the electrodes, peaking at the edges of the electrodes ($13\text{-}16\ V^2/m^3$) as seen in Figure 5.3-5 (a). The isometric view shows blue DEP force arrows that indicate the log force at $10\ \mu\text{m}$. The forces are strongest radially from the interface between the two electrodes compared to the forces in the centre of the electrode lobule. DEP forces are present at the edges of the lobule in the range of ($12\text{-}13\ V^2/m^3$). Inside of the patterning area, the middle section has the weakest DEP forces due to the fact that the counter electrodes are not alongside.

Additionally the DEP forces created by the electrode arrangement create a circular pattern seen in centre of the slice plot of Figure 5.3-5 (a). The electric field at the ends of the electrodes is stronger than the counter-electrode edges at the centre of the electrode lobule as shown in 5.3.2. The effect of this is that the DEP forces at the ends of the electrodes are in the region of $16 \text{ V}^2/\text{m}^3$ as opposed to the forces at the edges of the counter electrode arms spreading from the centre ($12\text{-}14 \text{ V}^2/\text{m}^3$). This is a limitation of the approach to the design by placing both electrodes on the same surface. However this is an unavoidable defect in the pattern as the system must remain open to allow removal of the gel post-patterning. Using an ITO based system and/or microfluidic handling would mean that this removal step would not be possible.^{76, 225}

The plot of a $30 \mu\text{m}$ slice is shown in Figure 5.3-5 (b). Analysis of the electric field previously showed that $30 \mu\text{m}$ from the electrode surface the electric field was in the region of $50\text{-}70 \text{ kV/m}$, the area of which covers the edges and surrounding area of the electrode arms. These results confirm that the electric field provides DEP force in the regions designated by the electrode design. In correspondence to the reduction of the electric field with relation to distance from the electrode, the DEP forces at the edges of the electrodes has decreased as well, to the range of $11\text{-}14.9 \text{ V}^2/\text{m}^3$. The maximum force has reduced slightly to $14 \text{ V}^2/\text{m}^3$ and the force in the centre of the lobule is $1 \text{ V}^2/\text{m}^3$ lower than that of the edges.

This continues in the $100 \mu\text{m}$ slice illustrated in Figure 5.3-5 (c) with the maximum force decreasing further to $12.8 \text{ V}^2/\text{m}^3$. The blue DEP force arrows indicate that the direction of the forces were strongly now in the x-axis. The gradients show the patterning at this distance from the electrodes was not as defined as at the 10 or $30 \mu\text{m}$ slice. This is in agreement with the expected drop in electric field at this distance. DEP force can be seen to be pushing away from the centre. Isometric images of the model display this more clearly with the black ribbons which show potential paths of particles as they are subjected to DEP forces in the volume. Following a particle from the middle of the volume directly above the centre point, the trajectory follows what can be described as the side of a dome to the tip of the outer electrodes. Generally speaking, particles will be gradually pulled into the electrodes mostly with x-axis movement.

5.4 Methods

5.4.1 Microfabrication

The liver lobule like structure of the electrodes was fabricated using the methods described in Section 2.7.2. Liver lobule mimetic electrodes were fabricated using photolithography and metallisation to define electrodes of Pt (10 nm)/Au(100 nm) suitable for DEP, connectors were then soldered to the electrodes.

5.4.2 Operation of the micro liver patterning system for heterogeneous hepatic cells

The illustrations in Figure 5.4-1 show the operation of the liver lobule mimetic patterning. Microfabricated Pt/Au electrodes on the surface of a glass substrate are used to build a micro liver in agar with a paper substrate. In order to keep the 1% agar-cell solution in a liquid state (typically 60 mPa.s)²⁵⁵ to allow for cell patterning a Peltier system was installed to maintain the temperature in the region of 37 °C as shown in Figure 5.4-1 (a).

This is because the HepG2/C3A cell line originates from a 15 year old Caucasian male; the optimal core body temperature of a human is 36.8 °C ± 0.5 °C depending on external factors.²⁵⁶ A cover designed in SolidWorks and built with the HP DesignJet encloses the system while allowing connections for electrodes, Peltier and thermocouple to reduce the effect of evaporation. (b) Hepatic cell line C3A cells are then trapped by DEP forces in the pattern designated by the electrodes induced by an AC electric field Figure 5.4-1 (b).

Following patterning, the system is then cooled to 18 °C by reversing the current of the Peltier and the AC field is switched off Figure 5.4-1 (c) once the air temperature has dropped to 25 °C. This cooling temperature was selected because agar 1% solution when in the range of 18-20 °C complete gelation occurs.²²⁴ Additionally, it has been observed that agar 1% solution enters the gel phase at 25 °C meaning that the DEP forces are no longer required to hold the cells in place.

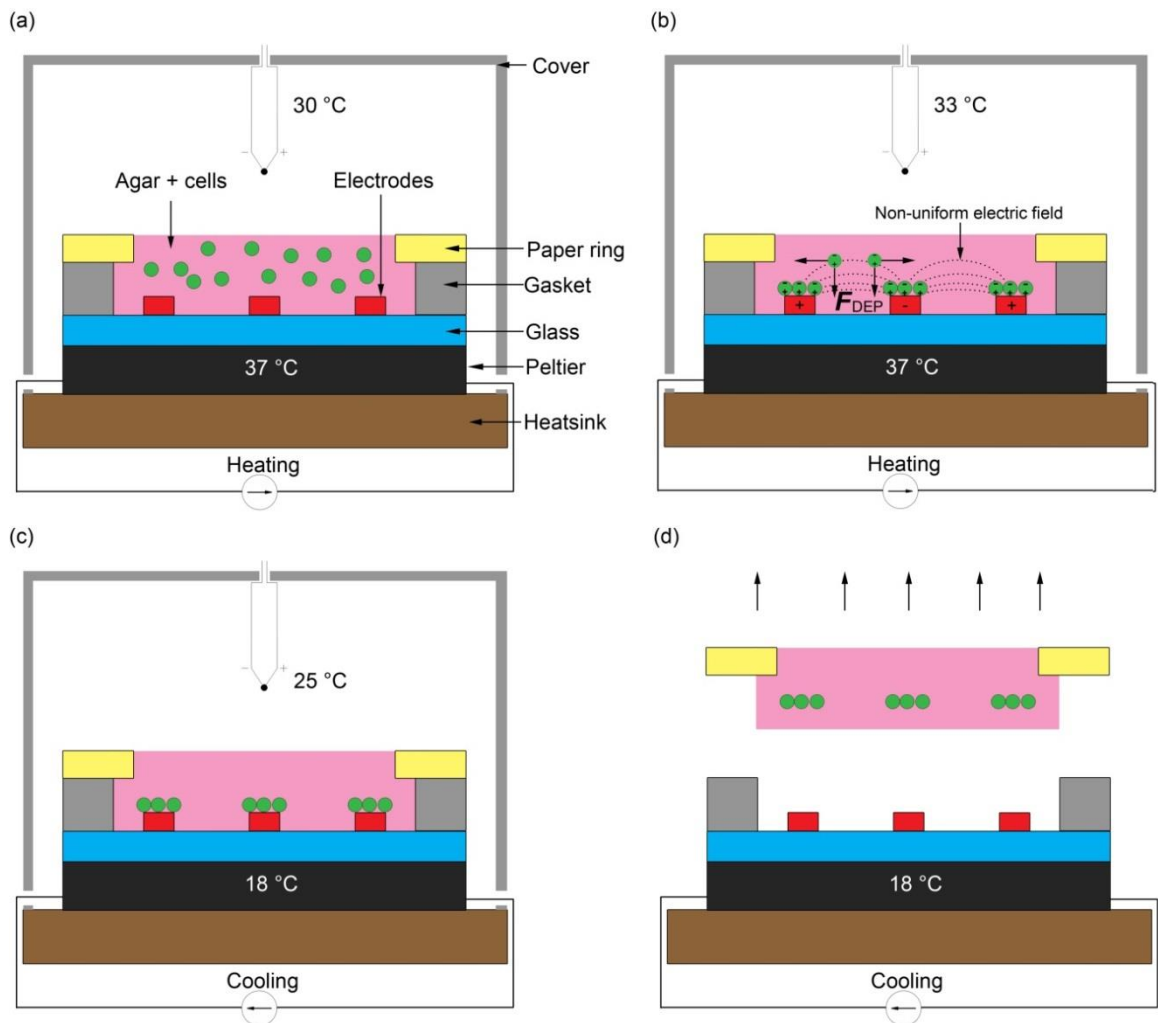


Figure 5.4-1 – The system setup and operation for patterning liver like structures within an agar gel with a paper substrate. (a) Warmed 1% agar solution with randomly distributed cells at 37 °C was pipetted into volume designated by the gasket. The Peltier warmed the glass substrate on which the electrodes are situated and enclosed with a cover. (b) Hepatic cells were captured by positive DEP forces (F_{DEP}) induced by a non-uniform electric field. (c) Once patterning was completed the Peltier was switched to cooling mode dropping the temperature of the agar to 18 °C curing the gel. Once the air temperature reached 25 °C the AC field was switched off. Agar 1% solution enters gel phase at this temperature.²²⁴ (d) The cells patterned by the DEP forces are not held in place by the cured agar. The paper substrate containing a biomimetic micro liver is used to manipulate the patterned cells into a culture system.

Reversing the current of the power supply while keeping the value constant at 0.28 A was found to deliver a temperature of 18 °C. Thus 18 °C was selected as the temperature used to induce gelation. This temperature is below the optimal temperature for cell activity which was stated previously as 37 °C. It has been shown that long-term exposure to temperatures as low as 28 °C will reduce mammalian cells (mouse leukemic cell line, L5178Y) proliferation.²⁵⁷ However this was a short term exposure therefore long-term damage to cells was not expected. The pattern was then held by the cured agar which in turn was attached to the paper substrate ring. This ring can be used to remove the biomimetic micro liver from the patterning system to a culture system Figure 5.4-1(d).

5.4.3 Cell patterning process

5.4.3.1 STEP 1 – Sterilisation

The pattern process is detailed in Figure 5.4-2. The system was setup inside a biosafety cabinet all items entering the hood were sprayed with 70% EtoH. All possible implements to be used in the process were sterilised by autoclave: tweezers, paper rings, pipette tips, Eppendorf tubes. Boxes were wrapped in aluminium foil to maintain sterility in the hood over the course of one week after which they were renewed. Gaskets were sterilised in 70% EtoH for 5 minutes before being left to dry in a glass Petri dish. DEP electrodes both for patterning and control were sterilised in the same manner. 10 μ l pipette tips were placed inside 1.5 ml Eppendorf tubes using tweezers and closed. These were then placed in a 37 °C water bath with a water bath float. Eppendorf tubes for holding cells and agar were also placed in the water bath float.

5.4.3.2 STEP 2 – Assembly

The heat sink was placed on the hood surface and thermal paste was applied in a thin layer to the top surface before pressing two Peltiers on top side by side. Electrodes were then placed on top of Peltiers with a drop of D.I. H₂O acting as a loose adhesive and thermal connection to the electrodes Figure 5.4-2(a). The drop of water was renewed between experiments due to evaporation. Electrical connections were then made to the frequency generator and PSU as well as the thermocouple. All connections were taped in place to a metal block to reduce cable movement disrupting the setup. The Peltiers were switched on (0.28 A) to bring the surface temperature of the electrodes to 37 °C. The cover was placed on the heat sink closing the system. Air temperature was observed using the thermocouple to be 30 °C with the cover on, the hood temperature typically was 25 °C.

5.4.3.3 STEP 3 – Patterning of C3A cells in agar (HEATING)

Once surface and air temperature had been reached, the Agar 2% solution as described in Section 2.7.3.3 was used to wet the paper rings before being placed on the perimeter of the 5 mm hole punched in the gasket, the cover was then replaced Figure 5.4-2 (a). The signal generator was then switch on (10 Vpp, 10 MHz, sine wave). Prepared cells in agar as described in Section 2.7.3.3 were then retrieved from the water bath and kept warm as well as 2% agar solution. Two 1.5 ml Eppendorf tubes containing warmed pipette tips were also retrieved from the water bath. The first pipette used to collect 10 μ l of 2% agar solution.

Two paper rings were saturated with 2% agar before being placed around the circumference of the 5 mm hole in the gasket. This was used to impede wicking of agar solution with cells into the paper as it was designed as a substrate for the agar, not a culture environment for the cells. The second pipette was used to collect 10 μ l of 1% agar cell solution. This was pipetted into the volume created by the paper ring and gasket Figure 5.4-2 (b). This step was repeated for the control and the cover replaced. DEP forces were left to pattern the cells for 2 minutes. This was because the viscosity of the agar cell solution was in the region of 60 times greater than that of water ($60 > 0.7$) mPa.s, therefore the patterning time was increased accordingly. Patterning time using DEP forces is well documented to increase linearly with viscosity.²¹⁶ This was shown in an equation derived by *Albrecht et al.* balancing the forces between DEP force and drag forces on neutrally buoyant particles. Typically the air temperature was found to reach 33 °C during this step. In addition to the enclosure reducing air-flow across the drop this 5 °C difference in the air temperature minimised evaporation of the agar-cell drop.

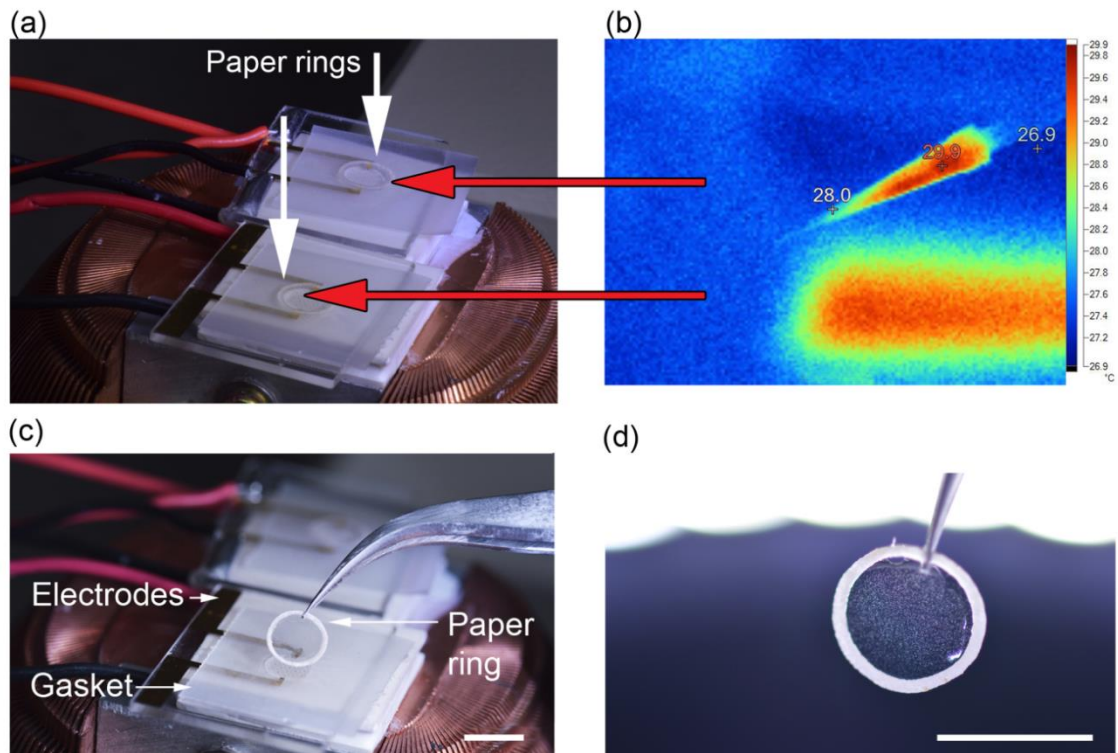


Figure 5.4-2 – Micro liver patterning protocol. (a) Photograph showing the system assembly with wetted paper rings. (b) IR image of warmed pipette with 10 μ l of cell agar solution to be pipetted into the volume of the gasket. (c) Photograph post-patterning with cured micro liver pattern being removed from the electrodes. (d) Photograph of a cured micro liver being moved to a 9-well plate. Scale bars are 5 mm.

5.4.3.4 STEP 4 - Patterning of C3A cells in agar (COOLING)

After 2 minutes had passed, the polarity of the Peltier cooler was reversed (-0.28 A). The temperature dropped to 18 °C on the surface of the gel, the air temperature would rapidly drop to 25 °C (hood temp). Once the hood temperature had been reached the signal generator was switched off to allow the agar to cure for 2 minutes. Typically agar gels are left to enter the gel phase by resting at room temperature, this can take 20-30 minutes depending on the agar concentration.²⁵⁸ However as the application was to culture mammalian cells it was vital to place the patterned cells in culture conditions quickly. Rapid cooling of agar gels has been investigated by *Mohammed et al.* observing that gels formed in this way were 50% lower in elastic modulus (305 Pa·s compared to 545 Pa·s for gradual cooling at 1 °C min⁻¹)²⁵⁹ no other negative effects were observed in quenching of agar.

5.4.3.5 STEP 5 - Micro liver cell pattern removal to culture

On completion of this step the micro liver patterned agar was immediately removed from the electrodes Figure 5.4-2 (c)(d). The paper ring was flipped over so that the patterned side would be face up and then placed inside a 96-well plate well. This step was repeated for the unpatterned control. A 2D control group, or cells cultured in standard 2D format, was created at this time by adding 5 µl of cell solution prepared Section 2.7.3.2 to wells, 200 µl of EMEM was added all wells. The 96-well plate was then placed in an incubator at 37 °C, 5% CO₂. When multiple micro liver samples were required, the gasket was wiped with lint free tissue and 70% EtOH between patterns. All collected micro liver samples in the 96-well plate were then left in the incubator for long-term cell culturing.

This was carried out immediately in order to maintain viability as the cells were not in optimum conditions as stated by the supplier lacking 5% CO₂ and a physiological medium (EMEM) during patterning. Prolonged exposure to these conditions resulted in cell death hence cell patterns were moved to culture conditions immediately after the patterning process was concluded.

5.4.4 Cell viability assay

The live/dead kit viability kit was used to assess the health of the C3A cells by simultaneously staining the living and dead cells. The distinction was made by the green-fluorescent calcein-AM (494/517 nm) staining the membranes of all cells indicating intracellular esterase activity and the red-fluorescent ethidium homodimer-1 (EthD) (528/617 nm) to report loss of plasma membrane integrity¹⁸⁹, indicative of cell death.

Medium was collected from wells and stored in 1.5 ml Eppendorf tubes at 4 °C for use in albumin protein analysis. Samples were then washed with 200 µl of PBS then replaced with PBS (4 µM calcein-AM, 2 µM EthD) and incubated at 37 °C for 20 minutes. Inverted fluorescent microscopy was used to visualise the micro liver structures and control samples.

5.4.5 Albumin protein synthesis ELISA assay

Using the cell culture medium samples described in Section 5.4.4 albumin protein concentration was measured using the human albumin assay kit supplied as described in Section 2.3.2. Assays were performed in duplicate for each sample. Medium samples from micro liver patterns, one control and 2D control were collected per day and stored at -20 °C until assayed. The assay was used to determine the difference in albumin being secreted by the C3A cells due to patterning into a micro liver structure.

5.5 Results and discussion

5.5.1 Patterning using agar and paper handling

The human liver cell line C3A, ranging in diameter 10 to 15 µm were used for all liver cell patterning experiments. Cells were prepared as described previously to a concentration of 2.5×10^6 cells/200 µl mixed with a 1% agar solution. A time sequence of microscope images is shown in Figure 5.5-1 demonstrating the use of a non-uniform electric field pattern cells by DEP forces. In this experiment the preferred conditions of 10 Vpp at 10 MHz was utilised. Figure 5.5-1 (a) shows the C3A cells randomly distributed in the volume before DEP forces were introduced. Figure 5.5-1 (b) shows the cells being attracted to the regions of high electric field strength due to positive DEP forces. This was because a non-uniform electric field created a local maximum electric-field gradient between the electrodes as shown in simulations (Section 5.3). Figure 5.5-1 (c) shows the pattern after 45 seconds. Cell numbers at the edges of the electrodes increased due to the non-uniform electric-field attracting and trapping cells. Also it has observed that clusters and chaining of cells between electrodes increased. This was due to the influence of field-induced cell-cell attraction also known as “pearl chaining”.²⁶⁰ Figure 5.5-1 (d) shows that two minutes after the non-uniform electric field was applied, the cells have formed a lobule like structure. The cells concentrated into the areas of high electric field as designed by the electrodes.

Successful manipulation of patterned cells encapsulated in agar was observed using the paper ring substrate. Of particular note, it was observed that the manipulation of patterned cells encapsulated within agar retained the pattern as shown in Figure 5.5-2. Deformation of the pattern due to removal of the pattern from the electrodes was not observed. Relocation of the cell patterns into culture conditions was shown not to deform.

It was observed that patterning of cells using DEP buffer as shown in Figure 5.5-1 occurred within seconds of applying the non-uniform electric field. However, the viscosity of 1% (wt/vol) agar at 37 °C is approximately 60 mPa.s, the viscosity of the DEP buffer at 37 °C is approximately 1 mPa.s.²⁵⁵

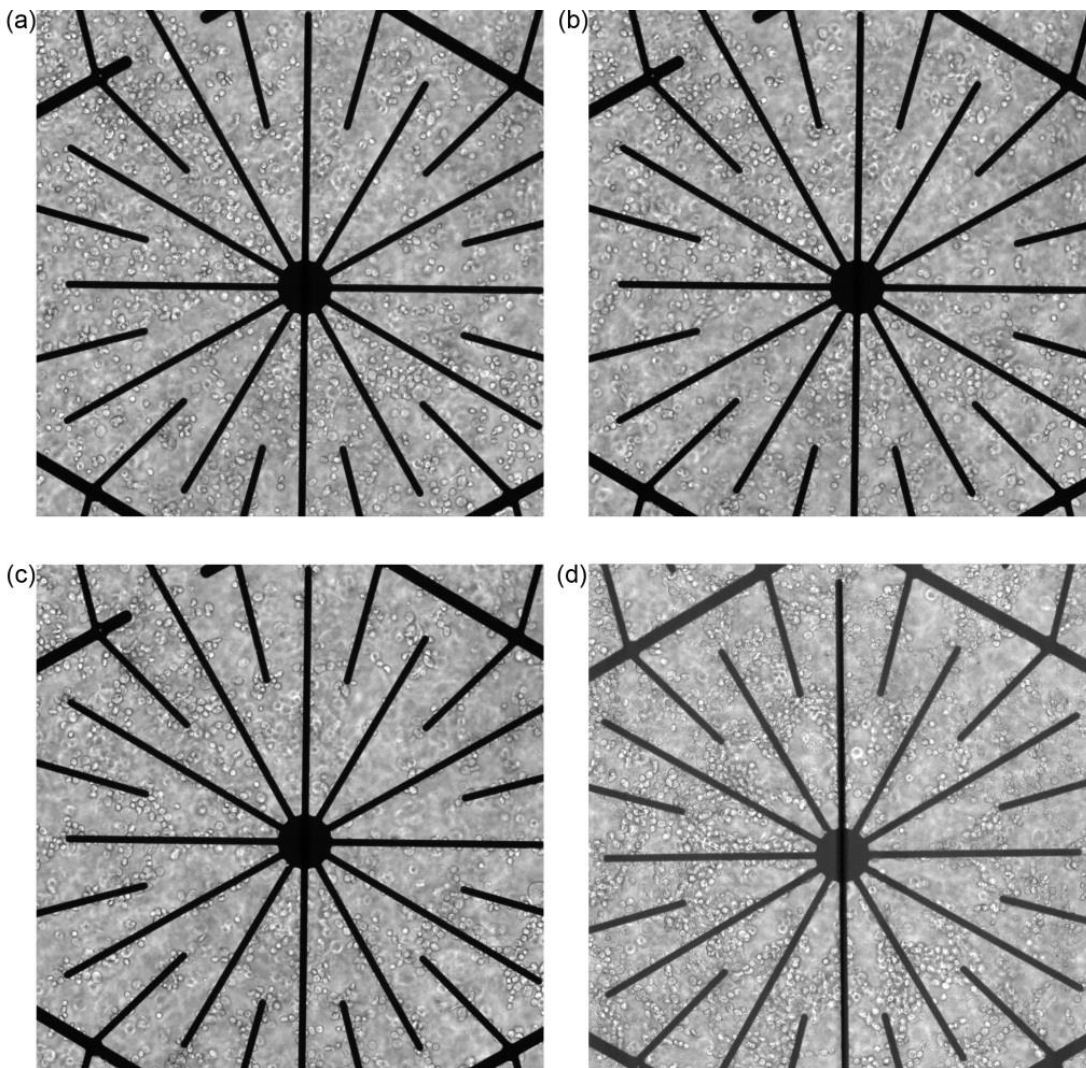


Figure 5.5-1 – Time sequence of images for patterning liver cells (C3A) with a non-uniform DEP force filed under the DEP voltage of 10 V peak to peak at 10 Mhz. (a) The cell patterning electrodes had 10 μ l of cell pipetted onto the surface which are randomly distributed before DEP forces are induced. (b) Image shows cells being manipulated one second after the AC field was induced. Cell being to align to the areas of high electric field strength created at the electrodes. (c) This image shows patterning 15 seconds after DEP forces are induced. (d) This image shows the patterning after two minutes of patterning. Cell have aggregated at the areas of high electric field strength forming a biomimetic lobule pattern.

Viscosity of the buffer linearly affects the velocity at which cells move relative to the non-uniform electric field as stated by *Albrecht et al.*²¹⁶ Patterning for 2 seconds in DEP buffer yielded cell patterning that represented the electrode design. Thus it was decided that for patterning in agar the patterning time should be increased by a factor of 60 providing a patterning time of 120 seconds. Longer patterning times were attempted however significant reduction in cell viability was observed. This was expected as has been reported by *Glasser and Fuhr* that increased duration and the intensity of exposure of electric-fields will cause cell damage, death and reduction in proliferation rates.^{223, 261}

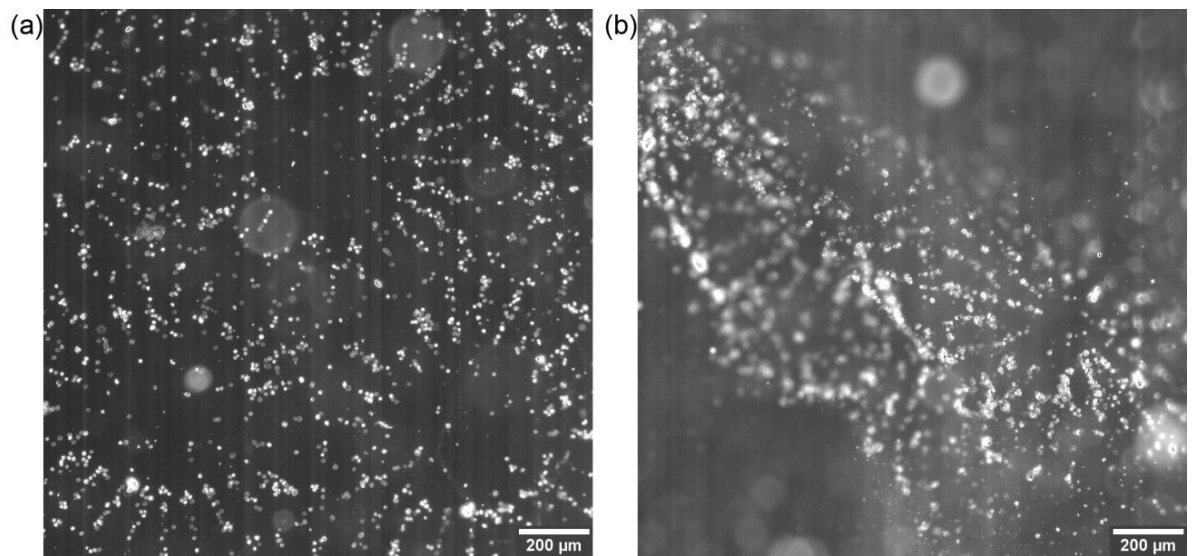


Figure 5.5-2 – Micro liver pattern handling of patterned C3A cells by DEP forces in agar with a paper substrate. (a) C3A cells patterned in biomimetic liver lobules pattern transferred successfully from electrodes to a petri dish. (b) Patterned C3A cells which the bond of the agar to the paper broke causing the agar to fold over itself, however the pattern is still intact despite this.

These results showed that the electrode pattern successfully formed a cell pattern mimicking a hepatic lobule pattern. Simulation results previously described in Section 5.3 indicated that the geometry generated an electric-field in the regions surrounding the electrodes. Comparison of the electric-field gradients generated in the simulations and experimental results show a strong correlation. It was concluded that the non-uniform electric-field was generated as designed and could be taken to the take logical step in testing.

5.5.2 Cell viability assessment for DEP cell patterning in agar

The *in vitro* cell viability was assessed using the mammalian live/dead assay kit (Section 2.4.3) which uses a fluorescence-straining method via Calcein AM/EthD-1. The viability of C3A lobule like structures in agar over a 72 hrs period as well as controls is shown in Figure 5.5-3. Images are a composite of both live cells (FITC) and dead cells (Rho)

images. The first column shows fluorescence images of patterned C3A cell in a lobule structure. Cell aggregation increased over the 3 days and high viability (80%) was maintained across all samples. Proliferation was slow compared to the 2D control but an increase in cell density was evident from pattern ratio data Figure 5.5-4. Viability of the control sample is shown in the second column which compares favourably with the patterned C3A cells. Aggregation was evident due to the high cell concentration and cell morphology was spherical indicating a lack of attachment to the ECM. The final column shows the 2D culture viability which also compares well to both the patterned and control samples. Cell proliferation was observed to be higher than that of the agar encapsulated C3A cells. Cell density was observed to double after 48 hrs and triple by 72 hrs. The starting cell count for the samples was 1×10^5 cells.

These viability results confirm the optimisation parameters defined in Section 2.7.4.1. Strong electric fields can impact on the viability of mammalian cells, due to current-induced Joule heating of the medium and direct field interactions inducing transmembrane potentials.²²³ The results shown in Figure 5.5-3 shown no indication of reduction in cell viability due to DEP patterning using electric fields in the range of 100 kVm^{-1} . The selected frequency of 10 MHz additionally has had no effect on viability. The transmembrane voltage is a function of the applied frequency and the electric field magnitude (depends on spacing between electrodes, electrode geometry and the applied voltage). With increase in the applied AC frequency the transmembrane voltage decreases and hence the chance of cell survival post DEP is much higher. Finally the optimised current (0.28) to heat and cool the electrodes ($37 \text{ }^\circ\text{C}$ and $18 \text{ }^\circ\text{C}$) has had no observable effect on the viability of the cells.

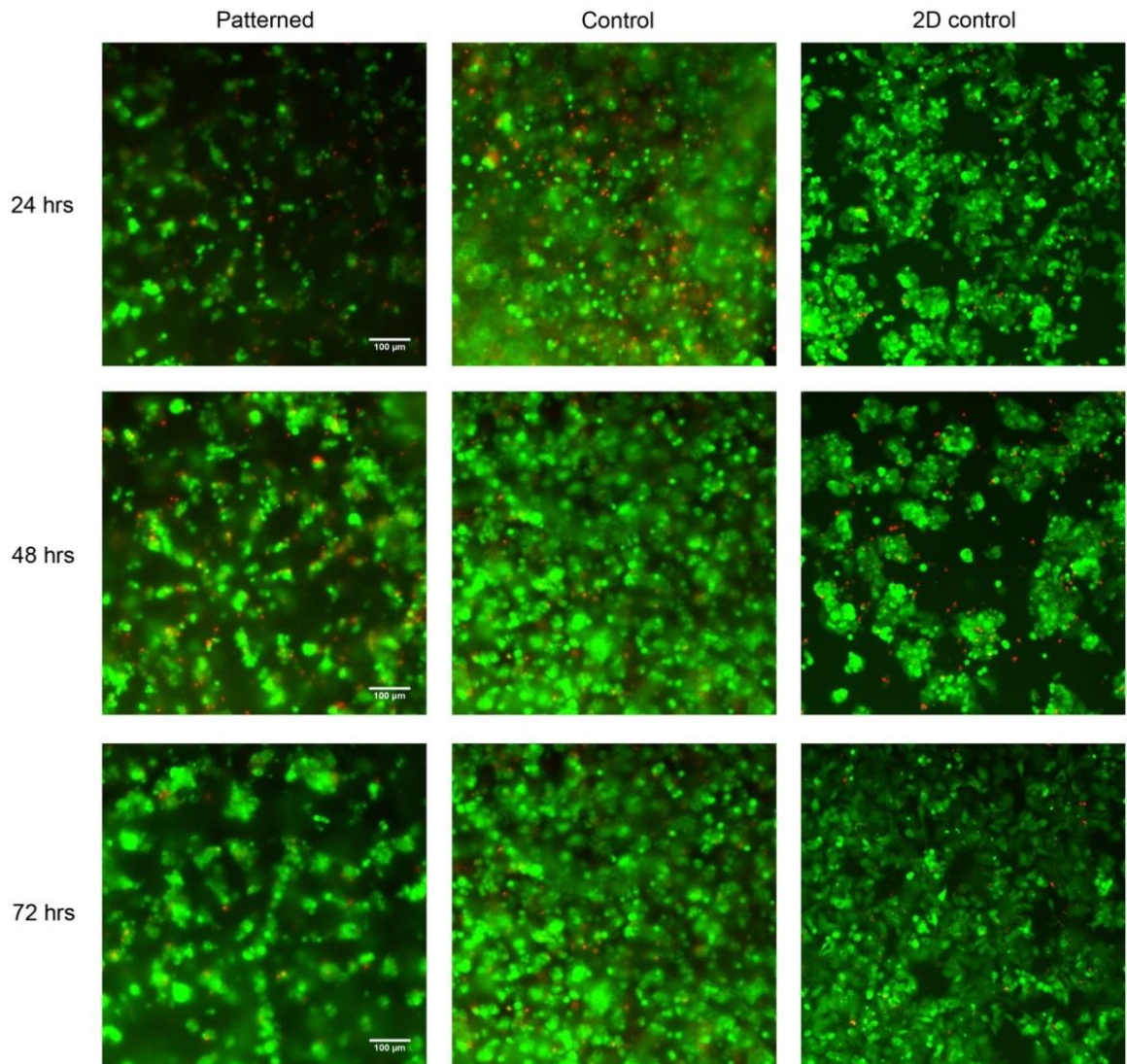


Figure 5.5-3 – Viability of C3A lobule like structures in agar over a 72 hrs period as well as controls. Images are a composite of both live cells (FITC) and dead cells (Rho) images. The first column shows fluorescence images of patterned C3A cell in a lobule structure. Cell aggregation increased over the 3 days and high viability (80%) is maintained. Proliferation was slow compared to the 2D control but an increase in cell density was evident from pattern ratio data. Viability in of the control sample is shown in the second column which compares favourably with the patterned C3A cells. The final column shows the 2D culture viability which also compares well to both the patterned and control samples. Cell proliferation was observed to be higher than that of the agar encapsulated C3A cells. Cell density was observed to double after 48 hrs and triple by 72 hrs. The starting cell count for the samples was 1×10^5 cells. Scale bars are 100 μm .

The morphology of the cells observed in the patterned samples shows different results from the control. The hepatocyte morphology was influenced by the pattern formed in the agar. Cells aggregated into shapes correlating to the original lobule pattern and fused with neighbouring cells, producing dense cord like chains of hepatocytes. Aggregation of cells was observed in the control however due to the random distribution of cells through the agar, only spheroid like aggregates were observed.

Pattern ratio of patterned cells as a function of time over 3 days of culture is shown in Figure 5.5-4. Live pattern ratios were observed to increase with time, dead ratios increased

after 48 hours before decreasing at 72 hours. The electric-field was induced for two minutes (10 MHz, 10 Vpp) at 37 °C following the optimised protocol. The normalised control threshold as expected is 1 ± 0.035 . The pattern ratio for live and dead cells is very similar after 24 hrs. The live pattern ratio increases steady up to a 1.9 ± 0.4 after 72 hrs. While the ratio increased after 48 hrs for dead cells after 72 hrs the ratio is lower than that of live cells (1.4 ± 0.3). As previously discussed in Section 2.7.3.4, the error bars for the threshold values arise from the manual alignment of the patterns and random pattern sample selection from the array. Software aided alignment, increased sample size and consistent sampling from patterns would reduce these errors.

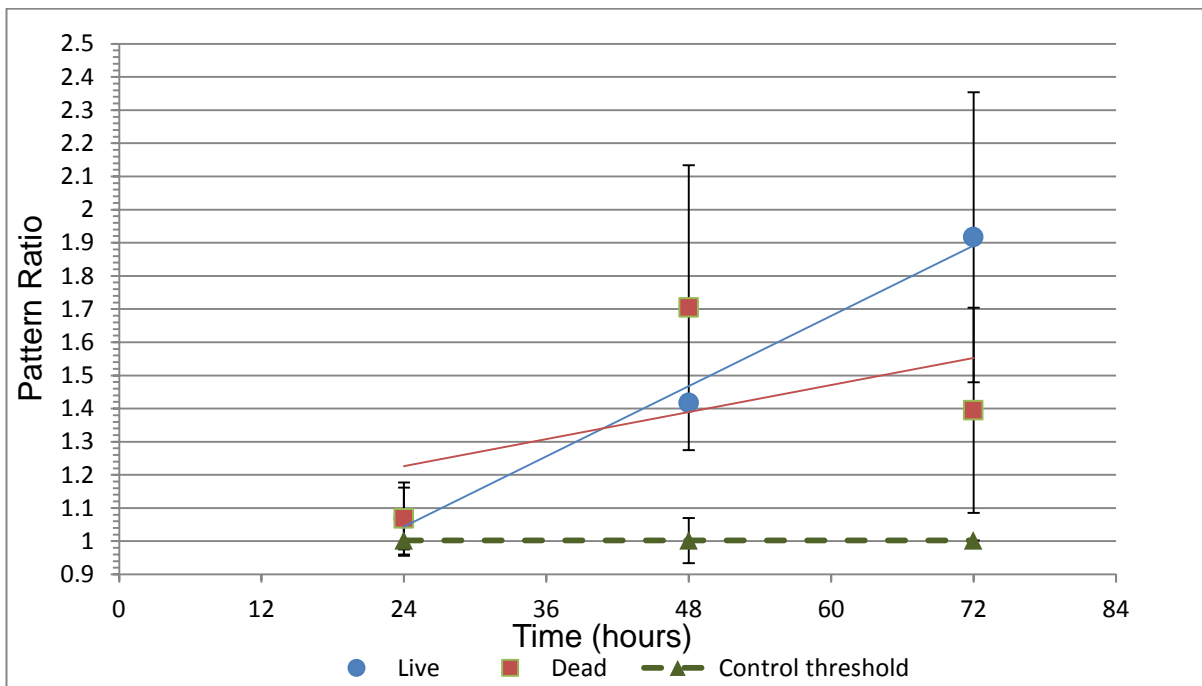


Figure 5.5-4 – Pattern ratio of patterned cells as a function of time over 3 days of culture. Live pattern ratios were observed to increase with time, dead ratios increased after 48 hours before decreasing at 72 hours. The electric-field was induced for two minutes (10 MHz, 10 Vpp) at 37 °C following the optimised protocol. The normalised control threshold as expected is 1 ± 0.035 . The pattern ratio for live and dead cells is very similar after 24 hrs. The live pattern ratio increases steady up to a 1.9 ± 0.4 after 72 hrs. While the ratio increased after 48 hrs for dead cells after 72 hrs the ratio is lower than that of live cells (1.4 ± 0.3). Error bars represent standard deviation of the mean (n = 4).

These results showed that patterned lobule like structures in agar retain the design of the electrodes over a period of 3 days. The ratio for live cells increases linearly over the time period, this showed that the cells were proliferating in the shape of the designed pattern. Viability and morphology results observed in Figure 5.5-3 support this hypothesis as it showed a viability of 80% at 24 and 48 hours. At 72 hours the viability was observed to increase displaying an increase in cell numbers and the viability increased to 90%; the dead cell ratio decreased at 72 hours which correlates strongly with this observation.

Proliferation of cells in control samples had negligible effects on the threshold while also maintaining a high viability of 80%. Cells in the control sample were observed to form spherical shape configuration with pockets of C3A aggregation over the culture period. This has result has previously been observed by *Lan et al*²⁶² and *Dvir-Ginzberg et al*.²⁶³ Agglomeration of HepG2 has been confirmed to be beneficial for cell function and viability as results obtained by *Surapaneni et al*. have shown.²⁶⁴ While the factors that modulate the hepatocyte phenotype *in vitro* remain unelucidated, it is accepted that heterotypic cell interaction between hepatocyte cells modulate cell growth, migration and/or differentiation.²¹⁹

Long term patterns using this system compares favourably with other liver DEP patterning systems. The system demonstrated by *Ho et al* showed DEP created liver-like lobule patterns within a microfluidic device.¹²² However as the cells attached to the surface of the electrodes within a period of 48 hours the cells would over run the surface and the pattern would disappear. The method presented in this work however showed that the pattern was maintained up to 72 hours due to the agar encapsulating the cell patterns. Similar effects would be expected to appear in the system developed by *Schütte et al*.⁷⁶, the cells are also patterned onto flat surfaces in this device. As the liver lobule like pattern formed by the system in this work was held by agar, the proliferation of the cells was limited meaning that number of cells within the patterns was more stable than cells grown on 2D surfaces. This reduced proliferation was not regarded as detrimental as this meant that cell number within the agar could be kept relatively consistent throughout albumin production.

5.5.3 Micro liver function assessment via albumin secretion

Albumin secretion, a liver-specific function for hepatocytes was selected as a marker because it requires liver-specific gene expression and intact translational and secretory pathways in the cells.²⁶⁵ The concentration of the albumin secreted by the cells in patterned, control and 2D samples over 72 hrs culture was assessed by human albumin ELISA shown in Figure 5.5-5. Patterned C3A cells had increased albumin secretion after 48 hrs of culture compared to the control and monolayer control. The control samples show a relatively stable production over the first two days before decreasing. The albumin concentration observed in the 2D culture after 24 hours was higher than the patterned and control samples before gradually decreasing to a similar value by day 3.

This result showed that the liver lobule-like cell patterns in addition to high viability had increased the liver specific function of albumin production compared to the control and 2D control samples. Aggregation of hepatocytes is critical to maintaining hepatic cellular functions²⁶³, as it has been observed that randomly dispersed low density seeding in agar reduces functionality and viability compared with high density. Tightly packed aggregates with an average diameter of 100 μm observed by *Dvir-Ginzberg et al* found that these groups of cells had increased albumin production compared with randomly dispersed cells.

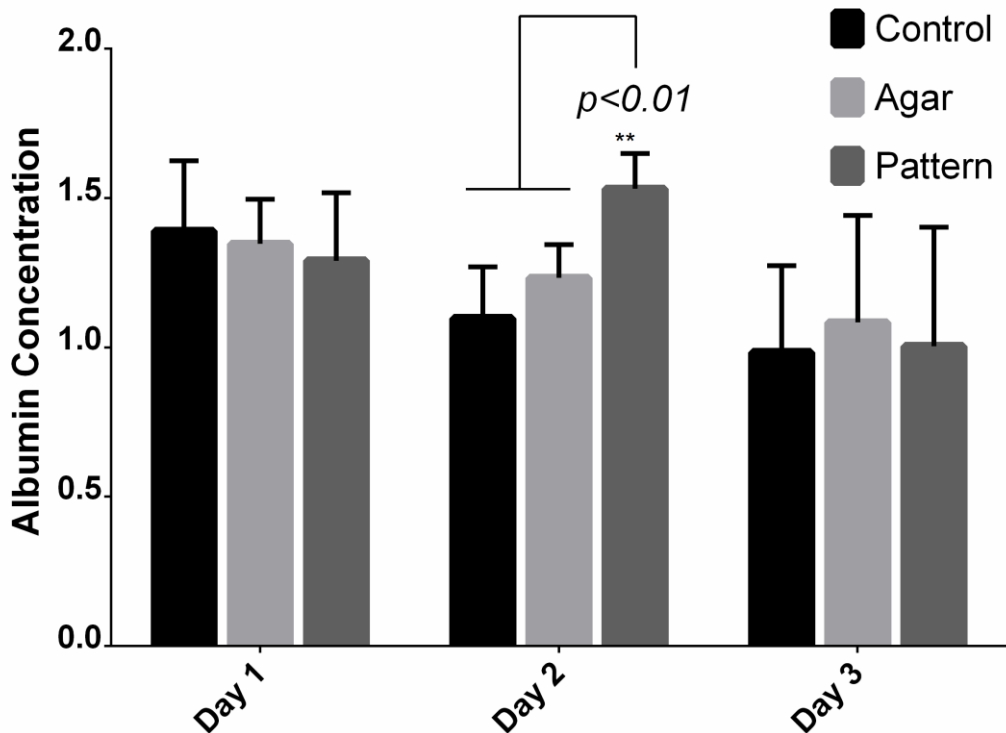


Figure 5.5-5 – Albumin secretion a liver-specific function for hepatocytes was selected as a marker to assess the functionality of the patterned micro liver-like cultures. The concentration of the albumin secreted by the cells in patterned, control and 2D samples over 72 hrs culture was assessed by human albumin ELISA shown in Figure 12. Patterned C3A cells had increased albumin secretion after 48 hrs of culture compared to the control and monolayer control. The control samples show a relatively stable production over the first two days before decreasing. The albumin concentration observed in the 2D culture after 24 hours was higher than the patterned and control samples before gradually decreasing similar value by day 3. Data represent the mean \pm STD for four independent repeats. The (***) indicates statistical increase in albumin protein of patterned cells relative to control and 2D cultures at day 2, $p < 0.01$ (ANOVA).

However, there is a drop in secretion after 72 hours for the patterned samples. Error in the pattern reproduction was expected as discussed previously that may have caused variation in albumin secretion. It was observed however that the decrease in albumin levels occurred for all samples after 72 hours of culture and standard deviation was of similar value for patterns, control and 2D culture samples ruling out this hypothesis.

Papers investigating the liver functionality of hepatocytes cultured within agar give insight to the observed results. Investigations of HepG2 spheroids cultured within agar gel by

Verma et al presented a similar effect.²¹⁸ Albumin secretion increased over 72 hours for cells cultured in agar; a decrease in albumin secretion for control 2D cultures was reported between 2 and 3 days. Additionally, work by *Dvir-Ginzberg et al* utilising agar gel for liver tissue investigated albumin secretion with relation to hepatocyte density.²⁶³ They observed that rat hepatocyte densities of 5×10^6 cells seeded in agar produced gradually decreasing albumin secretion. Further to evidence of these effects were presented by *Glicklis et al* as they observed the same albumin levels for hepatocytes cultured on agar compared to 2D culture controls. While the albumin level decreased after 72 hours for patterned cells, it did also for control and 2D cultures. The decrease in albumin secretion may be related to saturation of albumin in the medium, these results indicate that the liver-like patterns improve albumin production after 2 days of culture.

5.6 Conclusions

High resolution cell patterning techniques to engineer biomimetic cell geometry to preserve cell-to-cell interactions is an important aspect of constructing artificial liver tissue for toxicity testing. In this chapter, a novel technique employing DEP based cell patterning in agar with a paper substrate was demonstrated to reconstruct the livers' lobule-like structure using a specifically designed micro electrode array. Randomly distributed liver cells were manipulated using field-induced DEP forces to form an array of lobule-like structures throughout the agar. These liver-like patterns were then successfully removed from the patterning electrodes and placed in culture conditions within industry standard 96-well plates. High patterning reproduction and viability was observed using optimised DEP patterning conditions. The functionality of the liver-lobule structures in agar were investigated by examining the production of albumin. The enhancement of albumin production was observed for the micro liver engineered tissue. These results show that the geometrical arrangement of liver cells within an agar gel improves liver specific functionality. The use of the paper substrate allowed for the removal of the gel from the electrodes making the system reusable.

The design of the system was for integration with the previously discussed technologies of microfluidics in Chapter 4 and additive manufacturing in Chapter 6. By designing the pattern to be removable from the electrode substrate it can be fitted within custom culture platforms using microfluidic channels. Additionally, multiple layers of paper ring micro livers could be constructed to increase the volume and complexity of these tissue engineered organs.

6 Additive Manufactured Microfluidics

6.1 Abstract

This work describes a preliminary investigation of commercially available 3D printing technologies for rapid prototyping and low volume fabrication of Lab-on-a-Chip devices. Fabrication of devices for these experiments was completed using fused-deposition (FDM), stereo-lithography (SLA) and multi-jet modelling (MJM). Experiments showed that trapping of zebrafish was possible using these devices. Viability of zebrafish embryos cultured in chip conditions was shown to be successful for 72 hrs. Biocompatibility of the 3D printed materials in static conditions with 3D printer materials was shown to be highly toxic to zebrafish embryos resulting in embryo fatality. Post-processing steps increased viability by up to $85\% \pm 20$ for VisiJet Crystal material cultured with zebrafish 24 hour post fertilisation. Indications of toxicity were still present however leading to the conclusion that VisiJet Crystal remains toxic after post-processing to zebrafish embryos. Watershed material caused 100% mortality in zebrafish embryos. ABS plastic printed material was shown to have no visual effect on zebrafish development. A post-processing method was observed to render the photopolymer Dreve Fototec 7150 inert and thus biocompatible for zebrafish research.

6.2 Introduction

Lab-on-a-Chip (LOC) devices have developed significantly through advances in physics, electronics and material sciences.^{72, 266} Utilising these technologies to develop miniaturised systems for the *in-situ* analysis of small model organisms and embryos (both invertebrate and vertebrate) is a significant research area.^{151, 267} Small model organisms as discussed in Section 1.7 are a useful tool for studying toxicity, human diseases and genetics. Model organisms including nematodes (*Caenorhabditis elegans*, *Panagrolaminus davidi*) and fruit fly (*Drosophila melanogaster*) have seen automated manipulation through LOC systems.^{153, 268} Manipulation of millimetre scale organisms such as fish and amphibian embryos/larvae has also been investigated using LOC systems.^{154, 155, 158, 269} In particular the zebrafish (*Danio Rerio*) has shown to be capable of being cultured, imaged and tested for toxicological analysis using LOC systems.^{155, 160}

The small size ($\text{\O}1.5$ mm), optical transparency of organs, vertebrate nature and simple husbandry make zebrafish embryos a useful model for pharmacological and toxicological studies.^{270, 271} There is a need still however to develop chip-based systems using automated loading, transport, positioning and long-term immobilisation of large millimetre scale embryos for ecotoxicology, drug discovery and reproductive medicine.¹⁵⁷

Research in this area has been approached with several techniques including the culture of embryos within segmented flow of PTFE tubes;²⁷² the use of electrowetting-on-dielectric (EWOD) technique for transport of zebrafish embryos in macro sized droplets,²⁷³ a microwell culture flow system fabricated in glass¹⁵⁵, a gradient generator based system to supply drugs to zebrafish embryos cultured in microwells¹⁵⁶, the vertebrate automated screening technology (VAST) for automated manipulation and imaging of zebrafish larva within a glass capillary using a robotic system¹⁵⁹, and finally a robotic image based sorting system for single embryo dispensing into 96-well plates.¹⁵⁸ The approaches for automated sorting of zebrafish embryos has been reviewed recently.^{269, 274} However while these techniques achieve high-speed, automated and gentle sorting, trapping and long-term immobilisation of embryos, the size and cost of these systems can be reduced further. The current fabrication methods also restrict the design of such devices to two dimensional or two and a half dimensional structures.^{155, 160}

6.2.1 3D printing as a novel fabrication technique

A range of fabrication techniques have been developed for the purpose of automated zebrafish sorting and imaging. However one such method that has not been explored is the use of rapid prototyping technology as described in Section 1.8 . The range of applications for these technologies in biomedical engineering include biomodels for diagnosis, surgical training, hard and soft tissue replacement, biodevices and tissue engineering.¹⁶² In particular biodevices for tissue engineering has seen development using a wide range of additive materials.²⁷⁵ Fabrication of microstructure scaffolds using rapid prototyping has been investigated using selective laser sintering²⁷⁶, layered hydrospinning²⁷⁷, laser stereolithography²⁷⁸, digital light projection²⁷⁹, and two-photon lithography²⁸⁰ with a range of different materials.

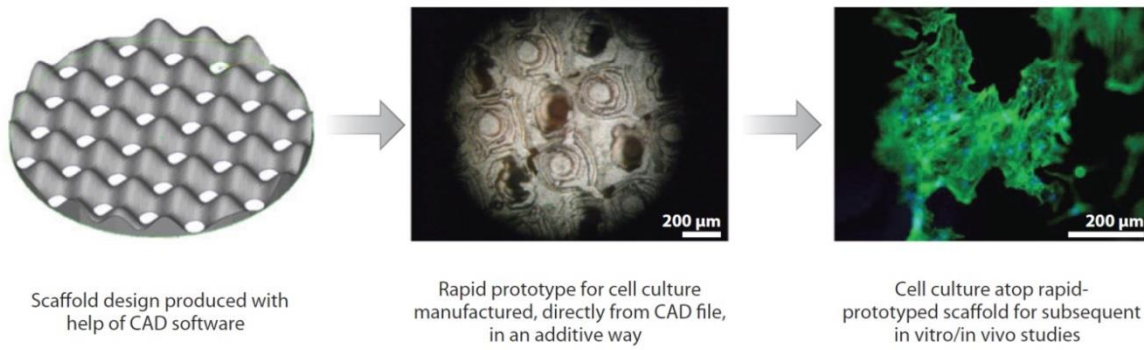


Figure 6.2-1 – Schematic description showing tissue engineering process from computer-aided design (CAD), to cell culture scaffolds produced by a 3D printer. Reproduced from reference ¹⁸⁸.

The process for this involved the design of a CAD model of scaffold geometry for cell culture, which is subsequently fabricated by rapid-prototyping methods as show in Figure 6.2-1. Cells are then cultured using *in vitro* trials to assess cell viability or pharmaceutical assessment. Successful trails can then lead to *in vivo* animal studies to validate the therapeutic approaches.¹⁸⁸

Despite this growth in the use of rapid-prototyping in tissue engineering among other areas of biomedical engineering, microfluidics has seen relatively little development. This has been due to two major factors: lack of sufficient resolution of current rapid-prototyping methods ($100\ \mu\text{m} <$) and optical transparency to allow *in vitro* imaging. Microfluidic application has been shown by *McCullough et al* by surface modification of 3D printed, fused deposition modelling (FDM) devices using poly (acrylonitrile butadiene styrene) (ABS).¹⁸⁶ This allowed for the creation of a non-biofouling surface LOC device suitable for chemical reactions, however optical transparency was not possible due to use of ABS and channels. A similar approach by *Kitson et al* demonstrated that chemical reactionware for millifluidic and microfluidic LOC devices can be fabricated using basic FDM based printing.¹⁸⁵ However neither of these methods allow for high-resolution fabrication ($500\ \mu\text{m} \leq$) or for transparent parts suitable for imaging of channel contents.

6.2.2 Aims of this chapter

This work builds on advances by *Akagi et al* and *Wlodkowic et al*^{160, 269}, but approaches a new fabrication method in order to achieve on-chip zebrafish embryo loading, immobilisation, culture and analysis. This chapter describes a preliminary investigation of commercially available 3D printing technologies for rapid prototyping and low volume fabrication of Lab-on-a-Chip devices. The main motivation of the work was to use off-the-shelf 3D printing methods to rapidly and inexpensively build microfluidic devices with

complex geometric features and reduce the need to use clean room environment and conventional microfabrication techniques. The development of an automated micro analysis platform (μ AP) was also engineered incorporating the 3D printed chip, mini-microscope and pumping system.

Both multi-jet modelling (MJM) and stereolithography (SLA) processes were explored. MJM printed devices were fabricated using a HD3500+ (3D Systems) high-definition printer with a thermo-polymer VisiJet Crystal (3D Systems) substratum that allows for a z-axis resolution of 16 μ m and 25 μ m x-y accuracy. SLA printed devices were produced using a Viper Pro (3D Systems) stereolithography system using Watershed 11122XC (DSM Somos) resin which allow for a z-axis resolution of 50 μ m and 25 μ m x-y accuracy.

Fabrication results compared favourably with other forms of rapid prototyping such as laser cut PMMA devices and PDMS moulded microfluidic devices of the same design. Both processes allowed for fabrication of monolithic, optically transparent devices with features in the 100 μ m range requiring minimal post-processing. Optical polymer qualities following different post-processing methods were also tested in both brightfield and fluorescence imaging of transgenic zebrafish embryos.

6.3 Materials and methods

6.3.1 On chip development system setup, loading and operation

On chip development was monitored real-time using the μ AP setup described in Section 3.5.3. First the chip was clipped into the detachable holder. The chip was then connected directly to the external piezoelectric micropump mp6 (Bartels Mikrotechnik GmbH - Otto-Hahn-Str, Germany)²⁸¹ controlled with a mp-x controller²⁸² unit also from Bartel. Using 1/16" polyurethane tubing the 3D printed chip was connected to the pump with an internal diameter allowing for the free movement of zebrafish embryos. The device was primed with 40% ethanol (v/v) to help wet the fluidic channels of the chip and persistence of air bubbles. Following this the chip was flushed with E3 fish medium. The holder was then slid into the platform and secured by inserting the holding pins.

Observing the video feed from the DinoCapture software zebrafish embryos with intact chorion between 6-24 hours post-fertilisation (hpf) were loaded by aspirating single embryos one by one at the flow rate of up to 2 ml/min. Trapping of embryos within the 3D chip was confirmed optically using software on the laptop. Once loaded the μ AP platform

was placed in an incubator (HERA Therm, Thermo Scientific, US) and connected to a 100 ml glass reservoir (Schott AG, Mainz, Germany) also within the incubator. At this time an array of 3 white LED's on a breadboard powered by 4 AA rechargeable batteries were placed in close proximity to the light reflector to provide underside lighting to the chip in addition to the top-lighting system of the DinoLite scope. E3 medium heated by the incubator was circulated by closed loop perfusion for up to 72 hours allows for an optimal embryo development temperature of 28.5 °C inside the 3D printed chip.

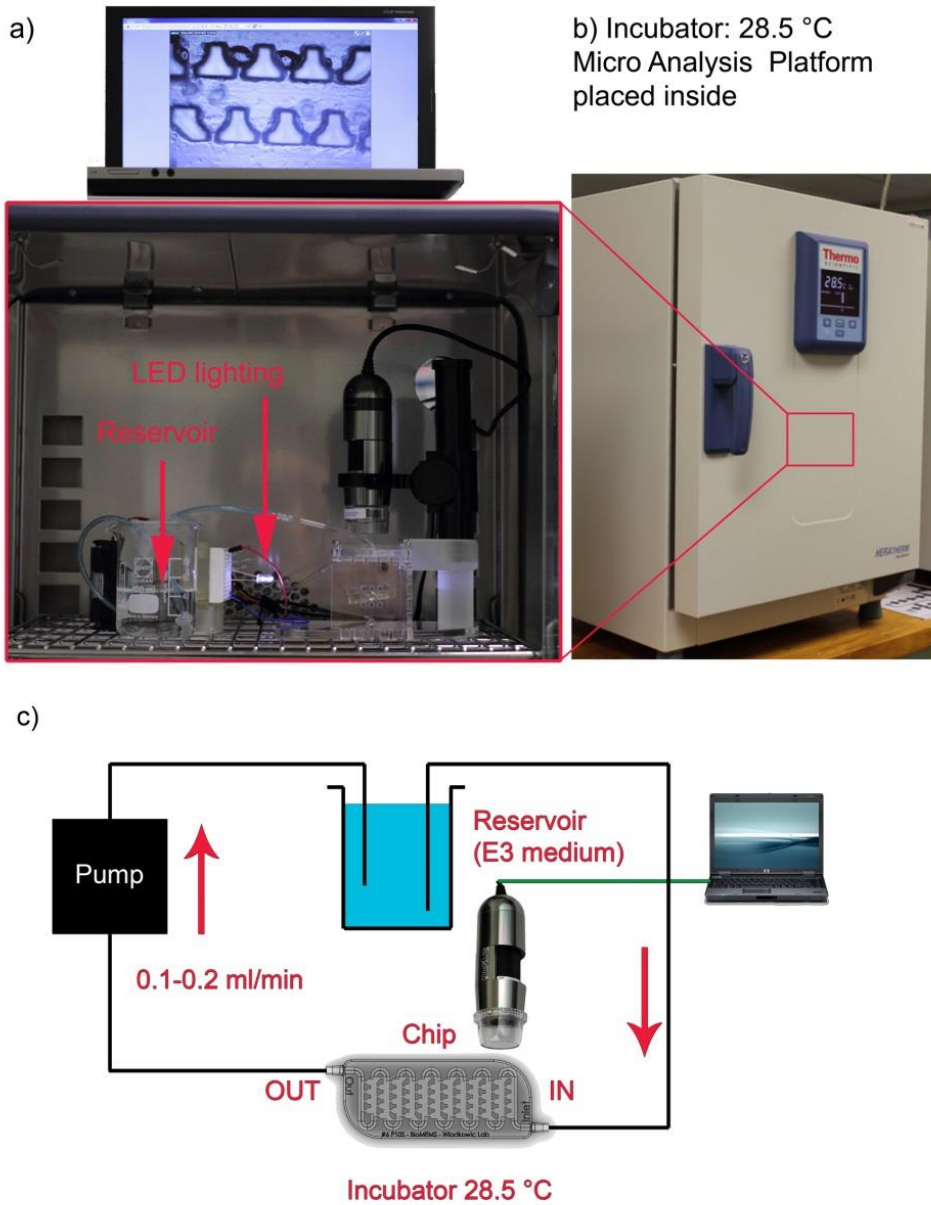


Figure 6.3-1 – Experimental setup for real-time analysis of zebrafish using the micro analysis platform. a) Photograph showing the interior of the incubator b) with μ AP, reservoir and lighting system. The mp-x pump control unit was placed on the shelf below (not pictured). C) Schematic illustrating the fluidic connections of the system and off-chip connections and hardware actuating the 3D printed zebrafish trapping device.

6.3.2 Biocompatibility of 3D printed materials

The polymers used for this device were tested using custom designed single well culture environments and disc shaped samples suitable for placement in standard 24-well plates. Discs measuring 15 mm in diameter and 1 mm thick were printed using both the VisiJet Crystal and Watershed polymers using the same protocol as described in Section 6.3.2 system for testing of biocompatibility with zebrafish embryos Figure 6.3-2(a). The single well culture system was printed using the HD3500+, Viper Pro (Watershed + Dreve) and HP DesignJet Figure 6.3-2(c-d). The design for this culture well was based on the commercially available Corning 24-well plate dimensions.²⁸³ With this design the lid fits loosely to allow the diffusion of gases into the culture well but securely enough not to be dislodged during handling. The disc samples printed using HD3500+ and Viper were diluted in 1 litre of DI water and stirred using a stir bar for a period of 24 hrs.

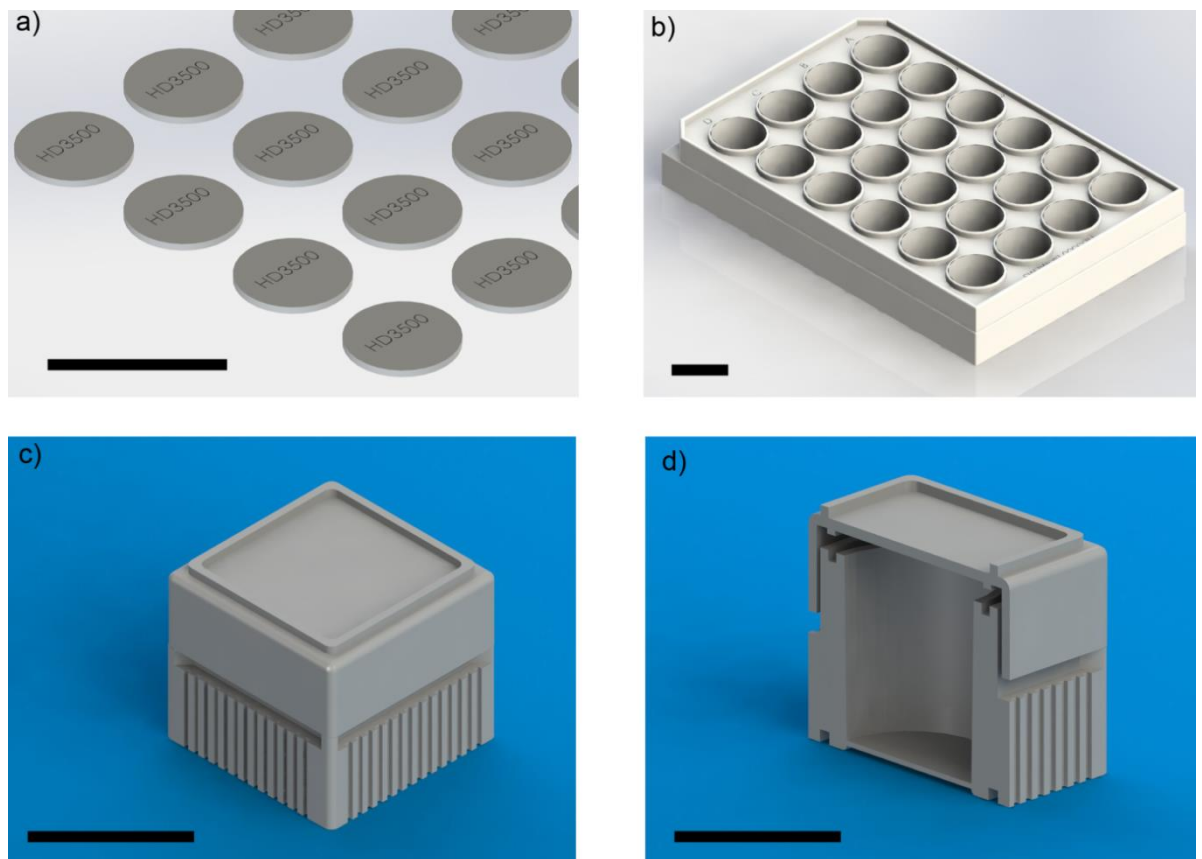


Figure 6.3-2 – 3D rendered images of designed used for biocompatibility of 3D printed materials with zebrafish embryos. A) Discs for inserting into a 24-well plate, engraved here with HD3500 label (15 mm in diameter, 1 mm thick). B) 24-well plate based on flat-bottomed Corning plates available commercially.²⁸³ C) Single-well culture device with lid. D) Cross-section of single well culture device. Scale bars are 20 mm.

The water was then changed and the process was repeated for 5 days. Samples were then dried and placed in sealed plastic bags for transport. One disc per well was placed in a 24-well plate with 5 embryos with 1 ml of E3.

The embryos were maintained at 28.5 °C over a period of up to 72 hours, images were recorded twice a day of embryo development. Selected samples were dechorionated using tweezers and immobilised in 2% agarose solution for improved imaging. Experiments comparing the response of 3D printed material with or without wax support material were completed using a 3D printed 24-well plate Figure 6.3-2(b). Designs were printed both right side up and upside down forcing the printer to place the wax support material on opposite sides of the plate. Post-processing was completed as described in Section 0. Conditions for the experiments with the 24-well printed plate, and single-well were the same as the conditions used for the disc based biocompatibility experiments minus the discs.

Printed single wells were washed in DI water. In solvent rinsing tests, 70% ethanol, 99% ethanol and 99% isopropanol were used to rinse the wells for up to two minutes. Then the wells were dried under nitrogen atmosphere. In solvent soaking tests, 99% ethanol was used to soak the wells for 24 hours. The wells were then dried under nitrogen atmosphere. Pre experiment, unfertilised embryos were removed 6 hours post fertilisation (hpf), and then manually transferred into 3D printed wells, 5 embryos per well, with 1 ml of E3 fish medium. For each experiment 5 wells were used.

6.3.3 Zebrafish Husbandry

Adult zebrafish were kept in a 14 hrs light, 10 hours dark cycle fish facility and fed twice daily with artemia and daily with dry feed. Wild-type zebrafish (Danio rero, AB line; Zebrafish International resource Centre Oregon, Eugene, OR, USA) for all experiments. Research on animals was conducted with approval from The University of Auckland Animal Ethical Committee (approval ID R661/1)²²⁶

6.3.4 Embryo Culture, Treatment and Phenotype Analysis

The zebrafish embryos were obtained from random pair-wise mating using the marbling technique.²⁸⁴ Embryos were then collected, dead/unfertilised embryos and debris was removed by pipette. Embryos were kept at 28.5 °C in E3 medium and developmentally staged as described earlier.^{226, 227} Embryos of 4-6 and/or 24 hpf were chosen for experimentation. In according to zebrafish developmental stages, the viability of zebrafish was observed by checking: (1) Lethal endpoints (cumulative mortality): coagulation, tail detachment, lack of somite formation; (2) Sublethal developmental endpoints: development of eyes, spontaneous movement, heartbeat and blood circulation, pigmentation, formation of edemata; (3) Endpoints of teratogenicity: malformations of

head/face/arches/jaw general retardation^{157, 285, 286}. The potential of hatching and time was also considered^{157, 285}. Tricaine mesylate (0.2 mg/ml) was perfused through chips 15 minutes before image acquisition when imaging swimming zebrafish larva. This was only a temporary anaesthesia to inhibit intrinsic movements during fluorescent imaging. Post experiment all hatched zebrafish were euthanized at -20 °C.

6.3.5 Imaging

Time-lapse imaging of developing embryos cultured on chip based devices was performed using a USB Dinolite microscope (AD7013MZT Dino-Lite Premier microscope, AnMo Electronics Corp, Taiwan) connected to a laptop. For images of FLI1a eGFP zebrafish a Nikon SMZ1500 (Nikon, Tokyo, Japan) connected to a DS-U2/L2 camera was used. Fluorescent images were also taken using an AM4113T-GFBW Dino-Lite Premier USB microscope. Imaging of printed devices was captured using a Leica MZ7.5 stereomicroscope equipped with a Leica DFC295 CMOS camera running under the LAS Multitime software (Leica Microsystems, Wetzlar, Germany). For biocompatibility experiments the zebrafish were imaged using a Nikon SMZ1500 (Nikon, Tokyo, Japan) with a Nikon E5400 Coolpix camera.

6.3.6 Data Analysis and Controls

Data analysis and presentation was performed using the LAS (Leica Microsystems); ImageJ¹⁹⁴; Microsoft Excel 2010; SolidWorks 2012 and SolidView 2012²⁸⁷.

All controls measurements are provided in detail within Figure legends. In general comparisons between the chip-based device and static 24-well microtiter plates was conducted for μ AP studies. Biocompatibility controls were run in tandem with experimental samples for direct comparison.

6.4 Results and Discussion

6.4.1 On chip embryo trapping and culture using the micro analysis platform

The principles and validation of embryo trapping performance due to continuous perfusion experiments has been detailed by *Akagi et al.*¹⁶⁰ To demonstrate the feasibility for developmental analysis of zebrafish within a 3D printed chip long term culture experiments were conducted. Zebrafish embryos were trapped and perfused on a chip at a flow rate of 0.5 ml/min for up to 72 hours. Embryos were observed to develop at a normal rate over a 72 hour period, development appeared uniform across the array as shown in Figure 6.4-1. Microperfusion was shown to slow down embryo hatching which was expected.¹⁶⁰

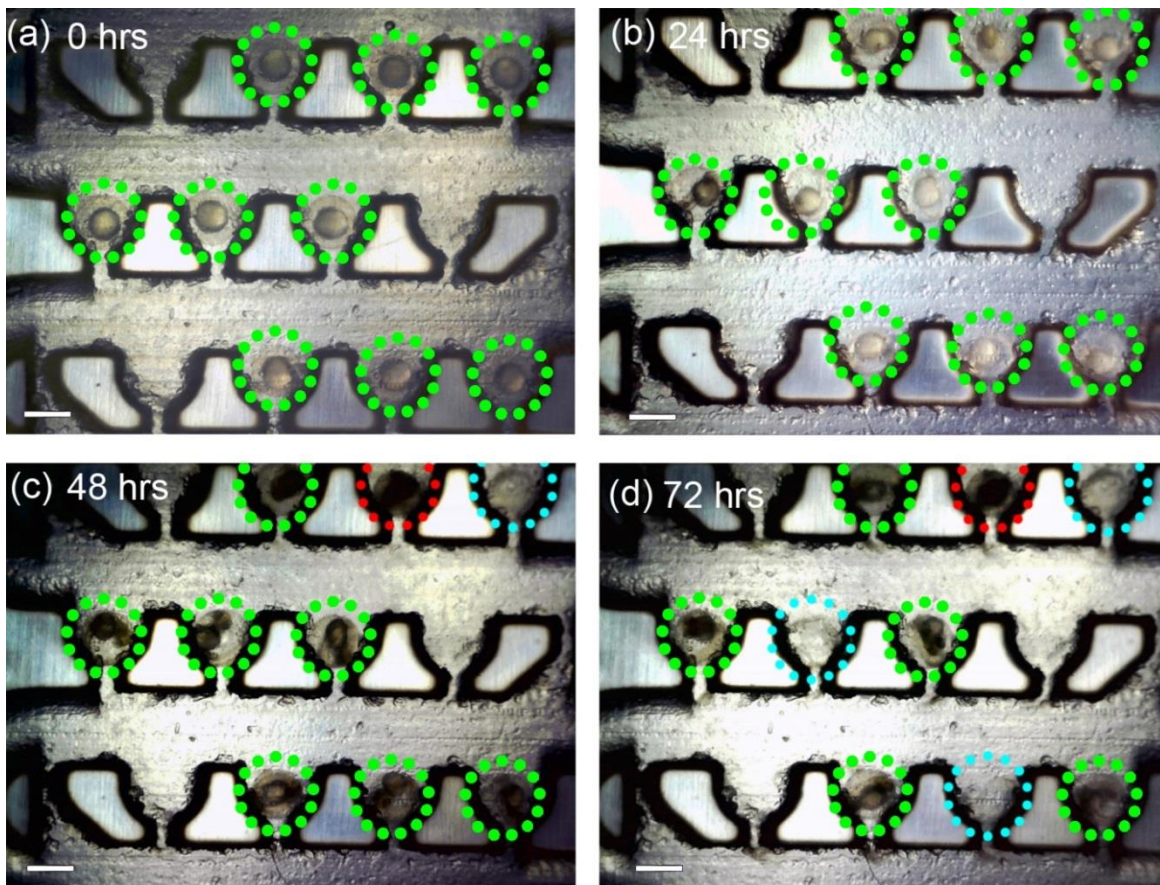


Figure 6.4-1– Assessment of microenvironmental conditions inside the chip. Time-lapse images of developing zebrafish embryos collected every 30 minutes over 52 hours. Embryos were loaded on a chip at a volumetric flow rate of 2 ml/min. Subsequently the chip was perfused at a rate of 0.5 ml/min for up to 72 hours. Green dotted circles indicate healthy zebrafish embryos, red dead zebrafish embryos and cyan hatched zebrafish embryo. Scale bar is 1 mm.

However on disconnection of the perfusion system a 100% mortality rate of embryos was observed within 4 hours of disconnection from the perfusion system Figure 6.4-2. The

embryos appeared to have reached a healthy stage after 48 hours Figure 6.4-2(a). However on disconnecting the flow, the embryos suffered cell death as well as free-swimming larva Figure 6.4-2(b). It was hypothesised that the oxygen level was rapidly diminishing within the restricted volume of the chip or that dead embryos were causing the medium to become toxic. It was also hypothesised that the material used for the support material (S3000) or the VisiJet Crystal material itself was potentially toxic to the zebrafish embryos when left in a static condition.

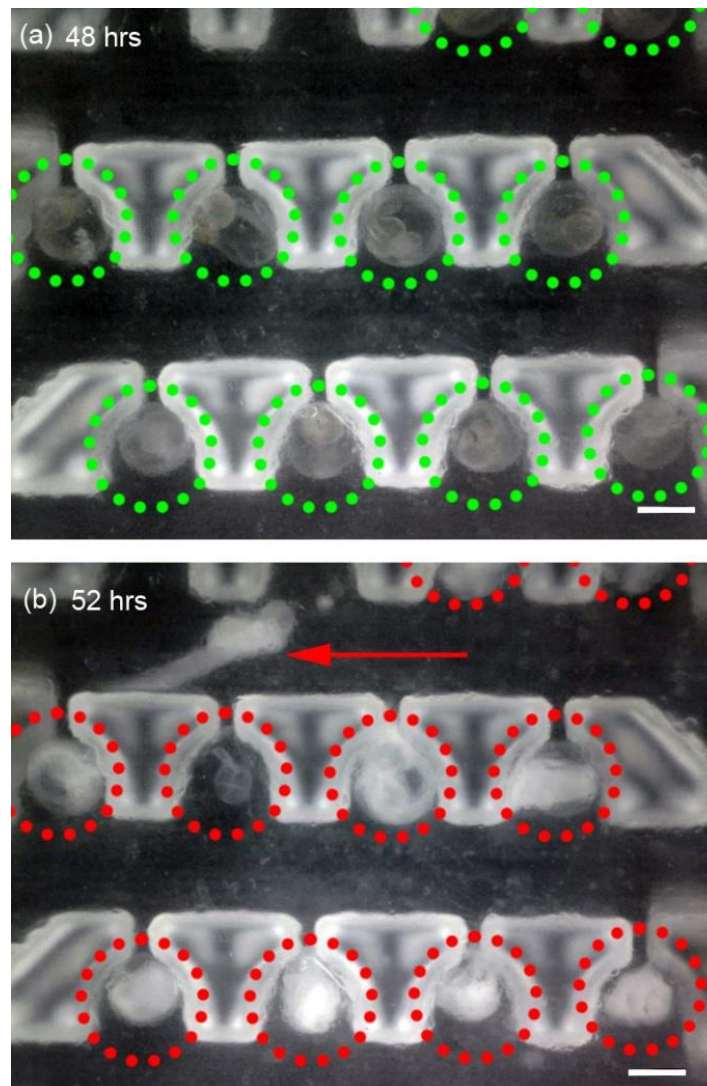


Figure 6.4-2 – Assessment of viability of zebrafish embryos cultured inside the chip. a) Microphotograph showing zebrafish embryos developed over 48 hours with a flow rate of 0.5 ml/min. Zebrafish developed and were viable. b) Microphotograph 4 hours after switching off the volumetric flow. One hatched zebrafish larva escaped a trap and remained in the channel, a 100% mortality rate of embryos was observed. Scale bar 1 mm.

It was in itself a concern that VisiJet Crystal material was potentially toxic as it is rated United States Pharmacopeia (USP) Class VI and hence certified for medical devices.²⁸⁸ The definition of biocompatibility by *Williams* is, “the ability of a material to perform with

an appropriate host response in a specific application.”²⁸⁹ Essentially, biocompatibility of the material depends on the context as well as the material.

Considering this, USP Class VI tests were primarily designed to evaluate plastics for pharmaceutical packaging. The tests are performed over a 5 day period including three tests: systemic injection, intracutaneous testing and implantation tests; all of which are performed on animals. This means it would be possible for a material to pass Class VI without testing of cytotoxic, mutagenic, hemolytic or sensitising. The ISO 10993 biological evaluation of medical devices set by the Food and Drug Administration (FDA) however has more rigorous testing matrix with a total of up to 20 different tests. A list of tests and further details regarding the FDA regulations on medical devices can be found in these references.^{290, 291} At the time of writing VisiJet Crystal has not passed the ISO 10993 tests suggesting that further data on the biocompatibility of VisiJet Crystal for medical devices should be conducted.

6.4.2 Biocompatibility testing of 3D printed materials

Investigating the effects on zebrafish embryo development and viability due to culture with 3D printed materials was conducted. The materials VisiJet Crystal, VisiJet S300 Support Material (wax), Watershed 11122XC and ABS polymers were tested for biocompatibility with zebrafish embryos.

6.4.3 Long term culture zebrafish embryos in VisiJet Crystal and S300 wax support material

These assumptions were validated by performing a long-term culture of zebrafish embryos in static conditions with the VisiJet Crystal 3D printed material and S300 support wax.

Wild-type AB zebrafish were placed in 3D printed 24-well plate dishes and standard Corning 24-well plates²⁸³. Each well had 5 embryos placed inside with 1 ml of E3 and maintained at 28.5 °C over the 90 hour experiment. Embryos were cultured in 3D printed 24-well plates with and without having had wax support material present using the printed process. Control samples were melted wax support material (10 mg) at the bottom of a 24-well plate and clean untreated wells. The optical results are shown in Figure 6.4-4.

Development of zebrafish in a 3D printed well without wax was entirely unsuccessful, 100% mortality rate was observed by 19 hours Figure 6.4-4. It was observed that 70% \pm 30% of zebrafish embryos within 3D printed wells with wax developed after 24 hours exposure shown in Figure 6.4-3(a). By 43 hours almost all (90%) of zebrafish were dead in

this sample, at 90 hours all zebrafish had experienced cell death. Wax and control samples were observed to have normal uniform development Figure 6.4-3(b).²²⁷

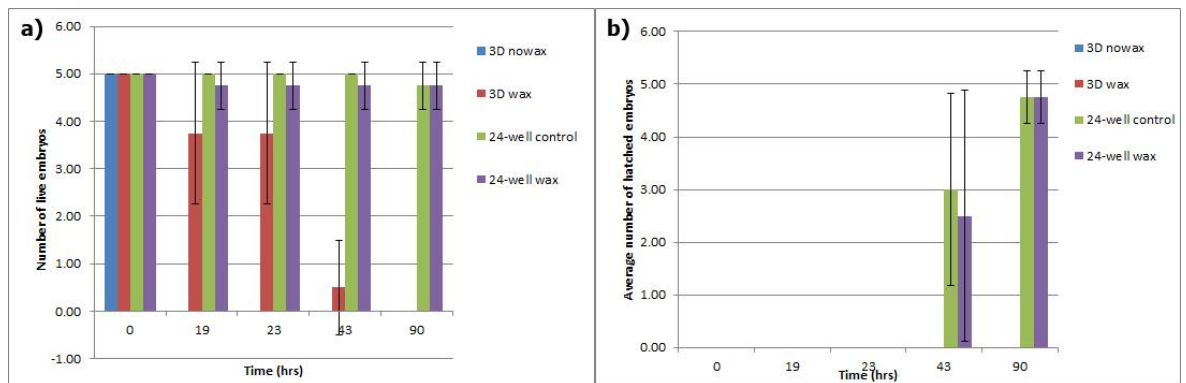


Figure 6.4-3 – Development of zebrafish embryos in 3D printed material VisiJet Crystal and VisiJet S300 support wax: a) Cumulative survival of zebrafish embryos, ‘3D nowax’ indicates 3D printed wells with no support material present, ‘3D wax’ indicates support wax had been present in the well and had been removed pre-experiment. B) Hatching success of embryos held with 3D printed materials.

From these experiments it was concluded that the VisiJet S300 wax support material was non-toxic to zebrafish embryos. It was also concluded that VisiJet Crystal was toxic to zebrafish embryos. The presence of unremoved wax support in the 3D printed wells deferred cell death by up to 43 hours but did not stop cell death from occurring. It was hypothesised that the wax support material was impeding the diffusion of toxic material into the E3 medium. VisiJet Crystal material printed parts were deemed unsuitable for zebrafish culture without detoxification treatment.

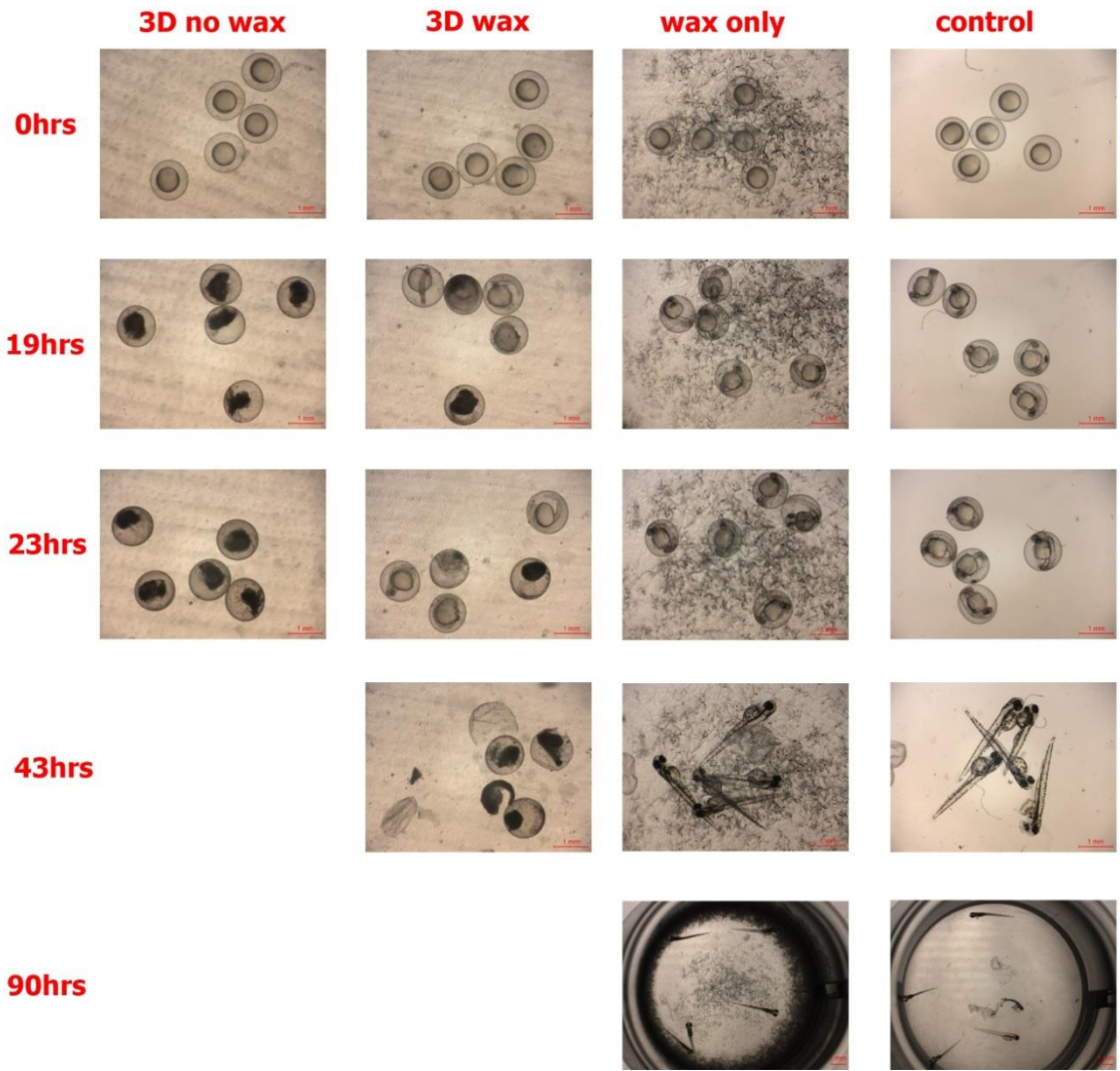


Figure 6.4-4 – Development of zebrafish embryos in HD3500+ printed VisiJet Crystal wells: Culture of zebrafish was conducted within 3D printed samples with and without wax support. Control samples consisted of wax support material melted on the bottom of 24-well plates and untreated 24-well plates. Cell death occurred in zebrafish within the 3D printed no wax samples within 24 hours. Embryos in the wax coated 3D printed wells followed at 47 hours. Wax and untreated samples developed normally.

6.4.4 Reduction of toxicity of 3D printed materials and improvements to biocompatibility

To test this hypothesis, 3D printed materials were pre-treated with washing steps. As toxic material was able to diffuse from the VisiJet Crystal (HD3500+) it was presumed that it could be removed by suitable dilution within a fluid. The testing of Watershed and ABS material was also conducted to compare the results of the VisiJet Crystal. For these experiments the 3D printed discs described in Section 6.3.2 were fabricated in both Watershed (Viper Pro) and VisiJet Crystal (HD3500+) as well as the single well fabricated in ABS plastic (HP DesignJet).

The results of incubating 1.5 hpf zebrafish embryos with disc samples are shown in figure Figure 6.4-5. It was found that washing both VisiJet Crystal discs and Watershed discs

improved survival of zebrafish embryos by 70 and 75% respectively after 4 hours. This was a small improvement on unwashed Watershed samples with a survival rate of 55%. The VisiJet Crystal and Watershed control unwashed samples dropped after 22 hours incubation. Mortality rate of all Watershed samples was 100%, survival rate of VisiJet Crystal was 10%. This compares well to the previous experiment results Figure 6.4-3. Watershed and VisiJet Crystal washed samples remained similar at 22 hours decreasing to 70% before decreasing again at 47 hours to 5%. By 52 hours only the control samples survived at 85% success. The drop in control was due to unfertilised eggs, control embryos were observed to develop normally as shown in Figure 6.4-6(a).

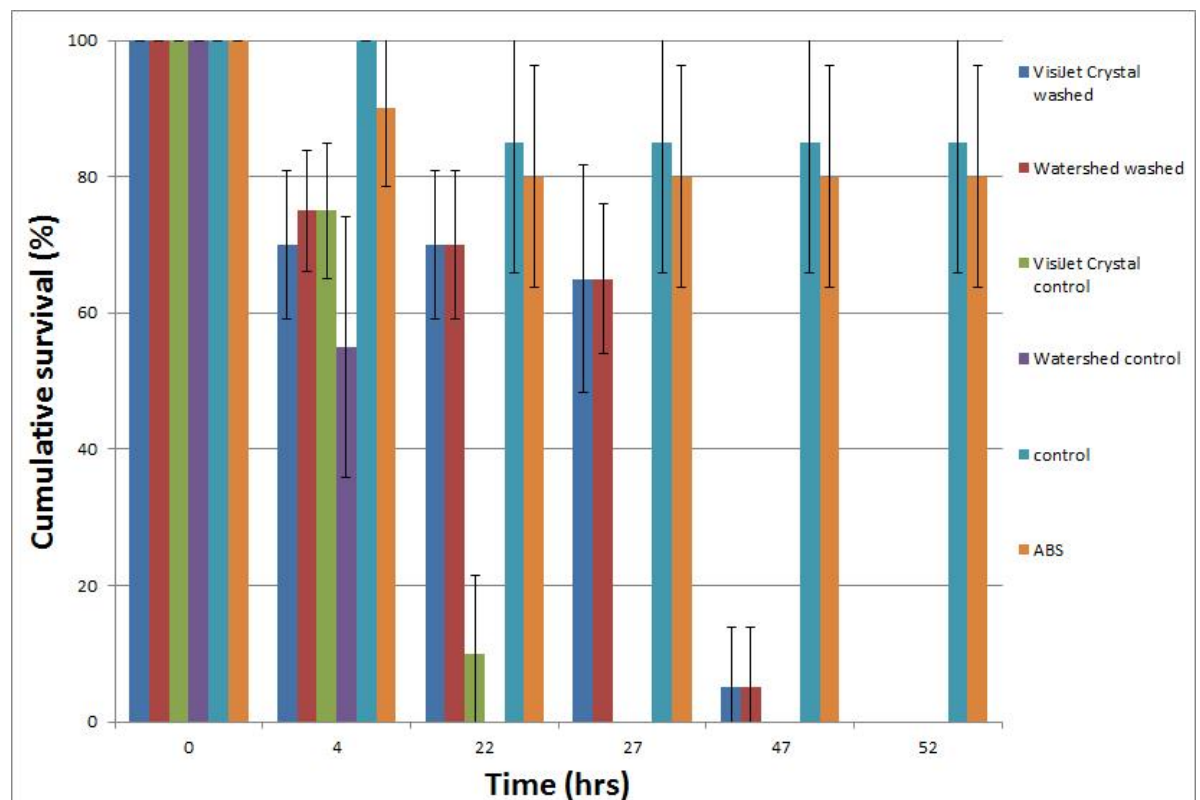


Figure 6.4-5 – Survival of zebrafish cultured with 3D printed materials. Zebrafish at 1.5 hpf were incubated with washed HD3500+ and Viper Pro samples, as well as unwashed samples. As expected unwashed samples caused cell death within 24 hours, cell death for washed samples was deferred to 52 hours. Survival rates of washed samples dropped to 70-75% within 4 hours and maintained at 70% for 22 hours, dropping again at 27 hours to 65%. By 47 hours of incubation washed sample survival had dropped to 5%. Confirmation of 0% survival was visualised at 52 hours. Control and ABS samples showed normal development and maintained a survival rate of 85-100% throughout the experiment. (n=4)

The development of Watershed incubated zebrafish appeared stunted by 2-3 hours compared to the control sample. Eyes and pigmentation were present however a darkening of the yolk sac and enlarged yolk extension was observed Figure 6.4-6(b). Further stunted growth was observed in VisiJet Crystal incubated samples Figure 6.4-6(c). Comparatively with the control sample in Figure 6.4-6(a) the zebrafish are 5 hours behind in terms of development. Eyes and pigmentation were missing, yolk sac and extension had abnormal

shapes and appearance darker. Overall the embryo was retarded in shape and size compared to the control.

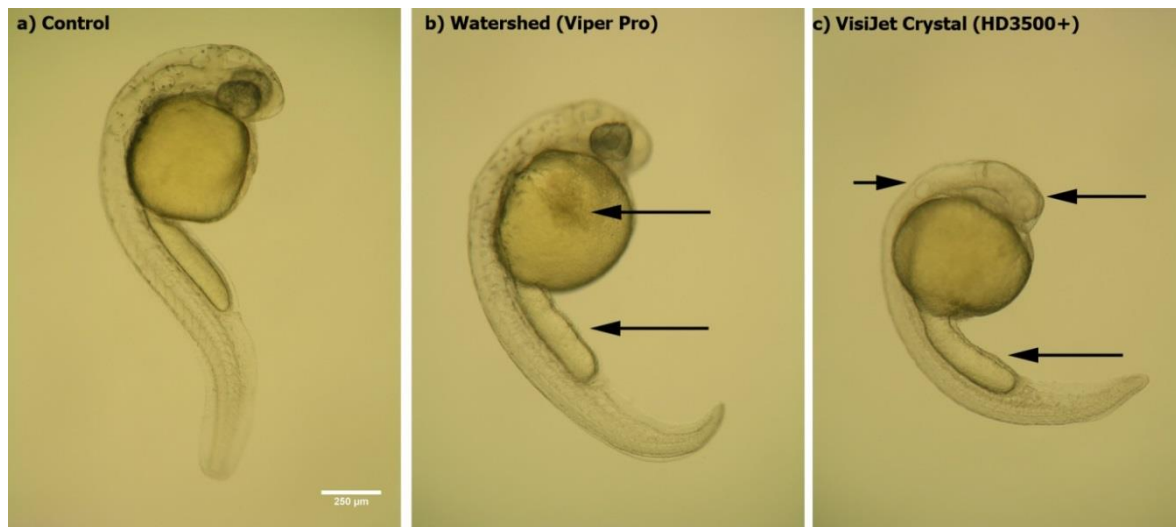


Figure 6.4-6 – Morphology analysis at 27 hours incubation of zebrafish with 3D printed materials. Stereomicroscopy images of dechorionated zebrafish embryos immobilised in agar: a) Control zebrafish embryo cultured in a 24-well plate development was normal. B) Image of zebrafish cultured with Watershed (Viper Pro) material. Development has been stunted, appears 2-3 hours behind control, darkening of yolk sac and roughing and widening yolk extension.²²⁷ C) Image of zebrafish cultured with VisiJet Crystal (HD3500+) printed disc. Development has been stunted by 5 hours, still in the 25-somites stage. Eyes and brain have not developed, pigmentation was not present, unusual yolk sac and yolk extension shape all show retardation.

6.4.5 Study of hatching success and survival rate with relation to incubation with 3D printed materials

In further study of these effects on the toxicity of 3D printed materials on zebrafish embryos this experiment was repeated with 24 hpf embryos. The hypothesis was that different effects on the zebrafish embryo development and increased survival rate will be apparent compared to 0 hpf. For these experiments washed VisiJet Crystal materials was incubated as well as unwashed Watershed and VisiJet Crystal control samples. Washed Watershed was thought to be not needed in this experiment as Watershed had been determined to be not only optically inferior to the VisiJet Crystal but also more toxic. Results indicated that even with 24 hpf Watershed samples were equally toxic to zebrafish embryos Figure 6.4-7(a).

It was shown that 6 hours of incubation with samples did not affect zebrafish survival significantly. However, after 25 hours of incubation with Watershed samples all zebrafish embryos experienced cell death. Survival remained high for washed VisiJet Crystal samples at 97%. Control unwashed VisiJet Crystal samples dropped to 80% while the control maintained at 97%. By 31 hours the unwashed samples had dropped significantly to 57%, washed samples only dropped by 3% to 95%. At the end of the experiment 17

hours later after 48 hours of incubation survival rate of unwashed samples dropped further to 22% with a large variance in rates across samples. The washed samples remained high at 85% with the variance increasing to 20%.

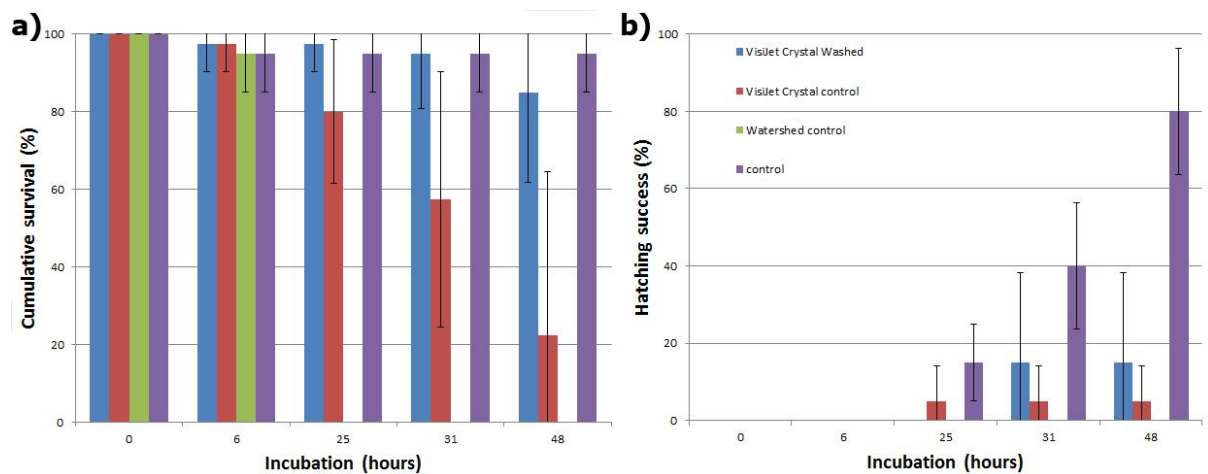


Figure 6.4-7 - Survival rate and hatching success of 24 hpf zebrafish cultured with 3D printed materials: a) Cumulative survival rate of zebrafish over a 48 hour incubation period. Watershed unwashed samples caused cell death within 25 hours of incubation. VisiJet Crystal controls shows a steady reduction of survival, washed samples however have increased survival, b) Cumulative hatching success of zebrafish embryos over a 48 hour incubation period. Watershed unwashed hatching rate was 0%. Washing of VisiJet Crystal samples improved hatching success to 15% compared to 5% for unwashed samples. Hatching of control samples was 80%. (n=4)

The control sample remained stable throughout the experiment from 6 hours of incubation with a survival rate of 95%. While the survival rate of the embryos appeared to have improved due to incubating zebrafish at 24 hpf, the hatching rate had not increased Figure 6.4-7(b). For unwashed samples only 10% hatched by 25 hours and remained constant. Washed samples were only marginally higher at 15% by 31 hours and again remained constant. The control samples increased at a normal rate until 48 hours where the hatching rate was 80%. These results show that despite the increase in survival due to using 24 hpf zebrafish embryos, development of the embryos was still being inhibited by the 3D printed materials. Changes to the zebrafish morphology development were also observed during these experiments as shown in Figure 6.4-8.

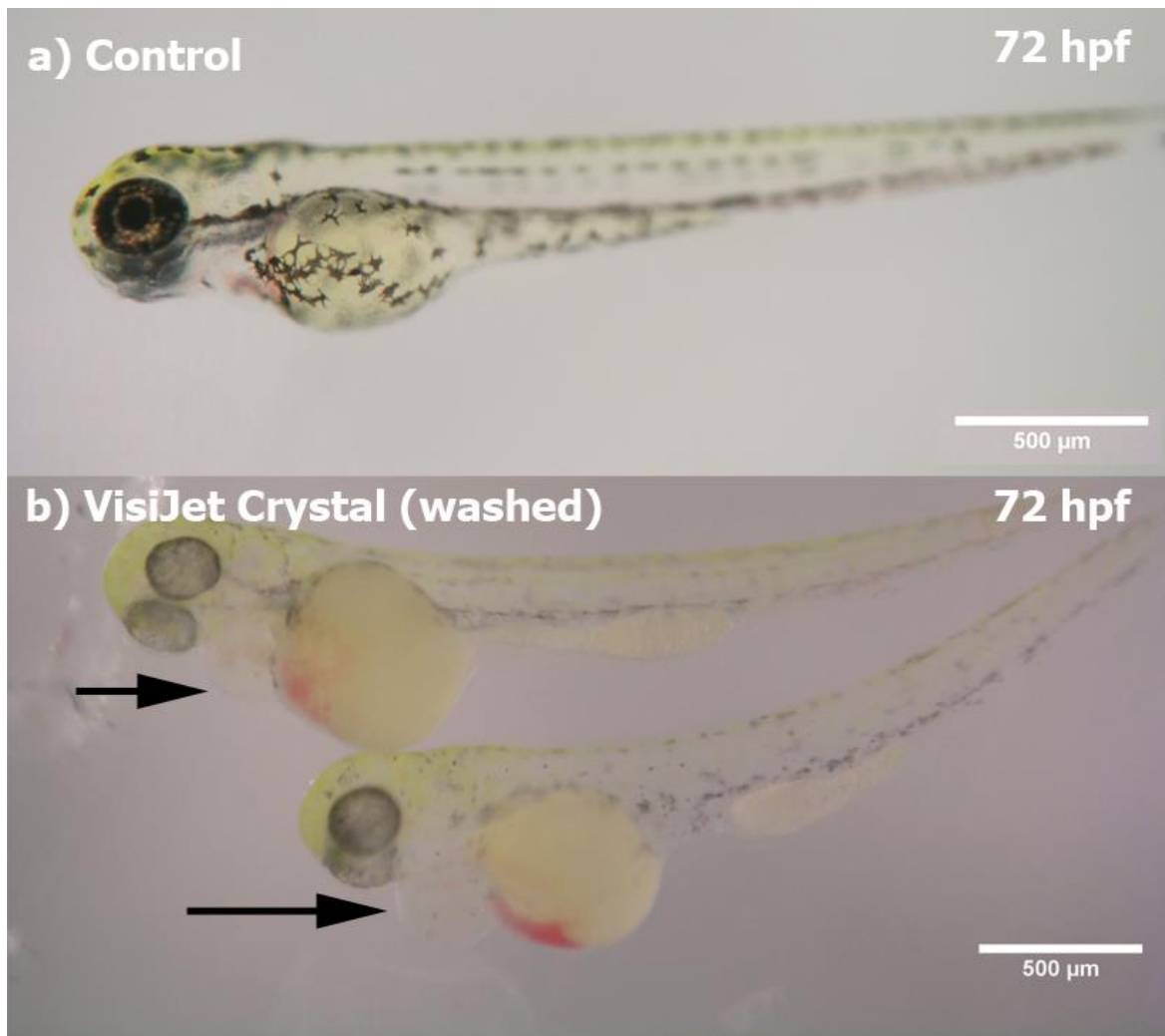


Figure 6.4-8 – Morphology changes during incubation with 3D printed materials of 72 hpf zebrafish: a) Stereomicroscopy of hatched zebrafish embryo control showing normal morphology development. B) Zebrafish after 48 hours of incubation with washed VisiJet Crystal samples. These fish are grossly normal, but show signs of developmental delay, hypopigmentation, heart edema, blood pooling and reduced yolk extensions. Scale bars are 500 μm.

The control samples developed normally with no observed defects Figure 6.4-8(a), however changes to the zebrafish development were recorded with the washed VisiJet Crystal samples Figure 6.4-8(b). The hatched larva appeared to have developed normally but slower than the control as indicated by the lower count of melanocytes. However, significant bleeding in the yolk sac which was also observed in the head area was present. The heart area was also seen to be swollen and enlarged compared to the control; these characteristics are not representative of healthy zebrafish embryo development.²²⁷ Culture of zebrafish embryos with the ABS printed single well showed no visible defects compared to the control Figure 6.4-9.

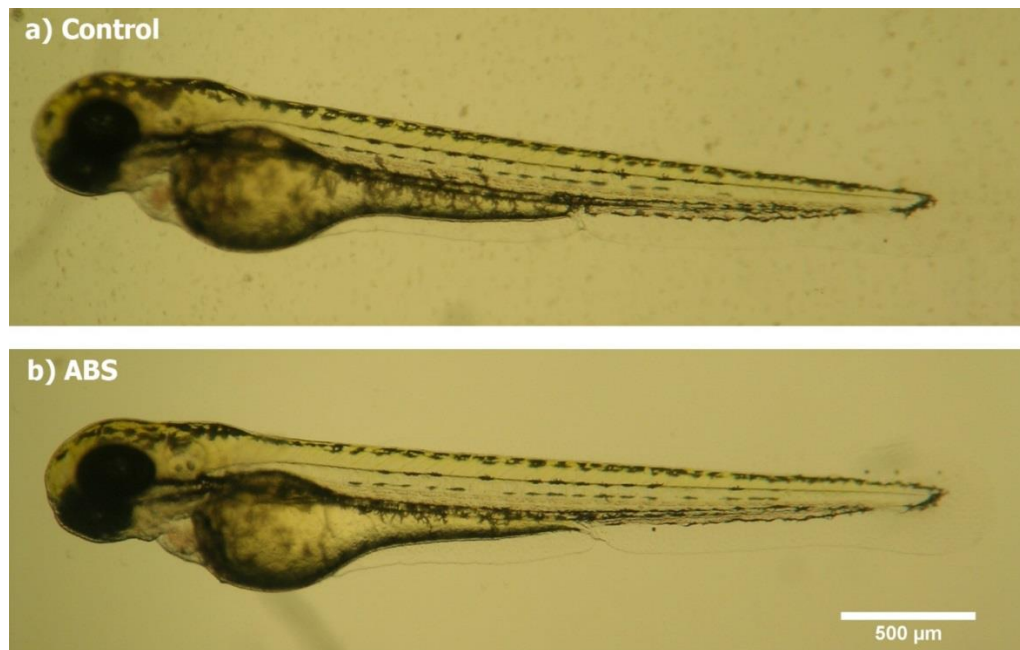


Figure 6.4-9 - Zebrafish incubated within a 3D printed single well of ABS for 72 hours: a) Control sample, b) Zebrafish incubated with ABS, no visible defects are present. Scale bar 500 μm .

To the author's knowledge at time of writing very little research has been completed in regard to toxicity of 3D materials. Work completed by *Stephens et al* has shown that ultra-fine particles (UFP), small, nanosized particles less than 100 nm in diameter are produced by commercially available 3D printers.²⁹² Their study concentrated on home 3D printers using polylactic acid (PLA) and ABS materials which are commonly used in low-resolution 3D printers without air-ventilation. The health implications for humans and UFP are serious because they deposit efficiently in both the pulmonary and alveolar regions of the lung²⁹³ and also in air headways. They considered that the use of unventilated 3D printers should be done with caution.²⁹² One important limitation to this studies on zebrafish is that we had no access to the exact chemical composition^{229, 288} of the 3D printed materials and hence any UFP being released into the medium.

However, condensation of synthetic organic vapours from the thermoplastic feedstock are possibly a large contributor.²⁹² There are significant differences in the three materials tested which led to differences in toxicity due to chemical composition. Studies looking at the toxicity effects of nanoparticles and their size have been conducted on zebrafish, including silver²⁹⁴, Titanium dioxide and zinc oxide.²⁹⁵ Both chemical composition and particle size have an effect on which cell type is affected and is size-dependent.²⁹⁴ Regardless, biocompatibility in relation to chemical composition of materials and particle size and/or coagulation should be explored in future studies.

6.4.6 Long term zebrafish embryos culture in 3D printed single wells

These results show that culturing zebrafish embryos in untreated 3D printed materials were unsuccessful. It was observed that all embryos in VisiJet Crystal and DSM Watershed wells yielded a 100% mortality rate after 18 hour of incubation (24 hpf); while in Dreve Fototec wells, embryos were still alive after 18 hour of incubation. Tail and eyes were partially developed, but embryos experienced cell death after 24 hour of incubation. It was concluded that untreated 3D printed materials are toxic to aquatic organisms. Primary post-treatments for printed parts were insufficient to minimise the toxicity.

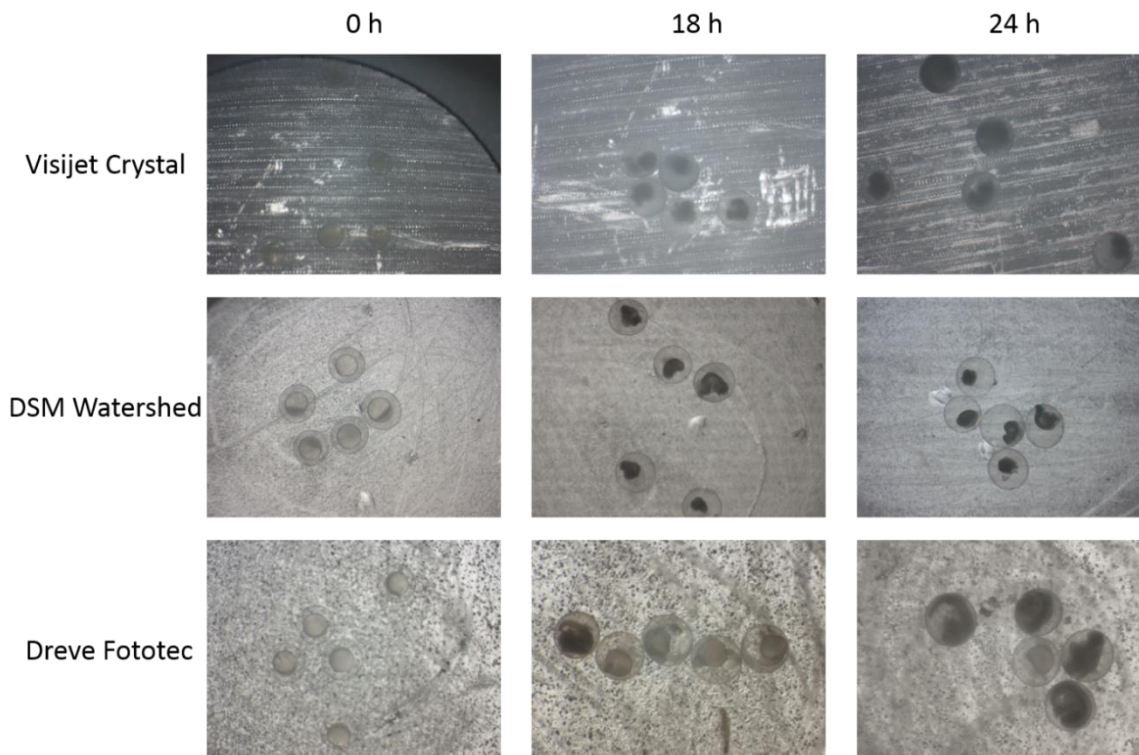


Figure 6.4-10 – Stereomicroscopy images of zebrafish embryos cultured on untreated 3D printed wells. Unfertilised embryos were sorted out at 6 hour post fertilisation (hpf), then were manually transferred into the wells. After 18 hour of incubation time, embryos from VisiJet Crystal and Watershed printed wells were died while most of embryos from Dreve Fototec printed wells were still alive. However, they experienced cell death after 24 hour of incubation.

It was hypothesised that water soluble residue from the materials was causing the death of aquatic organisms. Therefore, it was assumed that the material biocompatibility could be improved by washing the wells with organic solvents. For this study 70% ethanol, 99% ethanol and 99% isopropanol were selected because they are hydrophilic and readily available in the laboratory.

The results indicate that the solvent treatments increased the biocompatibility of 3D printed wells. The treatments prolonged the embryo lifetime up to 66 hour incubation in 70%

ethanol and 99% isopropanol rinsed wells and 77 hour incubation in 99% ethanol rinsed wells.

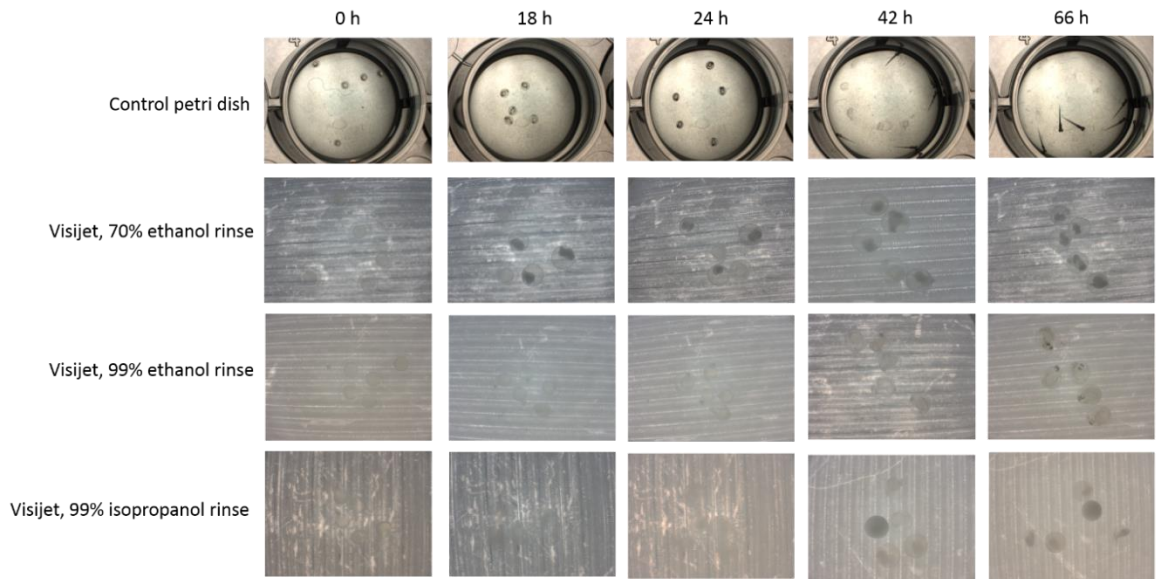


Figure 6.4-11 - Stereomicroscopy images of zebrafish embryos cultured on solvent rinsed 3D printed wells. Unfertilised embryos were sorted out at 6 hour post fertilisation (hpf), then were manually transferred into the wells. Wells were rinsed by solvents for up to two minutes. Embryos cultured in 99% isopropanol rinsed and 70% ethanol rinsed wells experienced 100% mortality after 66 hours incubation. Embryos from 99% ethanol rinsed wells were still alive but their embryogenesis were significantly delayed.

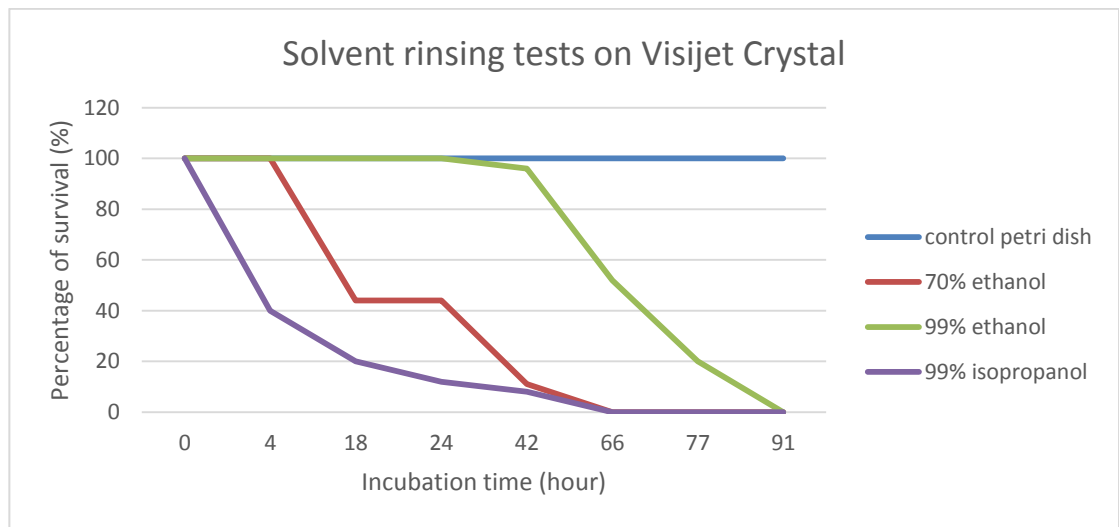


Figure 6.4-12 – Embryo survival percentages of different treatments over incubation time. Embryos from 99% ethanol, 70% ethanol and 99% isopropanol treated wells survived for up to 91, 66 and 66 hours respectively.

However embryo development was significantly delayed compared with embryos in control petri dish. After 18 hours, the difference in embryogenesis was subtle among all experiments. After 42 hours, 45% embryos in petri dish hatched whereas embryos in 99% ethanol rinsed wells did not develop complete eyes and tail. Embryo development stopped after 66 hours, the mortality rate was 100% by 77 hour incubation.

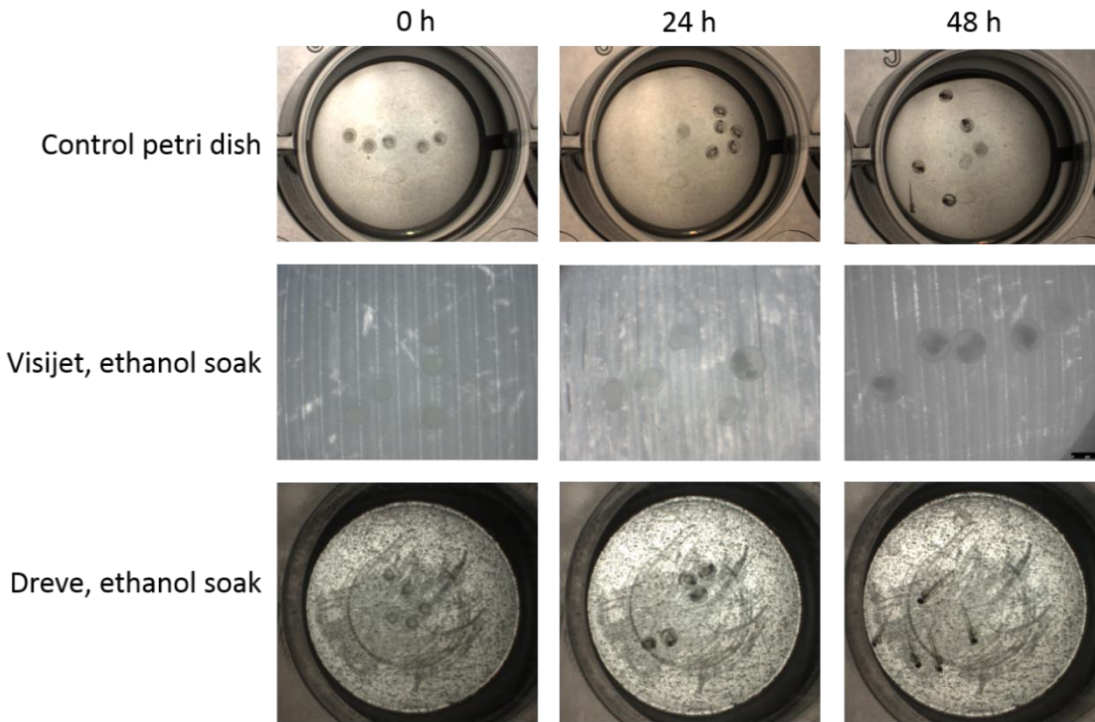


Figure 6.4-13 - Stereomicroscopy images of zebrafish embryos cultured on solvent rinsed 3D printed wells. Unfertilised embryos were sorted out at 6 hour post fertilisation (hpf), then were manually transferred into the wells. Wells were soaked in solvents for 24 hours. 50% embryos cultured in 99% ethanol soaked VisiJet Crystal wells experienced mortality after 48 hours of incubation. Meanwhile in 99% ethanol soaked Dreve Fototec wells, all embryos survived, the hatching rate was up to 48%.

Compared with all three treatments, rinsing with 99% ethanol achieved the highest level of biocompatibility followed by rinsing 70% ethanol and 99% isopropanol. However, the embryos mortality was 100% after 91 hour incubation. It was concluded that rinsing the 3D printed wells with 99% ethanol was a practical way to improve biocompatibility.

Thus, it was attempted to remove of all toxic residues by soaking 3D printed wells in 99% ethanol for 24 hours. This method was also applied to the wells printed in DSM Watershed and Dreve Fototec. After soaking, it was found that the bottom layer of the well printed in DSM Watershed dissolved, thus it was inapplicable for further tests.

The results show that 100% mortality occurred at 72 hours incubation for 99% ethanol soaking of VisiJet Crystal single wells. Up to 50% of embryos experienced cell death after 48 hours incubation the remainder were delayed in development. However, in Dreve Fototec polymer printed wells, embryos developed normally compared with those in control petri dish. Results show 10% of the unfertilised embryos experienced cell death in Dreve Fototec wells, as well as in the control petri dish. Survival rate of remaining

embryos for ethanol soaked Dreve Fotec single wells was 100%, and it was observed that 48% of hatched by 48 hours of incubation. This result strongly correlated with the experiment in control petri dish conditions.

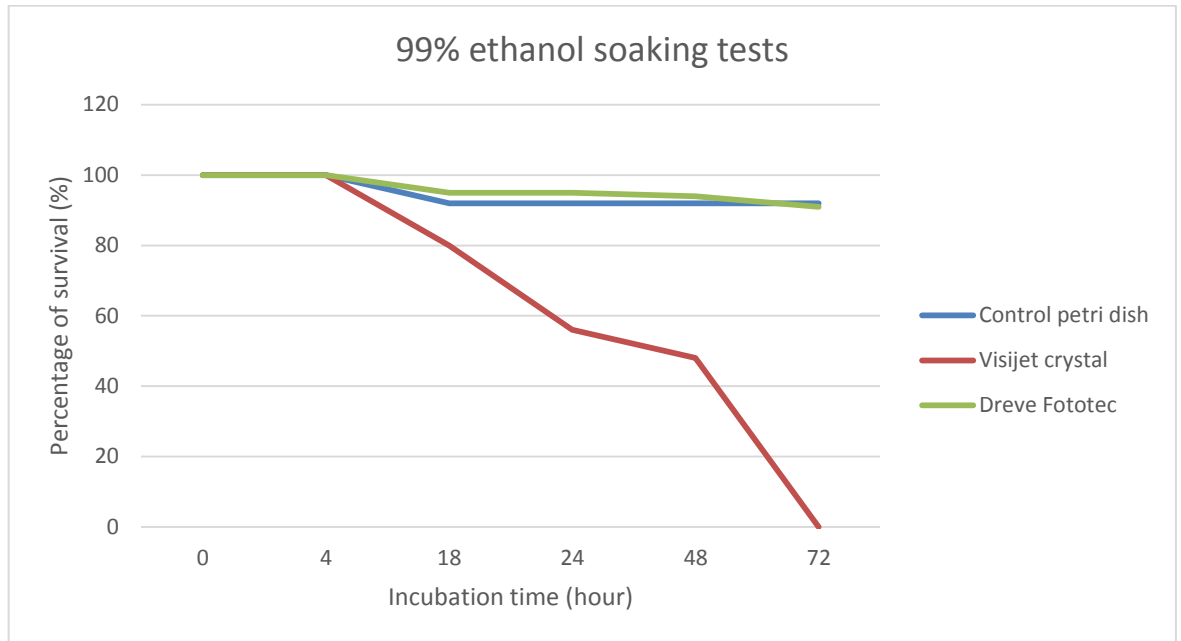


Figure 6.4-14 - Embryo survival percentages of different materials after 99% ethanol soaking over incubation time. Embryos from VisiJet Crystal printed wells experienced 100% mortality after 72 hours incubation. Apart from unfertilised embryos, all embryos from Dreve Fototec printed well survived after 72 hours incubation.

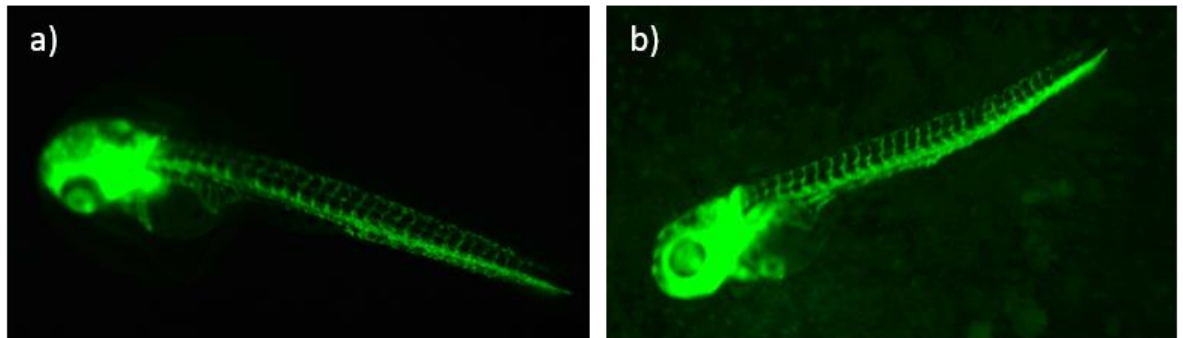


Figure 6.4-15 – Intersegment vessels (ISV) analysis morphology on hatched zebrafish larvae cultured from a) control petri dish and b) Dreve Fototec printed wells. After 72 hours of incubation in Dreve Fototec printed wells that soaked in 99% ethanol, larvae hatched and ISV were completely developed, in line with those cultured from control petri dish.

Intersegment vessel (ISV) morphology analysis on transgenic zebrafish embryos and larvae showed that larvae hatched from Dreve Fototec 3D printed wells treated with 99% ethanol, had normal ISV development compared with larvae hatched from control petri dish. Thus it was concluded that after 99% ethanol soaking treatment, wells printed by Dreve Fototec polymer became completely inert to zebrafish embryos and larvae.

6.5 Conclusions

In this chapter rapid prototyping methods were explored with regard to fabrication of microfluidic chips for the automated trapping, imaging and analysis of zebrafish embryos. Both multi-jet modelling (MJM) and stereolithography (SLA) processes were explored for this application. Monolithic microfluidic chips printed with the HD3500+ using VisiJet Crystal were fabricated to have optical quality and fluidic sealing suitable for visualisation and trapping of zebrafish embryos. The optical quality allowed for suitable detail to perform angiogenesis assays. The Viper Pro chips printed with Watershed material was found to be unsuitable for these purposes but allowed for brightfield imaging and trapping. Fabrication results compared favourably with other forms of rapid prototyping such as laser cut PMMA devices and PDMS moulded microfluidic devices of the same design. Both processes allowed for fabrication of monolithic, optically transparent devices with features in the 100 μm range requiring minimal post-processing.

It was shown that VisiJet Crystal (HD3500+) and Watershed (Viper Pro) materials are toxic to zebrafish embryos. The toxicity of these materials was reduced, however, zebrafish survivability was still low. Single wells printed in ABS (DesignJet) were found to have comparable viability with control samples indicating biocompatibility with zebrafish embryos. Untreated Dreve Fototec material was also found to be toxic to zebrafish embryos, but after soaking in 99% ethanol for 24 hours, they were completely inert to zebrafish embryos. Therefore, microfluidic chip devices fabricated using Dreve Fototec material with proper ethanol treatment can be used for small model organism *in-situ* analysis.

7 Conclusions and Future Work

7.1 Summary

“More complex cultures are needed for more complex questions”, Linda Griffith¹¹³

As the review on organ-on-a-chip technology by Monya Baker demonstrated, building living systems is a challenging field of research.¹¹³ A number of lab-on-a-chip based solutions specifically for the liver have been introduced to the market to address legislations banning the use of animals and relevance of animal studies for toxicity testing.^{30, 296} However, many of these solutions are based on monolayer (2D) cultures of cells as opposed to organ-on-a-chip or small-model organisms. The basis of this thesis was to develop new biological platforms for toxicity studies with regard to the 3R's of animal testing.

A high-throughput microfluidic device for the culture and toxicity analysis of hepatocytes using micro patterned substrates was developed.

A novel technique to build a liver-like biomimetic structure within an agar gel patterned using dielectrophoresis and a paper substrate for handling was demonstrated. This technique was successfully implemented allowing for the successful patterning and viability of liver-like structures over 72 hours; liver lobule-like tissue constructs were observed to positively affect liver functionality.

Finally, a novel fabrication technique for building automated zebrafish trapping chips was demonstrated using additive manufacturing. Additionally, a first of its kind research into the biocompatibility of 3D printed materials with zebrafish has been conducted.

7.2 Achievements and impact

Chapter 4 presented the results of a high-throughput microfluidic biochip platform using patterned liver cells on a flat surface for toxicity testing. Hepatocyte functionality (specifically the P450 enzyme) was investigated by use of the EROD assay; this was performed on micro-arrayed cell cultures within a microfluidic device. Three different microfluidic devices were tested with this approach: demonstration of primary hepatocyte culture on micro-arrays within a Dolomite microfluidic device and two PDMS custom

devices. The Dolomite single chamber device was shown to yield viable cells and cell arrays. The two PDMS microfluidic devices showed that micro-arrays of primary hepatocytes were viable and successfully attached to the micro-arrays within the device. Attachment of hepatocytes to the micro-array was reduced however from that of the results observed in Petri dish cultures. Micro-array cultures of hepatocytes within microfluidic devices were observed to have decreased levels of P450 activity compared to Petri dish conditions.

Chapter 5 presented and discussed the results of the novel biomimetic technique described in Chapter 2 to provide a liver lobule-like structure for toxicology. Through the use of dielectrophoretic forces hepatocyte cells (HepG2/C3A) were assembled within agar using laser cut paper as support. This allowed for the successful engineering of a physiologically relevant micro liver structure. Patterned hepatocytes were shown to proliferate in the shape of the pattern and remain viable over 72 hours. Albumin secretion was observed to increase due to the patterning showing an enhancement of hepatocyte functionality. This novel technique may prove to be useful to the scientific community in fabricating liver-like structures for organ-on-a-chip technology as well as for other organs.

Chapter 6 presented and discussed the results of zebrafish embryos cultured within microfluidic chips fabricated using the methods described in Chapter 3. This novel work developed monolithic microfluidic devices fabricated with multi-jet-modelling (MJM) using an HD3500+ 3D printer suitable for the automated trapping and optical analysis of zebrafish on-chip. Incubation of perfused zebrafish embryos on-chip over a 52 hours period was shown to yield development of zebrafish. However this study showed that photopolymers WaterShed XC 11122 and Dreve Fototec 7150 in addition to VisiJet Crystal were toxic to zebrafish embryos in static fluidic conditions. Investigation into the treatment of these materials to improve the biocompatibility of these materials was conducted. Improvement of zebrafish embryo viability was observed in VisiJet Crystal and WaterShed due to deionised water and EtOH 99% soaking, however it was not sufficient to remove toxicity completely. It was found that soaking of Dreve material in 99% EtOH rendered the material biocompatible for zebrafish embryo culture over a 72 hour period. Additionally, it was found that acrylonitrile butadiene styrene (ABS) printed devices was not harmful to zebrafish over a 72 hours incubation period.

7.3 Limitations of the thesis

The first part of this thesis approached this problem by developing microfluidic biochips which could provide a more realistic *in vitro* environment for ADME-Tox studies. The design and fabrication of a multi-chambered microfluidic device in PDMS was used to culture hepatocytes as discussed in Section 4.1.

Successful patterning hepatocytes on micro patterns was observed, and successfully integrated into the microfluidic device. However, due to the limited supply of primary cell line hepatocytes (rat and human) and difficulty in maintaining long term cultures⁵⁵ this method was not extensively investigated. Results collected showed that the culture of micro patterned hepatocytes within the device did not yield results that improved on controls completed in petri-dishes as shown in Section 4.6.

In the development of the micro patterns for hepatocytes used in this work, successful co-culture of 3T3 and hepatocyte cells was demonstrated,²⁰⁴ not however within a microfluidic device. Co-culture of 3T3 and hepatocytes has been shown to improve the production of important liver specific functions such as albumin production and urea secretion.^{119, 219}

The second part of the thesis investigated using positive dielectrophoresis (DEP) patterning within agar hydrogel with a paper ring substrate as described in Section 5.5.3. While the increase of albumin secretion was detected for patterned samples, the concentration of the albumin decreased after 72 hours. It is possible that longer term studies (up to 2 weeks)²⁶² could have given more insight to this effect. However, as it stood, the scope of this thesis was to develop platforms suitable for toxicity testing which normally manifest within 72 hours. This technique developed for this thesis allowed for a stable liver lobule-like structure within a biocompatible 3D culture environment.

This was possible because of the use of agar as a culture environment and method for retaining the liver lobule-like pattern post-DEP. As a biocompatible material with an ideal gel phase temperature (30 °C) agar was selected for this work. However, as *Lan et al* showed due to the lack of adhesion molecules available within the alginate matrix, attachment is inhibited.²⁶² Inclusion of adhesion promoting molecules such as poly(ethylene glycol)²⁵¹ can improve the cell viability and functionality²⁹⁷ as the hepatocytes can attach to the ECM as shown by *Taguchi et al* and *Glicklis et al*. Future

work using this technique for patterning liver lobule-like structures in agar should investigate the use of modified agar for improved liver specific functions.

7.4 Future research directions

7.4.1 Methods

7.4.2 Design and 3D printing

The microfluidic device was designed and printed using SolidWorks and the HD3500+ as described in Section 3.5. Schematics of the design can be found in Appendix C.

7.4.3 Result and discussion

The three technologies developed in this thesis provide a strong basis for a toxicity based analysis platform. With increasing resolution, accessibility and decreasing cost of 3D printing technology the adopting of this technology into microfluidics is achievable. The discovery of a technique to render the photopolymer Dreve Phototec 7150 inert creates momentum to continue research of 3D printing materials for small organism handling. Biocompatibility testing should be conducted with regard to investigating toxins present and possible ultra-fine particles which may be present. While the provider of 3D printers and materials remain legally able to withhold full chemical composition of materials, techniques such as mass spectrometry and Raman spectrometry should be used to investigate these polymers.

Further development of chip design for automated zebrafish handling should be pursued. In addition to zebrafish embryo immobilisation, hatched larvae can now be considered. Additive manufacturing technology proves the unique ability to define traps in 3D. The relief of traps could be designed to fit specifically to the shape of dechorionated zebrafish larvae to immobilise them during development. This would allow an automated system to monitor the effects of zebrafish larvae during early stage development without the need for additional invasive manipulation. The discovery of post-processing that renders Dreve biocompatible with zebrafish embryos is significant for the zebrafish research community. Stereolithography will become more accessible for labs and research groups meaning additive manufacture will not just be a prototyping tool, but a machine capable of building working devices for zebrafish handling.

The micro patterning platform for liver lobule-like patterns could be developed into a large-scale device for fabricating more complex tissue cultures for organs-on-chip.

Additional complexity to the design could be made for microfluidic delivery of nutrients and analytes for toxicity testing. Specifically, micro pillars in the region of 100 μm in height could be fabricated to provide a fluidic channel in the centre of the liver lobule-like pattern in hydrogel. This height would correspond to the height of the paper ring substrate also in the region of 100 μm . Control of the patterning volume would be optimised for the patterning system which would use computer controlled processing to remove human error and improve repeatability. This can be achieved using microcontroller based systems or with a PC running computer software such as LabView. Using this method, multiple stacks of patterned agar gel paper discs similar to work by *Derda et al*²⁹⁸ can be made to construct different cell type cultures, analysis cell-cell interactions and build larger tissue-like cell cultures.

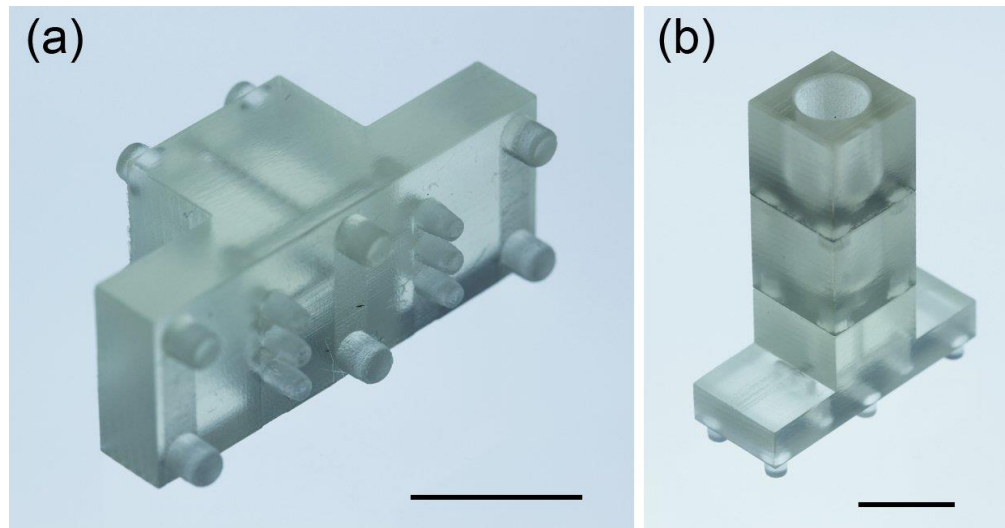


Figure 7.4-1 – Photographs showing results of multi-jet modelling (MJM) fabricated fluidic system. (a) The base of the system shown here splits the flow from a central vertical channel into six spate channels ending in connecting nozzles. This bottom piece could be connected to a 3D printed enclosure for liver lobule-like tissue constructs to provide nutrients and analytes. (b) Connected system using interlocking pins. The top cube chambers could act as medium reservoirs for adding analytes to the system. Scale bars are 10 mm.

These single or multiple stack cell discs could be integrated into microfluidic systems using resealable devices fabricated using 3D printed devices following the conformation of biocompatibility of Dreve with mammalian cell cultures. The design of the 3D printed device would allow for a complex fluidic network mimicking the liver lobule blood supply from the hepatic portal veins. The general concept displayed in Figure 7.4-1 shows interlocking fluidic components that can be easily assembled/disassembled. This supply of medium carrying nutrients (and during tests analytes), would drain through the liver lobule-like structure into the centre channel mimicking the central vein. Analysis of the resulting medium by industry standard assays would investigate albumin protein secretion, urea production and metabolised analytes due to cytochrome P450 enzymes. Once

biocompatible polymers have been achieved for mammalian cells, further research into the utilisation of this promising technology can be fully embraced by the tissue engineering and biomedical engineering community.

7.5 Conclusion

As stated by *Russell and Burch*:

“Refinement is never enough, and we should always seek further reduction and if possible replacement. . . . Replacement is always a satisfactory answer.”¹⁵

This thesis has successfully investigated microfluidic, dielectrophoretic and additive manufacturing techniques to develop strategies to replace and reduce the need for animal studies. A new method of creating a physiologically relevant micro liver was developed. In the future, this could be used to layer multiple cell types to form complex, physiologically relevant micro-liver models for toxicity testing. In addition the robustness of the agar and paper construction would allow integration into microfluidic systems fabricated using stereolithography. The discovery of a post-processing method to render photopolymers for stereolithography biocompatibility has the potential to be greatly beneficial for the zebrafish research community. Automation and analysis of zebrafish handling facilitated through additive manufacturing will have a significant impact to replace, reduce and refine the use of mammalian animal testing for toxicity.

Appendix A

Etch process parameters

STS multiplex inductively coupled plasma (ICP) machine etch process parameters for 100 μm etch:

Coil power 600W for etch and passivation; platen power 12W; gases flow rates: C_4F_8 : 85 sccm, SF_6 : 130 sccm, O_2 : 10 sccm; etch pressure 35 mT; passivation pressure 25 mT; chamber temperature 50 $^\circ\text{C}$.

PDMS mould

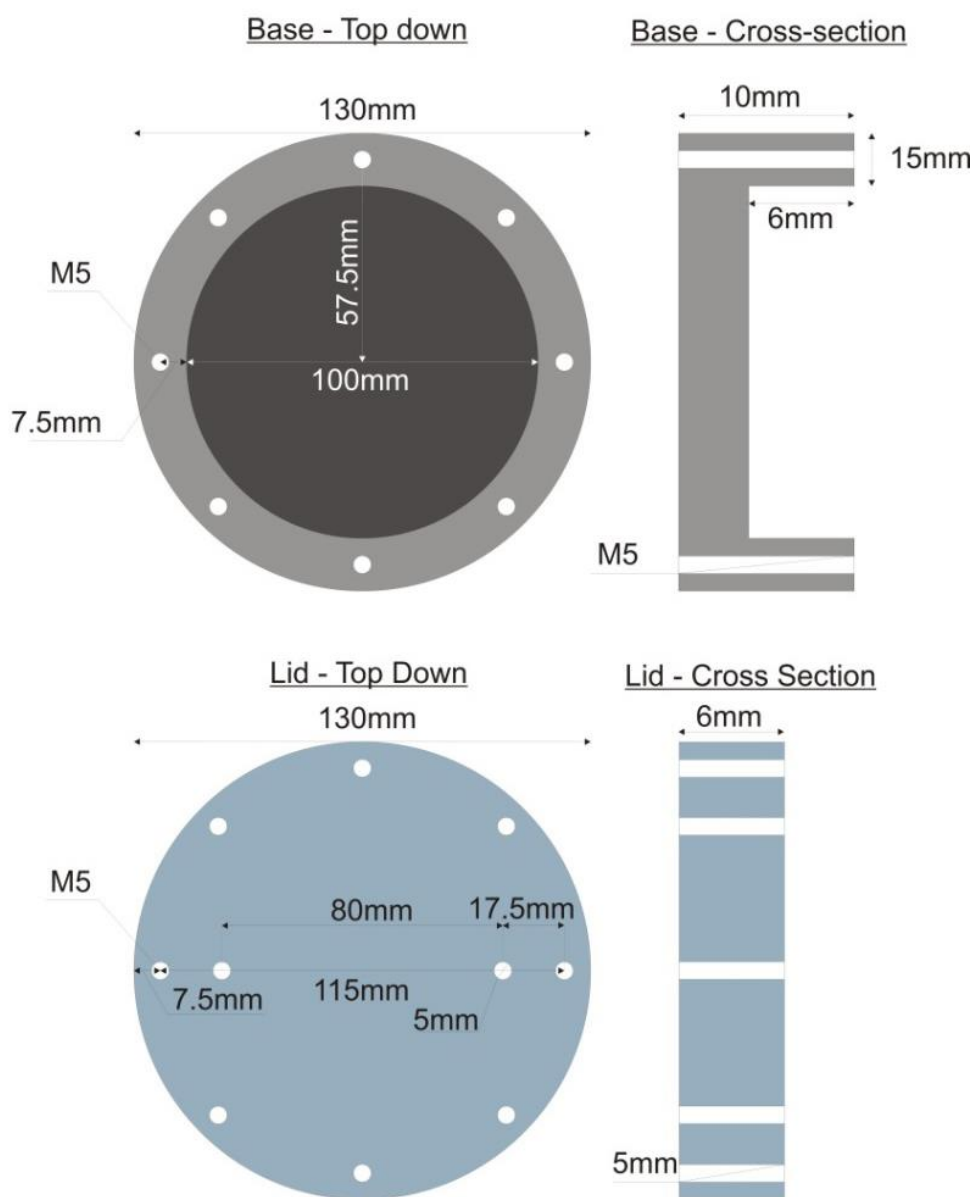


Figure A-1 – PDMS mould design. The lid is fabricated from polycarbonate. The base is fabricated from aluminium.

Clamp design for microfluidic clamp system

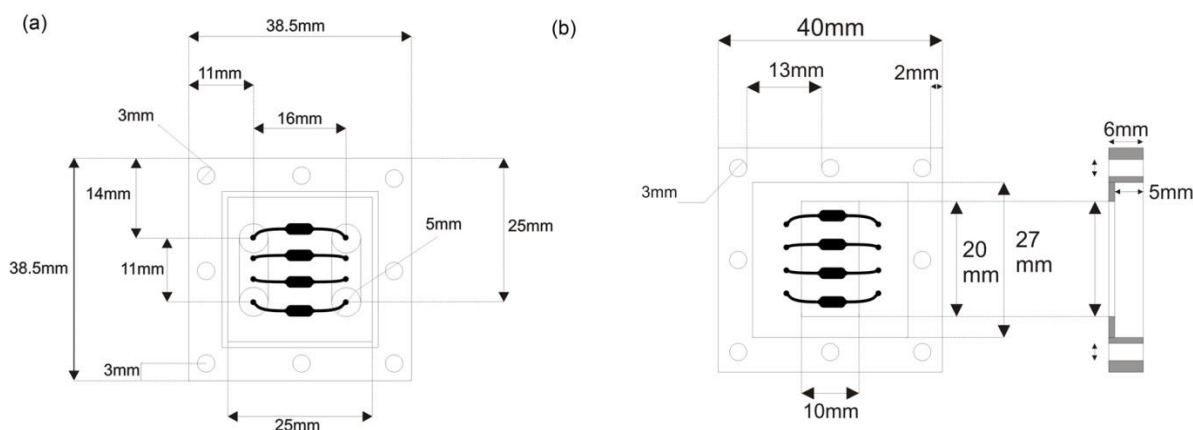


Figure A-2 - Computer aided design (CAD) design of clamp system with relation to the 4 chamber microfluidic chip (a) shows the Perspex top with channel positioning. (b) shows the aluminium bottom with cross section.

Valve bread board design

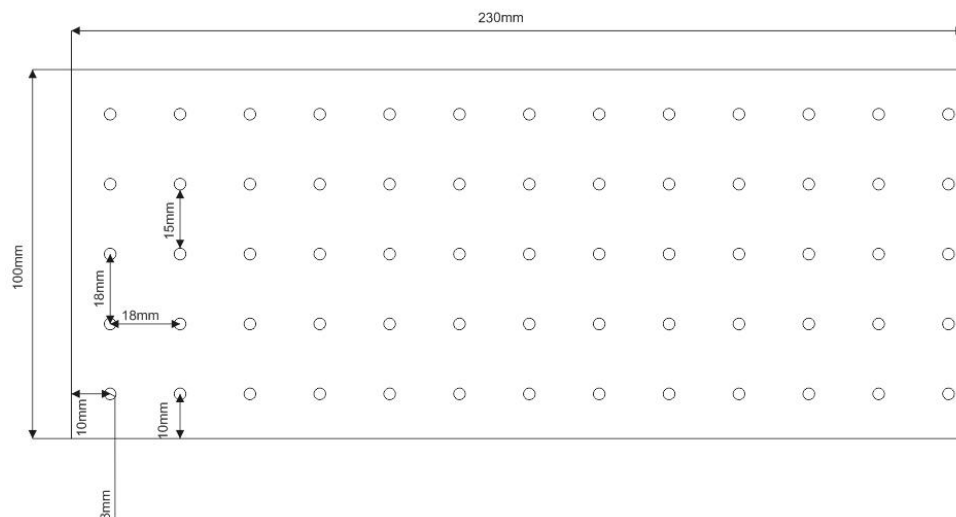


Figure A-3 – Designed to attach microbore valves securely to a flat surface, minimising movement of the interconnecting tubing between the pumps and the device. Rubber feet were attached to each of the corners to allow it to grip the microscope stage.

Appendix B

DEP pattern cover design

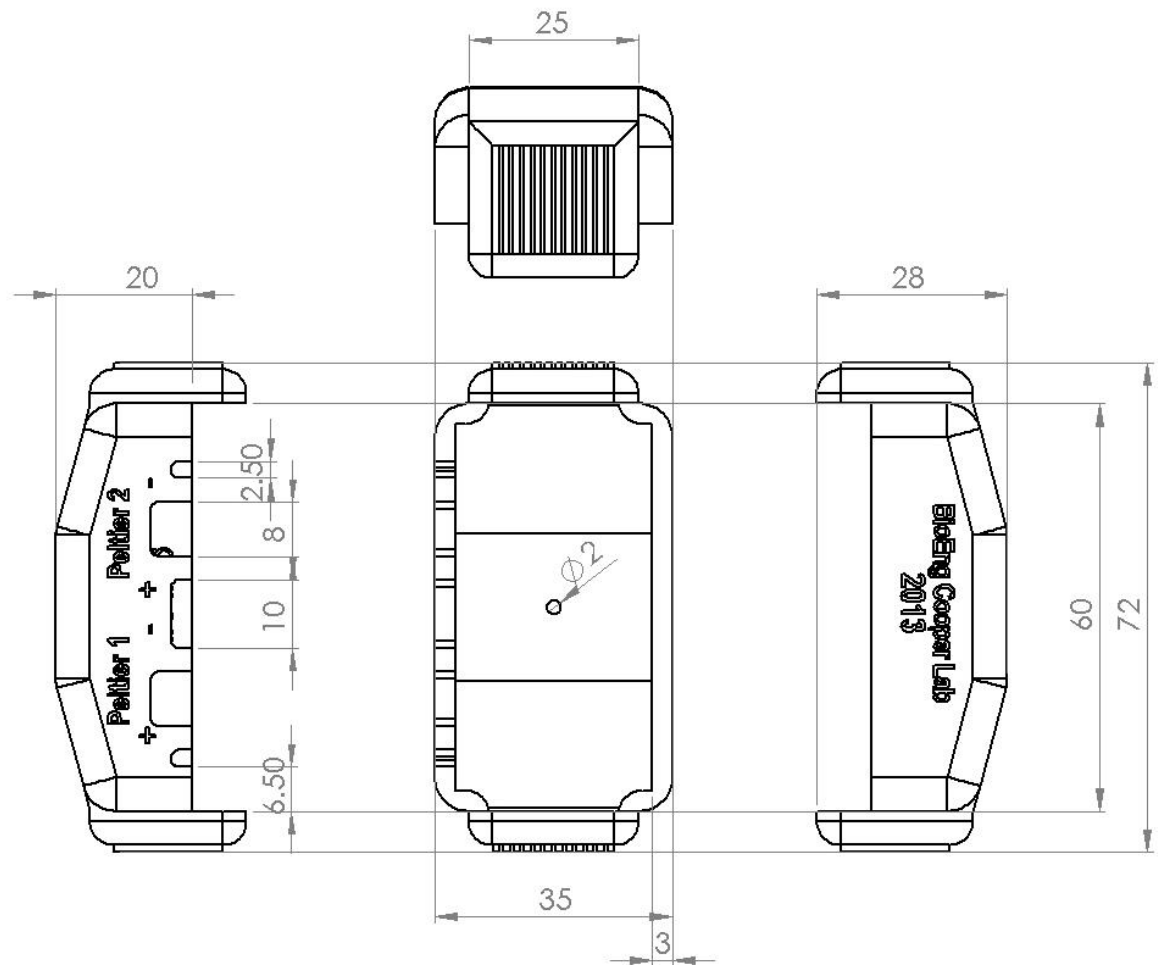


Figure B-1 – Schematic of cover design used for the liver lobule-like patterning system. Measurements are in mm.

Appendix C

Stackable interlocking fluidic system

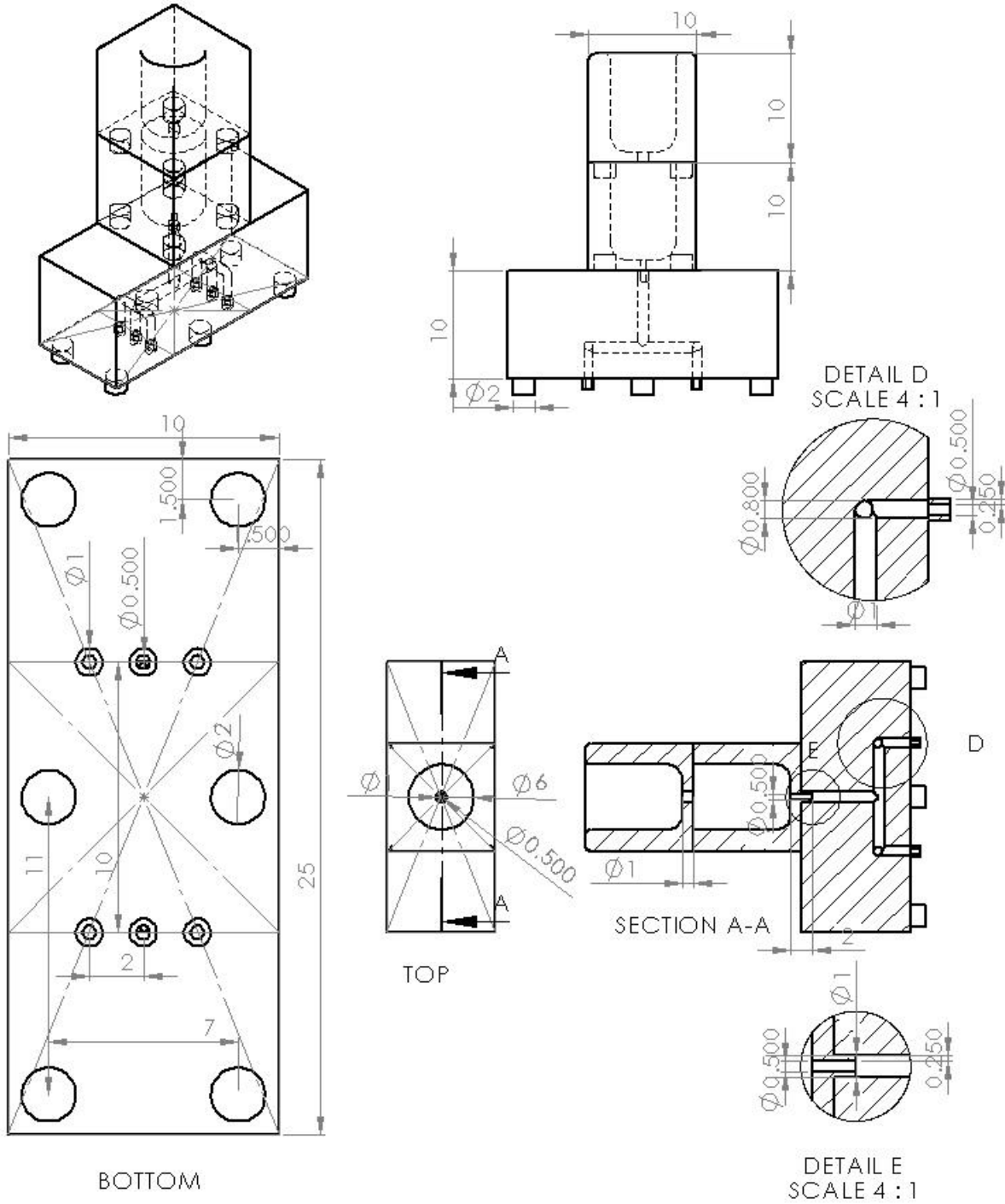


Figure C-1 – Schematic of design for a stackable interlocking fluidic system. Measurements are in mm.

Bibliography

1. Shuler, M.L. Modeling Life. *Annals of Biomedical Engineering* **40**, 1399-1407 (2012).
2. Adams, C.P. & Brantner, V.V. Estimating the cost of new drug development: Is it really \$802 million? *Health Affairs* **25**, 420-428 (2006).
3. Esch, M.B., King, T.L. & Shuler, M.L. The role of body-on-a-chip devices in drug and toxicity studies. *Annu Rev Biomed Eng* **13**, 55-72 (2011).
4. Kola, I. & Landis, J. Can the pharmaceutical industry reduce attrition rates? *Nature Reviews Drug Discovery* **3**, 711-715 (2004).
5. McKenzie, R., Fried, M.W., Sallie, R., Conjeevaram, H., Di Bisceglie, A.M., Park, Y. *et al.* Hepatic Failure and Lactic Acidosis Due to Fialuridine (FIAU), an Investigational Nucleoside Analogue for Chronic Hepatitis B. *New England Journal of Medicine* **333**, 1099-1105 (1995).
6. Knight, A. Systematic reviews of animal experiments demonstrate poor human clinical and toxicological utility. *Altern Lab Anim* **35**, 641-659 (2007).
7. Pound, P., Ebrahim, S., Sandercock, P., Bracken, M.B., Roberts, I. & Grp, R. Where is the evidence that animal research benefits humans? *British Medical Journal* **328**, 514-517 (2004).
8. Seok, J., Warren, H.S., Cuenca, A.G., Mindrinos, M.N., Baker, H.V., Xu, W. *et al.* Genomic responses in mouse models poorly mimic human inflammatory diseases. *Proceedings of the National Academy of Sciences* (2013).
9. Pat, D.L., J., *The Experiment Is on Us: Science of Animal Testing Thrown into Doubt*, Available from: <<http://independentsciencenews.org/news/the-experiment-is-on-us-animal-toxicology-testing-science/>>. [08/06/13]
10. Regan, T. The case for animal rights. (University of California Press, Berkeley; 1983).
11. *Meeting the Deadline of the 2013 EU Marketing Ban A Scientific Review of Non Animal Tests for Cosmetics*, The British Union for the Abolition of Vivisection (BUAV), Available from: <http://ec.europa.eu/consumers/sectors/cosmetics/files/pdf/animal_testing/at_responses/eceae_ia_2013_2_en.pdf>.
12. *Modification to the ICATM Memorandum of Cooperation*, National Toxicology Program, Available from: <http://ntp.niehs.nih.gov/iccvam/docs/about_docs/ICATM-MOC-Mar11.pdf>. [22/03/14]
13. Business, E., *Full EU ban on animal testing for cosmetics*, EU Business, Available from: <<http://www.eubusiness.com/topics/health/cosmetics-testing-ban>>. [08/06/13]
14. *Cruelty Free International in China*, BUVA, Available from: <<http://www.buav.org/article/1279/cruelty-free-international-in-china>>.
15. Russell, W.M.S. & Burch, R.L. The principles of humane experimental technique. (Methuen, London,; 1959).
16. Festing, M.F.W. & Altman, D.G. Guidelines for the design and statistical analysis of experiments using laboratory animals. *ILAR journal / National Research Council, Institute of Laboratory Animal Resources* **43**, 244-258 (2002).
17. Fitts, D.A. Ethics and Animal Numbers: Informal Analyses, Uncertain Sample Sizes, Inefficient Replications, and Type I Errors. *Journal of the American Association for Laboratory Animal Science* **50**, 445-453 (2011).
18. Johnson, P.D. & Besselsen, D.G. Practical aspects of experimental design in animal research. *ILAR journal / National Research Council, Institute of Laboratory Animal Resources* **43**, 202-206 (2002).
19. Lappin, G. & Garner, R.C. The utility of microdosing over the past 5 years. *Expert Opinion on Drug Metabolism & Toxicology* **4**, 1499-1506 (2008).
20. *ABPI Guidelines Project Licence Application*, ABPI, Available from: <<http://www.abpi.org.uk/our-work/library/guidelines/Documents/phase1-trial-guidelines.pdf>>. [22/03/14]
21. Langley, G., Harding, G., Hawkins, P., Jones, A., Newman, C., Swithenby, S. *et al.* Volunteer studies replacing animal experiments in brain research - Report and recommendations of a Volunteers in Research and Testing workshop. *Atla-Alternatives to Laboratory Animals* **28**, 315-331 (2000).
22. Andersen, M.E. & Krewski, D. Toxicity Testing in the 21st Century: Bringing the Vision to Life. *Toxicological Sciences* **107**, 324-330 (2009).
23. Krewski, D., Acosta, D., Andersen, M., Anderson, H., Bailar, J.C., Boekelheide, K. *et al.* Toxicity Testing in the 21st Century: A Vision and a Strategy. *Journal of Toxicology and Environmental Health-Part B-Critical Reviews* **13**, 51-138 (2010).
24. Knight, A. Non-animal methodologies within biomedical research and toxicity testing. *Altex-Alternativen Zu Tierexperimenten* **25**, 213-231 (2008).
25. Harvey, W. On the motion of the heart and blood in animals. (Prometheus Books, Buffalo, N.Y.; 1993).
26. Allen, D.D., Caviedes, R., Cardenas, A.M., Shimahara, T., Segura-Aguilar, J. & Caviedes, P.A. Cell lines as in vitro models for drug screening and toxicity studies. *Drug Development and Industrial Pharmacy* **31**, 757-768 (2005).

190 Bibliography

27. Jones, H.W., Jr., McKusick, V.A., Harper, P.S. & Wu, K.D. George Otto Gey. (1899-1970). The HeLa cell and a reappraisal of its origin. *Obstet Gynecol* **38**, 945-949 (1971).
28. Levintow, L. & Eagle, H. Biochemistry of Cultured Mammalian Cells. *Annual Review of Biochemistry* **30**, 605-& (1961).
29. Augustit.G & Sato, G. Establishment of Functional Clonal Lines of Neurons from Mouse Neuroblastomae. *Proceedings of the National Academy of Sciences of the United States of America* **64**, 311-& (1969).
30. Adler, S., Basketter, D., Creton, S., Pelkonen, O., van Benthem, J., Zuang, V. *et al.* Alternative (non-animal) methods for cosmetics testing: current status and future prospects-2010. *Arch Toxicol* **85**, 367-485 (2011).
31. Aarons, L. Physiologically based pharmacokinetic modelling: a sound mechanistic basis is needed. *British Journal of Clinical Pharmacology* **60**, 581-583 (2005).
32. Gerlowski, L.E. & Jain, R.K. Physiologically based pharmacokinetic modeling: principles and applications. *J Pharm Sci* **72**, 1103-1127 (1983).
33. Atkinson, A.J., Jr. & Smith, B.P. Models of physiology and physiologically based models in clinical pharmacology. *Clin Pharmacol Ther* **92**, 3-6 (2012).
34. Lin, J.H. & Lu, A.Y.H. Role of pharmacokinetics and metabolism in drug discovery and development. *Pharmacological Reviews* **49**, 403-449 (1997).
35. Teorell, T. Kinetics of distribution of substances administered to the body I The extravascular modes of administration. *Archives Internationales De Pharmacodynamie Et De Therapie* **57**, 205-225 (1937).
36. Paalzow, L.K. Torsten Teorell, the Father of Pharmacokinetics. *Uppsala Journal of Medical Sciences* **100**, 41-46 (1995).
37. Segre, G. Kinetics of Interaction between Drugs and Biological Systems. *Farmaco-Edizione Scientifica* **23**, 907-& (1968).
38. Khalil, F. & Laer, S. Physiologically Based Pharmacokinetic Modeling: Methodology, Applications, and Limitations with a Focus on Its Role in Pediatric Drug Development. *Journal of Biomedicine and Biotechnology* (2011).
39. Maurel, P. Hepatocytes: Methods and Protocols. (Humana Press, 2010).
40. Gunawan, B.K. & Kaplowitz, N. Mechanisms of drug-induced liver disease. *Clin Liver Dis* **11**, 459-475, v (2007).
41. Gomez-Lechon, M.J., Castell, J.V. & Donato, M.T. Hepatocytes--the choice to investigate drug metabolism and toxicity in man: in vitro variability as a reflection of in vivo. *Chem Biol Interact* **168**, 30-50 (2007).
42. Schiff, L. & Schiff, E.R. Diseases of the liver, Edn. 7th. (Lippincott, Philadelphia; 1993).
43. Zakim, D. & Boyer, T.D. Hepatology : a textbook of liver disease, Edn. 3rd. (W.B. Saunders, Philadelphia; 1996).
44. Saxena, R., Theise, N.D. & Crawford, J.M. Microanatomy of the human liver - Exploring the hidden interfaces. *Hepatology* **30**, 1339-1346 (1999).
45. *Structure of a Hepatic Lobule*, Available from: <http://illuminationstudios.com/archives/150/structure-of-a-hepatic-lobule>. [10/06/13]
46. Kiernan, F. The Anatomy and Physiology of the Liver. *Philosophical Transactions of the Royal Society of London* **123**, 711-770 (1833).
47. Berry, M.N. & Friend, D.S. High-yield preparation of isolated rat liver parenchymal cells: a biochemical and fine structural study. *J Cell Biol* **43**, 506-520 (1969).
48. Berry, M.N. & Edwards, A.M. The hepatocyte review. (Kluwer Academic Publishers, Dordrecht ; Boston; 2000).
49. Chiba, M., Ishii, Y. & Sugiyama, Y. Prediction of Hepatic Clearance in Human From In Vitro Data for Successful Drug Development. *AAPS J* **11**, 262-276 (2009).
50. Yamazaki, S., Skaptason, J., Romero, D., Vekich, S., Jones, H.M., Tan, W. *et al.* Prediction of oral pharmacokinetics of cMet kinase inhibitors in humans: physiologically based pharmacokinetic model versus traditional one-compartment model. *Drug Metab Dispos* **39**, 383-393 (2011).
51. Hosea, N.A., Collard, W.T., Cole, S., Maurer, T.S., Fang, R.X., Jones, H. *et al.* Prediction of human pharmacokinetics from preclinical information: comparative accuracy of quantitative prediction approaches. *J Clin Pharmacol* **49**, 513-533 (2009).
52. Cho, C.H., Berthiaume, F., Tilles, A.W. & Yarmush, M.L. A new technique for primary hepatocyte expansion in vitro. *Biotechnol Bioeng* **101**, 345-356 (2008).
53. Guguen-Guillouzo, C. & Guillouzo, A. General review on in vitro hepatocyte models and their applications. *Methods Mol Biol* **640**, 1-40 (2010).
54. Cho, C.S., Hoshiba, T., Harada, I. & Akaike, T. Regulation of hepatocyte behaviors by galactose-carrying polymers through receptor-mediated mechanism. *Reactive and Functional Polymers* **67**, 1301-1310 (2007).

55. Tuschl, G., Hrach, J., Hewitt, P.G. & Mueller, S.O. in Hepatotoxicity 139-174 (John Wiley & Sons, Ltd, 2008).
56. Graaf, I.A.M., Groothuis, G.M.M. & Olinga, P. Precision-cut tissue slices as a tool to predict metabolism of novel drugs. *Expert Opinion on Drug Metabolism & Toxicology* **3**, 879-898 (2007).
57. Morris, K.M., Aden, D.P., Knowles, B.B. & Colten, H.R. Complement biosynthesis by the human hepatoma-derived cell line HepG2. *J Clin Invest* **70**, 906-913 (1982).
58. Kelly, J.H. & Sussman, N.L. A fluorescent cell-based assay for cytochrome P-450 isozyme 1A2 induction and inhibition. *J Biomol Screen* **5**, 249-254 (2000).
59. Artursson, P. & Borchardt, R. Intestinal Drug Absorption and Metabolism in Cell Cultures: Caco-2 and Beyond. *Pharmaceutical Research* **14**, 1655-1658 (1997).
60. Gallagher, R. & Appenzeller, T. Beyond Reductionism. *Science* **284**, 79 (1999).
61. Tsuda, Y., Kikuchi, A., Yamato, M., Chen, G. & Okano, T. Heterotypic cell interactions on a dually patterned surface. *Biochemical and Biophysical Research Communications* **348**, 937-944 (2006).
62. Manson, S.M. Simplifying complexity: a review of complexity theory. *Geoforum* **32**, 405-414 (2001).
63. Huh, D., Hamilton, G.A. & Ingber, D.E. From 3D cell culture to organs-on-chips. *Trends in Cell Biology* **21**, 745-754 (2011).
64. Janmey, P.A., Winer, J.P., Murray, M.E. & Wen, Q. The Hard Life of Soft Cells. *Cell Motility and the Cytoskeleton* **66**, 597-605 (2009).
65. Langer, R. & Vacanti, J. Tissue engineering. *Science* **260**, 920-926 (1993).
66. Katz, B.Z., Zamir, E., Bershadsky, A., Kam, Z., Yamada, K.M. & Geiger, B. Physical state of the extracellular matrix regulates the structure and molecular composition of cell-matrix adhesions. *Mol Biol Cell* **11**, 1047-1060 (2000).
67. Pampaloni, F., Reynaud, E.G. & Stelzer, E.H.K. The third dimension bridges the gap between cell culture and live tissue. *Nat Rev Mol Cell Biol* **8**, 839-845 (2007).
68. Mazzoleni, G., Di Lorenzo, D. & Steimberg, N. Modelling tissues in 3D: the next future of pharmaco-toxicology and food research? *Genes & Nutrition* **4**, 13-22 (2009).
69. Elliott, N.T. & Yuan, F. A review of three-dimensional in vitro tissue models for drug discovery and transport studies. *Journal of pharmaceutical sciences* **100**, 59-74 (2011).
70. Lazarovici, P., Li, M., Perets, A., Mondrinos, M.J., Lecht, S., Koharski, C.D. *et al.* in Drug Testing in vitro 1-51 (Wiley-VCH Verlag GmbH & Co. KGaA, 2006).
71. Bashir, R. BioMEMS: state-of-the-art in detection, opportunities and prospects. *Advanced Drug Delivery Reviews* **56**, 1565-1586 (2004).
72. Whitesides, G.M. The origins and the future of microfluidics. *Nature* **442**, 368-373 (2006).
73. Qi, H., Du, Y., Wang, L., Kaji, H., Bae, H. & Khademhosseini, A. Patterned Differentiation of Individual Embryoid Bodies in Spatially Organized 3D Hybrid Microgels. *Advanced Materials* **22**, 5276-5281 (2010).
74. Zamanian, B., Masaeli, M., Nichol, J.W., Khabiry, M., Hancock, M.J., Bae, H. *et al.* Interface-Directed Self-Assembly of Cell-Laden Microgels. *Small* **6**, 937-944 (2010).
75. Hui, E.E. & Bhatia, S.N. Micromechanical control of cell-cell interactions. *Proc Natl Acad Sci U S A* **104**, 5722-5726 (2007).
76. Schütte, J., Hagemeyer, B., Holzner, F., Kubon, M., Werner, S., Freudigmann, C. *et al.* "Artificial micro organs"—a microfluidic device for dielectrophoretic assembly of liver sinusoids. *Biomedical Microdevices* **13**, 493-501 (2011).
77. Frimat, J.-P., Becker, M., Chiang, Y.-Y., Marggraf, U., Janasek, D., Hengstler, J.G. *et al.* A microfluidic array with cellular valving for single cell co-culture. *Lab on a Chip* **11**, 231-237 (2011).
78. Ghaemmaghami, A.M., Hancock, M.J., Harrington, H., Kaji, H. & Khademhosseini, A. Biomimetic tissues on a chip for drug discovery. *Drug Discovery Today* **17**, 173-181 (2012).
79. Sant, S., Hancock, M.J., Donnelly, J.P., Iyer, D. & Khademhosseini, A. Biomimetic gradient hydrogels for tissue engineering. *The Canadian Journal of Chemical Engineering* **88**, 899-911 (2010).
80. Stuart, M.A., Huck, W.T., Genzer, J., Muller, M., Ober, C., Stamm, M. *et al.* Emerging applications of stimuli-responsive polymer materials. *Nat Mater* **9**, 101-113 (2010).
81. Shi, J., Votruba, A.R., Farokhzad, O.C. & Langer, R. Nanotechnology in Drug Delivery and Tissue Engineering: From Discovery to Applications. *Nano Letters* **10**, 3223-3230 (2010).
82. Dvir, T., Timko, B.P., Kohane, D.S. & Langer, R. Nanotechnological strategies for engineering complex tissues. *Nat Nanotechnol* **6**, 13-22 (2011).
83. Tay, C.Y., Irvine, S.A., Boey, F.Y.C., Tan, L.P. & Venkatraman, S. Micro-/Nano-engineered Cellular Responses for Soft Tissue Engineering and Biomedical Applications. *Small* **7**, 1361-1378 (2011).

192 Bibliography

84. Khademhosseini, A., Langer, R., Borenstein, J. & Vacanti, J.P. Microscale technologies for tissue engineering and biology. *Proceedings of the National Academy of Sciences of the United States of America* **103**, 2480-2487 (2006).
85. El-Ali, J., Sorger, P.K. & Jensen, K.F. Cells on chips. *Nature* **442**, 403-411 (2006).
86. Squires, T.M. & Quake, S.R. Microfluidics: Fluid physics at the nanoliter scale. *Reviews of Modern Physics* **77**, 977-1026 (2005).
87. Stone, H.A., Stroock, A.D. & Ajdari, A. Engineering flows in small devices: Microfluidics toward a lab-on-a-chip. *Annual Review of Fluid Mechanics* **36**, 381-411 (2004).
88. Manz, A., Harrison, D.J., Verpoorte, E.M.J., Fettingner, J.C., Paulus, A., Ludi, H. *et al.* Planar Chips Technology for Miniaturization and Integration of Separation Techniques into Monitoring Systems - Capillary Electrophoresis on a Chip. *Journal of Chromatography* **593**, 253-258 (1992).
89. Wu, M.-H., Huang, S.-B. & Lee, G.-B. Microfluidic cell culture systems for drug research. *Lab on a Chip* **10**, 939-956 (2010).
90. Dittrich, P.S. & Manz, A. Lab-on-a-chip: microfluidics in drug discovery. *Nat Rev Drug Discov* **5**, 210-218 (2006).
91. Gupta, K., Kim, D.-H., Ellison, D., Smith, C., Kundu, A., Tuan, J. *et al.* Lab-on-a-chip devices as an emerging platform for stem cell biology. *Lab on a Chip* **10**, 2019-2031 (2010).
92. van Noort, D., Ong, S.M., Zhang, C., Zhang, S., Arooz, T. & Yu, H. Stem cells in microfluidics. *Biotechnology Progress* **25**, 52-60 (2009).
93. Wlodkowic, D. & Cooper, J.M. Tumors on chips: Oncology meets microfluidics. *Current Opinion in Chemical Biology* **14**, 556-567 (2010).
94. Ziolkowska, K., Kwapiszewski, R. & Brzozka, Z. Microfluidic devices as tools for mimicking the in vivo environment. *New Journal of Chemistry* **35**, 979-990 (2011).
95. Yeo, L.Y., Chang, H.-C., Chan, P.P.Y. & Friend, J.R. Microfluidic Devices for Bioapplications. *Small* **7**, 12-48 (2011).
96. Paguirigan, A.L. & Beebe, D.J. From the cellular perspective: exploring differences in the cellular baseline in macroscale and microfluidic cultures. *Integrative Biology* **1**, 182-195 (2009).
97. Meyvantsson, I. & Beebe, D.J. in *Annual Review of Analytical Chemistry*, Vol. 1 423-449 (Annual Reviews, Palo Alto; 2008).
98. Ahmed, T., Shimizu, T.S. & Stocker, R. Microfluidics for bacterial chemotaxis. *Integrative Biology* **2**, 604-629 (2010).
99. Chung, S., Sudo, R., Vickerman, V., Zervantonakis, I. & Kamm, R. Microfluidic Platforms for Studies of Angiogenesis, Cell Migration, and Cell-Cell Interactions. *Annals of Biomedical Engineering* **38**, 1164-1177 (2010).
100. Zervantonakis, I.K., Kothapalli, C.R., Chung, S., Sudo, R. & Kamm, R.D. Microfluidic devices for studying heterotypic cell-cell interactions and tissue specimen cultures under controlled microenvironments. *Biomicrofluidics* **5**, 13406 (2011).
101. Le Gac, S. & van den Berg, A. Single cells as experimentation units in lab-on-a-chip devices. *Trends Biotechnol* **28**, 55-62 (2010).
102. Kaji, H., Yokoi, T., Kawashima, T. & Nishizawa, M. Directing the flow of medium in controlled cocultures of HeLa cells and human umbilical vein endothelial cells with a microfluidic device. *Lab on a Chip* **10**, 2374-2379 (2010).
103. Domansky, K., Inman, W., Serdy, J., Dash, A., Lim, M.H.M. & Griffith, L.G. Perfused multiwell plate for 3D liver tissue engineering. *Lab on a Chip* **10**, 51-58 (2010).
104. Sim, W.Y., Park, S.W., Park, S.H., Min, B.H., Park, S.R. & Yang, S.S. A pneumatic micro cell chip for the differentiation of human mesenchymal stem cells under mechanical stimulation. *Lab on a Chip* **7**, 1775-1782 (2007).
105. Hancock, M.J., He, J., Mano, J.F. & Khademhosseini, A. Surface-Tension-Driven Gradient Generation in a Fluid Stripe for Bench-Top and Microwell Applications. *Small* **7**, 892-901 (2011).
106. Wu, J.M., Chung, Y.K., Belford, K.J., Smith, G.D., Takayama, S. & Lahann, J. A surface-modified sperm sorting device with long-term stability. *Biomedical Microdevices* **8**, 99-107 (2006).
107. Wu, J., Tu, G. & Luo, Y. Distributed voltage emergency control based on coordination of multi-methods. *Gaodianya Jishu/High Voltage Engineering* **32**, 99-101+107 (2006).
108. Kim, S.B., Bae, H., Cha, J.M., Moon, S.J., Dokmeci, M.R., Crokek, D.M. *et al.* A cell-based biosensor for real-time detection of cardiotoxicity using lensfree imaging. *Lab on a Chip* **11**, 1801-1807 (2011).
109. Figueroa, X.A., Cooksey, G.A., Votaw, S.V., Horowitz, L.F. & Folch, A. Large-scale investigation of the olfactory receptor space using a microfluidic microwell array. *Lab on a Chip* **10**, 1120-1127 (2010).
110. Kirby, B. *Micro- and nanoscale fluid mechanics : transport in microfluidic devices.* (Cambridge University Press, New York; 2010).
111. Bruus, H. *Theoretical microfluidics*, Vol. 18. (Oxford University Press, 2008).

112. Happel, J. & Brenner, H. Low Reynolds number hydrodynamics: with special applications to particulate media, Vol. 1. (Springer, 1965).
113. Baker, M. Tissue models: A living system on a chip. *Nature* **471**, 661-665 (2011).
114. Huh, D., Matthews, B.D., Mammoto, A., Montoya-Zavala, M., Hsin, H.Y. & Ingber, D.E. Reconstituting Organ-Level Lung Functions on a Chip. *Science* **328**, 1662-1668 (2010).
115. Zeck, G. & Fromherz, P. Noninvasive neuroelectronic interfacing with synaptically connected snail neurons immobilized on a semiconductor chip. *Proceedings of the National Academy of Sciences* **98**, 10457-10462 (2001).
116. Sung, J.H., Yu, J., Luo, D., Shuler, M.L. & March, J.C. Microscale 3-D hydrogel scaffold for biomimetic gastrointestinal (GI) tract model. *Lab on a Chip* **11**, 389-392 (2011).
117. Materne, E.-M., Tonevitsky, A.G. & Marx, U. Chip-based liver equivalents for toxicity testing - organotypicalness versus cost-efficient high throughput. *Lab on a Chip* **13**, 3481-3495 (2013).
118. Gershell, L.J. & Atkins, J.H. A brief history of novel drug discovery technologies. *Nat Rev Drug Discov* **2**, 321-327 (2003).
119. Khetani, S.R. & Bhatia, S.N. Microscale culture of human liver cells for drug development. *Nat Biotechnol* **26**, 120-126 (2008).
120. Toh, Y.-C., Lim, T.C., Tai, D., Xiao, G., van Noort, D. & Yu, H. A microfluidic 3D hepatocyte chip for drug toxicity testing. *Lab on a Chip* **9**, 2026-2035 (2009).
121. van Midwoud, P.M., Merema, M.T., Verweij, N., Groothuis, G.M. & Verpoorte, E. Hydrogel embedding of precision-cut liver slices in a microfluidic device improves drug metabolic activity. *Biotechnol Bioeng* (2011).
122. Ho, C.T., Lin, R.Z., Chang, W.Y., Chang, H.Y. & Liu, C.H. Rapid heterogeneous liver-cell on-chip patterning via the enhanced field-induced dielectrophoresis trap. *Lab Chip* **6**, 724-734 (2006).
123. Albrecht, D.R., Underhill, G.H., Wassermann, T.B., Sah, R.L. & Bhatia, S.N. Probing the role of multicellular organization in three-dimensional microenvironments. *Nat Methods* **3**, 369-375 (2006).
124. Olsavsky Goyak, K.M., Laurenzana, E.M. & Omiecinski, C.J. in, Vol. 640 115-138(2010).
125. Wlodkowic, D. & Cooper, J. Microfabricated analytical systems for integrated cancer cytomics. *Analytical and Bioanalytical Chemistry* **398**, 193-209 (2010).
126. Khoshmanesh, K., Nahavandi, S., Baratchi, S., Mitchell, A. & Kalantar-zadeh, K. Dielectrophoretic platforms for bio-microfluidic systems. *Biosensors and Bioelectronics* **26**, 1800-1814 (2011).
127. Manz, A., Graber, N. & Widmer, H.M. Miniaturized Total Chemical-Analysis Systems - a Novel Concept for Chemical Sensing. *Sensors and Actuators B-Chemical* **1**, 244-248 (1990).
128. Pethig, R. Review Article-Dielectrophoresis: Status of the theory, technology, and applications. *Biomicrofluidics* **4** (2010).
129. Menachery, A., Kremer, C., Wong, P.E., Carlsson, A., Neale, S.L., Barrett, M.P. *et al.* Counterflow Dielectrophoresis for Trypanosome Enrichment and Detection in Blood. *Sci. Rep.* **2** (2012).
130. Khoshmanesh, K., Akagi, J., Nahavandi, S., Skommer, J., Baratchi, S., Cooper, J.M. *et al.* Dynamic Analysis of Drug-Induced Cytotoxicity Using Chip-Based Dielectrophoretic Cell Immobilization Technology. *Analytical Chemistry* **83**, 2133-2144 (2011).
131. Gascoyne, P.R., Noshari, J., Anderson, T.J. & Becker, F.F. Isolation of rare cells from cell mixtures by dielectrophoresis. *Electrophoresis* **30**, 1388-1398 (2009).
132. Ramadan, Q., Samper, V., Poenar, D., Liang, Z., Yu, C. & Lim, T.M. Simultaneous cell lysis and bead trapping in a continuous flow microfluidic device. *Sensors and Actuators B-Chemical* **113**, 944-955 (2006).
133. Labeed, F.H., Coley, H.M., Thomas, H. & Hughes, M.P. Assessment of multidrug resistance reversal using dielectrophoresis and flow cytometry. *Biophysical Journal* **85**, 2028-2034 (2003).
134. Pohl, H.A. Dielectrophoresis : the behavior of neutral matter in nonuniform electric fields. (Cambridge University Press, Cambridge ; New York; 1978).
135. Wang, X.B., Huang, Y., Becker, F.F. & Gascoyne, P.R.C. A Unified Theory of Dielectrophoresis and Traveling-Wave Dielectrophoresis. *Journal of Physics D-Applied Physics* **27**, 1571-1574 (1994).
136. Huang, Y., Holzel, R., Pethig, R. & Wang, X.B. Differences in the AC electrostatics of viable and non-viable yeast cells determined through combined dielectrophoresis and electrorotation studies. *Phys Med Biol* **37**, 1499-1517 (1992).
137. Höber, R. Ein zweites Verfahren, die Leitfähigkeit im Innern von Zellen zu messen. *Pflüger's Archiv für die gesamte Physiologie des Menschen und der Tiere* **148**, 189-221 (1912).
138. Zellner, P. & Agah, M. Silicon insulator-based dielectrophoresis devices for minimized heating effects. *Electrophoresis* **33**, 2498-2507 (2012).
139. Jones, T.B. Liquid dielectrophoresis on the microscale. *Journal of Electrostatics* **51-52**, 290-299 (2001).
140. Marsh, J.L. & Thompson, L.M. Drosophila in the study of neurodegenerative disease. *Neuron* **52**, 169-178 (2006).

194 Bibliography

141. Leung, M.C.K., Williams, P.L., Benedetto, A., Au, C., Helmcke, K.J., Aschner, M. *et al.* Caenorhabditis elegans: An emerging model in biomedical and environmental toxicology. *Toxicological Sciences* **106**, 5-28 (2008).
142. Spitsbergen, J.M. & Kent, M.L. The state of the art of the zebrafish model for toxicology and toxicologic pathology research--advantages and current limitations. *Toxicol Pathol* **31 Suppl**, 62-87 (2003).
143. Rand, M.D. Drosophotoxicology: The growing potential for Drosophila in neurotoxicology. *Neurotoxicology and Teratology* **32**, 74-83 (2010).
144. Lieschke, G.J. & Currie, P.D. Animal models of human disease: zebrafish swim into view. *Nature Reviews Genetics* **8**, 353-367 (2007).
145. Hill, A.J., Teraoka, H., Heideman, W. & Peterson, R.E. Zebrafish as a Model Vertebrate for Investigating Chemical Toxicity. *Toxicological Sciences* **86**, 6-19 (2005).
146. *Zebrafish Make a Splash in FDA Research*, US Food and Drug Administration, Available from: <<http://www.fda.gov/ForConsumers/ConsumerUpdates/ucm343940.htm>>. [18/06/13]
147. Wilson, S., *Neuroanatomy*, Available from: <<http://www.ucl.ac.uk/zebrafish-group/research/neuroanatomy.php>>. [18/06/13]
148. *In Memory of George Streisinger "Founding Father" of Zebrafish Developmental and Genetic Research*, Institute of Neuroscience, University of Oregon, Available from: <http://www.neuro.uoregon.edu/k12/george_streisinger.html>. [18/06/13]
149. Parng, C. In vivo zebrafish assays for toxicity testing. *Curr Opin Drug Discov Devel* **8**, 100-106 (2005).
150. Sukardi, H., Chng, H.T., Chan, E.C.Y., Gong, Z.Y. & Lam, S.H. Zebrafish for drug toxicity screening: bridging the in vitro cell-based models and in vivo mammalian models. *Expert Opinion on Drug Metabolism & Toxicology* **7**, 579-589 (2011).
151. Khoshmanesh, K., Akagi, J., Hall, C.J., Crosier, K.E., Crosier, P.S., Cooper, J.M. *et al.* New rationale for large metazoan embryo manipulations on chip-based devices. *Biomicrofluidics* **6**, 24102-2410214 (2012).
152. Hulme, S.E., Shevkopyas, S.S., McGuigan, A.P., Apfeld, J., Fontana, W. & Whitesides, G.M. Lifespan-on-a-chip: microfluidic chambers for performing lifelong observation of *C. elegans*. *Lab on a Chip* **10**, 589-597 (2010).
153. Lucchetta, E.M., Munson, M.S. & Ismagilov, R.F. Characterization of the local temperature in space and time around a developing *Drosophila* embryo in a microfluidic device. *Lab on a Chip* **6**, 185-190 (2006).
154. Khoshmanesh, K., Kiss, N., Nahavandi, S., Evans, C.W., Cooper, J.M., Williams, D.E. *et al.* Trapping and imaging of micron-sized embryos using dielectrophoresis. *Electrophoresis* **32**, 3129-3132 (2011).
155. Wielhouwer, E.M., Ali, S., Al-Afandi, A., Blom, M.T., Olde Riekerink, M.B., Poelma, C. *et al.* Zebrafish embryo development in a microfluidic flow-through system. *Lab on a Chip* **11**, 1815-1824 (2011).
156. Yang, F., Chen, Z., Pan, J., Li, X., Feng, J. & Yang, H. An integrated microfluidic array system for evaluating toxicity and teratogenicity of drugs on embryonic zebrafish developmental dynamics. *Biomicrofluidics* **5**, 24115 (2011).
157. Lammer, E., Kamp, H.G., Hisgen, V., Koch, M., Reinhard, D., Salinas, E.R. *et al.* Development of a flow-through system for the fish embryo toxicity test (FET) with the zebrafish (*Danio rerio*). *Toxicology in Vitro* **23**, 1436-1442 (2009).
158. Graf, S.F., Hotzel, S., Liebel, U., Stemmer, A. & Knapp, H.F. Image-Based Fluidic Sorting System for Automated Zebrafish Egg Sorting into Multiwell Plates. *Jala* **16**, 105-111 (2011).
159. Pardo-Martin, C., Chang, T.Y., Koo, B.K., Gilleland, C.L., Wasserman, S.C. & Yanik, M.F. High-throughput in vivo vertebrate screening. *Nature Methods* **7**, 634-U646 (2010).
160. Akagi, J., Khoshmanesh, K., Evans, B., Hall, C.J., Crosier, K.E., Cooper, J.M. *et al.* Miniaturized Embryo Array for Automated Trapping, Immobilization and Microperfusion of Zebrafish Embryos. *Plos One* **7**, e36630 (2012).
161. Che-Hsin, L., Gwo-Bin, L., Bao-Wen, C. & Guan-Liang, C. A new fabrication process for ultra-thick microfluidic microstructures utilizing SU-8 photoresist. *Journal of Micromechanics and Microengineering* **12**, 590 (2002).
162. Lantada, A.D. & Morgado, P.L. in Annual Review of Biomedical Engineering, Vol 14, Vol. 14. (ed. M.L. Yarmush) 73-96 (Annual Reviews, Palo Alto; 2012).
163. Malek, C.G.K. Laser processing for bio-microfluidics applications (part II). *Analytical and Bioanalytical Chemistry* **385**, 1362-1369 (2006).
164. Hruby, J. Overview of LIGA microfabrication. *High Energy Density and High Power Rf* **625**, 55-61 (2002).

165. Islam, M.Z., McMullin, J.N. & Tsui, Y.Y. Rapid and cheap prototyping of a microfluidic cell sorter. *Cytometry Part A* **79A**, 361-367 (2011).
166. Ogilvie, I.R.G., Sieben, V.J., Floquet, C.F.A., Zmijan, R., Mowlem, M.C. & Morgan, H. Reduction of surface roughness for optical quality microfluidic devices in PMMA and COC. *Journal of Micromechanics and Microengineering* **20** (2010).
167. Yuen, P.K. & Goral, V.N. Low-cost rapid prototyping of flexible microfluidic devices using a desktop digital craft cutter. *Lab on a Chip* **10**, 384-387 (2010).
168. Suriano, R., Kuznetsov, A., Eaton, S.M., Kiyani, R., Cerullo, G., Osellame, R. *et al.* Femtosecond laser ablation of polymeric substrates for the fabrication of microfluidic channels. *Applied Surface Science* **257**, 6243-6250 (2011).
169. Klank, H., Kutter, J.P. & Geschke, O. CO₂-laser micromachining and back-end processing for rapid production of PMMA-based microfluidic systems. *Lab on a Chip* **2**, 242-246 (2002).
170. Malek, C.G.K. Laser processing for bio-microfluidics applications (part I). *Analytical and Bioanalytical Chemistry* **385**, 1351-1361 (2006).
171. Melchels, F.P.W., Domingos, M.A.N., Klein, T.J., Malda, J., Bartolo, P.J. & Huttmacher, D.W. Additive manufacturing of tissues and organs. *Progress in Polymer Science* **37**, 1079-1104 (2012).
172. Hong, T.F., Ju, W.J., Wu, M.C., Tai, C.H., Tsai, C.H. & Fu, L.M. Rapid prototyping of PMMA microfluidic chips utilizing a CO₂ laser. *Microfluidics and Nanofluidics* **9**, 1125-1133 (2010).
173. Hull, C.W., *Apparatus for production of three-dimensional objects by stereolithography*, US Patent 4575330 A, 1986
174. Gorjup, D.M. & Soc Plast, E. Stereolithography - A System for Rapid Turnaround of Plastic Models and Patterns. *Improving Competitiveness through Plastics Innovation (Preprint)*, T1-T5 (1988).
175. Zhang, X., Jiang, X.N. & Sun, C. Micro-stereolithography of polymeric and ceramic microstructures. *Sensors and Actuators a-Physical* **77**, 149-156 (1999).
176. *Additive Manufacturing Technologies*, NZ Rapid Manufacturing Association, Available from: <<http://www.ciri.org.nz/nzrma/technologies.html>>. [12/10/2013]
177. *Viper si-2 SLA system*, 3D Systems, Available from: <http://www.3dsystems.com/products/datafiles/viper/datasheets/International/viper_si2_uk.qxd.pdf>. [15/09/13]
178. Barnett, J., Batchelder, J.S., Crump, S.S., Sampson, T., Zinniel, R.L., Crump, S. *et al.*, *Digital manufacturing system for building three-dimensional (3D) object with metal-based alloy*, US Patent 2009314391-A1, 2008
179. Masood, S.H. Intelligent rapid prototyping with fused deposition modelling. *Rapid Prototyping Journal* **2**, 24-33 (1996).
180. *FDM: Materials & datasheets*, Materialise, Available from: <<http://prototyping.materialise.com/fdm-materials-datasheets-0>>. [12/10/13]
181. Mannoor, M.S., Jiang, Z., James, T., Kong, Y.L., Malatesta, K.A., Soboyejo, W.O. *et al.* 3D Printed Bionic Ears. *Nano Letters* **13**, 2634-2639 (2013).
182. *HD 3100 and HD Plus Pro*, 3D Systems, Available from: <<http://printin3d.com/3d-printers/projet-hd-3510-3d-professional-3d-printer>>. [19/06/13]
183. *Objet30 Pro*, Stratasys Available from: <<http://www.stratasys.com/3d-printers/design-series/precision/objet30-pro>>. [12/10/2013]
184. Harvey, H.W.S.M.P.I.E.C. Application of fused deposition modeling rapid prototyping system to the development of microchannels. *BioMEMS and Smart Nanostructures* **4590**, 213-220 (2001).
185. Kitson, P.J., Rosnes, M.H., Sans, V., Dragone, V. & Cronin, L. Configurable 3D-Printed millifluidic and microfluidic 'lab on a chip' reactionware devices. *Lab on a Chip* **12**, 3267-3271 (2012).
186. McCullough, E.J. & Yadavalli, V.K. Surface modification of fused deposition modeling ABS to enable rapid prototyping of biomedical microdevices. *Journal of Materials Processing Technology* **213**, 947-954 (2013).
187. Binder, T.M., Moertl, D., Mundigler, G., Rehak, G., Franke, M., Delle-Karth, G. *et al.* Stereolithographic biomodeling to create tangible hard copies of cardiac structures from echocardiographic data: In vitro and in vivo validation. *Journal of the American College of Cardiology* **35**, 230-237 (2000).
188. Lantada, A.D., Endrino, J.L., Vaquero, V.S., Mosquera, A., Lafont, P. & García-Ruiz, J.P. Tissue Engineering Using Novel Rapid Prototyped Diamond-Like Carbon Coated Scaffolds. *Plasma Processes and Polymers* **9**, 98-107 (2012).
189. *LIVE/DEAD® Viability/Cytotoxicity Kit, for mammalian cells*, Life Technologies, Available from: <<http://products.invitrogen.com/ivgn/product/L3224>>. [20/06/13]
190. Qin, D., Xia, Y.N., Rogers, J.A., Jackman, R.J., Zhao, X.M. & Whitesides, G.M. Microfabrication, microstructures and microsystems. *Microsystem Technology in Chemistry and Life Science* **194**, 1-20 (1998).

196 Bibliography

191. Moreau, W.M. & Moreau, W. Semiconductor lithography: principles, practices, and materials, Vol. 233. (Plenum Press New York, 1988).
192. Xia, Y. & Whitesides, G.M. Soft Lithography. *Annual Review of Materials Science* **28**, 153-184 (1998).
193. Xia, Y., McClelland, J.J., Gupta, R., Qin, D., Zhao, X.-M., Sohn, L.L. *et al.* Replica molding using polymeric materials: A practical step toward nanomanufacturing. *Advanced Materials* **9**, 147-149 (1997).
194. *ImageJ*, Available from: <<http://rsbweb.nih.gov/ij/>>. [05/07/13]
195. Zaouk, R., Park, B. & Madou, M. in *Microfluidic Techniques*, Vol. 321. (ed. S. Minteer) 5-15 (Humana Press, 2006).
196. Kiewit, D.A. Microtool Fabrication by Etch Pit Replication. *Review of Scientific Instruments* **44**, 1741-1742 (1973).
197. Ayon, A., Lin, C., Braff, R., Schmidt, M. & Bayt, R. Etching Characteristics and Profile Control in a Time Multiplexed Inductively Coupled Plasma Etcher. (1998).
198. Chang, C.L., Wang, Y.F., Kanamori, Y., Shih, J.J., Kawai, Y., Lee, C.K. *et al.* Etching submicrometer trenches by using the Bosch process and its application to the fabrication of antireflection structures. *Journal of Micromechanics and Microengineering* **15**, 580-585 (2005).
199. Xia, Y.N., Kim, E., Zhao, X.M., Rogers, J.A., Prentiss, M. & Whitesides, G.M. Complex optical surfaces formed by replica molding against elastomeric masters. *Science* **273**, 347-349 (1996).
200. Zhao, X.M., Xia, Y.N. & Whitesides, G.M. Fabrication of three-dimensional micro-structures: Microtransfer molding. *Advanced Materials* **8**, 837-& (1996).
201. Khanafer, K., Duprey, A., Schlicht, M. & Berguer, R. Effects of strain rate, mixing ratio, and stress-strain definition on the mechanical behavior of the polydimethylsiloxane (PDMS) material as related to its biological applications. *Biomedical Microdevices* **11**, 503-508 (2009).
202. *BASi Syringe pumps*, BASi, Available from: <<http://www.basinc.com/products/iv/MDperf-pumps.php>>. [19/10/13]
203. *Omnifit Connectors & Connectors with valves*, Omnifit, Available from: <<http://www.omnifit.com/pdf/Connectors.pdf>>. [26/07/13]
204. Zarowna-Dabrowska, A., McKenna, E.O., Schutte, M.E., Glidle, A., Chen, L., Cuestas-Ayllon, C. *et al.* Generation of primary hepatocyte microarrays by piezoelectric printing. *Colloids Surf B Biointerfaces* **89**, 126-132 (2012).
205. *Cell Biology - Liver and Pancreas*, Yale School of Medicine, Available from: <http://medcell.med.yale.edu/systems_cell_biology/liver_and_pancreas.php>. [27/09/13]
206. Motta, P. & Porter, K. Structure of rat liver sinusoids and associated tissue spaces as revealed by scanning electron microscopy. *Cell and tissue research* **148**, 111-125 (1974).
207. Bonfiglio, A., Leungchavaphongse, K., Repetto, R. & Siggers, J.H. Mathematical Modeling of the Circulation in the Liver Lobule. *Journal of Biomechanical Engineering-Transactions of the Asme* **132** (2010).
208. Wambaugh, J. & Shah, I. Simulating Microdosimetry in a Virtual Hepatic Lobule. *Plos Computational Biology* **6**, 16 (2010).
209. *Microplate Dimension Sheets 96 Wells*, Corning Life Sciences, Available from: <http://catalog2.corning.com/lifesciences/media/equipment_compatibility/MD_Microplate_Dimension_Sheets_96_Well.pdf>. [14/10/13]
210. Nahmias, Y., Berthiaume, F. & Yarmush, M.L. Integration of technologies for hepatic tissue engineering. *Adv Biochem Eng Biotechnol* **103**, 309-329 (2007).
211. MacSween, R.N., Anthony, P.P. & Scheuer, P.J. Pathology of the liver. (Churchill Livingstone Edinburgh, 1979).
212. Kuntz, E. & Kuntz, H.-D. Hepatology: textbook and atlas: history, morphology, biochemistry, diagnostics, clinic, therapy. (Springer, 2008).
213. Mitchell, D.G., Carney, F.J. & Woolsey, E.J., *Interconnect system and method of fabrication*, US Patent 5773359 A, 1998
214. Kuhlmann, I. The prophylactic use of antibiotics in cell culture. *Cytotechnology* **19**, 95-105 (1995).
215. Vonen, B. & Morland, J. Penicillin toxicity in isolated rat hepatocytes revealed by decreased incorporation of valine into proteins. *Acta Pharmacol Toxicol* **51**, 81-86 (1982).
216. Albrecht, D.R., Sah, R.L. & Bhatia, S.N. Geometric and material determinants of patterning efficiency by dielectrophoresis. *Biophysical Journal* **87**, 2131-2147 (2004).
217. Stevens, M.M., Mayer, M., Anderson, D.G., Weibel, D.B., Whitesides, G.M. & Langer, R. Direct patterning of mammalian cells onto porous tissue engineering substrates using agarose stamps. *Biomaterials* **26**, 7636-7641 (2005).
218. Verma, P., Verma, V., Ray, P. & Ray, A.R. Agar-gelatin hybrid sponge-induced three-dimensional in vitro 'liver-like' HepG2 spheroids for the evaluation of drug cytotoxicity. *Journal of Tissue Engineering and Regenerative Medicine* **3**, 368-376 (2009).

219. Bhatia, S.N., Balis, U.J., Yarmush, M.L. & Toner, M. Effect of cell-cell interactions in preservation of cellular phenotype: cocultivation of hepatocytes and nonparenchymal cells. *FASEB J* **13**, 1883-1900 (1999).
220. Tang, J., Mao, R., Tung, M.A. & Swanson, B.G. Gelling temperature, gel clarity and texture of gellan gels containing fructose or sucrose. *Carbohydrate Polymers* **44**, 197-209 (2001).
221. Gray, D.S., Tan, J.L., Voldman, J. & Chen, C.S. Dielectrophoretic registration of living cells to a microelectrode array. *Biosens Bioelectron* **19**, 1765-1774 (2004).
222. Jones, T.B. Basic theory of dielectrophoresis and electrorotation. *Ieee Engineering in Medicine and Biology Magazine* **22**, 33-42 (2003).
223. Glasser, H. & Fuhr, G. Cultivation of cells under strong ac-electric field—differentiation between heating and trans-membrane potential effects. *Bioelectrochemistry and Bioenergetics* **47**, 301-310 (1998).
224. Nordqvist, D. & Vilgis, T. Rheological Study of the Gelation Process of Agarose-Based Solutions. *Food Biophysics* **6**, 450-460 (2011).
225. Ho, C.-T., Lin, R.-Z., Chen, R.-J., Chin, C.-K., Gong, S.-E., Chang, H.-Y. *et al.* Liver-cell patterning Lab Chip: mimicking the morphology of liver lobule tissue. *Lab on a Chip* (2013).
226. Hall, C., Flores, M.V., Chien, A., Davidson, A., Crosier, K. & Crosier, P. Transgenic zebrafish reporter lines reveal conserved Toll-like receptor signaling potential in embryonic myeloid leukocytes and adult immune cell lineages. *J Leukoc Biol* **85**, 751-765 (2009).
227. Kimmel, C.B., Ballard, W.W., Kimmel, S.R., Ullmann, B. & Schilling, T.F. Stages of embryonic development of the zebrafish. *Dev Dyn* **203**, 253-310 (1995).
228. AD7013MZT Dino-Lite Premier, Dino-Lite, Available from: <http://www.dino-lite.com/products_list_minute.php?product_number=AD7013MZT%20Dino-Lite%20Premier>. [09/10/13]
229. Watershed XC 11122, DSM Somos, Available from: <http://www.marmaxdesign.com/pdf/ST_Watershed%2011122XC.pdf>. [19/10/13]
230. Ye, Q., Spencer, P., Wang, Y. & Misra, A. Relationship of solvent to the photopolymerization process, properties, and structure in model dentin adhesives. *Journal of Biomedical Materials Research Part A* **80A**, 342-350 (2007).
231. Geiger, B., Bershady, A., Pankov, R. & Yamada, K.M. Transmembrane crosstalk between the extracellular matrix and the cytoskeleton. *Nat Rev Mol Cell Biol* **2**, 793-805 (2001).
232. Gomez-Lechon, M.J., Donato, M.T., Castell, J.V. & Jover, R. Human hepatocytes as a tool for studying toxicity and drug metabolism. *Curr Drug Metab* **4**, 292-312 (2003).
233. Tuschl, G., Lauer, B. & Mueller, S.O. Primary hepatocytes as a model to analyze species-specific toxicity and drug metabolism. *Expert Opin Drug Metab Toxicol* **4**, 855-870 (2008).
234. Grant, M.H., Morgan, C., Henderson, C., Malsch, G., Seifert, B., Albrecht, W. *et al.* The viability and function of primary rat hepatocytes cultured on polymeric membranes developed for hybrid artificial liver devices. *J Biomed Mater Res A* **73**, 367-375 (2005).
235. Revzin, A., Rajagopalan, P., Tilles, A.W., Berthiaume, F., Yarmush, M.L. & Toner, M. Designing a hepatocellular microenvironment with protein microarraying and poly(ethylene glycol) photolithography. *Langmuir* **20**, 2999-3005 (2004).
236. Nebert, D.W. & Gonzalez, F.J. P450 genes: structure, evolution, and regulation. *Annu Rev Biochem* **56**, 945-993 (1987).
237. Lynch, T. & Price, A. The effect of cytochrome P450 metabolism on drug response, interactions, and adverse effects. *Am Fam Physician* **76**, 391-396 (2007).
238. Park, K., Williams, D.P., Naisbitt, D.J., Kitteringham, N.R. & Pirmohamed, M. Investigation of toxic metabolites during drug development. *Toxicol Appl Pharmacol* **207**, 425-434 (2005).
239. Hammond, D.K. & Strobel, H.W. Ethoxyresorufin O-Deethylase Activity in Intact Human-Cells. *Toxicology in Vitro* **6**, 41-46 (1992).
240. Kane, B.J., Zinner, M.J., Yarmush, M.L. & Toner, M. Liver-specific functional studies in a microfluidic array of primary mammalian hepatocytes. *Anal Chem* **78**, 4291-4298 (2006).
241. Resealable Chip Interface, thin Part Number: 3000306, Dolomite Microfluidics UK, Available from: <http://www.dolomite-microfluidics.com/images/stories/PDFs/datasheets/3000305_resealable_chip_interface_product_datasheet.pdf>. [12/06/13]
242. Linear Connector 4-way (Part Number: 3000024), Dolomite Microfluidics UK, Available from: <http://www.dolomite-microfluidics.com/webshop/connectors-m1-connectors-linear-c-1_3_4/linear-connector-4-way-p-3>. [08/10/13]
243. Roth, E.A., Xu, T., Das, M., Gregory, C., Hickman, J.J. & Boland, T. Inkjet printing for high-throughput cell patterning. *Biomaterials* **25**, 3707-3715 (2004).

198 Bibliography

244. Folch, A., Ayon, A., Hurtado, O., Schmidt, M.A. & Toner, M. Molding of deep polydimethylsiloxane microstructures for microfluidics and biological applications. *J Biomech Eng* **121**, 28-34 (1999).
245. Zhang, S., Tong, W., Zheng, B., Susanto, T.A., Xia, L., Zhang, C. *et al.* A robust high-throughput sandwich cell-based drug screening platform. *Biomaterials* **32**, 1229-1241 (2011).
246. Mehta, G., Mehta, K., Sud, D., Song, J., Bersano-Begey, T., Futai, N. *et al.* Quantitative measurement and control of oxygen levels in microfluidic poly(dimethylsiloxane) bioreactors during cell culture. *Biomedical Microdevices* **9**, 123-134 (2007).
247. Toh, Y.C., Zhang, C., Zhang, J., Khong, Y.M., Chang, S., Samper, V.D. *et al.* A novel 3D mammalian cell perfusion-culture system in microfluidic channels. *Lab Chip* **7**, 302-309 (2007).
248. *Consolidated List of Products Whose Consumption and/or Sale Have Been Banned, Withdrawn, Severely Restricted or not Approved by Governments Fourteenth Issue*, E.a.S. Affairs, United Nations, **14th edition**, 2009
249. Allen, J.W. & Bhatia, S.N. Improving the next generation of bioartificial liver devices. *Semin Cell Dev Biol* **13**, 447-454 (2002).
250. Paul, S.M., Mytelka, D.S., Dunwiddie, C.T., Persinger, C.C., Munos, B.H., Lindborg, S.R. *et al.* How to improve R&D productivity: the pharmaceutical industry's grand challenge. *Nature Reviews Drug Discovery* **9**, 203-214 (2010).
251. Taguchi, T., Rao, Z., Ito, M. & Matsuda, M. Induced albumin secretion from HepG2 spheroids prepared using poly(ethylene glycol) derivative with oleyl groups. *Journal of Materials Science-Materials in Medicine* **22**, 2357-2363 (2011).
252. Abbott, A. Cell culture: Biology's new dimension. *Nature* **424**, 870-872 (2003).
253. Seo, S.J., Kim, I.Y., Choi, Y.J., Akaike, T. & Cho, C.S. Enhanced liver functions of hepatocytes cocultured with NIH 3T3 in the alginate/galactosylated chitosan scaffold. *Biomaterials* **27**, 1487-1495 (2006).
254. *Multiphysics AC/DC module*, COMSOL, Available from: <<http://www.uk.comsol.com/acdc-module>>. [16/08/13]
255. Zhang, L., Che, L.M., Zhou, W.B. & Chen, X.D. Rheological Behavior of Agar Solution in Relation to the Making of Instant Edible Bird's Nest products. *International Journal of Food Engineering* **8** (2012).
256. Mackowiak, P.A., Wasserman, S.S. & Levine, M.M. A critical appraisal of 98.6°f, the upper limit of the normal body temperature, and other legacies of Carl Reinhold August Wunderlich. *JAMA* **268**, 1578-1580 (1992).
257. Watanabe, I. & Okada, S. Effects of temperature on growth rate of cultured mammalian cells (L5178Y). *J Cell Biol* **32**, 309-323 (1967).
258. Labropoulos, K.C., Niesz, D.E., Danforth, S.C. & Kevrekidis, P.G. Dynamic rheology of agar gels: theory and experiments. Part II: gelation behavior of agar sols and fitting of a theoretical rheological model. *Carbohydrate Polymers* **50**, 407-415 (2002).
259. Mohammed, Z.H., Hember, M.W.N., Richardson, R.K. & Morris, E.R. Kinetic and equilibrium processes in the formation and melting of agarose gels. *Carbohydrate Polymers* **36**, 15-26 (1998).
260. Jones, T.B. *Electromechanics of particles*. (Cambridge University Press, 2005).
261. Fuhr, G., Glasser, H., Müller, T. & Schnelle, T. Cell manipulation and cultivation under a.c. electric field influence in highly conductive culture media. *Biochimica et Biophysica Acta (BBA) - General Subjects* **1201**, 353-360 (1994).
262. Lan, S.-F., Safiejko-Mrocicka, B. & Starly, B. Long-term cultivation of HepG2 liver cells encapsulated in alginate hydrogels: A study of cell viability, morphology and drug metabolism. *Toxicology in Vitro* **24**, 1314-1323 (2010).
263. Dvir-Ginzberg, M., Gamlieli-Bonshtein, I., Agbaria, R. & Cohen, S. Liver tissue engineering within alginate scaffolds: effects of cell-seeding density on hepatocyte viability, morphology, and function. *Tissue Eng* **9**, 757-766 (2003).
264. Surapaneni, S., Pryor, T., Klein, M.D. & Matthew, H.W. Rapid hepatocyte spheroid formation: optimization and long-term function in perfused microcapsules. *Asaio J* **43**, M848-853 (1997).
265. Bissell, D.M., Caron, J.M., Babiss, L.E. & Friedman, J.M. Transcriptional regulation of the albumin gene in cultured rat hepatocytes. Role of basement-membrane matrix. *Mol Biol Med* **7**, 187-197 (1990).
266. Becker, H. Hype, hope and hubris: the quest for the killer application in microfluidics. *Lab on a Chip* **9**, 2119-2122 (2009).
267. Hwang, H. & Lu, H. Microfluidic tools for developmental studies of small model organisms – nematodes, fruit flies, and zebrafish. *Biotechnology Journal* **8**, 192-205 (2013).
268. Hulme, S.E., Shevkoplyas, S.S. & Samuel, A. Microfluidics: streamlining discovery in worm biology. *Nat Meth* **5**, 589-590 (2008).

269. Wlodkowic, D., Khoshmanesh, K., Akagi, J., Williams, D.E. & Cooper, J.M. Wormometry-on-a-chip: Innovative technologies for in situ analysis of small multicellular organisms. *Cytometry Part A* **79A**, 799-813 (2011).
270. Wheeler, G.N. & Brandli, A.W. Simple vertebrate models for chemical genetics and drug discovery screens: lessons from zebrafish and *Xenopus*. *Dev Dyn* **238**, 1287-1308 (2009).
271. Zon, L.I. & Peterson, R.T. In vivo drug discovery in the zebrafish. *Nat Rev Drug Discov* **4**, 35-44 (2005).
272. Funfak, A., Brosing, A., Brand, M. & Kohler, J.M. Micro fluid segment technique for screening and development studies on *Danio rerio* embryos. *Lab Chip* **7**, 1132-1138 (2007).
273. Son, S.U. & Garrell, R.L. Transport of live yeast and zebrafish embryo on a droplet digital microfluidic platform. *Lab Chip* **9**, 2398-2401 (2009).
274. Miscevic, F., Rotstein, O. & Wen, X.Y. Advances in Zebrafish High Content and High Throughput Technologies. *Combinatorial Chemistry & High Throughput Screening* **15**, 515-521 (2012).
275. Li, M.G., Tian, X.Y. & Chen, X.B. A brief review of dispensing-based rapid prototyping techniques in tissue scaffold fabrication: role of modeling on scaffold properties prediction. *Biofabrication* **1**, 1758-5082 (2009).
276. Lohfeld, S., Tyndyk, M., Cahill, S., Flaherty, N., Barron, V. & McHugh, P. A method to fabricate small features on scaffolds for tissue engineering via selective laser sintering. (2010).
277. Tzezana, R., Zussman, E. & Levenberg, S. A layered ultra-porous scaffold for tissue engineering, created via a hydrospinning method. *Tissue Engineering Part C: Methods* **14**, 281-288 (2008).
278. Díaz-Lantada, A., Mosquera, A., Endrino, J.L. & Lafont, P. Design and rapid prototyping of DLC coated fractal surfaces for tissue engineering applications. *Journal of Physics: Conference Series* **252**, 012003 (2010).
279. Stampfl, J., Fouad, H., Seidler, S., Liska, R., Schwager, F., Woesz, A. *et al.* Fabrication and moulding of cellular materials by rapid prototyping. *International Journal of Materials and Product Technology* **21**, 285-296 (2004).
280. Infuehr, R., Pucher, N., Heller, C., Lichtenegger, H., Liska, R., Schmidt, V. *et al.* Functional polymers by two-photon 3D lithography. *Applied Surface Science* **254**, 836-840 (2007).
281. *mp6 Micropump*, Bartels Mikrotechnik GmbH, Available from: <<http://www.bartels-mikrotechnik.de/index.php/mp6.html>>. [09/10/13]
282. *mp-x Controller*, Bartels Mikrotechnik GmbH, Available from: <<http://www.bartels-mikrotechnik.de/index.php/mp-x.html>>. [09/10/13]
283. *24 well plate with cover drawings*, Corning, Available from: <http://catalog2.corning.com/lifesciences/media/microplate_drawings/24_well_ps_plate_with_cover.pdf>. [15/10/12]
284. Westerfield, M. The zebrafish book : a guide for the laboratory use of zebrafish (*Brachydanio rerio*). (M. Westerfield, Eugene, Oregon; 1993).
285. Lammer, E., Carr, G.J., Wendler, K., Rawlings, J.M., Belanger, S.E. & Braunbeck, T. Is the fish embryo toxicity test (FET) with the zebrafish (*Danio rerio*) a potential alternative for the fish acute toxicity test? *Comp Biochem Physiol C Toxicol Pharmacol* **149**, 196-209 (2009).
286. Fraysse, B., Mons, R. & Garric, J. Development of a zebrafish 4-day embryo-larval bioassay to assess toxicity of chemicals. *Ecotoxicol Environ Saf* **63**, 253-267 (2006).
287. *SolidView Lite*, SolidView, Available from: <<http://www.solidview.com/>>. [18/03/14]
288. *VisiJet Crystal EX200*, 3D systems, Available from: <<http://www.3dsystems.com/sites/www.3dsystems.com/files/24184-S02-00-B-MSDS-US-English-EX-200-Crystal.pdf>>. [30/09/12]
289. Williams, D.F. On the mechanisms of biocompatibility. *Biomaterials* **29**, 2941-2953 (2008).
290. *List of the standards in the 10993 series*, Wikipedia, Available from: <http://en.wikipedia.org/wiki/ISO_10993>. [21/03/14]
291. *Medical Devices*, U.S. Food and Drug Administration, Available from: <<http://www.fda.gov/MedicalDevices/DeviceRegulationandGuidance/default.htm>>. [21/03/14]
292. Stephens, B., Azimi, P., El Orch, Z. & Ramos, T. Ultrafine particle emissions from desktop 3D printers. *Atmospheric Environment* **79**, 334-339 (2013).
293. Morawska, L., He, C., Johnson, G., Jayaratne, R., Salthammer, T., Wang, H. *et al.* An Investigation into the Characteristics and Formation Mechanisms of Particles Originating from the Operation of Laser Printers. *Environmental Science & Technology* **43**, 1015-1022 (2009).
294. Park, M., Neigh, A.M., Vermeulen, J.P., de la Fonteyne, L.J.J., Verharen, H.W., Briede, J.J. *et al.* The effect of particle size on the cytotoxicity, inflammation, developmental toxicity and genotoxicity of silver nanoparticles. *Biomaterials* **32**, 9810-9817 (2011).
295. Xiong, D.W., Fang, T., Yu, L.P., Sima, X.F. & Zhu, W.T. Effects of nano-scale TiO₂, ZnO and their bulk counterparts on zebrafish: Acute toxicity, oxidative stress and oxidative damage. *Science of the Total Environment* **409**, 1444-1452 (2011).

200 Bibliography

296. Hartung, T., Blaauboer, B.J., Bosgra, S., Carney, E., Coenen, J., Conolly, R.B. *et al.* An Expert Consortium Review of the EC-commissioned Report "Alternative (Non-Animal) Methods for Cosmetics Testing: Current Status and Future Prospects-2010". *Altex-Alternatives to Animal Experimentation* **28**, 183-209 (2011).
297. Glicklis, R., Shapiro, L., Agbaria, R., Merchuk, J.C. & Cohen, S. Hepatocyte behavior within three-dimensional porous alginate scaffolds. *Biotechnol Bioeng* **67**, 344-353 (2000).
298. Derda, R., Tang, S.K.Y., Laromaine, A., Mosadegh, B., Hong, E., Mwangi, M. *et al.* Multizone Paper Platform for 3D Cell Cultures. *Plos One* **6**, 14 (2011).